Measurement of the longitudinal polarization of the top quark in top-antitop events using the ATLAS detector.

A thesis submitted by

Samuel Frederick Hamilton

in partial fulfillment of the requirements for the degree of

Doctor of Philosophy

in

Physics

Tufts University

February 2014

Adviser: Dr. Krzysztof Sliwa

Abstract

This thesis presents measurements of the longitudinal polarization of the top quark in top-antitop quark pair events, using 4.7 fb^{-1} of proton-proton collision data recorded with the ATLAS detector at the Large Hadron Collider at $\sqrt{s} = 7$ TeV. The final state considered contains one isolated lepton (electron or muon) and jets. Two measurements of the product of the charged lepton's spin-analyzing power and its degree of longitudinal polarization, $\alpha_\ell P$, are performed assuming that the longitudinal polarization of the top quark is induced by either a CP conserving process or a maximally CP violating process. The resulting measurements, $\alpha_\ell P_{\text{CPC}} = -0.034 \pm 0.017\,(\text{stat.})^{+0.038}_{-0.037}\,(\text{syst.})$ and $\alpha_\ell P_{\text{CPV}} = 0.023 \pm 0.019\,(\text{stat.})^{+0.012}_{-0.011}\,(\text{syst.})$ are in good agreement with the standard model expectation of negligible longitudinal polarization of the top quark in top-antitop quark pair production.

Acknowledgements

Writing this acknowledgment has afforded me the opportunity to reflect on all of the wonderful people who have helped me successfully pursue a PhD in high energy particle physics. This thesis would not be possible without the support, mentoring, and love from those individuals. It truly does take a village.

First and foremost, I would like to acknowledge my wife Hannah by dedicating this thesis to her. She has helped guide me through the toughest of challenges by providing me with her unwavering support and encouragement, instilling in me the belief that those challenges could be met. Half of this degree belongs to you.

Next, this thesis would not be possible without the dedicated support of my adviser Krzysztof Sliwa. I cannot thank him enough for providing me with the opportunity to work at the most interesting experiment in the world. As my adviser, Krzysztof has taught me how to be a thorough, creative, and dedicated research scientist. He has instilled his work ethic and passion into me during the past six and a half years through careful and honest mentoring. As my colleague, he has demonstrated the level of responsibility and teamwork that is necessary to succeed in a collaboration. As a professor, he has facilitated my intellectual growth in the classroom. Krzysztof pours his heart into the well being of his students, ensuring that they have the most positive experience during their stay at Tufts. I will certainly miss attending Journal Club.

I would also like to acknowledge my thesis committee for their time and effort during the defense process. Thank you Dr. Austin Napier, Dr. Roger Tobin, Dr. Hugh Gallagher, and Dr. Joao Guimaraes da Costa.

The notion of two ministers raising a son that would eventually work at the "god" particle experiment sounds like the punchline of a really bad joke; bad jokes aside, that is the reality for me and my parents. I owe a debt of gratitude to my parents for providing me with the intellectual foundation on which I have built upon. Their constant love and support has helped me immensely. To my other parents, Karen and Elliot, I also thank you for your love and support. I could not have achieved this goal without their help in the development my project management skills. In addition, I'd like to thank the Berman, Glickman, Kalmbach and Piatt families for their love and support.

The analysis presented in this thesis was in collaboration with many individuals, all of whom I'd like to thank. I would like to make special mention to the ATLAS top polarization team members: Matt Rudolph, Yvonne Peters, Sara Borroni, Ralph Schäfer, and Cécile Deterre. I had an amazing experience working with the top polarization team and wish them the best of luck with future physics measurements. I would also like to acknowledge my fellow ATLAS colleagues at Tufts University: Austin Napier, Hugo Beauchemin, Jeffrey Wetter, and Sharka Todorova. Each member of the Tufts ATLAS team played a pivotal roll in my development as an ATLAS physicist. A special thank you is in order for Sharka; she was the first person to introduce me to ATLAS software and provided great support during my trips to CERN. In addition, I'd like to thank my friends at CERN for making my visits so enjoyable.

There are many people at Tufts University who deserve praise for making my graduate education a first class experience. First, I'd like to thank Gary Goldstein for his time and effort in helping me to understand the theory behind top quark physics. I'd also like to thank the faculty members in the Physics and Astronomy department. They are

some of the finest instructors that higher education has to offer, and I feel privileged for having participated in their classrooms. I'd like to thank my fellow Tufts students who participated in homework sessions, journal club, and social activities; you made the Tufts experience extremely enjoyable. A special thanks goes to Ozgur for taking pictures at the thesis defense. Last, but certainly not least, I'd like to thank the secretaries. Gayle Grant helped me to acclimate myself to the department when I first arrived at Tufts; she and Shannon Landis were also a great resource as the years progressed. My experience at Sci Tech would not have been the same without Jean Intoppa and Jackie DiMichele, whose hard work and friendliness made working at Sci Tech a pleasure.

It is due to my friend and classmate Nik Hartman and my professor Dr. Chandralekha Singh of the University of Pittsburgh that I made my decision to attend graduate school, acquiring a PhD in physics. I was hooked on physics after being introduced to Dr. Singh's superb teaching style and dedication to the study of physics education. She also had a profound effect on Nik, which sparked a great friendship between us. After many late night study sessions and coding exercises, we both ended up attending graduate school for a PhD in physics.

On the same lines as Nik, my friend and fellow ATLAS colleague at Tufts, Jeffrey Wetter, helped me in my quest for a PhD. He and I began the same year and spent many hours studying together. After class work had ended, we both began research on the ATLAS experiment, spending numerous hours debugging code and working on top quark analyses. He has been a great resource and an even better friend.

Finally, I'd like to thank my mentor John Bobrowich for helping me determine the next steps after graduate school. He has done a spectacular job of introducing me to a wide variety of potential opportunities by plugging me into his network. His time and effort is greatly appreciated.

Contents

List of Tables

List of Figures

Measurement of the longitudinal polarization of the top quark in top-antitop events using the ATLAS detector.

Chapter 1.

Introduction

High energy particle physics is a branch of physics concerned with the constitution, properties, and interactions of elementary particles. When compared to current data, the most accurate theoretical description of the fundamental interactions between particles is described by the Standard Model (SM) of particle physics, incorporating the electromagnetic, weak, and strong forces. The SM is a quantum gauge field theory that predicts two types of fundamental point like particles, quarks and leptons, whose interactions are mediated by gauge bosons. The quarks and leptons of the SM comprise three generations of matter (anti-matter) particles; each generation containing particles (anti-particles) with the same properties across the different generations, but with larger masses as the generations increase. The most familiar particles that humans interact with are electrons, protons, and neutrons. Electrons are fundamental first generation leptons; meanwhile, protons and neutrons are composite particles formed by their constituent valence quarks, the first generation up and down quarks. Composite particles formed by quarks, such as the proton and neutron, are referred to as hadrons.

The second and third generation quarks and leptons are extremely rare to encounter. They are much more massive than their first generation counterparts and are unstable, decaying promptly into other particles. Moreover, the production of second and third generation quarks and leptons require conditions that foster highly energetic particle

interactions, conditions that can only be met by particle accelerators and astrophysical processes. To detect the particles created in such processes, particle detectors are used, employing various technologies to measure the momenta, energies, and spatial positions of the particles.

This thesis presents a measurement of the longitudinal polarization[1] of the top quark in top-antitop quark pair production using 4.7 fb^{-1} of proton-proton collision data collected by the ATLAS detector at a center of mass energy of 7 TeV. The LHC and ATLAS detector are both located at the European Organization for Nuclear Research (CERN).

Despite being theorized in 1973 [1], the top quark was not discovered until 1995 at the Tevatron by the CDF and DØ collaborations [2, 3]. The Tevatron, which ceased operations on September 30, 2011, collided protons and anti-protons at a maximum center of mass energy of 1.96 TeV; the resulting particles from the collisions were measured by the CDF and DØ detectors.

Top quarks are produced in two different ways: as single top (antitop) quarks and as top-antitop quark pairs. Single top quarks are produced via the weak interaction, while top-antitop quark pairs are produced via both the weak and strong interactions. Resulting from the nature of proton-antiproton collisions, the predominant production mechanism for top quark pairs at the Tevatron was through the strong interaction process of quark-quark fusion; conversely, the predominant production mechanism of top quark pairs at the LHC is through the strong interaction process of gluon-gluon fusion.

The LHC offers a unique opportunity to study properties of the top (antitop) quark. The Tevatron's center of mass collision energy was close to the threshold for producing top quark pairs, limiting the number of top quark pair events produced. Since the collision

[1] The longitudinal polarization of a particle is defined as the expectation value of the projection of the particle's spin onto an axis defined by its momentum direction.

energies and luminosity at the LHC are larger than that at the Tevatron, the LHC has the ability to provide larger statistics for top quark pair production, enabling increased sensitivity for some top quark analysis. In addition, the proton-proton collisions at the LHC offers a probe into the strong production of top quark pairs via gluon-gluon fusion, which was suppressed at the Tevatron relative to the strong production of top quark pairs via quark-quark fusion. This analysis will exploit both of these properties of the LHC.

One of the most interesting features of the top quark is its short lifetime; unlike the other quarks, its lifetime is shorter than the timescale for hadronization, a strong interaction process that forms hadrons from quarks and gluons. An important feature of the hadronization process is that it washes out the spin information of the initial quark or gluon. Instead of hadronizing, the top quark decays via the weak interaction; contrary to the process of hadronization, the chiral nature of the weak interaction preserves the spin information of the initial decay product, leaving the top quark as the only quark that allows for access to its spin state.

One method for accessing the spin state of the top quark is through the angular distributions of its final state decay products. Top quarks decay predominantly into a W^+-boson and a $\bar{b}$-quark; the W^+-boson subsequently decays before detection via the weak interaction into a quark and anti-quark (hadronically) or into a charged antilepton and its corresponding neutrino (leptonically). This leaves three decay topologies for top-antitop quark pairs: the all hadronic channel where both W-bosons decay hadronically, the single lepton channel where one W-boson decays leptonically and the other hadronically, and the dilepton channel where both W-bosons decay leptonically. The spin information of the top quark is also preserved by the weak decay of the W-boson and may be accessed through the angular distribution of the charged lepton, neutrino, or final state quarks.

To produce longitudinally polarized top quarks in top-antitop quark pair production, a parity violating production mechanism, such as the weak interaction, is needed. Due to parity conservation in the strong interaction, the SM predicts a negligible longitudinal polarization of the top quark in top-antitop quark pair production at the LHC operating at $\sqrt{s} = 7$ TeV. In addition to the SM prediction, there are a number models that go beyond the SM (BSM), introducing parity violating couplings to the top quarks, that predict a non-negligible longitudinal polarization of the top quark in top-antitop quark pair production at the LHC at $\sqrt{s} = 7$ TeV. The discrepancy between the SM and BSM predictions makes the measurement of the longitudinal polarization of the top quark extremely interesting, as it has the power to determine if the SM prediction is accurate, as well as having the power to discriminate between BSM models if a non-negligible longitudinal polarization is measured.

For this analysis, the single lepton decay topology is used, which includes an isolated lepton (electron or muon) and three or more jets. The angular distribution of the charged lepton is utilized to extract the experimental observable $\alpha_\ell P$, the product of the spin-analyzing power of the charged lepton and the degree of longitudinal polarization of the top quark, by performing a template fit of partially polarized top quarks to the data. Two measurements of $\alpha_\ell P$ are performed assuming that the longitudinal polarization is induced by either a CP conserving (CPC) or a CP violating (CPV) mechanism for top-antitop quark pair production. The results are then compared to the predictions given by the SM and to predictions given by select BSM models.

This thesis is organized in such a way as to present a coherent description of the measurements presented; this is achieved by explaining the theory that motivates the experimental observable $\alpha_\ell P$, the experimental apparatus utilized to produce and collect the data, the analysis technique employed to extract $\alpha_\ell P$ from the data, and the conclusions drawn from the results.

The format of this thesis is as follows, Chapter 2 begins by introducing the SM, placing an emphasis on physics pertinent to the SM and BSM predictions for the longitudinal polarization of the top quark in top-antitop quark pair production. This is followed by Chapter 3, which gives a description of CERN, the LHC, and the ATLAS experiment. The analysis techniques used to perform the measurements of $\alpha_\ell P$ are explained in Chapter 4; this includes explanations and studies regarding the estimation of the signal and background processes, object and event selection, event reconstruction, and the template fit to the data. Appendices A to D provide additional information and studies regarding the analysis techniques used in this analysis. Chapter 5 discusses the sources of systematic uncertainty in the analysis, presents the results for $\alpha_\ell P$, compares the results to the SM and BSM predictions, and discusses potential improvements to the measurement. Additional tables of systematic uncertainties are given in Appendix F. In addition, information intended specifically for members of the ATLAS collaboration is given in Appendix E.

Chapter 2.

Theoretical Underpinnings of this Thesis

The measurements presented in this thesis are compared to theoretical predictions given by the Standard Model of Particle Physics. Any deviation from the predictions given by the Standard Model may be interpreted as evidence for physics beyond the Standard Model. The ability to present a coherent interpretation of these results hinges upon a proper description of the Standard Model and an introduction to selected theories beyond the Standard Model.

This chapter gives an introduction to the SM in Section 2.1 followed by a description of the top quark's properties in Section 2.2. The chapter concludes with a section dedicated to the longitudinal polarization of the top quark in top-antitop quark pair production in Section 2.3.4.

2.1. The Standard Model of Particle Physics

The Standard Model of Particle Physics or for brevity, the Standard Model (SM), is a Quantum Field Theory (QFT) used to describe three of the four fundamental interactions of nature: Electromagnetism, Weak Interactions, and Strong Interactions. In a QFT,

fundamental matter particles are described as quantum fields with half integer spin, which are called fermions, as they obey Fermi statistics. To be more precise, the SM is a Quantum Gauge Field Theory, where each interaction is related to a particular continuous local gauge transformation which leads to a conserved current. The requirement of gauge invariance leads to integer spin fields known as gauge fields whose excitations correspond to particles called gauge bosons. These gauge bosons are the mediators of the fundamental interactions.

The SM describes matter with 6 leptons and 6 quarks (spin-$\frac{1}{2}$), which appear in three generations; 12 mediating gauge bosons (spin-1); and the mass generating Higgs boson (spin-0). Each fermion (leptons and quarks) has an anti-particle, which has the same mass, but opposite quantum numbers, such as electric charge. Tables 2.1 and 2.2 display the properties of the leptons and quarks, while Table 2.3 displays the properties of the gauge bosons. All quarks come in three different color charges, but due to the nature of the strong interaction, quarks are only observed as constituents of colorless bound state composite particles called hadrons. There are two types of hadrons, mesons and baryons, the former are a bound state of a quark and anti-quark pair and the latter are composed of three quarks.

Particle	Generation	Charge (e)	Mass	Forces
$e^{\pm}$	1	± 1	511 keV	electromagnetic, weak
ν_e	1	0	< 2eV	weak
$\mu^{\pm}$	2	± 1	105.7 MeV	electromagnetic, weak
ν_μ	2	0	< 2eV	weak
$\tau^{\pm}$	3	± 1	1.78 GeV	electromagnetic, weak
ν_τ	3	0	< 2eV	weak

Table 2.1.: Properties of the leptons in the SM [4].

Particle	Generation	Charge (e)	Mass	Forces
u (up)	1	2/3	2.3 MeV	electromagnetic, weak, strong
d (down)	1	-1/3	4.8 MeV	electromagnetic, weak, strong
c (charm)	2	2/3	1.275 GeV	electromagnetic, weak, strong
s (strange)	2	-1/3	95.0 MeV	electromagnetic, weak, strong
t (top)	3	2/3	173.07 GeV	electromagnetic, weak, strong
b (bottom)	3	-1/3	4.18 GeV	electromagnetic, weak, strong

Table 2.2.: Properties of the quarks in the SM [4].

Gauge Boson	Charge (e)	Mass	Forces
γ	0	$< 1 \times 10^{-18}$eV	electromagnetic
$W^{\pm}$	± 1	80.4 GeV	weak
Z^0	0	91.2 GeV	weak
8 gluons	0	0	strong

Table 2.3.: Properties of the gauge bosons in the SM [4].

For all of the theoretical and experimental success that the SM has had, it fails in providing a full explanation of nature. In particular, it does not say anything about unifying gravity with the other three fundamental forces. Moreover, the SM only accounts for visible matter, which composes only 4.6% of the universe's energy density [5]. Meanwhile, the SM cannot account for cold dark matter nor dark energy which compose 24% and 71.4% of the universe's energy density, respectively.

The principle of local gauge invariance will be discussed in Section 2.1.1 and the quantum gauge field theories that comprise the SM will be discussed in Sections 2.1.2 and 2.1.3.

2.1.1. Gauge Transformations

Local gauge invariance is a crucial concept that must be understood when discussing the SM. To highlight the fundamental concepts of local gauge invariance, we'll use the Lagrangian density for a Dirac field, which describes spin-$\frac{1}{2}$ fermions, which is given by

$$\mathcal{L}_D = i\bar{\psi}\gamma^\mu\partial_\mu\psi - m\bar{\psi}\psi, \tag{2.1}$$

where ψ and $\bar{\psi}$ are the spin-1/2 fermionic field operators, γ^μ are the gamma matrices, and m is the mass of the particles. We require that Eq. (2.1) be invariant under a local U(1) phase transformation. Under a local U(1) phase transformation, the fermionic field operators transform as:

$$\psi \to \psi' = e^{-i\alpha(x)}\psi \tag{2.2}$$

and

$$\bar{\psi} \to \bar{\psi}' = e^{i\alpha(x)}\bar{\psi}, \tag{2.3}$$

where $\alpha(x)$ is a space-time dependent phase factor. Substituting Eq. (2.2) and Eq. (2.3) into Eq. (2.1) we are left with the modified Lagrangian:

$$\mathcal{L}'_D = i\bar{\psi}\gamma^\mu\partial_\mu\psi - m\bar{\psi}\psi + \bar{\psi}\gamma^\mu\psi\partial_\mu\alpha(x). \tag{2.4}$$

The fact that $\mathcal{L}_D \neq \mathcal{L}'_D$ shows that the Lagrangian described in Eq. (2.1) is not invariant under local U(1) phase transformations. To ensure invariance under such transformations,

we must introduce an additional vector field $A_\mu(x)$ to Eq. (2.1) which renders a new Lagrangian:

$$\mathcal{L}_D = i\bar{\psi}\gamma^\mu\partial_\mu\psi - m\bar{\psi}\psi - q\bar{\psi}\gamma^\mu\psi A_\mu(x), \tag{2.5}$$

where q is the charge of the fermionic field. $A_\mu(x)$ transforms under local U(1) phase transformations as:

$$A_\mu(x) \rightarrow A'_\mu(x) = A_\mu(x) + \partial_\mu\mathcal{X}(x) \tag{2.6}$$

, where $q\mathcal{X}(x) = \alpha(x)$. Substituting Eq. (2.6), Eq. (2.2), and Eq. (2.3) into Eq. (2.5) shows that $\mathcal{L}_D = \mathcal{L}'_D$. This leaves Eq. (2.5) invariant under local U(1) phase transformations, but most importantly, the third term introduces a new interaction between the complex scalar fields ψ ($\bar{\psi}$) and the vector field A_μ.

The new vector field A_μ is massless and appears purely as a consequence of requiring that the Dirac Lagrangian be invariant under local U(1) gauge transformations. The Lagrangian describing the forces present in the SM are required to be invariant under particular local gauge transformations. For instance, Quantum Electrodynamics, or QED, is a quantum gauge field theory whose Lagrangian is invariant under U(1) local transformations, resulting in the vector field A_μ^{QED} whose quanta correspond to the photon. The quanta of the massless field(s) generated by the requirement of local gauge invariance are referred to as gauge bosons and are responsible for mediating the forces in the SM.

2.1.2. Electro-Weak Interactions

The theory of electro-weak interactions was proposed in the 1960's by Glashow, Salam, and Weinberg [6–8] which unified QED with the weak interaction. The electro-weak

interaction combines the symmetry groups of the weak interaction, SU(2) weak-isospin, and that of the QED interaction, U(1) charge, to form the electro-weak symmetry group of $\mathrm{SU(2)_L} \otimes \mathrm{U(1)_Y}$. The resulting electro-weak interaction is a chiral $V - A$ theory where the left-handed fermions (right-handed anti-fermions) appear as doublets of weak-isospin. The weak-isospin doublets contain two particles that have the same weak isospin ($T = 1/2$), but different projections of the weak-isospin onto an arbitrary axis ($T_3 = \pm\frac{1}{2}$). The massive right-handed fermions and left-handed anti-fermions appear as weak-isospin singlets, and therefore, only transform under the $U(1)_\mathrm{Y}$ symmetry. Equation (2.8) depicts the weak-isospin doublet and singlet structure of the leptons and quarks. Electro-weak interactions are invariant under weak-isospin transformations ($\mathrm{SU(2)_I}$) and are also invariant under U(1) hypercharge transformations ($\mathrm{U(1)_Y}$). The hypercharge and third component of the weak-isospin are related to the electric charge by the relation

$$Q = \frac{Y}{2} + T_3. \tag{2.7}$$

It is important to note that for massless particles, the handedness of its chirality is equivalent to the handedness of its helicity, which is the projection of its spin onto its momentum direction. Figure 2.1 depicts the left- and right-handed helicity states of a particle. The chirality of a particle is determined by how it transforms under a Poincaré group of transformations, which contains Lorentz transformations, translations, and space rotations. For massive particles, a chiral left- or right-handed particle may have both left- and right-handed helicities since an observer can Lorentz boost into a frame where the helicity is flipped.

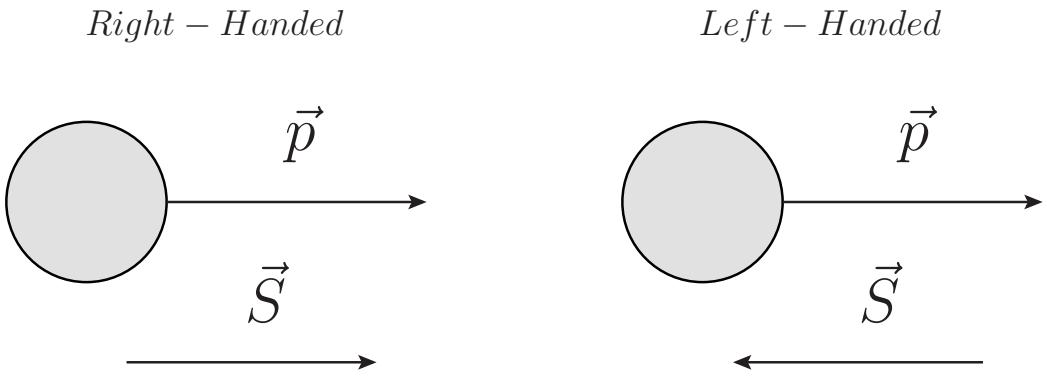

Figure 2.1.: Diagram depicting the right- and left-handed helicity states of a particle.

$$
\begin{gathered}
\underbrace{\begin{pmatrix} T_3 = +\frac{1}{2} \\ T_3 = -\frac{1}{2} \end{pmatrix}_{\mathrm{L}}}_{T=\frac{1}{2}\text{ doublet}} \qquad \underbrace{\Big(T_3 = 0\Big)_{\mathrm{R}}}_{T=0\text{ singlet}} \\
\begin{pmatrix} \nu_e \\ e^- \end{pmatrix}_{\mathrm{L}}, \Big(e^-\Big)_{\mathrm{R}}, \Big(\nu_e\Big)_{\mathrm{R}}, \begin{pmatrix} u \\ d \end{pmatrix}_{\mathrm{L}}, \Big(u\Big)_{\mathrm{R}}, \Big(d\Big)_{\mathrm{R}} \\
\begin{pmatrix} \nu_\mu \\ \mu^- \end{pmatrix}_{\mathrm{L}}, \Big(\mu^-\Big)_{\mathrm{R}}, \Big(\nu_\mu\Big)_{\mathrm{R}}, \begin{pmatrix} c \\ s \end{pmatrix}_{\mathrm{L}}, \Big(c\Big)_{\mathrm{R}}, \Big(s\Big)_{\mathrm{R}} \\
\begin{pmatrix} \nu_\tau \\ \tau^- \end{pmatrix}_{\mathrm{L}}, \Big(\tau^-\Big)_{\mathrm{R}}, \Big(\nu_\tau\Big)_{\mathrm{R}}, \begin{pmatrix} t \\ b \end{pmatrix}_{\mathrm{L}}, \Big(t\Big)_{\mathrm{R}}, \Big(b\Big)_{\mathrm{R}}
\end{gathered}
\tag{2.8}
$$

The $\mathrm{SU}(2)_{\mathrm{I}}$ symmetry's corresponding massless gauge fields are W^i_μ, where the roman index corresponds to the weak-isospin components. The $\mathrm{U}(1)_Y$ corresponding massless

gauge field is B_μ. The Lagrangian for the electro-weak interaction is given by

$$\begin{aligned}\mathcal{L}_{EW} = -\frac{1}{4}W^i_{\mu\nu}W_i^{\mu\nu} - \frac{1}{4}B_{\mu\nu}B^{\mu\nu} + \psi_{\mathrm{L}}^\dagger\gamma^\mu\left(i\partial_\mu - g\frac{\tau_i}{2}W^i_\mu - \frac{g'}{2}YB_\mu\right)\psi_{\mathrm{L}} \\ +\psi_{\mathrm{R}}^\dagger\gamma^\mu\left(i\partial_\mu - \frac{g'}{2}YB_\mu\right)\psi_{\mathrm{R}},\end{aligned} \tag{2.9}$$

where ψ_{L} (ψ_{R}) are the left- (right-) handed fermion fields; τ_i are the Pauli matrices, which are the generators of the $\mathrm{SU(2)_I}$ symmetry group; Y is the hypercharge, which is the generator of the $\mathrm{U(1)_Y}$ symmetry group, g (g') are the couplings to W^i_μ (B_μ), and $W^i_{\mu\nu}$ and $B_{\mu\nu}$ are the field strength tensors. The field strength tensors are defined as

$$\begin{aligned}W^i_{\mu\nu} &= \partial_\mu W^i_\nu - \partial_\nu W^i_\mu + g\epsilon^{ijk}W^j_\mu W^k_\nu \\ B_{\mu\nu} &= \partial_\mu B_\nu - \partial_\nu B_\mu.\end{aligned} \tag{2.10}$$

The first two terms of Eq. (2.9) represent the kinetic term of the gauge fields and the last two terms represent the interactions between the fermions mediated by the gauge bosons.

The mixing between the two bosons, appearing due to their symmetries $\mathrm{SU(2)_I}$ and $\mathrm{U(1)_Y}$, in the electro-weak interaction is described by the Weinberg (or weak mixing) angle, θ_W, given by

$$\sin\theta_W = \frac{g'}{\sqrt{g^2 + g'^2}}, \tag{2.11}$$

which describes how the gauge bosons in QED and the weak interaction are related to the gauge bosons of the electro-weak theory. The physical fields $W^\pm$, Z^0, and γ are

expressed in terms of the Weinberg angle by

$$\begin{aligned} W^{\pm} = W_{\mu}^{\pm} &= \frac{1}{\sqrt{2}}\left(W_{\mu}^{1} \mp i W_{\mu}^{2}\right) \\ Z^{0} = Z_{\mu} &= \cos(\theta_W) W_{\mu}^{3} - \sin(\theta_W) B_{\mu} \\ \gamma = A_{\mu} &= \sin(\theta_W) W_{\mu}^{3} + \cos(\theta_W) B_{\mu}. \end{aligned} \tag{2.12}$$

In addition, the couplings g and g' are related to the electric charge by

$$e = g \sin\theta_W = g' \cos\theta_W. \tag{2.13}$$

The fermion and boson fields described in Eq. (2.9) are massless; the mechanism to generate masses for these fields is through electro-weak symmetry breaking, better known as the Higgs mechanism [9–12]. The Higgs mechanism introduces a complex scalar field SU(2) doublet, given by

$$\phi = \frac{1}{2}\begin{pmatrix} \phi_1 + i\phi_2 \\ \phi_3 + i\phi_4 \end{pmatrix} = \begin{pmatrix} \phi^{+} \\ \phi^{0} \end{pmatrix}, \tag{2.14}$$

which is added into the SM Lagrangian by hand as

$$\mathcal{L}_{\text{Higgs}} = \left(\partial_\mu \phi\right)^{\dagger} \left(\partial^\mu \phi\right) + \mu^2 \phi^{\dagger}\phi - \lambda\left(\phi^{\dagger}\phi\right)^2. \tag{2.15}$$

The last two terms describe the scalar potential, which is invariant under $\mathrm{SU(2)_L} \otimes \mathrm{U(1)_Y}$ transformations. If the values for μ and λ are chosen as $\mu^2 < 0$ and $\lambda > 0$, then the vacuum expectation value for the potential is given by

$$v = \frac{\pm\mu}{\sqrt{\lambda}}, \tag{2.16}$$

which is non-zero. This gives the vacuum a preferred value in weak-isospin space causing spontaneous symmetry breaking of the electro-weak theory, resulting in a Higgs boson with mass $m_{\text{Higgs}} = \sqrt{2}\mu$ and spin 0. The masses of the gauge bosons and the fermions in the SM are related to the vacuum expectation value, v, by

$$\begin{aligned} m_W &= \frac{1}{2}gv \\ m_Z &= \frac{1}{2}v\sqrt{g^2+g'^2} \\ m_\gamma &= 0 \\ m_{fermion} &= \frac{1}{\sqrt{2}}G_f v, \end{aligned} \tag{2.17}$$

where G_f is the Yukawa coupling[1] of the fermion field to the Higgs field. The Higgs boson was recently discovered by the ATLAS and CMS collaborations at the LHC in 2012 [13, 14] at a mass near 125 GeV.

An important aspect of the electro-weak theory is the mixing of the weak eigenstates of the quarks through the Cabibbo-Kobayashi-Maskawa matrix (CKM) [1, 15]. The unitary, diagonalizable CKM matrix, V_{CKM}, transforms the mass eigenstates of the quarks, q, to their weak eigenstates, q', by

$$\begin{pmatrix} d' \\ s' \\ b' \end{pmatrix} = \underbrace{\begin{pmatrix} V_{ud} & V_{us} & V_{ub} \\ V_{cd} & V_{cs} & V_{cb} \\ V_{td} & V_{ts} & V_{tb} \end{pmatrix}}_{V_{CKM}} \begin{pmatrix} d \\ s \\ b \end{pmatrix} \tag{2.18}$$

The flavor changing processes that occur on the off-diagonal elements of the CKM matrix are only possible in charged current decays (decays with the exchange of a $W^\pm$-boson). The magnitudes of the CKM matrix elements have been determined by performing a

[1] A Yukawa coupling is the coupling of a scalar field (ϕ) to a Dirac field (ψ) of the form $g\bar{\psi}\phi\psi$ (scalar) or $g\bar{\psi}i\gamma^5\phi\psi$ (pseudoscalar)

global fit to data from many experiments [4]and are given by

$$\begin{pmatrix} |Vud| & |Vus| & |Vub| \\ |Vcd| & |Vcs| & |Vcb| \\ |Vtd| & |Vts| & |Vtb| \end{pmatrix} = \begin{pmatrix} 0.97427 \pm 0.00015 & 0.22534 \pm 0.00065 & 0.00351^{+0.000015}_{-0.00014} \\ 0.22520 \pm 0.00065 & 0.97344 \pm 0.00016 & 0.0412^{+0.0011}_{-0.0005} \\ 0.00867^{+0.00029}_{-0.00031} & 0.0404^{+0.0011}_{-0.0005} & 0.999146^{+0.000021}_{-0.000046} \end{pmatrix} \tag{2.19}$$

For any unitary $N \times N$ matrix, the number of free parameters is equal to $(N-1)^2$. Since the CKM matrix is a 3×3 matrix, it has four free parameters, three quark mixing angles and a CP violating complex phase. The extension of the 2×2 Cabibbo matrix, whose only free parameter is the Cabibbo mixing angle, to the CKM matrix was necessitated by the discovery of CP violations in the weak interaction by Cronin and Fitch in 1963 [16]. The weak interaction also violates parity, which was first observed in the Wu experiment in 1956 [17]. Parity violation in the weak decays of top quarks is an important property to understand for this thesis and will be discussed further in Section 2.2.

2.1.3. Strong Interactions

Quantum chromodynamics (QCD) is the quantum gauge field theory used to describe the strong interactions between the quarks and gluons in the SM. The charge of QCD is known as color charge, having values of red (R), blue (B), and green (G); anti-quarks have anti-color charge $\bar{R}$, $\bar{B}$, and $\bar{G}$. QCD is invariant under $\mathrm{SU(3)}_{\mathrm{Color}}$ transformations whose massless gauge bosons are the eight independent color states called a color octet of gluons.

The Lagrangian of QCD is given by

$$\mathcal{L}_{\text{QCD}} = \bar{\psi}_q \left(i\gamma^\mu \partial_\mu - m\right) \psi_q - g_s \bar{\psi}_q \gamma^\mu T_a \psi_q G^a_\mu - \frac{1}{4} G^a_{\mu\nu} G^{\mu\nu}_a, \tag{2.20}$$

where ψ_q are the quark fields, G^a_μ are the gluon fields, $G^a_{\mu\nu}$ is the field strength tensor, T_a are the generators of the $\text{SU}(3)_{\text{Color}}$ symmetry, and the index a runs from 1 to 8 since there are 8 generators. The generators are related to the Gell-Mann matrices, λ_a, by the relation

$$T_a = \frac{1}{2}\lambda_a; \tag{2.21}$$

the Gell-Mann matrices in $\text{SU}(3)_{\text{Color}}$ are analogous to the Pauli matrices in $\text{SU}(2)_{\text{L}}$. The field strength tensor is given by

$$G^a_{\mu\nu} = \partial_\mu G^a_\nu - \partial_\nu G^a_\mu - g_s f_{abc} G^b_\mu G^c_\nu, \tag{2.22}$$

where f_{abc} is determined by the commutation relations of the generators T_a

$$[T_a, T_b] = i f_{abc} T_c. \tag{2.23}$$

The coupling constant g_s that appears in Eq. (2.20) is related to the strong coupling constant, α_s, by

$$\alpha_s = \frac{g_s^2}{4\pi}. \tag{2.24}$$

The coupling constant α_s is in fact, not constant, α_s runs with the momentum transfer of the interaction, Q^2, by

$$\alpha_s(Q^2) = \frac{\alpha_s(\mu^2)}{1 + \frac{\alpha_s(\mu^2)}{12\pi}(33 - 2n_f)\log\left(\frac{Q^2}{\mu^2}\right)}, \tag{2.25}$$

where μ is the renormalization scale and n_f is the number of quark flavors. One of the features of Eq. (2.25) is that α_s decreases as the energy of the interactions increases, meaning that at high Q^2 (or short distance interactions) the quarks and gluons appear as free objects, allowing for perturbative QCD calculations. This feature of QCD is known as asymptotic freedom [18, 19]. Conversely, at low Q^2 interactions (or long distances), the value of α_s becomes large.

Another important feature of QCD is quark confinement. All hadrons appear as colorless objects, meaning that the quark and anti-quark of mesons must be $R\bar{R}$, $B\bar{B}$, or $G\bar{G}$ and that baryons (anti-baryons) must have a quark (anti-quark) of each color, RBG ($\bar{R}\bar{B}\bar{G}$). When quarks are produced in particle collisions, it is energetically favorable for them to form bound states with quarks from the vacuum (hadronization). When a quark is produced at a particle physics experiment, it is observed in the detector as a larger number of color neutral hadrons, which taken together are called jets. This is true for all quarks except for the top quark. The top quark's lifetime is much shorter than the hadronization time scale and decays via the weak interaction. This is an extraordinary feature of the top quark and it will be exploited in this analysis, as discussed in Section 2.2 and Chapter 4.

2.2. Top Quark Physics in the Standard Model

In 1973, Kobayashi and Maskawa generalized the Cabibbo 2 x 2 quark mixing matrix [15] to a 3 x 3 matrix to account for the experimentally measured CP violation in electro-weak decays [1]. The resulting CKM matrix introduces a third generation of quarks, the bottom and top, which allows for the matrix to include a complex phase which allows for CP violation effects. This was the first theoretical proposal of the bottom and top quarks. The bottom quark was discovered through the $b\bar{b}$ resonance, the Υ meson, in 1977 by the E288 experiment at the Tevatron, led by Lederman [20]. The existence of the top quark proved to be elusive until its eventual discovery in 1995 by the CDF and DØ collaborations at the Tevatron [2, 3].

Since its discovery, the top quark and its properties have been studied extensively. One of its most intriguing properties is its short lifetime. Due to its large mass, the top quark's lifetime is approximately 20 times shorter than the strong interaction time scale; as a result, the top quark decays before hadronization can occur [21]. Consequently, information regarding properties of the top quark are preserved and can be measured through its decay products. This enables experimentalists to make precise measurements of top quark properties which can be compared to SM or BSM predictions.

There are two main mechanisms for producing top quarks at hadron colliders: top quark pair production and single top production. Section 2.2.1 will discuss single top production at the LHC and Section 2.2.2 will discuss top quark pair production at the LHC. Meanwhile, the longitudinal polarization of top quarks in $t\bar{t}$ production will be discussed in Section 2.3.

2.2.1. Single Top Production

Individual top quarks are produced via the electro-weak interaction in a process known as single top quark production. There are three mechanisms responsible for the production of single top quarks: timelike (s-channel), which produces a top and bottom quark together; spacelike (t-channel), which produces an additional quark, most likely a light flavor quark; and the Wt-channel which produces a top quark in association with an on-shell W-boson. Fig. 2.2 depicts the leading-order Feynman diagrams that contribute to single top production. At the LHC, the predominant mechanism for single top production is the t-channel with a smaller contribution from the Wt-channel and the s-channel provides a negligible contribution. The production of single top quarks dominates over the production of single antitop quarks at the LHC due to the fact that the colliding particles are protons. Both channels require a quark to annihilate with an antiquark (sea quark from proton) and the proton contains two up quarks compared to one down quark. Given the charge of the up quark ($+\frac{2}{3}e$), it is more likely for a W^+ to be produced which decays into a top and $\bar{b}$ quark.

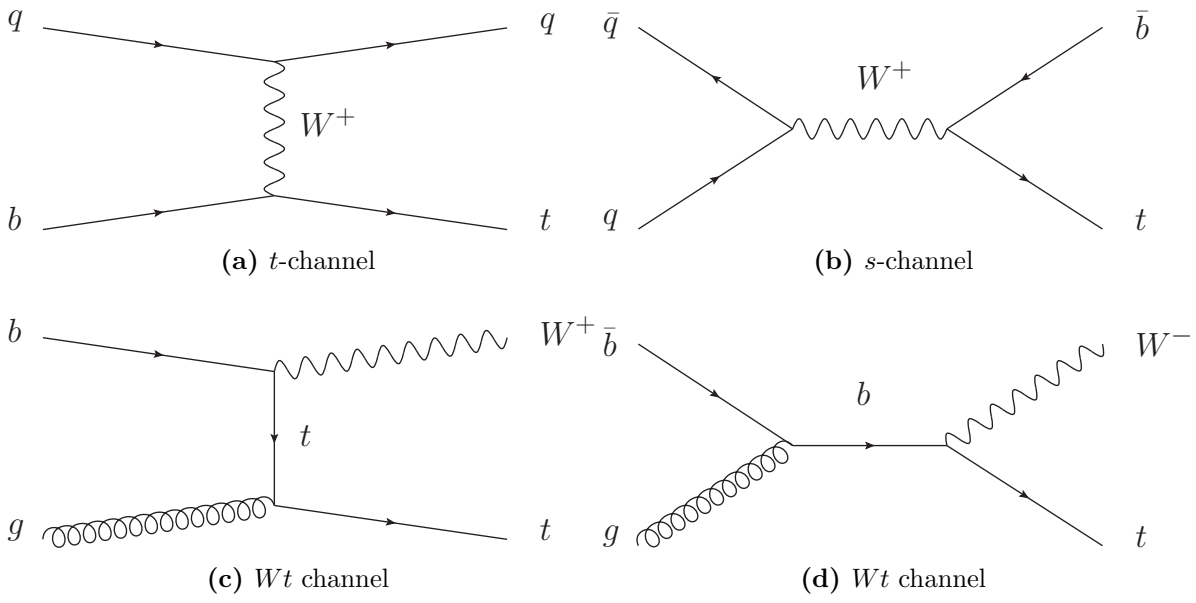

(a) t-channel **(b)** s-channel

(c) Wt channel **(d)** Wt channel

Figure 2.2.: Leading-order Feynman diagrams for single top production at the LHC.

2.2.2. Top Quark Pair Production

A top quark and an anti-top quark pair ($t\bar{t}$) are produced via the strong and weak interactions through two mechanisms: gluon fusion and $q\bar{q}$ annihilation. Figure 2.4 depicts the leading-order Feynman diagrams responsible for top quark pair production. When the LHC is operated at $\sqrt{s} = 7$ TeV, gluon fusion is the primary process for $t\bar{t}$ production, accounting for roughly 80% [4] of the top quark pairs produced, leaving $q\bar{q}$ annihilation responsible for the other 20%. The process of $q\bar{q}$ annihilation, depicted in Fig. 2.4d, is disfavored with respect to gluon fusion at the LHC due to the fact that protons are colliding with protons. Since the proton's valence quarks do not contain anti-quarks, a sea-quark from one of the protons is needed to produce $q\bar{q}$ annihilation. Moreover, partons with a small fraction of the proton's longitudinal momentum can produce top quark pairs at the LHC due to the high center-of-mass energy, which favors gluon fusion. Figure 2.3 displays the proton's parton distribution function at $Q^2 = 10$ GeV^2, where one can clearly see that the gluon content is much more enhanced at low x compared to the other partons.[2]

2.2.3. Top quark decay

Top quarks decay through the weak interaction, predominately into a W-boson and a down type quark (d,s,b)[3]. Due to the CKM matrix elements, the Ws and Wd final states are highly suppressed relative to the Wb final state. The theoretical decay width of the Wb final state relative to the Wq decay width, assuming unitarity of the CKM matrix,

[2] Parton distribution functions are a function of the momentum transfer, Q^2, and x, the fraction of the proton's longitudinal momentum carried by a particular parton.

[3] Top quarks may also decay into a Z-boson and a light quark (u,c), a photon and a light quark, or a gluon and a light quark; however, these flavor changing neutral current (FCNC) modes are highly suppressed at tree level due to the GIM mechanism [22].

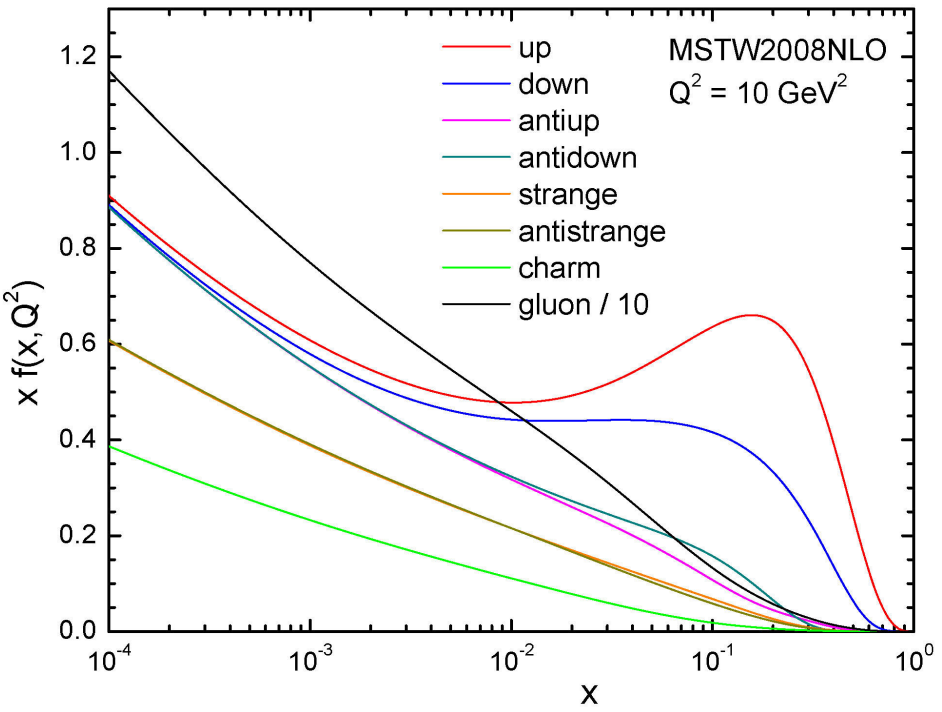

Figure 2.3.: Distributions of x times the unpolarized parton distributions $f(x, Q^2)$ for the proton, using the MSTW2008NLO PDF set at a scale $Q^2 = 10$ GeV^2.

is given by

$$\frac{\Gamma(Wb)}{\Gamma(Wq(q = d, s, b))} = 0.91 \pm 0.04, \tag{2.26}$$

indicating that Wb is the dominant decay mode of the top quark [4].

The mass of the top quark from direct measurements is found to be $m_t = 173.5^{+0.8}_{-0.8}$ GeV and its decay width[4] is measured as $\Gamma_t = 2.0^{+0.7}_{-0.6}$ GeV [4]. These properties have a profound effect on the way that the top quark decays since the spin decorrelation time scale of the top quark, m_t/Λ^2_{QCD} [21], is significantly larger than the lifetime of the top quark. Consequently, the top quark decays before hadronization can occur, allowing for the spin

[4]The decay width of a particle, Γ, is equal to $\hbar/\tau$, where τ is the lifetime of the particle.

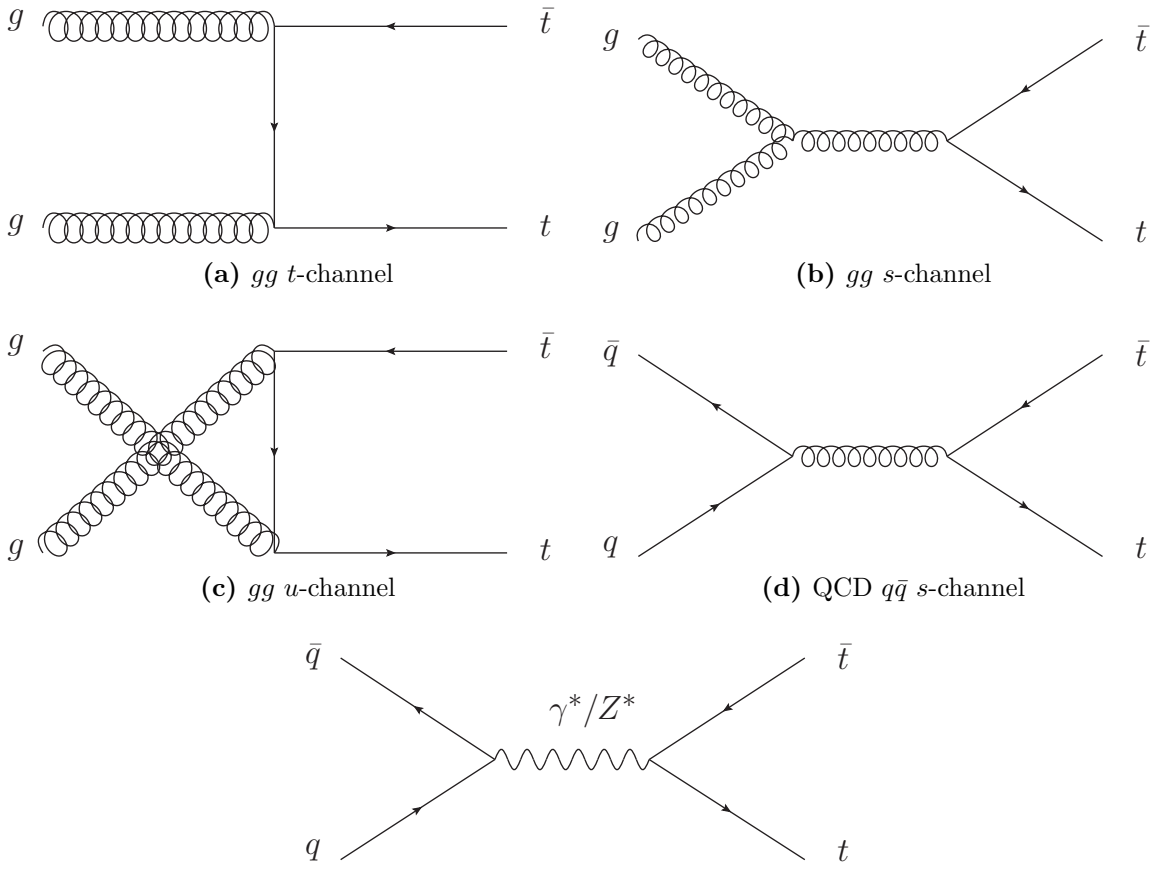

(a) gg t-channel **(b)** gg s-channel

(c) gg u-channel **(d)** QCD $q\bar{q}$ s-channel

(e) EW $q\bar{q}$ s-channel

Figure 2.4.: Leading-order Feynman diagrams for $t\bar{t}$ production at the LHC.

information of the top quark to be accessed through its final state decay products. This unique property of the top quark will be exploited in the analysis and is discussed further in Section 2.3.

Single top and $t\bar{t}$ decays are classified by the decay products of the W-boson originating from the top decay(s). The W^+-boson can decay in two ways, leptonically ($W^+ \to \ell^+\nu_\ell$) or hadronically ($W^+ \to q\bar{q}$). The final state particles of the leptonic W^+-boson decay are $e^+\nu_e$, $\mu^+\nu_\mu$, or $\tau^+\nu_\tau$; meanwhile, the hadronic decay final state particles are $u\bar{d}$ or $c\bar{s}$. Each of the hadronic final state quark pairs are color neutral, allowing for three color combinations of the quark pairs $R\bar{R}$, $G\bar{G}$, $B\bar{B}$. The three leptonic final states and the six

hadronic final states of the W-boson are approximately equally probable, each occurring at a rate of approximately 11% [4].

This analysis studies properties of top quarks in $t\bar{t}$ production, where each top quark decays into a W-boson and a b-quark. The final state decay products in $t\bar{t}$ decays are categorized into three channels: the all hadronic channel, where both W-bosons decay hadronically; the single lepton channel (semi-leptonic) where one W-boson decays leptonically and the other hadronically; and the dilepton channel, where both W-bosons decay leptonically. Figure 2.5 depicts the three $t\bar{t}$ decay channels. The branching ratios for each of the possible decay modes in $t\bar{t}$ production are shown in Fig. 2.6. It should be noted that measurements in the single lepton and dilepton channels typically consider $\tau + jets$ events only if the τ decays leptonically into an electron or muon[5]. Each channel offers unique advantages and disadvantages for physics measurements. The all hadronic channel occurs most frequently, allowing for high statistics, but has a very large background due to QCD multi-jet events and does not have a charged lepton in the final state to provide a clear signature. The dilepton channel contains two charged leptons in the final state, providing a distinct signature, which allows for signal and background separation; however, the dilepton channel provides smaller statistics since it occurs at such a low rate. In addition, the presence of two neutrinos in the final state, which leave the detector unmeasured, makes it complicated to reconstruct the $t\bar{t}$ system[6]. For this analysis, the single lepton channel (ℓ+jets) is chosen, because it provides ample statistics, manageable backgrounds, and a clear signature with a charged lepton in the final state. Moreover, the ℓ+jets channel only has one neutrino in the final state that escapes detection, making it possible to reconstruct the $t\bar{t}$ system using kinematic equations and the measured $E_{\mathrm{T}}^{\mathrm{miss}}$ in the detector.

[5]The τ lepton decays into a ν_τ and an e (μ) and ν_e (ν_μ) approximately 35% of the time [4], otherwise, it decays hadronically.

[6]To reconstruct the $t\bar{t}$ system in the dilepton channel, a set of kinematic equations that are under constrained must be solved, which can lead to a set of solutions. The most likely solution needs to be determined, which can result in computationally intensive calculations.

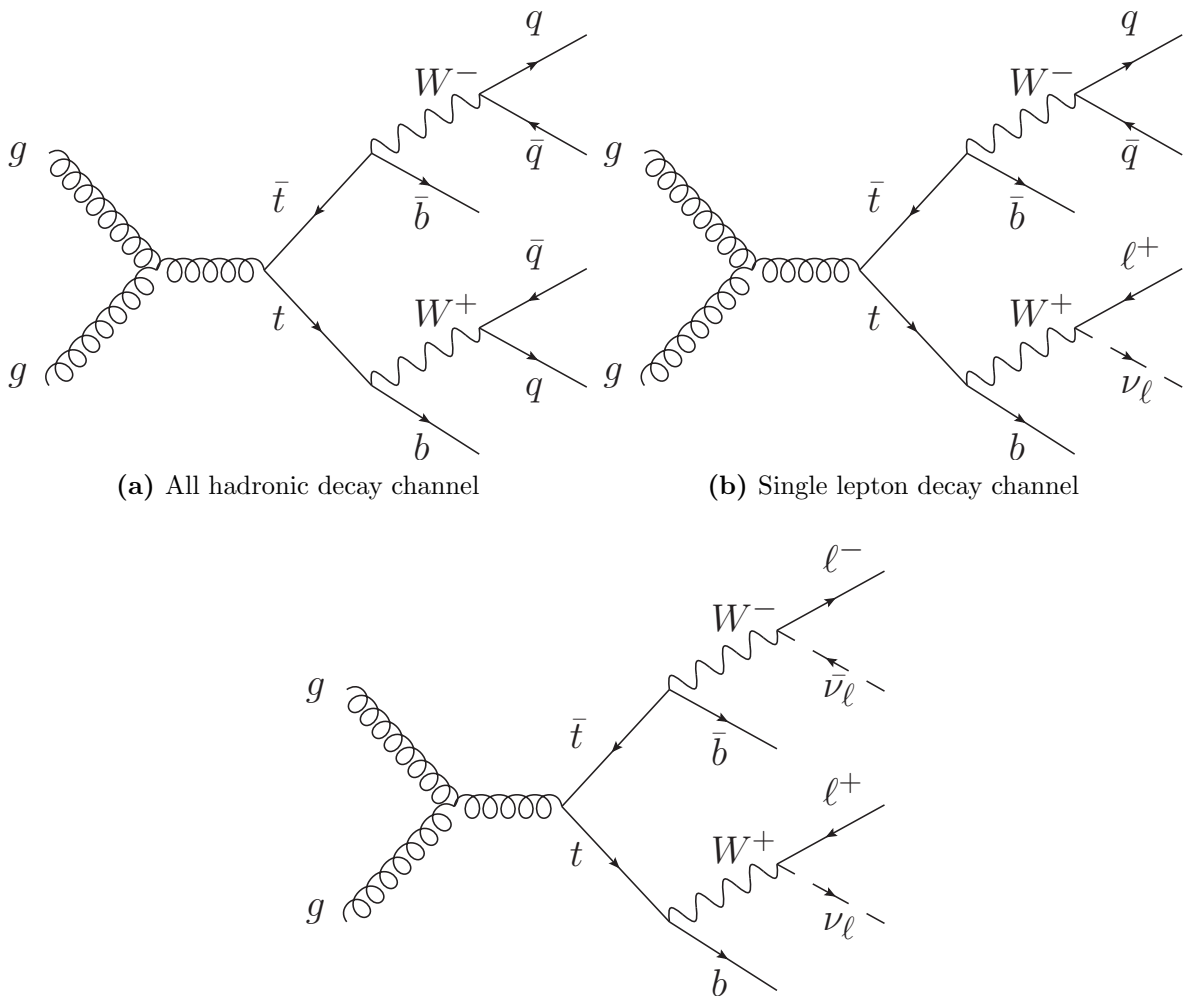

(a) All hadronic decay channel

(b) Single lepton decay channel

(c) Dilepton decay channel

Figure 2.5.: Leading-order Feynman diagrams for $t\bar{t}$ decay.

2.3. Longitudinal Polarization of the Top Quark in $t\bar{t}$ Production

As stated in Section 2.2.3, the top quark decays before hadronization can occur, allowing for the spin information of the top quark to be accessed through its decay products. This feature is unique to the top quark with respect to the other quarks, allowing for the top quark's spin observables to be studied in detail, such as the focus of this thesis, the longitudinal polarization of the top quark in $t\bar{t}$ production.

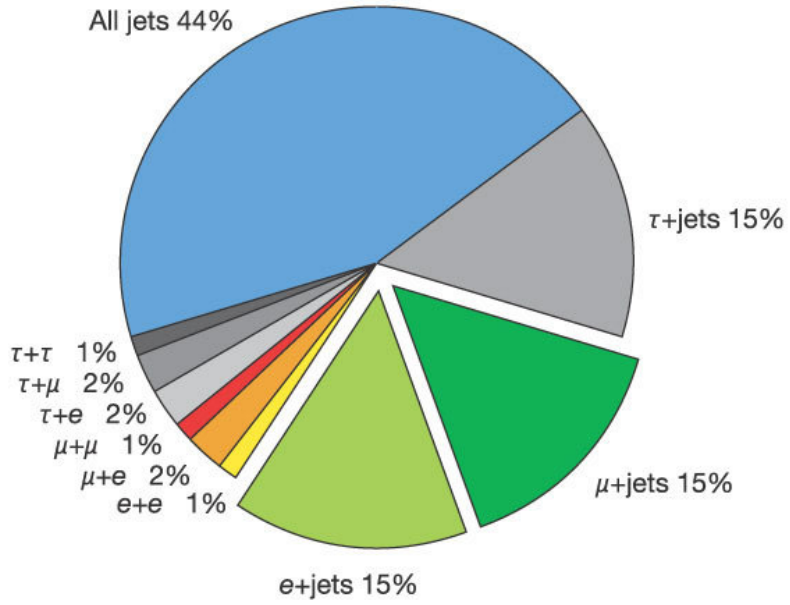

Figure 2.6.: Chart depicting the branching ratios of each of the possible decay modes for $t\bar{t}$ production.

The degree of longitudinal polarization of a particle, P, is the expectation value of the particle's helicity[7], given by

$$P = \left\langle \vec{S} \cdot \hat{p} \right\rangle , \tag{2.27}$$

where $\vec{S}$ is the spin of the particle and $\hat{p}$ is a unit vector in the direction of the particle's momentum. A fermion particle which is maximally polarized has a projection of its spin onto its momentum direction of $\pm \frac{\hbar}{2}$; the positive (negative) projection is called parallel (antiparallel). Under a parity transformation, $\mathcal{P}$, the degree of longitudinal polarization

[7]The helicity of a particle is the projection of its spin onto an axis defined by its momentum direction.

transforms as

$$\mathcal{P}(P) = \mathcal{P}\left(\left\langle \vec{S}\cdot\hat{p}\right\rangle\right) \tag{2.28}$$

$$\mathcal{P}\left(\left\langle \vec{S}\cdot\hat{p}\right\rangle\right) = \left(\left\langle \vec{S}\cdot\left(-\hat{p}\right)\right\rangle\right) \tag{2.29}$$

$$\left(\left\langle \vec{S}\cdot\left(-\hat{p}\right)\right\rangle\right) = -\left(\left\langle \vec{S}\cdot\hat{p}\right\rangle\right) \tag{2.30}$$

$$\mathcal{P}(P) = -P; \tag{2.31}$$

therefore, the longitudinal polarization is parity-odd and any mechanism that generates a longitudinally polarized particle must violate parity symmetry.

Due to parity conservation in the strong production of $t\bar{t}$, the SM predicts a negligible longitudinal polarization[8] of the top quark [23]; however, many BSM models used to explain the anomalous forward-backward asymmetry (A_{FB}), measured by the DØ [24, 25] and CDF [26] experiments at the Tevatron, include a parity violating chiral coupling to the top quarks that predict a larger longitudinal polarization of the top quark in $t\bar{t}$ production than the SM. The motivation for performing a measurement of the longitudinal polarization of the top quark in $t\bar{t}$ production is two fold: to validate the SM prediction and to distinguish between the various BSM models proposed for $t\bar{t}$ production if a non-negligible polarization is measured. At the most basic level, the longitudinal polarization of the top quark may be used as a probe for the structure of the couplings responsible for the production of $t\bar{t}$.

Section 2.3.1 discusses how the longitudinal polarization of the top quark can be extracted from the angular distributions of its final state decay products. The topics of top quark spin correlations in $t\bar{t}$ production and transverse polarization will be introduced in Sections 2.3.2 and 2.3.3. Spin correlations and the transverse polarization of the top quark do not directly affect the longitudinal polarization of the top quark, but are

[8] The SM predicts zero longitudinal polarization of the top quark in top-antitop quark pair production at leading order QCD. A small contribution arises from electroweak corrections.

important to understand for this analysis. The mechanisms for inducing longitudinal polarization of the top quark in $t\bar{t}$ production within the SM and in BSM theories, as well as their predictions for the value of P, will be explored in Section 2.3.4.

2.3.1. Angular Distributions of $t\bar{t}$ Final State Decay Products

There are two methods for measuring spin observables of the top quark in $t\bar{t}$ production: one is through the angular distributions of its decay products [23, 27–29], the other is to measure the fraction of the energy carried by the charged lepton with respect to its parent top quark's energy [30]. The measurement presented in this thesis focuses on the prior method, utilizing the angular distribution of the top's (antitop's) final state decay products to measure the longitudinal polarization of the top quark in $t\bar{t}$ production.

To understand how the top quark's longitudinal polarization can be extracted from the angular distributions of its final state decay particles, one must consider the spin states of the particles involved in the top decay and the subsequent W-boson decay, both of which are $V-A$ electro-weak interactions. Figure 2.7 depicts a top quark decaying in its center-of-mass frame, with the spin of each particle projected onto the quantization axis.[9] Typically, the momentum of the b-quark in the decay is much larger than its mass; therefore, the b-quark may be considered as a massless particle and the handedness of its helicity will be approximately the same as its chirality. All fermions (anti-fermions) are left-handed (right-handed) chiral objects and in the massless regime, left-handed (right-handed) chiral objects will have the projection of their spin anti-parallel (parallel) to their momentum.

Figure 2.7 depicts a top quark decay in its rest frame. The top quark's spin is projected onto a quantization axis defined by its decay products momentum direction

[9] Since the W-boson is a spin-1 object and is produced on shell in the top quark decay, it has three values for its spin projected onto a chosen quantization axis: -1,0,1. The spin-$\frac{1}{2}$ fermions have two values for its spin projected onto a chosen quantization axis: $-\frac{1}{2}$ and $+\frac{1}{2}$.

and is in the spin state $\left|\frac{1}{2}, +\frac{1}{2}\right\rangle$. The spin-$\frac{1}{2}$ b-quark and spin-1 W^+-boson can either be in a total spin state of spin-$\frac{3}{2}$ or spin-$\frac{1}{2}$. Given the initial spin state of the top quark, the b-quark and W^+-boson must be in the total spin state of $\left|\frac{1}{2}, +\frac{1}{2}\right\rangle$. In the massless limit, the b-quark must be in the spin state $\left|\frac{1}{2}, -\frac{1}{2}\right\rangle$. The rules for the addition of angular momentum leave two possible spin states for the W^+-boson: $|1, 0\rangle$, corresponding to the $\Lambda = 0$ helicity state and $|1, -1\rangle$, corresponding to the $\Lambda = -1$ helicity state. Figure 2.7a depicts the case where the b-quark is emitted in the direction of the top quark's spin, causing the spin of the W-boson to be aligned anti-parallel to its motion, leaving it in the helicity state, $\Lambda = -1$. Conversely, Fig. 2.7b depicts the case where the b-quark is emitted in the opposite direction of the top quark's spin, causing the W-boson's spin projection onto the z-axis to be zero, leaving it in the helicity state, $\Lambda = 0$. The $\Lambda = +1$ helicity state is inaccessible to the W-boson in the massless limit of the b-quark and is highly suppressed, even when the non-zero mass is taken into account.

Since properties of the top quark cannot be measured directly, the most important aspect of the top quark decay is that one can infer the spin state of the top quark by measuring the helicity of the W-boson in the top quark's rest frame. If Λ_{W^+} in the top quark's rest frame is measured to be -1, then the top quark's spin was aligned anti-parallel to the W-boson's momentum direction. Similarly, if Λ_{W^+} in the top quark's rest frame is measured to be 0, then the top quark's spin was aligned parallel to the momentum direction of the W-boson.

The W-boson allows access to spin observables of the top quark, which is a great feature. The spin configuration of a W-boson is determined through its decay products. Similar to the top quark decay, the electro-weak $V - A$ coupling of the W-boson to its decay products, $\ell\bar{\nu}_\ell$ or $q\bar{q}$, allows for the spin information of the W-boson to be accessed through the spin states of its decay products. Figure 2.8 depicts the decay of a W^+ into a charged anti-lepton and its associated neutrino in the W-boson's center-of-mass frame.

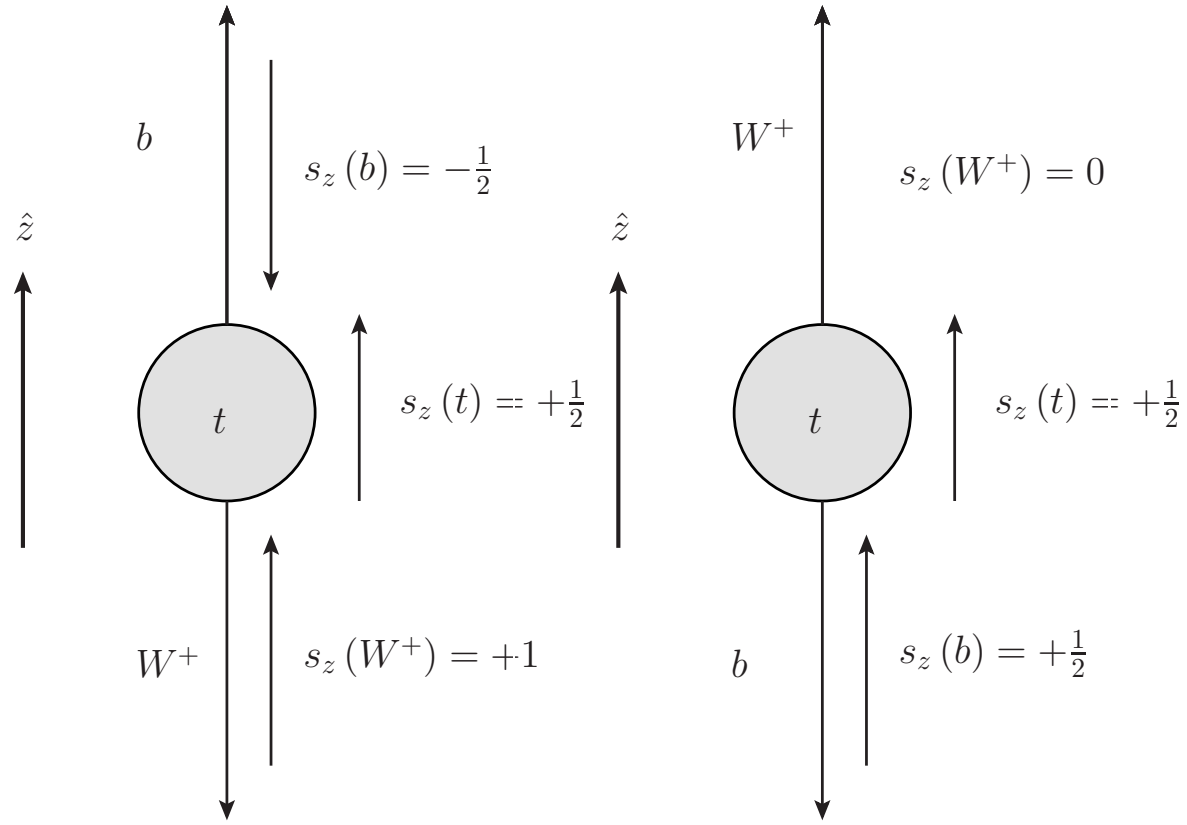

(a) Top decay with $\Lambda_{W^+} = -1$ **(b)** Top decay with $\Lambda_{W^+} = 0$

Figure 2.7.: Top quark decay in the top quark's rest frame with the spin of each particle projected onto the z-axis. For both cases, the b-quark is considered to be massless; therefore, the helicity, Λ, of the b-quark has the same handedness as its chirality (left handed), which imposes the requirement that the W-boson's helicity state must conserve the initial z-component of spin. In Fig. 2.7a, the W-boson must have Λ = -1 (spin direction anti-parallel to its momentum), to conserve the spin component in the z direction; while in Fig. 2.7b, the W-boson must have $\Lambda = 0$ (projection of its spin onto the z-axis equals 0).

Similar to spin constraints of the top quark decay, the spin projection of the W-boson along the z-axis must be conserved by the spin projections of the charged anti-lepton and the neutrino. The chiral coupling (in the massless limit of the charged anti-lepton and neutrino) will force the W^+-boson to decay into a right-handed charged anti-lepton and a left-handed neutrino. To ensure that the projection of W^+-boson's spin onto the z-axis is conserved, the momentum of the charged anti-lepton (neutrino) must be parallel (anti-parallel) to the spin projection of the W^+-boson. Consequently, by measuring the

direction of the charged lepton's momentum in the W^+-boson's rest frame, one can access the spin state of the W^+-boson. This only true for W^+-bosons in the $\Lambda = \pm 1$ helicity states; the charged leptons originating from the decay of W^+-bosons in the $\Lambda = \pm 0$ helicity states will not have a preferred direction.

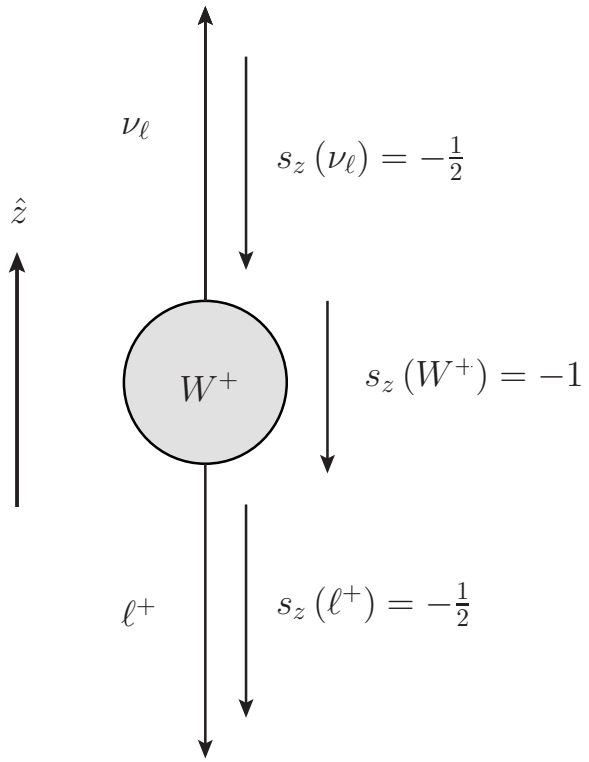

Figure 2.8.: The decay of a W^+ to an anti-lepton and its associated neutrino in the W-boson's center-of-mass frame. The spin of each particle is projected onto the z-axis. In the massless limit of the charged lepton and neutrino, the charged anti-lepton (neutrino) must have its momentum direction parallel (anti-parallel) to the spin projection of the W-boson due to the fact that fermions in the SM are left-handed and antifermions are right-handed.

Considering that the spin state of the W-boson in its rest frame can be accessed through the angular distribution of its decay products and that the top quark's spin state in its rest frame can be determined by the W-boson's spin state (provided it's in the helicity state $\Lambda = \pm 1$), one can determine the top quark's spin state in its rest frame by measuring its final state decay products momentum vectors, provided that one properly boosts the final state decay product into the W-boson's rest frame and properly boost

the W-boson's spin state into the top quark's rest frame. The equations describing the top quark's longitudinal polarization in $t\bar{t}$ production using angular distributions of the top quark's final state products were calculated using this method.

This analysis utilizes single and double angular distributions of the top quark(s) in $t\bar{t}$ production. The double differential cross sections for $t\bar{t}$ decays in the polar angles θ_1 (θ_2) of one of the top's (antitop's) final state decay products, with respect to a given quantization axis is given by

$$\frac{1}{\sigma}\frac{d^2\sigma}{d\cos\theta_1 d\cos\theta_2} = \frac{1}{4}(1 + \alpha_1 P_1 \cos\theta_1 + \alpha_2 P_2 \cos\theta_2 - C\cos\theta_1\cos\theta_2), \tag{2.32}$$

where $\alpha_1 P_1$ ($\alpha_2 P_2$) corresponds to the spin-analyzing power, $\alpha_{1,2}$, of one of the final state decay products of the top (antitop) quark times the degree of polarization along the chosen quantization axis, P, of the top (antitop), and C represents the $t\bar{t}$ spin correlation [31]. The angle θ_1 (θ_2) corresponds to the polar angle of one of the final state decay products of the top (antitop) quark. The spin analyzing power [32] is a measure of the daughter particle's sensitivity to its parent particle's spin state; the values of α for each of the final state decay products at tree level[10] may be found in Table 2.4. The single differential distribution in the polar angle of the top's decay products, θ_i, where the index i represents any of the possible decay products of the top quark, is also used in this analysis and is given by

$$\frac{1}{\sigma}\frac{d\sigma}{d\cos\theta_i} = \frac{1}{2}\left(1 + \alpha_i P \cos\theta_i\right). \tag{2.33}$$

An important feature of the single polar angle distribution is that it is not dependent upon the spin correlation of the top and antitop; to determine the spin correlation

[10] Corrections to the spin analyzing power have been calculated at NLO in QCD and were found to be negligible and will not be considered in this analysis [33].

from the polar angle distributions of the top and antitop's decay products, the double differential distribution must be exploited.

α_i	Particle Type
1.0	Charged Lepton
1.0	Down and Strange Quarks
-0.4	b Quark
-0.3	Neutrino
-0.3	Up Type Quark

Table 2.4.: Predicted tree level values of the spin-analyzing power, α_i, for the top quark final state decay products.

For the purpose of this analysis, the polar angle distribution of the charged lepton, $\cos\theta_\ell$, is used since it has the highest sensitivity to the top quark's spin state, $\alpha_\ell = 1$; in addition, leptons are easily identified and measured in the ATLAS detector. The quantization axis for this measurement is chosen as the parent top quark's momentum direction in the $t\bar{t}$ center-of-mass frame, otherwise known as the helicity basis. The polar angle θ_ℓ is measured from this quantization axis to the charged lepton's momentum direction in its parent top quark's rest frame, as depicted in Fig. 2.9. A detailed discussion on the top and antitop spin correlation is presented in Section 2.3.2 and the the degree of longitudinal polarization of the top quark in $t\bar{t}$ production is discussed in Section 2.3.4.

2.3.2. $t\bar{t}$ Spin Correlation

The degree of the top-antitop spin correlation in $t\bar{t}$ production, C, listed in Eq. (2.32) is defined as the fractional difference between the number of events where the top and antitop quark's spin orientations are aligned and events where the top quark spins are

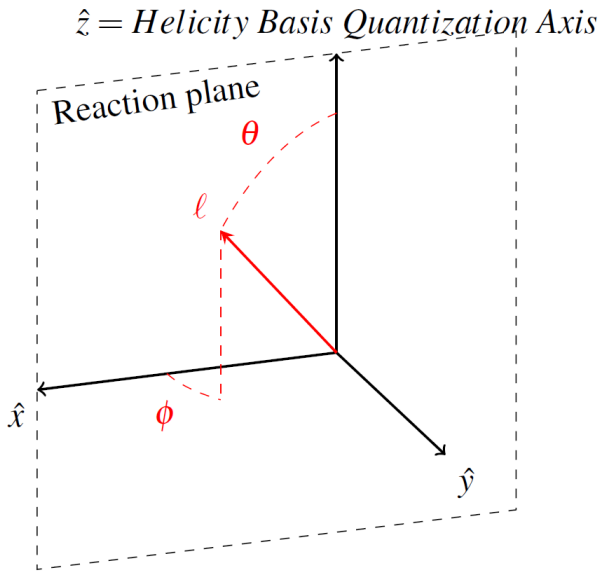

Figure 2.9.: Depiction of the charged lepton's polar angle θ with respect to the helicity basis quantization axis.

oppositely aligned. The degree of spin correlation takes the form

$$C = \frac{N(\uparrow\uparrow) + N(\downarrow\downarrow) - [N(\uparrow\downarrow) + N(\downarrow\uparrow)]}{N(\uparrow\uparrow) + N(\downarrow\downarrow) + N(\uparrow\downarrow) + N(\downarrow\uparrow)}, \tag{2.34}$$

where the left (right) arrow corresponds to the spin of the top (antitop) quark with respect to a chosen quantization axis for the top (antitop). Two quantization axis are needed for a spin correlation measurement: a top spin axis and an antitop spin axis. For instance, the helicity basis can be used to define the top (antitop) spin axis as the top (antitop) quark's momentum direction in the $t\bar{t}$ center-of-mass frame.

As mentioned in Section 2.2.2, the predominant mechanism for $t\bar{t}$ production at the LHC is through gluon fusion. At low invariant masses of the $t\bar{t}$ system, $m_{t\bar{t}}$, the gluon fusion is dominated by like-helicity gluon pairs, which produces left-left or right-right helicity configurations for the top quarks[11] [31] . In this low $m_{t\bar{t}}$ scenario, the spin correlation can be measured in the dilepton channel using the $\Delta\phi$ observable, which is

[11] At high $m_{t\bar{t}}$, the gluon pairs are of unlike-helicity, producing top quarks with unlike-helicity states, similar to $t\bar{t}$ spin states produced from $q\bar{q} \to t\bar{t}$.

the difference in azimuthal angle between the charged leptons in the lab frame. This is due to the chiral $V - A$ structure of the electroweak coupling, allowing for the spin information of the top quark to be passed on to its decay products. Figure 2.10 depicts the simulated distributions of $\Delta\phi$ at parton level assuming the SM predicted value of $C = 0.31$ and zero spin correlation.

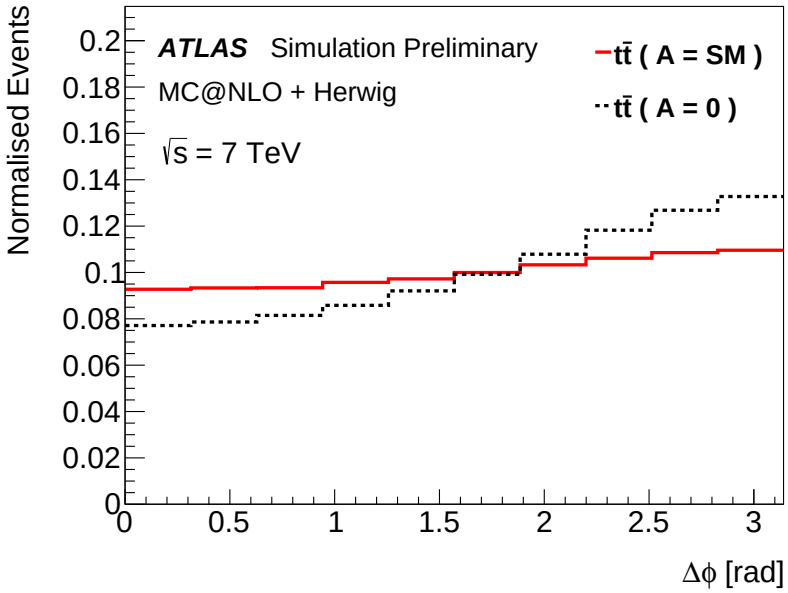

Figure 2.10.: ATLAS simulation of the observable $\Delta\phi$ between the charged leptons in the dilepton final state at parton level [34]. The solid line is the SM prediction of $C = 0.31$ and the dashed line indicates $t\bar{t}$ production with no spin correlation. The value of A in this plot is the value of C in this thesis.

The spin correlation of the top and antitop do not have an effect on the observable of interest for this analysis, $\cos\theta_\ell$, as can be seen in the single differential angular distribution of the top (antitop) decay products in Eq. (2.33). However, it does impact the double differential angular distribution of $t\bar{t}$ decay, given in Eq. (2.32). Figure 2.11 depicts the distribution of the product of the polar angles (in the helicity basis) of the positively and negatively charged leptons in the dilepton channel using ATLAS simulations for SM spin correlation and zero spin correlation. It is important to note that the mean of the

$\cos\theta_{\ell^+}\cos\theta_{\ell^-}$ distribution for SM spin correlation is shifted from that of the zero spin correlation; the mean of this distribution is used to extract the spin correlation.

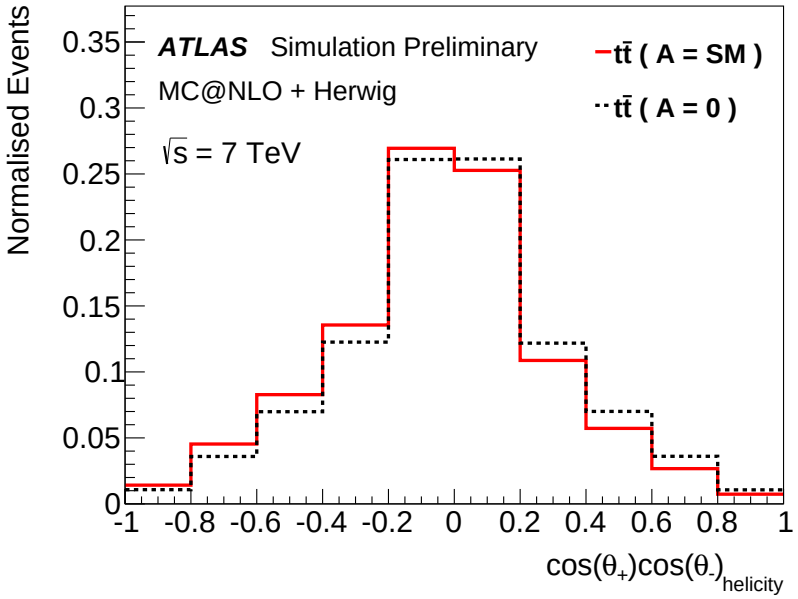

Figure 2.11.: ATLAS simulation of the observable $\cos\theta_{\ell^+}\cos\theta_{\ell^-}$, in the helicity basis, for the charged leptons in the dilepton final state at parton level [34]. The solid line is the SM prediction of $C = 0.31$ and the dashed line indicates $t\bar{t}$ production with no spin correlation. The value of A in this plot is the value of C in this thesis.

The CDF and DØ collaborations have performed measurements of the spin correlation [35–37] with DØ's most recent measurement reporting evidence for the presence of spin correlation in $t\bar{t}$ events with a significance of 3.1 standard deviations [38]. ATLAS has measured the spin correlation in $t\bar{t}$ events and found their measured value of C to be in good agreement with the NLO SM prediction; they also excluded the hypothesis of zero spin correlation at 5.1 standard deviations [39].

2.3.3. Transverse Polarization of the Top Quark

The degree of transverse polarization of the top quark in $t\bar{t}$ production is defined as the average of the projection of the spin of the top quark onto the direction transverse to

the interaction plane, given by

$$P_{\perp} = \left\langle \vec{S} \cdot \left(\vec{p} \times \hat{k} \right) \right\rangle , \tag{2.35}$$

where $\vec{S}$ is the spin of the top quark, $\vec{p}$ is the momentum of one of the incoming protons in the $t\bar{t}$ center-of-mass frame, $\vec{k}$ is the momentum of the top quark in the $t\bar{t}$ center-of-mass frame, and $\left(\vec{p} \times \vec{k} \right)$ defines a vector $\vec{n}$ whose direction is perpendicular to the scattering plane. The transverse polarization transforms under a parity transformation, $\mathcal{P}$, as

$$\mathcal{P}\left(P_{\perp}\right) = \mathcal{P}\left(\left\langle \vec{S} \cdot \left(\vec{p} \times \vec{k} \right) \right\rangle\right) \tag{2.36}$$

$$\mathcal{P}\left(\left\langle \vec{S} \cdot \left(\vec{p} \times \vec{k} \right) \right\rangle\right) = \left\langle \vec{S} \cdot \left[(-\vec{p}) \times \left(-\vec{k} \right) \right] \right\rangle \tag{2.37}$$

$$\left\langle \vec{S} \cdot \left[(-\vec{p}) \times \left(-\vec{k} \right) \right] \right\rangle = \left\langle \vec{S} \cdot \left[\vec{p} \times \vec{k} \right] \right\rangle \tag{2.38}$$

$$\mathcal{P}\left(P_{\perp}\right) = P_{\perp}, \tag{2.39}$$

which means that the production of transversely polarized top quarks in $t\bar{t}$ production is a parity conserving interaction. Therefore, the strong production of top quark pairs can give rise to a transverse polarization of the top quark.

The degree of transverse polarization may be measured in the dilepton channel at the LHC with the observable of interest $\mathcal{O}_{\perp}$, which is given by

$$\mathcal{O}_{\perp} = \pm \operatorname{sign}\left(\hat{p}_p \cdot \hat{k}_{t,\bar{t}} \right) \hat{n} \cdot \hat{\ell}^{+,-}, \tag{2.40}$$

where all vectors are defined in the $t\bar{t}$ center-of-mass frame and $\hat{p}_p$ is the direction of the incoming protons momentum, $\hat{\ell^{+,-}}$ is the direction of the charged leptons momentum direction, $\hat{k}_{t,\bar{t}}$ is the direction of the top (antitop) quark's momentum direction, and $\hat{n}$ is the direction normal to the reaction plane. The positively charged leptons pick up the plus sign at the beginning of Eq. (2.40) and the negatively charged leptons pick up the

minus sign. Equation (2.40) is related to the degree of transverse polarization by

$$P_\perp = \frac{N_\ell\left(\mathcal{O}_\perp > 0\right) - N_\ell\left(\mathcal{O}_\perp < 0\right)}{N_\ell} \tag{2.41}$$

Calculations show that QCD absorptive parts in the strong production of $t\bar{t}$ give rise to a transverse polarization of the top and antitop quark [40–42]. The SM prediction for the degree of transverse polarization for the LHC at $\sqrt{s} = 7$ TeV is $P_\perp = -0.042 \pm 1\%$ [23]. It is important to note that the degree of transverse polarization of the top quark in $t\bar{t}$ production does not affect the longitudinal polarization of the top quark in any way.

2.3.4. SM And BSM Predictions for the Longitudinal Polarization of the Top Quark in $t\bar{t}$ Production

The degree of the longitudinal polarization of the top quark in $t\bar{t}$ production may be measured through the angular distribution of the top and antitop's decay products, as was shown in Eq. (2.33). In particular, this analysis utilizes the polar angle distribution of the charged lepton in the helicity basis to extract $\alpha_\ell P$ using a template fit to the data[12], which is described in Chapter 4. This analysis considers two scenarios for the production of longitudinally polarized top quarks: a CP conserving case where $\alpha_{\ell^+} P_{\ell^+} = \alpha_{\ell^-} P_{\ell^-}$ and a CP violating case where $\alpha_{\ell^+} P_{\ell^+} = -\alpha_{\ell^-} P_{\ell^-}$. Figure 2.12 depicts the simulated distributions of $\cos\theta_\ell$ for three different cases: no top quark polarization ($\alpha_\ell P = 0$), partially positively polarized top quarks ($\alpha_\ell P = 0.3$), and partially negatively polarized top quarks ($\alpha_\ell P = -0.3$). The shapes of the $\cos\theta_\ell$ distributions for each case are dramatically different; the no polarization case is flat and the partially positively

[12] The product of α_ℓ and P is measured because the spin analyzing power changes independently of the polarization in the presence of anomalous couplings at the Wtb vertex [43]; therefore, under such anomalous couplings, a measurement of $\alpha_\ell P$ would continue to render a physically meaningful result.

(negatively) polarized top quark case leads to a positive (negative) slope in the $\cos\theta_\ell$ distribution.

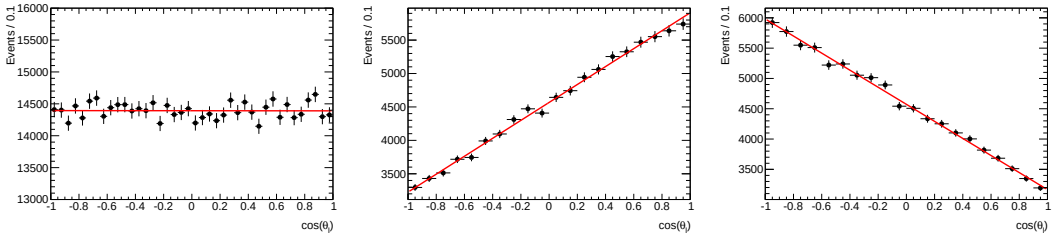

(a) $\alpha_\ell P = 0$ **(b)** $\alpha_\ell P = +0.3$ **(c)** $\alpha_\ell P = -0.3$

Figure 2.12.: Simulation of the observable $\cos\theta_\ell$ for three cases of longitudinally polarized top quarks: no top quark polarization shown in Fig. 4.27, partially positively polarized top quarks shown in Fig. 2.12b, and partially negatively polarized top quarks shown in Fig. 2.12c

The BSM models used to explain the A_{FB} predict values for P that are significantly different from the SM prediction. If a BSM model is responsible for the A_{FB}, it will impact the shape of the $\cos\theta_\ell$ distribution, making this analysis sensitive to the production mechanism of $t\bar{t}$. Moreover, many of the BSM models predict varying degrees of longitudinal polarization, allowing this analysis to distinguish between the models by measuring $\alpha_\ell P$. This section will discuss the SM prediction for the top quark's longitudinal momentum in $t\bar{t}$ production and will highlight a number of BSM model's predictions as well. The section will conclude by comparing the predicted results from both the SM and BSM models.

SM prediction

As was shown in Eq. (2.31), the mechanisms responsible for producing longitudinally polarized top quarks in $t\bar{t}$ production must be parity violating interactions. In the SM, strong interactions conserve parity; therefore, if there is to be any contribution to the top quark's longitudinal polarization from the SM production of top quark pairs at the LHC,

it must come from higher order electro-weak corrections to the strong production of $t\bar{t}$ or from the interference of the weak production of $t\bar{t}$. Figures 2.13 and 2.14 depict the Feynman diagrams for the higher order electro-weak corrections to the strong production of $t\bar{t}$, while the Feynman diagram for the leading order electro-weak production of $t\bar{t}$ is shown in Fig. 2.4e. These electro-weak corrections and interference terms to the strong production of $t\bar{t}$ produce a very small degree of longitudinal polarization of the top quark since they involve powers of the electro-weak coupling constant[13]. Each of the diagrams in Figs. 2.4e, 2.13 and 2.14 is CP conserving; the diagrams that produce longitudinally polarized top quarks through a CP violating interaction must contain multiple virtual W-boson exchanges that involve CP violating vertices from the CKM matrix. Due to this fact, CP violating production of $t\bar{t}$ within the SM predicts a negligible degree of longitudinal polarization (in the helicity basis) for the top quark at the LHC operating at $\sqrt{s} = 7$ TeV and at $\sqrt{s} = 8$ TeV, $P_{\text{CPV}} = 0$. The SM prediction for the degree of longitudinal polarization (in the helicity basis) of the top quark in $t\bar{t}$ production in the CP conserving scenario at the LHC operating at $\sqrt{s} = 7$ TeV and at $\sqrt{s} = 8$ TeV is $P_{\text{CPC}} = 0.003 \pm 1\%$ [23].

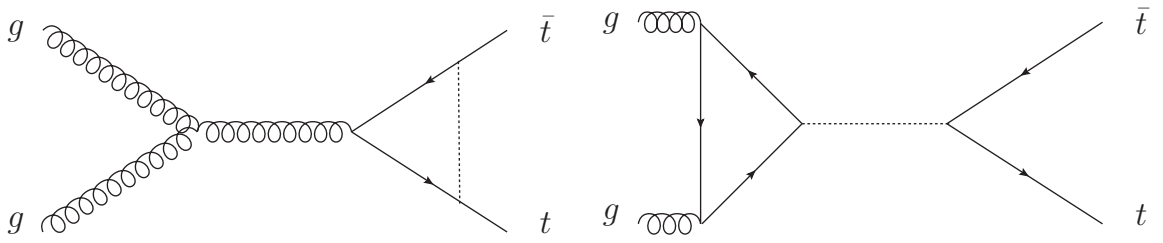

(a) s-channel correction **(b)** s-channel correction with fermion triangle

Figure 2.13.: Tree level QCD diagrams with parity violating 1-loop weak corrections to the s-channel $gg \to t\bar{t}$ production. The dashed line in Fig. 2.13a represents W/Z bosons or the Higgs boson H. The fermion triangle in Fig. 2.13b represents a t or b quark; the dashed line represents the subsequent s-channel exchange of a Z-boson.

[13]The ratio of the electro-weak coupling to the strong coupling, $\frac{\alpha_W}{\alpha_s}$, is approximately 10^{-7}

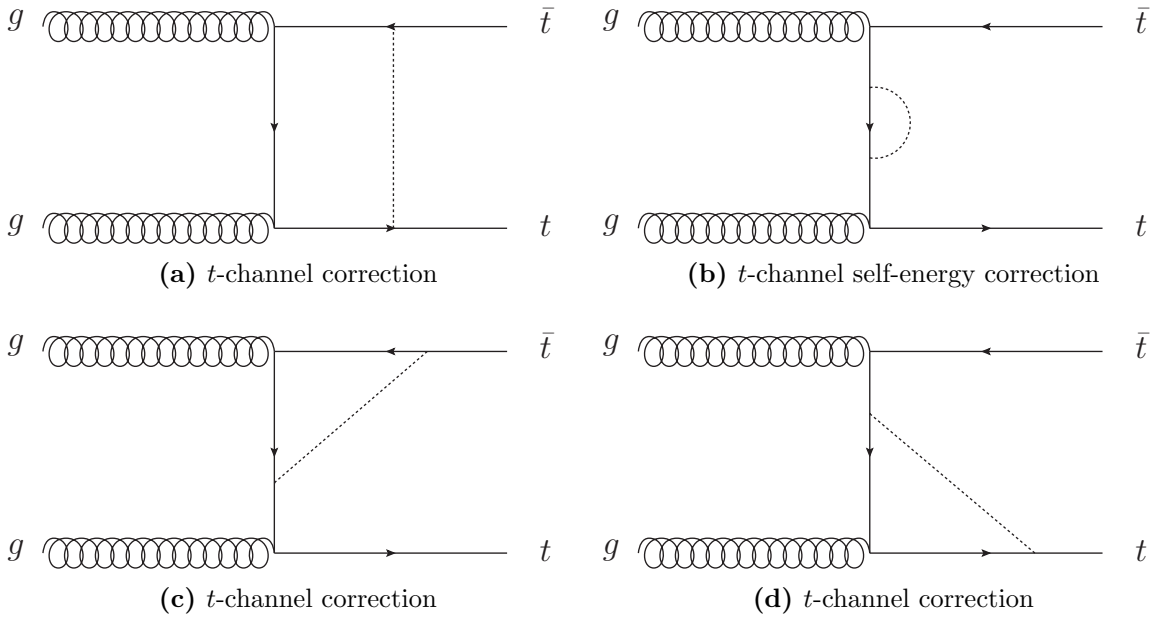

(a) t-channel correction **(b)** t-channel self-energy correction

(c) t-channel correction **(d)** t-channel correction

Figure 2.14.: Tree level QCD diagrams with parity violating 1-loop weak corrections to the t-channel $gg \to t\bar{t}$ production. The dashed line in Figs. 2.14a to 2.14d represents W,Z bosons or the Higgs boson H.

BSM prediction

In an attempt to explain the A_{FB} result from the Tevatron, BSM production mechanisms for $t\bar{t}$ that involve chiral couplings to top quarks have been introduced [27]. Due to the nature of their chiral couplings, they produce longitudinally polarized top quarks. The BSM models considered are required to generate the A_{FB} while producing a cross section for $t\bar{t}$ production that is consistent with experimental measurements. Two classes of models are considered, a color singlet t-channel production mechanism (W' vector boson) and a color octet s-channel production mechanism (axigluon vector bosons), each of which has parity violating couplings to the $t\bar{t}$ initial and final states. The axigluons comprise three cases, each having a different coupling to the top quarks: a fully axial coupling (G_A), left-handed coupling (G_L), and right-handed coupling (G_R).

In addition to the production mechanisms aimed at explaining the A_{FB}, a general BSM model for $t\bar{t}$ production that exchanges massive particles that couple to the chromo-electric dipole moments of the top quark generates longitudinally polarized top quarks [23]. This model will be referred to as NP_C.

Each BSM model's prediction for the longitudinal polarization (in the helicity basis) of the top quark in $t\bar{t}$ production was calculated and their results are tabulated in Table 2.5. A calculation of P_{CPV} in the helicity basis for a CP violating NP_C model was also performed and predicts that $NP_C\,(CPV) = 0.444 \pm\ 12\%$ at the LHC operating at $\sqrt{s} = 7$ TeV.

Model	P_{CPC}
NP_C	$0.538 \pm\ 4\%$
G_A	$0.01 \pm\ 1.2\%$
G_L	$-0.01 \pm\ 1.2\%$
G_R	$0.04 \pm\ 1.2\%$
W'	$0.18 \pm\ 1.2\%$

Table 2.5.: Predicted values of P_{CPC} in the helicity basis for various BSM $t\bar{t}$ production mechanisms at the LHC operating at $\sqrt{s} = 7$ TeV.

Comparison of SM and BSM Predictions

After comparing the SM and BSM predictions for P_{CPC} and P_{CPV}, it is clear that a measurement of the spin-analyzing power times the longitudinal polarization of the top quark in the helicity basis is sensitive to its production mechanism. Moreover, if a sizable $\alpha_\ell P$ is measured, it has the power to differentiate between BSM models. For instance, if $\alpha_\ell P_{\mathrm{CPC}}$ is measured to be on the order of 1%, it would favor the axigluon models. In that case, the measurement may be able to distinguish the production mechanism between the G_A, G_L, and G_R models. A measurement of $\alpha_\ell P_{\mathrm{CPC}}$ on the order of 10% would

suggest that the W' or NP_C are possible production mechanisms for $t\bar{t}$. A measurement of $\alpha_\ell P_{\mathrm{CPV}}$ in the helicity basis that significantly deviates from the SM prediction of zero would suggest that the production of $t\bar{t}$ originates from a new physics model.

Chapter 3.

Experimental Apparatus

The data analyzed in this thesis was collected by the ATLAS experiment which detects particle collisions produced by the Large Hadron Collider (LHC) at The European Organization for Nuclear Research (CERN). This chapter is dedicated to describing the organization of CERN, the design of the LHC, and the experimental apparatus of the ATLAS experiment.

3.1. The European Organization for Nuclear Research

The CERN laboratory was founded in 1954 and is currently the largest particle physics laboratory in the world. Being one of Europe's first joint ventures, the laboratory was chosen to be situated along the Franco-Swiss border near Geneva, Switzerland. CERN is comprised of twenty member states, with representatives who sit on a council responsible for all important decisions affecting the organization. The laboratory hosts the largest particle accelerator in the world, the LHC, which supplies particle collisions to seven experiments that use detectors to analyze the resulting particles. While the LHC has become the primary focus of research at CERN, there are many important experiments that employ smaller accelerators or facilities that are located at or related to

the laboratory. Over 10,000 visiting scientists from over 113 countries and 600 institutions utilize CERN for their research.

Experiments at CERN have helped shape our current understanding of particle physics through direct particle searches, precision measurements of the Standard Model's parameters, and innovations in detector technology. The research performed at CERN has resulted in two Nobel Prizes in Physics. The first Nobel Prize in Physics was received by Carlo Rubbia and Simon Van der Meer in 1984 for "their decisive contributions to the large project, which led to the discovery of the field particles W and Z, communicators of weak interaction." The discovery of the W and Z [44, 45] verified the unification of the weak and electromagnetic forces, validating the proposed electroweak theory of the Standard Model. The second Nobel Prize in Physics was received by Georges Charpak in 1992 for "his invention and development of particle detectors, in particular the multiwire proportional chamber, a breakthrough in the technique for exploring the innermost parts of matter." Charpak's invention of the multiwire proportional chamber was the genesis of modern electronic particle detection.

3.2. The Large Hadron Collider

The LHC [46] is the world's highest energy particle accelerator, designed to collide beams of protons and heavy ions at center of mass energies of up to $\sqrt{s} = 14$ TeV (protons). It is located in a 27 km long tunnel formerly used by the electron-antielectron collider (LEP). The tunnel housing the LHC lies at a mean depth of 100 m underneath the ground, crossing over the Franco-Swiss border. Inside the tunnel is a ring of superconducting magnets used to accelerate charged particles inside of an ultrahigh vacuum beam pipe. The LHC consists of two beam pipes with each pipe containing bunches of particles moving in opposite directions. One thousand two hundred and thirty two dipole magnets

(15 m in length) are used to bend the beams, three hundred and ninety two quadrapole magnets (5-7 meters long) are used to focus the beams and insertion magnets are used to squeeze the particles close together to maximize the probability of collisions when the beams cross. Due to a series of unexpected setbacks, the LHC has been unable to reach its intended center of mass energy for proton-proton (pp) collisions. Despite the technical impediments faced by the LHC, it was able to deliver stable beams of protons at a record $\sqrt{s} = 8$ TeV on April 5th 2012.

As mentioned in Section 3.1, the LHC provides particle collisions to seven experiments. The two largest experiments are ATLAS (**A** **T**oroidal **L**HC **A**pparatu**S**) and CMS (**C**ompact **M**uon **S**olendoid), which explore a broad range of physics using multi-purpose detectors. Because both detectors were conceived independently, they can be used to cross-check any potential discovery. There are also experiments that are intended to study very particular aspects of particle physics. ALICE (**A** **L**arge **I**on **C**ollider **E**xperiment) is an experiment that uses a heavy-ion detector to study the quark-gluon plasma produced during heavy ion collisions. LHCb (**L**arge **H**adron **C**ollider **B**eauty), investigates the properties of b-physics to determine the parameters of CP violation. Finally, there are three smaller experiments: LHCf, TOTEM, and MoEDAL. LHCf (**L**arge **H**adron **C**ollider **F**orward) uses forward collisions, particles produced close to the beam line, to replicate cosmic rays in the laboratory. LHCf's results will help guide physicists that are engaged in large-scale cosmic ray experiments. TOTEM (**TOT**al **E**lastic and diffractive cross-section **M**easurement) studies processes unavailable to ATLAS and CMS. They focus on studying forward particles because the two multi-purpose detectors are unable to measure particles close to the beam line. MoEDAL's (**Mo**nopole and **E**xotics **D**etector **A**t the **L**HC) primary purpose is to search for magnetic monopoles and highly ionizing Stable Massive Particles (SMP).

3.2.1. Technical Design

This section will be limited to the description of proton acceleration at the LHC; heavy-ion acceleration is outside the purview of this thesis.

Protons must pass through a series of accelerators before being injected into the LHC. Aside from each machine's purpose to increase the energy of the particle beams, most accelerators in the chain contain their own experiments that operate at lower energies. The chain of accelerators and the four major experiments at the LHC are depicted in Fig. 3.1.

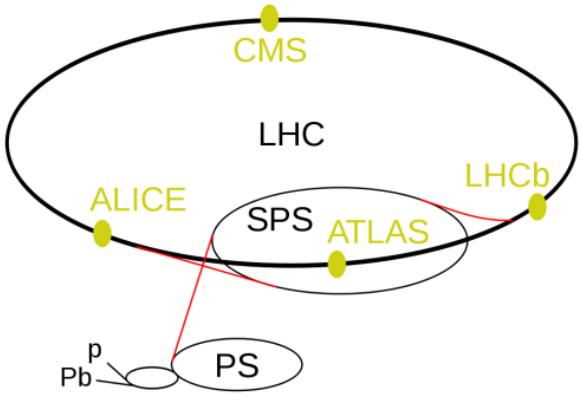

Figure 3.1.: Schematic of CERN's accelerator complex and the four major experiments at the LHC.

The source of protons for the acceleration process comes from a bottle of hydrogen gas. The hydrogen gas is passed through an electric field which strips electrons from the hydrogen atoms, yielding protons. The protons are then injected into the first accelerator of the chain, Linac2, a linear accelerator used to increase the energy of the protons to 50 MeV. Linear accelerators employ oscillating electric fields to accelerate charged particles in a linear beam line. From there, the protons are passed to the Proton Synchrotron Booster where the protons are accelerated to energies of 1.4 GeV. Synchrotron accelerators operate by applying a time-dependent magnetic field to the charged particles, bending

the particles into a closed path. The next step in the acceleration process is undertaken by the oldest accelerator in the chain, the Proton Synchrotron (PS), which increases the energy of the protons to 25 GeV. The protons are then injected into the second largest accelerator at CERN's complex, the Super Proton Synchrotron (SPS). Measuring 7 km in circumference, the SPS accelerates the protons to an energy of 450 GeV before their subsequent injection into the LHC. The SPS and the LHC are connected by two transfer lines, with each transfer line injecting protons into one of the two beam pipes of the LHC. Recalling from Section 3.2, one beam pipe circulates the protons clockwise while the other beam pipe circulates counterclockwise. Once the protons have been delivered to the LHC, it takes 20 minutes for the protons to achieve their maximum energy of 3.5 TeV per beam.[1] Having been optimized at their maximum energy, the beams are collided inside the four largest detectors at the LHC: ALICE, ATLAS, CMS, and LHCb.

The protons are accelerated within the accelerator chain in bunches. Under normal operating conditions, one bunch consists of up to 10^{11} protons with the LHC storing up to 2808 bunches at a bunch spacing of 25 ns (7 m). Accelerating the protons in bunches is a result of the radio frequency (RF) acceleration scheme employed by the LHC, which uses time-dependent electromagnetic fields to accelerate particles with a well defined energy. The bunch size varies as it traverses the LHC, with bunches far from the collision point measuring a few centimeters long and a millimeter wide. They are squeezed to 16 μm wide and 8 cm long at the interaction points to increase the probability of pp collisions.

Superconducting electromagnets are used to guide the protons as they traverse the ultra high vacuum beam pipes of the LHC.[2] The magnets are constructed out of coils of niobium-titanium wires that are cooled to a temperature of 1.9 K, allowing the magnets

[1] The analysis presented in this thesis was performed using the 2011 dataset, during which time the LHC operated at $\sqrt{s} = 7$ TeV. The maximum center of mass energy at the LHC was achieved in 2012 at $\sqrt{s} = 8$ TeV.

[2] The pressure within the beam pipes is approximately 10 times lower than on the Moon.

to operate in a superconducting state. Liquid helium is distributed throughout the LHC to cool the magnets and other operational components. As stated in Section 3.2, there are three main types of magnets employed by the LHC: dipole, quadrapole, and insertion.[3] The 1232 dipole magnets, each 15 m long and weighing 35 tons, provide magnetic fields up to 8.3 T over their length. Achieving such a large magnetic dipole field is one of the most significant technological achievements at the LHC because the maximum energy that can be achieved given a specific acceleration circumference is directly proportional to the strength of the dipole field. To keep the particles in a compact beam, 392 quadrapole magnets are used to squeeze the beam in both the transverse and longitudinal directions. Insertion magnets are constructed out of 3 quadrapole magnets called an inner triplet. Upon entering each of the four detectors, two insertion magnets are employed to focus the beam to its smallest dimensions to ensure the highest probability for pp collisions.

Aside from beam energies, the most important parameter of a particle collider is its luminosity. The integrated luminosity, number of collisions over a set period of time, is related to the number of events for a particular physical process by the formula:

$$N = \sigma \int \mathcal{L}\, dt, \tag{3.1}$$

where N is the number of events, σ is the cross section for that particular physical process, $\int \mathcal{L}\, dt$ is the integrated luminosity, and $\mathcal{L}$ is the instantaneous luminosity which is the number of interactions per second and unit area [$\text{cm}^{-2}\ \text{s}^{-1}$]. Integrated luminosity is typically expressed in the units of inverse picobarns ($\text{pb}^{-1} = 10^{36}\ \text{cm}^{-2}$) or inverse femtobarns ($\text{fb}^{-1} = 10^{39}\ \text{cm}^{-2}$); this convention will be used for the duration of this thesis. Fig. 3.2 shows the LHC's delivered integrated luminosity and ATLAS's collected integrated luminosity for the years of 2011 and 2012. For head on collisions of particle

[3]The LHC has approximately 9600 magnets ranging from dipoles to decapoles.

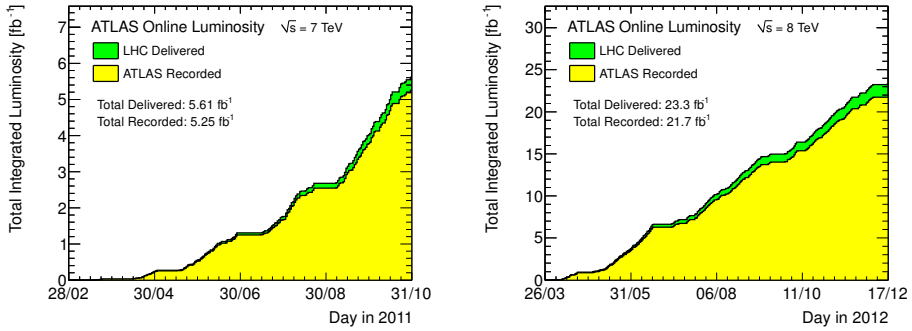

(a) Year of 2011 **(b)** Year of 2012

Figure 3.2.: Delivered integrated luminosity by the LHC and recorded integrated luminosity by ATLAS for the years of 2011 shown in Fig. 3.2a and 2012 shown in Fig. 3.2b.

bunches with gaussian transverse profiles, the instantaneous luminosity is given by:

$$\mathcal{L} = \frac{n_b N_b^2 f_{rev}}{4\pi\sigma_x\sigma_y}, \tag{3.2}$$

where n_b is the number of bunches per beam, N_b is the number of particles per bunch, f_{rev} is the collision frequency, and σ_x and σ_y are the root mean square widths of the beam in the transverse direction. The LHC does not collide particle bunches head on; as a result, Eq. (3.2) needs to be adjusted by a scale factor that accounts for the beams reduced region of interaction due to their crossing angle; the scale factor is constant for a given beam configuration. The LHC can increase its luminosity by increasing the number of particles per bunch, increasing the number of bunches, or by squeezing the beam's transverse profile.

3.3. The ATLAS Experiment

The ATLAS experiment comprises more than 3000 scientists from 174 institutes in 38 countries, employing the general purpose particle detector ATLAS (**A** **T**oroidal **L**HC **A**pparatu**S**) to collect data produced by pp collisions at the LHC. General purpose

detectors, such as ATLAS, are typically constructed out of layers of subsystems, each layer concentric with the beam pipe. Each subsystem is intended to detect a particular type of particle; Fig. 3.3 shows a schematic drawing of the typical subsystems found in a general purpose detector. The detectors are placed in a magnetic field to determine the momentum of charged particles by exploiting the properties of the Lorentz force.

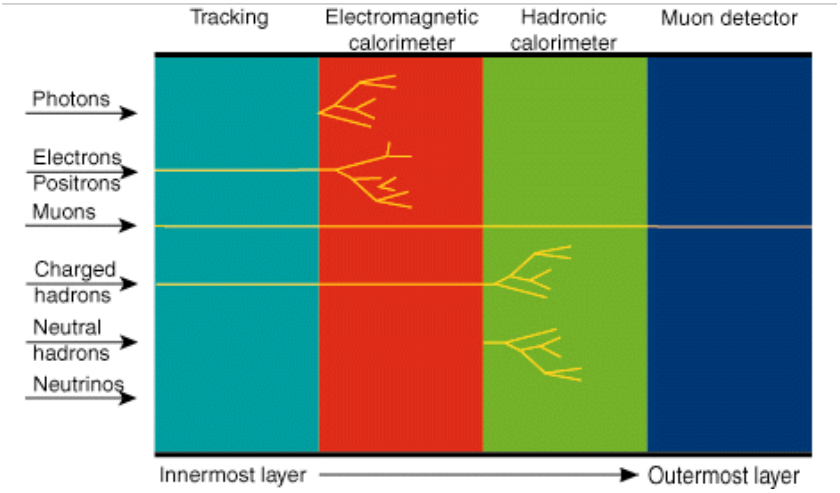

Figure 3.3.: Schematic of multi-purpose particle detector design.

Lying underneath Point 1, one of the four interaction points at the LHC, the ATLAS detector measures 44 m long by 25 m in diameter and weighs approximately 7,000 tons. The six subdetectors of ATLAS are distributed amongst cylindrical layers around the beam pipe and in two end-caps to ensure the maximum possible acceptance around the *pp* interaction point. Fig. 3.4 displays a schematic drawing of the ATLAS detector. There are four major constituents of the ATLAS detector: the Inner Detector (ID), which contains three of the subdetectors; the calorimeters, which contain two of the subdetectors; the muon spectrometer, which is the last of the subdetectors; and the magnet systems. Each of these constituents are discussed in detail in Sections 3.3.3 to 3.3.5.

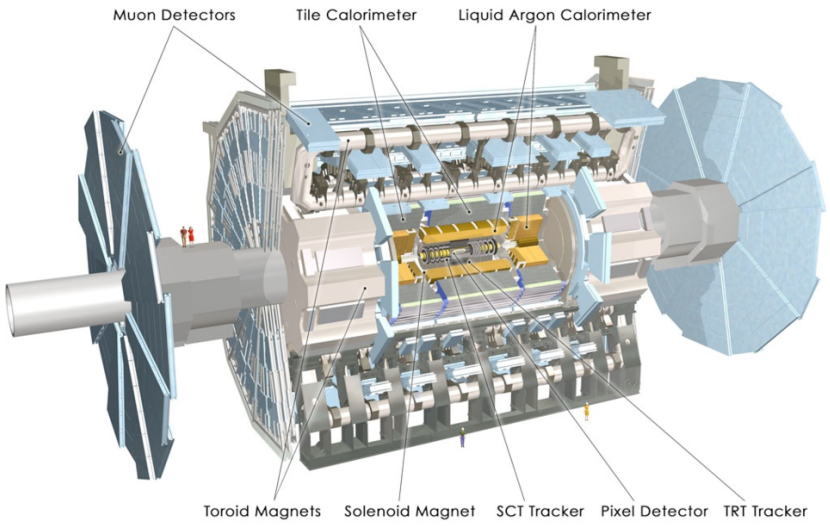

Figure 3.4.: Schematic of the ATLAS detector.

3.3.1. Detector Coordinates and Variables

The ATLAS experiment uses a right-handed coordinate system to describe the location of objects within the detector. The nominal interaction point in the center of the detector is used as the origin of the coordinate system and the z-axis is chosen to be along the beamline with positive $\hat{z}$ pointing toward Point 8. The x-axis points toward the center of the LHC ring and the y-axis points upward. The transverse plane is described in cylindrical coordinates (R, ϕ), where ϕ is the azimuthal angle around the beam pipe. The range of ϕ is $[-\pi, \pi]$, increasing clock-wise looking toward the positive $\hat{z}$ direction. The positive x-axis corresponds to $\phi = 0$. The polar angle, θ, ranges from $[0, \pi]$ and is measured from the positive z-axis.

The pseudo-rapidity, η, is a spatial coordinate used to describe the scattering angle of an object with respect to the beamline. It is defined in terms of the polar angle by

$$\eta = -\ln\left[\tan(\frac{\theta}{2})\right]. \tag{3.3}$$

For relativistic particles with low mass, η is an approximation of the rapidity y, which is given by

$$y = \frac{1}{2}\ln\frac{E + |p|\,c}{E - |p|\,c}. \tag{3.4}$$

The difference in rapidity between two objects, Δy, is invariant under Lorentz boosts along the beam axis, and under said approximation, $\Delta\eta$ is as well. At hadron colliders, variables that are invariant under Lorentz boosts in the beam direction are essential in describing objects since the longitudinal momentum in the partonic rest frame is unknown. ATLAS exploits this property of η and uses it instead of θ to describe the angle from the beamline to the x-axis. The ATLAS detector was constructed to be symmetric with respect to ϕ which allows the detector to be described in regions of η. For instance, large values of $|\eta|$ describe portions of the detector near the beamline, and are referred to as the forward region of the detector. Portions of the detector that are perpendicular to the beamline are at small values of $|\eta|$, and are referred to as the central region of the detector. The angles η and ϕ can be used to describe a rectangular coordinate system in which each variable is plotted on its respective axis. This allows for the angular distance between two objects to be expressed as the quantity ΔR, which is given by

$$\Delta R = \sqrt{(\Delta\eta)^2 + (\Delta\phi)^2}. \tag{3.5}$$

A common application of ΔR is its use as a parameter for isolating leptons and jets from other objects.

The energy and momenta of objects detected in ATLAS are commonly expressed in terms of their transverse components. The total transverse momentum is defined as

$$p_{\mathrm{T}} = |p| \sin(\theta). \tag{3.6}$$

and the transverse energy is defined as

$$E_{\mathrm{T}} = E \sin(\theta). \tag{3.7}$$

Objects with large p_{T} are of particular interest in hadron collisions, signifying partonic interactions with very large momentum transfers. Particles that rarely interact with matter, such as neutrinos, escape the detector without detection creating an imbalance between the initial and measured p_{T}.The transverse momentum of the particles that escape detection is referred to as the missing transverse energy, $E_{\mathrm{T}}^{\mathrm{miss}}$.

3.3.2. Magnets

By virtue of the Lorentz force, a charged particle's momentum can be determined by measuring the curvature of its trajectory through a magnetic field. Atlas employs this strategy by using a series of superconducting magnets designed such that each subdetector is situated within a magnetic field. A set of two magnet systems are used to provide the magnetic field to the subdetectors: a solenoid for the ID and a set of toroids for the Muon Spectrometer.

Solenoid

The central solenoid is located in between the ID and the calorimeter systems, providing a 2 T $\vec{B}$ field oriented along the positive $\hat{z}$ direction. The solenoid, measuring 5.8 m in

length and weighing 5.7 tons, is composed of a NbTi superconducting cable located in the center of an aluminum stabilizer. To minimize the amount of inactive material in the detector, the solenoid shares its crysostat, cooling system, and vacuum vessel with the liquid argon calorimeter. The solenoid nominally operates at 7.730 kA and a temperature of 4.5 K.

Toroid

The toroid magnet system, employed by the Muon Spectrometer, contains two sets of magnets: the barrel toroid, located just after the calorimeter system in the central region of the detector, and the end-cap toroids which are located in the forward region of the detector. Each magnet contains coils of Aluminum stabilized superconducting NbTi wire designed in the form of a flat race track. Eight coils housed in separate cryostats comprise the barrel toroid and provide a peak magnetic field of 3.9 T in the region $0 \leq |\eta| \leq 1.3$. Two end-cap toroids, each composed of eight coils cold linked in one cryostat, provide a peak magnetic field of 4.1 T to the region $1.6 \leq |\eta| \leq 2.7$. To maximize bending power and radial coverage in the interface between the toroids, the end-cap system is rotated at an angle of 22.5° with respect to the barrel toroids. Both systems nominally operate at 20.5 kA and at a temperature of 4.5 K.

3.3.3. Inner Detector

The ATLAS Inner Detector, the subdetector closest to the interaction point, is designed to provide high precision tracking for charged particles in the region of $|\eta| < 2.5$. The ID is placed inside a 2 T magnetic field produced by the solenoid and utilizes three separate technologies to measure charged particle's momenta: the pixel detector, semiconductor tracker (SCT), and transition radiation tracker (TRT). Each component of the ID is

arranged in layers of concentric cylinders about the beam pipe in the barrel region and in disks perpendicular to the beam pipe in the end-caps. The pixel detector is the highest granularity detector in the ID and is the closest to the interaction point. It provides precise measurements of charged particles momenta, determines the impact parameter resolution of tracks, and enables vertex reconstruction, which is needed to determine the primary vertices from pp interactions and secondary vertices from long lived particles such as B-mesons and τ leptons. Following the pixel detector, the SCT provides information regarding a track's impact parameter, the charged particle's momenta, and secondary vertex position. Both the pixel detector and the SCT are cooled to -10° C by using an evaporative cooling system. The TRT is the final layer of the ID, providing electron identification by measuring transition radiation from charged particles. Schematics of the ID are shown in Fig. 3.5. Each ID sub component decreases in granularity as you go out to higher radius, but is designed in such a way as to provide continuous tracking throughout the ID. The resolution is well matched between subdetectors, with a momentum resolution of $\frac{\sigma_{p_{\mathrm{T}}}}{p_{\mathrm{T}}} = 0.05\% p_{\mathrm{T}} \oplus 1\%$. The small curvature of high p_{T} charged particles is reflected in the first term of the resolution, meanwhile, the constant term is indicative of multiple scattering, affecting the trajectory of the charged particle. A typical track in ATLAS is required to have 3 hits in the pixel detector, 4 in the SCT, and 36 in the TRT.

Pixel Detector

Shown in Fig. 3.6, the pixel detector consists of three concentric cylinders in the barrel region, located from the interaction point at radii of 5 cm (L0/b-layer), 9 cm (L1), and 12 cm (L2), and two sets of three disks each, with radii of 9 to 15 cm, located in the end-cap. The pixel detector is constructed of 1456 modules in the barrel region and 288 in the end-cap, with each module containing 46080 n^{+}-on-n-doped silicon pixels read out

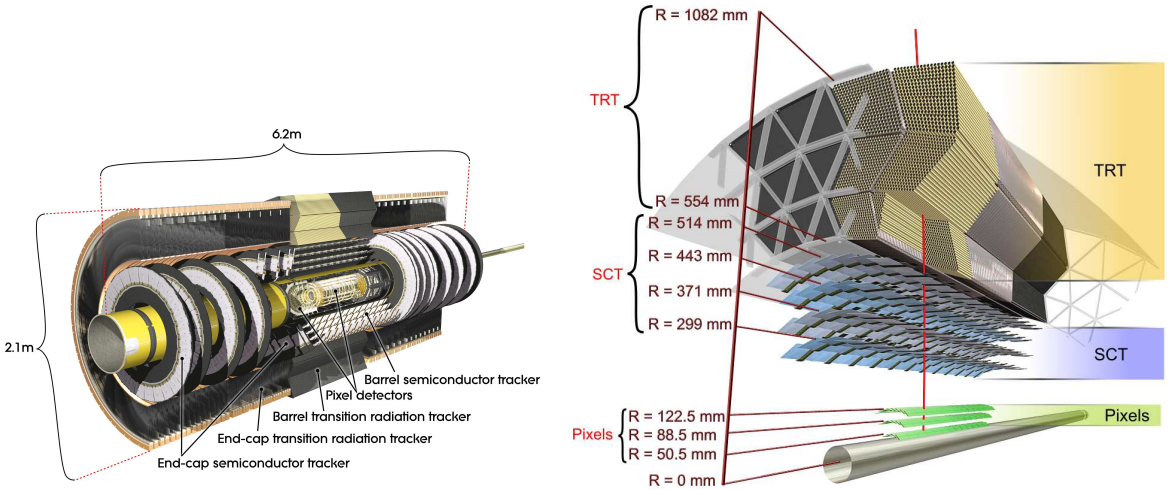

(a) Cut-away view **(b)** Cross sectional view

Figure 3.5.: Schematics of the ATLAS Inner Detector.

by 16 chips, each connected to an array of 18×160 pixels. As charged particles pass through the pixels, electrons are liberated from the silicon, creating a current detected by the read out chips. A typical track leaves a hit in each of the three layers in the pixel detector.

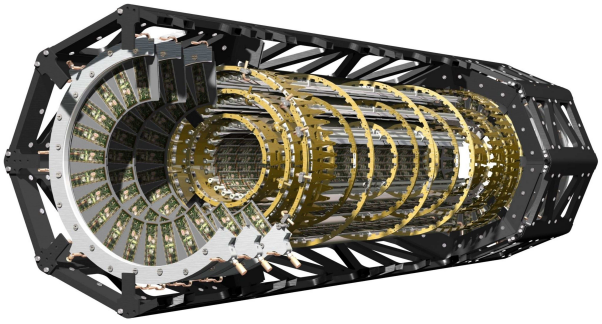

Figure 3.6.: Cut-away view of the ATLAS pixel detector.

Semiconductor Tracker

Similar to the pixel detector, the semiconductor tracker uses silicon to detect charged particles. However, the silicon detectors are arranged in over 6 million rectangular strips,

each 12 cm in length and 80 μm in pitch. In the barrel region, there are four cylindrical layers of back-to-back strips, with one of the strips parallel to the beam pipe and the other rotated by 40 mrad. There are two end-cap portions of the SCT as well, each containing 9 disks with a back-to-back configuration of the strips. In the end-cap, one set of the strips is mounted radially from the beam pipe and the other is rotated by 40 mrad. The back-to-back configuration increases spatial resolution and allows for three dimensional hit information. A typical track leaves hits in 8 strips of the SCT.

Transition Radiation Tracker

Aside from measuring a charged particle's momentum, the TRT provides particle identification by measuring its transition radiation between media. Transition radiation occurs when a highly relativistic particle crosses the boundary of two media with different dielectric constants, resulting in the emission of photons by the particle. Low mass particles tend to emit more transition radiation than heavier particles, a principle enabling the TRT to distinguish between an electron and a pion. The TRT is a straw detector composed of approximately 350000 straw tubes, each 4 mm in diameter with a gold-plated tungsten wire of 30 μm in diameter at the center. The straws are aligned parallel to the beam pipe in the barrel region and are aligned radially in the end-cap. To perform the tracking of charged particles, the straw is filled with an ionizable gas mixture of 70% Xe, 27% CO_2, and 3% O_2. To induce transition radiation, the tubes are placed in an array of polypropylene fibers. The TRT operates at two thresholds, low and high, to determine if the signal was caused by the ionization (low) or by transition radiation (high). Particle identification is achieved by discriminating on the ratio of high threshold hits to low threshold hits. Unlike the silicon trackers, the TRT covers the region of $|\eta| < 2.0$. A typical track leaves 36 hits in the TRT.

3.3.4. Calorimeters

The ATLAS calorimeter system is intended to measure the momentum of charged and neutral particles, and to measure the $E_{\mathrm{T}}^{\mathrm{miss}}$ of an event. To achieve these measurements, the calorimeter employs two sampling calorimeter systems: an electromagnetic calorimeter and a hadronic calorimeter. Sampling calorimeters function by placing an alternating series of absorbers (dense material) in front of active material that is capable of measuring ionization energy as charged particles traverse it. The absorbers have a high probability of interacting with particles that pass through it. Upon interaction with the absorber, the particle passing through creates a shower of charged particles which are measured by the active material. The number of secondary particles produced in the shower is proportional to the energy of the incoming particle, allowing the momentum of the incoming particle to be determined from the shower measurement. To accurately measure the incoming particle's momentum, it is of the utmost importance that it lose all of its energy within the calorimeter. This is also important to prevent the punch through of any particle, except a muon, into the muon spectrometer. These requirements are met by introducing the proper amount of absorbing material, so that showers are contained within their respective calorimeter systems. The electromagnetic calorimeter provides 24 radiation lengths, X_0, in the barrel region and 26 in the end-cap region, while contributing 2 nuclear interaction lengths, λ. The hadronic calorimeter imparts 9 additional nuclear interaction lengths to the calorimeter. The electromagnetic calorimeter is placed closest to the interaction point and is followed by the hadronic calorimeter; both are depicted along with the material budget in Fig. 3.7.

Electromagnetic Calorimeter

The electromagnetic (EM) calorimeter primarily measures electrons and photons, containing them within its boundaries. In addition, it has the ability to perform particle

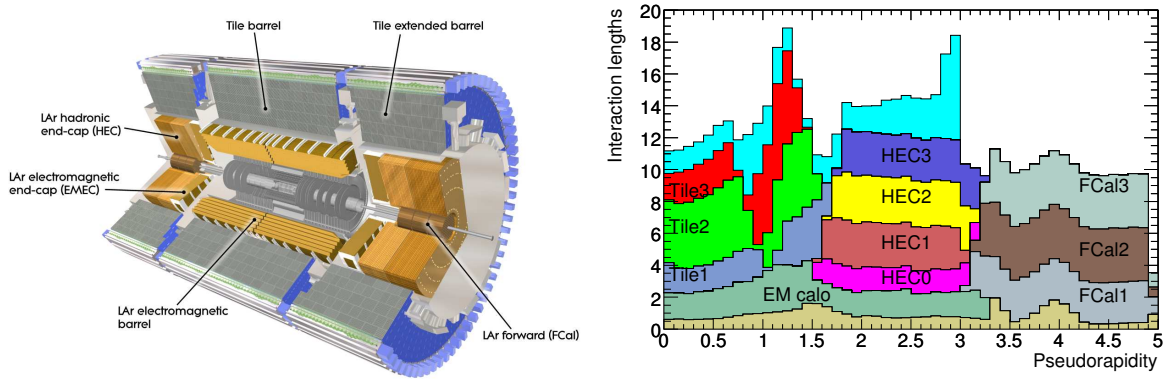

(a) Cut-away view of the calorimeter.

(b) Amount of material in terms of interaction lengths as a function of $|\eta|$.

Figure 3.7.: The ATLAS calorimeter system depicted in Fig. 3.7a and its material budget shown in terms of interaction lengths shown in Fig. 3.7b

identification. For example, a high energy electron ($E > 10$ MeV) loses most of its energy through bremsstrahlung radiation, compared to a high energy photon which loses its energy through pair production, causing the two particles to travel different path lengths in the calorimeter. The EM calorimeter is configured like an accordion, utilizing lead plates as its absorber and liquid argon as its active material. Divided into three sections, with each section contained in its own cryostat, the EM calorimeter covers a range of $|\eta| < 3.2$. The first section is located in the barrel-region spanning $|\eta| < 1.475$ with two end-cap coaxial wheels (inner and outer) covering $1.375 < |\eta| < 2.5$ and $2.5 < |\eta| < 3.2$ respectively. Used for precision measurements, the barrel and outer end-cap wheel are composed of three layers; while the inner wheel contains only two layers with coarser granularity. To compensate for energy loss in the ID, a thin layer of liquid argon is placed in the region of $|\eta| < 1.8$ to function as a presampler before the particles reach the first lead plate. The design resolution for the EM calorimeter is $\frac{\sigma_E}{E} = \frac{10\%}{\sqrt{E}} \oplus 7\%$, where the first term corresponds to the energy dependent statistical fluctuations in the absorption material and the second term reflects the systematic uncertainties in the calibration of the calorimeter.

Hadronic Calorimeter

Hadronic showers escaping the EM calorimeter are measured and contained within the hadronic calorimeter. The hadronic calorimeter employs 3 separate calorimeters to perform its measurements: the tile calorimeter, the hadronic end-cap calorimeter (HEC), and the forward calorimeter (FCal). In addition to hadronic shower measurements, the hadronic calorimeter plays a pivotal role in determining the $E_{\mathrm{T}}^{\mathrm{miss}}$ of an event.

The tile calorimeter utilizes steel as the absorber and polystyrene scintillator tiles as the active material. It is divided into three pieces amongst the barrel, covering the range $|\eta| < 1.7$. Each section contains three layers with a depth of 7.4 interaction lengths, with the central barrel extending from $|\eta| < 1.0$ and the two extended barrels covering $0.8 < |\eta| < 1.7$.

The HEC comprises two wheels on each end-cap spanning the range $1.5 < |\eta| < 3.2$. Each wheel contains two layers of alternating copper (absorber) and liquid argon (active material). The HEC and tile calorimeter's combined resolution is $\frac{\sigma_E}{E} = \frac{50\%}{\sqrt{E}}$. Contained within the HEC is the FCal, providing coverage from $3.1 < |\eta| < 4.9$. Three separate layers constitute the FCal, each with a specific purpose for detection and containment. All three sections employ liquid argon as the active material. The innermost section uses copper as the absorber, primarily measuring electromagnetic showers. The two outermost layers measure hadronic showers, employing tungsten as the absorber. Together, all three sections of the FCal provide coverage in the very forward region, enabling accurate $E_{\mathrm{T}}^{\mathrm{miss}}$ measurements and preventing the punch through of particles at high η. The FCal has a resolution of $\frac{\sigma_E}{E} = \frac{100\%}{\sqrt{E}}$

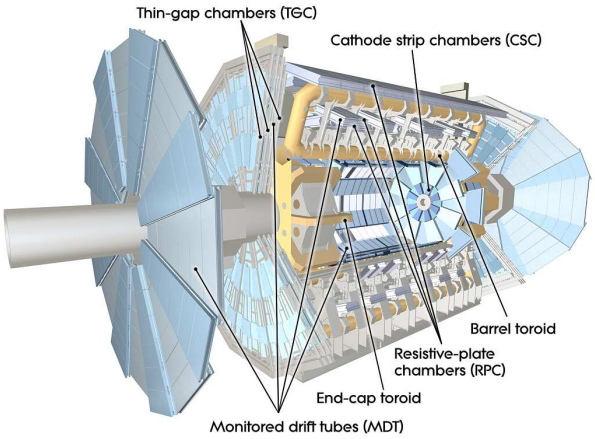

Figure 3.8.: Cut-away view of the muon spectrometer.

3.3.5. Muon Spectrometer

The muon spectrometer (MS) is a robust tracking system for muons, incorporating four separate technologies to deliver high precision tracking and fast triggering. The MS provides tracking using monitored drift tubes (MDT) and cathode strip chambers (CSC) in the range $|\eta| < 2.7$, with a resolution of 10% for a 1 TeV muon. In order for ATLAS to trigger on events with high p_{T} muons, the MS delivers fast triggering using resistive plate chambers (RPC) and thin gap chambers (TGC) for muons in the range $|\eta| < 2.4$. As discussed in Section 3.3.2, the MS is placed within a toroidal magnetic field, where the barrel toroids provide a field for $|\eta| < 1.0$ and the end-cap magnets serve the region $1.4 < |\eta| < 2.7$. The region of $1.0 < |\eta| < 1.4$ is known as the transition region, where the magnetic field fluctuates and additional chambers are needed for accuracy. The field produced by the toroids are orthogonal to the trajectories of the muons in most regions of the MS. The barrel region contains three cylindrical layers of chambers (MDT and RPC), meanwhile, the end-cap consists of four wheels on each side (MDT, TGC, and CSC). The muon spectrometer, depicted in Fig. 3.8, is the largest detector of ATLAS, spanning 40 m in length and 20 m in height.

Monitored Drift-Tube Chambers

The monitored drift-tube chambers are a set of aluminum proportional wire drift tubes measuring 3 cm in diameter, containing a gaseous mixture of Ar/CO_2 (97%/3%) and a tungsten-rhenium wire of 50 μm in diameter. The barrel region of the detector consists of three concentric layers of chambers spaced by 2.5 m, covering the region $|\eta| < 1.1$. Meanwhile, the end-cap comprises three wheels of chambers spaced by 7 m, where the two most outer wheels span the range $1.1 < |\eta| < 2.7$ and the innermost wheel covers the region of $|\eta| < 2.0$. Each chamber is constructed out of a set of drift tubes, with the innermost layer of the barrel and end-cap containing 8 layers of tubes per chamber and the middle and outer layers containing 6 layers of tubes per chamber.

Cathode Strip Chambers

The cathode strip chambers are utilized by ATLAS in place of the MDT's in the innermost layer of the end-cap, providing coverage in the region of $|\eta| > 2.0$. This is due to the MDT's ineffectiveness at the high rate of incident particles produced near the beamline. The CSC's are multi-wire proportional chambers with the cathode wires segmented into two strips. The anode strips are 30 μm in diameter and are oriented radially from the beamline.

Thin Gap Chambers

The thin gap chambers provide fast triggering in the forward region of the detector, covering the range $1.05 < |\eta| < 2.4$. The TGC's use multi-wire proportional chamber technology, similar to the CSC's, but with a larger distance between anode wires than the distance from the anode wire to the cathode strip, enabling faster signals for triggering.

Resistive Plate Chambers

In the barrel portion of the detector, resistive plate chambers are used to trigger on muons in the region $|\eta| < 1.05$. They employ gaseous parallel electrode-plate technology and are placed in three concentric cylinders around the beam pipe. A chamber comprises two detector layers, each layer containing plastic plates separated by an insulating spacer.

3.3.6. Trigger System

The LHC produces pp collisions at a rate of 40 MHz when operated at design specifications[4]. At this rate, ATLAS would need to store 60 Tb of data per second, which is not feasible due to bandwidth and data storage limitations. To reduce the number of events stored to a frequency of 200 Hz, while ensuring that interesting physics is not lost, ATLAS implements a three tiered trigger system: the level one trigger (L1), level two trigger (L2), and event filter trigger (EF). The L1 trigger is a hardware based trigger which determines if an event's information should be passed on to the software based L2 and EF triggers. The L2 and EF triggers, also known as the high level triggers (HLT), perform complex calculations to determine whether or not an event is recorded. Interesting physical processes typically contain any of these characteristics: high p_{T} jets or leptons, events with large $E_{\mathrm{T}}^{\mathrm{miss}}$, or events with large sums of transverse energy. The triggers are configured to quickly detect such characteristics, maximizing the number of events recorded. Due to ATLAS' limited bandwidth, some triggers are pre-scaled, meaning that only a portion of the trigger events are stored and then the events are scaled to agree with expectation. Pre-scaling occurs at all three trigger levels the scale dependent upon the trigger's p_{T} threshold and the proton beam's kinematics.

[4]The LHC is designed to collide protons at a luminosity of 10^{34} cm^{-2} s^{-1}, with a bunch spacing of 25 ns.

L1 Trigger

The L1 trigger incorporates a hardware based system, requiring coincidence or veto signals at a rate of 2.5 μs to determine whether an event should be passed along to the L2 trigger. Relying upon a subset of the ATLAS detector, the L1 trigger utilizes the calorimeter, at a coarser granularity, and the MS trigger system (RPC and TGC) to reduce the rate of events to 75 kHz. In addition to selecting events for the L2 trigger, the L1 trigger defines regions of interest (RoI) for the L2's algorithmns to narrow in on. The RoI contains the η, ϕ, and p_{T} measurements of the trigger towers that determined the selection of the event.

L2 Trigger

The L2 trigger relies upon software based algorithms to determine if an event is passed along to the EF trigger. It has access to information from the subdetectors located in the RoI, as well as information from the ID. On average, the L2 needs 40 ms to perform a basic reconstruction of the trigger object, reducing the rate of events to approximately 3 kHz.

EF Trigger

The EF trigger is the most sophisticated of the three, employing parallel processors to perform a robust reconstruction using information provided by all subdetectors. The 4 second computation utilizes p_{T} thresholds, as well as object quality requirements (e.g. isolation requirements), to reduce the event rate to approximately 200 Hz. Having passed the EF trigger, an event is recorded into four different data streams: muon, electron/photon, jet/tau/$E_{\mathrm{T}}^{\mathrm{miss}}$, and minimum bias. The minimum bias stream, having the largest pre-scaled trigger, randomly selects events with a low p_{T} threshold.

Chapter 4.

Analysis

The analysis presented in this thesis measures the longitudinal polarization of the top quark in $t\bar{t}$ production using the single lepton channel. With an experimentally observed lifetime of 3.29 x 10^{-25} s [47], the top quark decays before hadronization can occur, allowing the spin information of the top quark to be accessed through its decay products. By utilizing this property of the top quark, its longitudinal polarization can be determined by analyzing the angular distribution of its final state decay products. For this analysis, the polar angle distribution of the top quark's final state decay products is used, where the polar angle is defined as the angle between a given quantization axis and the final state decay product's momentum direction in its parent top quark's rest frame. The helicity basis is used to define the quantization axis in this analysis, where the quantization axis is chosen as the parent top quark's momentum direction in the $t\bar{t}$ center-of-mass frame. The distribution of the polar angle, θ_i, of each top quark's final state decay products, labeled by i, is given by

$$W\left(\cos\theta_i\right) = \frac{1}{2}\left(1 + \alpha_i P \cos\theta_i\right), \tag{4.1}$$

where P represents the degree of polarization along the chosen quantization axis and α_i is the spin-analyzing power of the final state decay product [32, 33], which is a measure of the sensitivity of the daughter particle to the parent particle's spin state. Table 4.1

shows the tree level values of the spin-analyzing power for the final state particles of the top decay. Due to its α_i value being 1, which gives it maximal sensitivity to the top quark's spin state, the charged lepton is utilized in this analysis to determine the longitudinal polarization of the top quark. The polar angle of the charged lepton, θ_ℓ, is determined by measuring the angle between the quantization axis and the charged lepton's momentum direction in its parent top quark's rest frame, which is depicted in Fig. 4.1.

α_i	Particle Type
1.0	Charged Lepton
1.0	Down and Strange Quarks
-0.4	b Quark
-0.3	Neutrino
-0.3	Up Type Quark

Table 4.1.: Predicted tree level values of the spin-analyzing power, α_i, for the top quark final state decay products.

In the SM, parity violating interactions producing $t\bar{t}$ pairs are responsible for generating longitudinal polarization of the top quark. The strong production of $t\bar{t}$ pairs in pp collisions conserves parity, rendering zero longitudinal polarization of the top quark. Meanwhile, P has been calculated for parity violating weak interactions and is shown to be equal to 0.003 [23]. An example of the diagrams included in this one-loop electroweak correction to the tree level QCD production of $t\bar{t}$ may be found Figs. 2.13 and 2.14. Many BSM models used to explain the forward-backward production asymmetry (A_{FB}) measured at the Tevatron experiments D0 [24, 25] and CDF [26] necessitate longitudinally polarized top quarks in $t\bar{t}$ production [27–29], with each BSM model predicting different values for P. Therefore, not only is measuring P a good cross check for the SM, it may have the power to distinguish between different BSM models in the event of significant polarization.

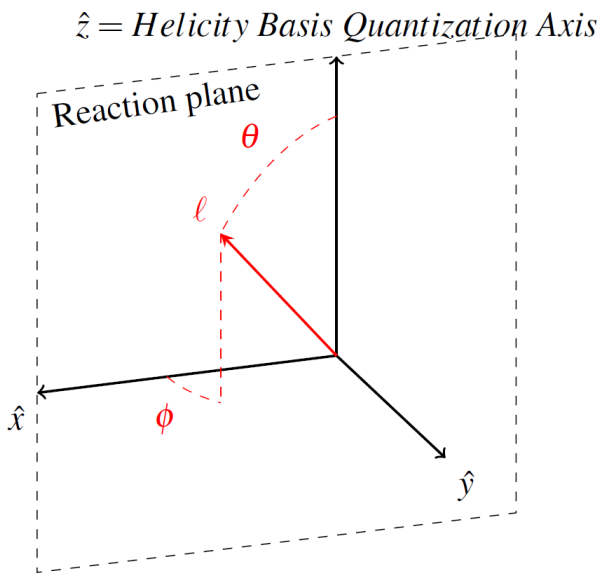

Figure 4.1.: Depiction of the charged lepton's polar angle θ with respect to the helicity basis quantization axis.

The strategy of this analysis is to use the $\cos\theta_\ell$ variable as an observable to measure $\alpha_\ell P$. The product of α_ℓ and P is measured because the spin analyzing power changes independently of the polarization in the presence of anomalous couplings at the Wtb vertex [43], therefore, under such anomalous couplings, a measurement of $\alpha_\ell P$ would continue to render a physically meaningful result. There are five major components to this analysis which will be discussed at length in Sections 4.1 to 4.5: signal and background estimation, a kinematic likelihood fit for $t\bar{t}$ reconstruction, $\cos\theta_\ell$ template production, and a binned maximum likelihood fit of the templates to the data. The D0 collaboration performed the first study on the longitudinal polarization of the top quark in $t\bar{t}$ events [48], showing good agreement between the data and SM expectation. Preliminary results for the longitudinal polarization in $t\bar{t}$ events have been produced by CMS in the dilepton channel [49] and by ATLAS in the single lepton channel [50]; the first published result was conducted by ATLAS, utilizing both the dilepton and single lepton channels [51]. The analysis presented in this thesis details the single lepton channel result, which has been published in the Physical Review Letters [51].

4.1. Signal and Background Estimation

The analysis presented in this thesis relies upon data collected by the ATLAS experiment using pp collisions produced in 2011 at $\sqrt{s} = 7$ TeV. It also relies upon Monte Carlo (MC) simulation and data driven techniques to model the signal and background estimations for $t\bar{t}$ production, with the main sources of background for this analysis being: a W-boson in association with jets (W+jets), a Z-boson in association with jets (Z+jets), Dibosons (WW, WZ, ZZ), single top production, and non-prompt/fake leptons. Due to the imprecise nature of the detector simulation, scale factors were used to bring the MC into agreement with what ATLAS observes in data. The scale factors were derived in dedicated studies by ATLAS's top working group. In addition, every MC sample is produced with multiple pp interactions superimposed on top of the generated event (pile-up), necessitating a scale factor to re-weight the distribution of the number of interactions per crossing produced in MC, bringing the distribution into agreement with what is observed in data. All MC samples are processed through a GEANT4 [52] simulation of the ATLAS detector [53]. Both MC and data events utilize the same reconstruction and analysis software.

4.1.1. Data

The 2011 ATLAS dataset of pp collisions at $\sqrt{s} = 7$ TeV, corresponding to an integrated luminosity of 4.66 ± 0.08 fb^{-1} [54] after data quality requirements, was used for this analysis. All MC samples are normalized to the integrated luminosity of this dataset.

4.1.2. Monte Carlo Simulation

$t\bar{t}$ Signal

The $t\bar{t}$ signal MC used in this analysis was simulated using the next-to-leading order (NLO) MC@NLO 3.41 [55] generator with the NLO parton density function (PDF) set CT10 [56], assuming a top mass of 172.5 GeV. Parton showering is modeled with HERWIG 6.510 [57] and the underlying event is generated using JIMMY 4.31 [58]. An assumed $t\bar{t}$ cross section of 167^{+17}_{-18} pb is used, which was calculated at approximate next-to-next-to-leading order (NNLO) in QCD with HATHOR 1.2 [59]. The signal MC is reweighted, using a technique described in Section 4.4, to induce longitudinal polarization of the top quarks since no dedicated MC sample with polarized $t\bar{t}$ events is available. The samples used for systematic uncertainties relating to signal MC generation are discussed in Section 5.1

Single top

Single top events were simulated using the MC@NLO generator for the Wt and s-channel, while the ACERMC [60] generator was used for the t-channel.

W/Z+jets

The production of W and Z bosons in association with jets was simulated using the ALPGEN [61] generator interfaced with HERWIG and JIMMY. The shapes of the kinematic distributions produced from the W+jets background are taken from the MC, however, the overall normalization of the events is scaled based on ATLAS's charge asymmetry[1] measurement [62].

[1] There are more valence up quarks than valence down quarks in a proton, and since ATLAS measures pp collisions, W^++jets events are more likely to occur than W^-+jets events.

Diboson

Diboson (WW,WZ,ZZ) events were simulated using the HERWIG generator.

4.1.3. Data driven estimation of non-prompt/fake leptons

Non-prompt leptons originate from semi-leptonic hadron decays, meanwhile, fake leptons originate from jets that fragment in such a way that they pass the lepton selection criteria. The mis-identification rate of these QCD multijet events is small, however, they still contaminate the signal region because the production cross sections for QCD multijet events are orders of magnitude greater than the cross section for $t\bar{t}$ production. QCD multijet events resulting in non-prompt/fake (NPF) leptons are not modeled well in MC, so a data driven matrix method [63, 64] is employed to estimate the contribution of multijet events to the non-prompt/fake leptons background. The number of NPF events is estimated by the matrix method by calculating the number of events passing "tight" and "loose" criteria, described in Section 4.2, and the efficiencies for real and NPF leptons passing these criteria. The number of NPF leptons contributing to the background is calculated as the number of fake leptons passing the tight selection criteria, N_{fake}^{tight}, which is given by

$$N_{fake}^{tight} = \frac{\epsilon_{fake}}{\epsilon_{real} - \epsilon_{fake}}(N^{loose}\epsilon_{real} - N^{tight}), \tag{4.2}$$

where N^{loose} and N^{tight} are the number of events passing the loose and tight criteria respectively and ϵ_{fake} and ϵ_{real} are the efficiencies of fake and real leptons passing loose event criteria that also pass tight criteria. A tag and probe method using $Z \to \ell\ell$ data is

used to determine ϵ_{real}, while ϵ_{fake} is determined by different mechanisms for muons and electrons, which are described in Section 4.2.3.

4.2. Object and Event Selection

The data sample is enriched in $t\bar{t}$ events by applying cuts based on the single lepton topology, requiring one isolated lepton, at least 4 jets, one of which is b-tagged; and sufficient MET. Section 4.2.1 discusses the object selection criteria and Section 4.2.2 details the event selection for single lepton $t\bar{t}$ decays.

4.2.1. Objects

For the purpose of this section, objects passing the selection criteria defined below will be referred to as "good" objects.

Jets

Jets are reconstructed from clustered energy deposits in the calorimeter using the anti-k_t algorithm [65] with a radius parameter of $R = 0.4$. Energy and η dependent correction factors are applied to a jet's energy, bringing it into agreement with the average of the total energy of the stable particles emitted towards the jet. In addition, a residual correction determined from in situ measurements is applied [66, 67]. Jets are required to have $p_{\mathrm{T}} > 25$ GeV, $|\eta| < 2.5$, and a jet vertex fraction (JVF [2]) > 0.75. Any jet within a cone of $\Delta R < 0.2$ of a good electron is removed from the event. Jets originating from

[2] A cut on the jet vertex fraction is employed to find jets associated with the hard scatter interaction. It is calculated as the fraction of the scalar sum of all the tracks associated with the jet that originated from the primary vertex.

a b-quark are identified (b-tagged) using the a neural network tagging algorithm which operates at a 70% working point and rejects light partons with a factor of 140 [68–70].

Electrons

In order to separate isolated electrons from jets, a series of cuts are implemented, including cuts on calorimetry, tracking, and combined variables [71]. Reconstructed electrons must be associated with a calorimeter cluster that lies within the region $|\eta_{\text{cl}}| < 2.47$, with the exception of the transition region $1.37 < |\eta_{\text{cl}}| < 1.52$. A cut is placed on the transverse energy of the reconstructed electron, given by $E_T = E_{\text{cl}}/\cosh(\eta_{\text{track}})$. In addition, electrons must pass an E_T isolation requirement of $\Delta R = 0.2$ and a p_T isolation requirement of $\Delta R = 0.3$, both of which operate at 90% efficiency. The longitudinal impact parameter, z_0, of the electron with respect to the primary vertex must be less than 2 mm. After performing the removal of jets to close by electrons, electrons that overlap with a jet in a cone of $\Delta R < 0.4$ are removed from the event.

Muons

To reconstruct muons, a dedicated algorithm is used to match tracks in the ID to those in the MS [72]. To eliminate jets being reconstructed as muons, muons are required to have $p_T > 20$ GeV, $|\eta| < 2.5$, and to satisfy a number of isolation cuts. Muon tracks are isolated from no more than 4 GeV of calorimetry energy in a cone of $R = 0.2$ within the calorimeter and the sum of the p_T of tracks reconstructed in the inner tracker within a cone of $R = 0.3$ to the muon track must be less than 2.5 GeV. Track requirements are also imposed on good muons:

- At least 1 pixel hit or one crossed dead pixel sensor
- At least six (SCT hits + number of crossed dead SCT sensors)

- SCT holes + pixel holes must be less than three
- One B-layer hit must be found if one is expected
- For muons with $|\eta| < 1.9$, nTRThits + nTRTOutliers > 5 and nTRTOutliers / (nTRTHits + nTRTOutliers) < 0.9
- For muons with $|\eta| \geq 1.9$, nTRTOutliers / (nTRTHits + nTRTOutliers) < 0.9, only if (nTRTHits + nTRTOutliers) > 5.

The muon's z_0 with respect to the primary vertex is required to be less than 2 mm and any muon that overlaps with a good jet within a cone of $\Delta R < 0.4$ is removed from the event.

Missing Transverse Energy

The components of the E_T^{miss} for an event is calculated [73] as the negative of the vectorial sum of all transverse energy deposited in the calorimeters. The calorimeter cells are calibrated according to which high p_T object they are associated to, which includes electrons, muons, jets, and photons.

Trigger Requirements

The ℓ+jets channel requires exactly one lepton matched to the appropriate trigger.

4.2.2. Event Selection

To ensure data quality, event cleaning cuts are performed:

- To reject non-collision events background, a good event must have at least one reconstructed vertex with at least 5 associated tracks.

- Events that have a calorimeter jet in the vicinity of the LAr hole[3] are vetoed in data and MC.
- To ensure the quality of the E_T^{miss} measurement, events that contain jets with a $p_T > 20$ GeV that do not overlap with a good lepton are tested using an algorithm that determines whether the event is vetoed.
- Due to noise bursts in the LAr calorimeter, events are tested for data integrity errors.

Having performed the data quality selection, the ℓ+jets topology is utilized to enrich the data sample with $t\bar{t}$ events and to reject background events. The event selection is as follows:

- Exactly one good lepton matching the trigger object that fired the event
- At least four good jets
- $E_{\mathrm{T}}^{\mathrm{miss}} > 30$ GeV for the electron channel and $E_{\mathrm{T}}^{\mathrm{miss}} > 20$ GeV for the muon channel
- Cuts on the transverse mass of the W boson, given by $m_{\mathrm{T}} = \sqrt{2p_{\mathrm{T}}^{\ell}E_{\mathrm{T}}^{\mathrm{miss}}[1 - \cos(\phi^{\ell} - \phi(E_{\mathrm{T}}^{\mathrm{miss}}))]}$ are employed. The electron channel requires that $m_{\mathrm{T}} > 30$ GeV and the muon channel requires that $m_{\mathrm{T}} + E_{\mathrm{T}}^{\mathrm{miss}} > 60$ GeV.
- At least one b-tagged jet

4.2.3. Non-prompt/fake lepton selection

As discussed in Section 4.1.3, non-prompt/fake leptons are estimated using a data driven technique that follows the same selection criteria described in Section 4.2.2, except that leptons are not required to be isolated. There are two methods used to determine the

[3]From run 180614 to run 184169, 6 front end boards were not operational

contribution from non-prompt/fake muons. The first method also employs an inverted triangular cut on the transverse mass of the W-boson and missing transverse energy, $m_{\mathrm{T}} < 20$ GeV and $E_{\mathrm{T}}^{\mathrm{miss}} + m_{\mathrm{T}} < 60$ GeV. The second method defines a control region using a cut on the missing transverse energy, 5 GeV $< E_{\mathrm{T}}^{\mathrm{miss}} < 15$ GeV. MC is used in both methods to estimate the contamination from W+jets and Z+jets events in the non-prompt/fake lepton sample. The contribution from non-prompt/fake electrons employs an inverted triangular cut on the missing transverse energy, 5 GeV $< E_{\mathrm{T}}^{\mathrm{miss}} < 20$ GeV.

4.2.4. Data and MC Comparison

After the event selection was performed, the yields and kinematic distributions from data of the e+jets and μ+jets channels are compared to expectations. Table 4.2 lists the expected signal and background contributions rounded yields compared to the data; the systematic uncertainties reported are explained in detail in Section 5.1. Figures 4.2 and 4.3 show comparisons between the data and expectation for a number of kinematic distributions in both channels; a more complete set of data to expectation distributions, including distributions in control region with no b-tagged jets, may be found in Appendix A. All distribution's data and expectations are found to be in agreement.

Source	e+jets	μ+jets
$t\bar{t}$	16200	26500
Background	5100	9400
Total	21300	35900
Uncertainty	$\pm$ 1300	$\pm$ 1700
Data	21956	37919

Table 4.2.: Expected signal and background rounded yields compared to data for each of the single lepton channels considered. The total systematic and statistical uncertainties are reported.

The expectation in the electron channel is in good agreement with the data, however, the muon channel is underestimated with respect to the data. Given the difference in the discrepancies between data and expectation between the two channels, a study was performed to check for a bias in both of the channels. Double ratios of distributions for the electron data to expectation and the muon data to expectation were plotted and are shown in Fig. 4.4. The double ratio's show that the discrepancy between the electron and muon channels data to expectation are covered within the uncertainty, because each point in the distribution is consistent with 1 within the uncertainty bands. The asymmetric uncertainty bands may be explained by Fig. 4.5, which shows how the double ratio of the reconstructed $\cos\theta_\ell$ [4] distribution is affected by individual systematic uncertainties; Figures 4.5a and 4.5b show that the asymmetric uncertainty comes from the non-prompt/fake lepton uncertainties. In addition, Figs. 4.5e and 4.5f show that non-lepton related systematics contribute very little to the overall systematic bands shown in Fig. 4.4.

[4]The method for $t\bar{t}$ reconstruction, and therefore $\cos\theta_\ell$ reconstruction, is described in Section 4.3

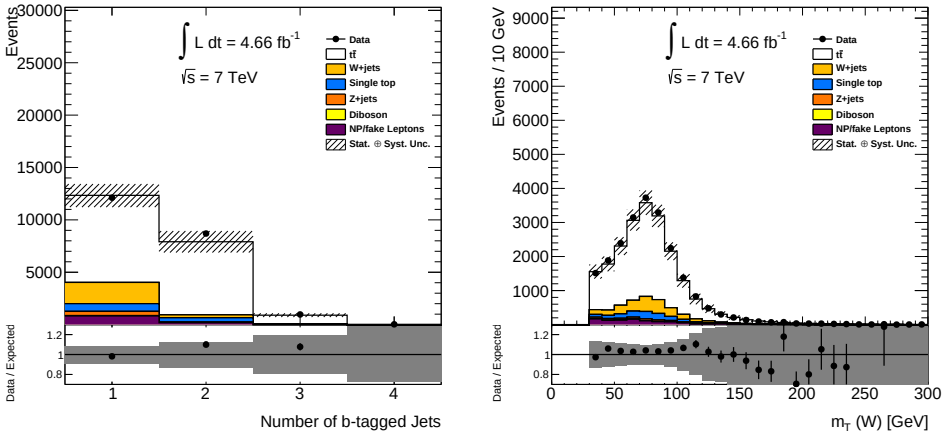

(a) Number of b-tagged jets

(b) m_{T}

(c) Number of jets

(d) $E_{\mathrm{T}}^{\mathrm{miss}}$

Figure 4.2.: Kinematic distributions for the e+jets channel, including the ratio of the data to the expectation; the error bands are the quadratic sum of the statistical and systematic uncertainties.

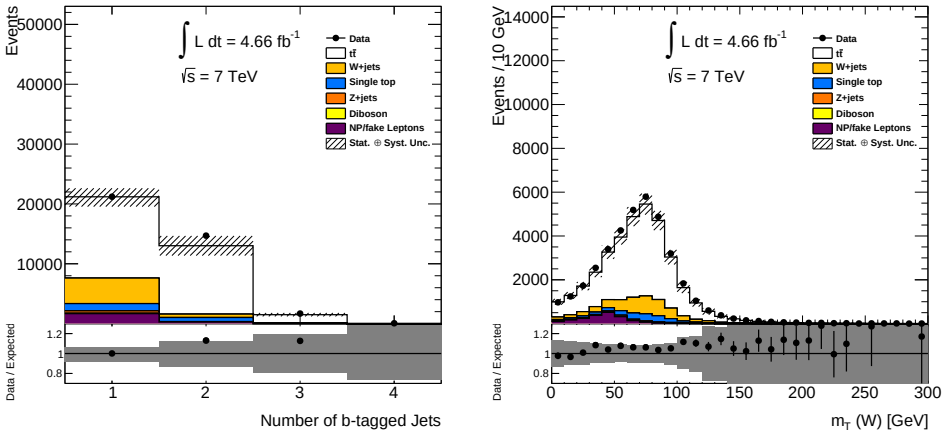

(a) Number of b-tagged jets **(b)** m_{T}

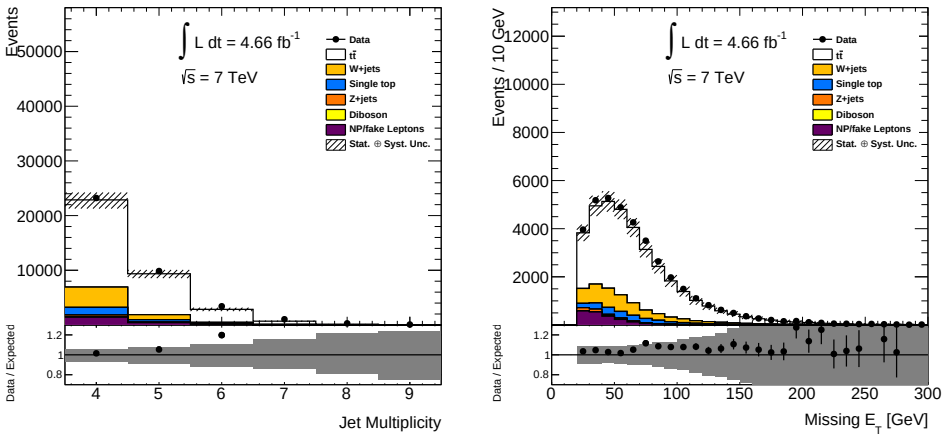

(c) Number of jets **(d)** $E_{\mathrm{T}}^{\mathrm{miss}}$

Figure 4.3.: Kinematic distributions for the μ+jets channel, including the ratio of the data to the expectation; the error bands are the quadratic sum of the statistical and systematic uncertainties.

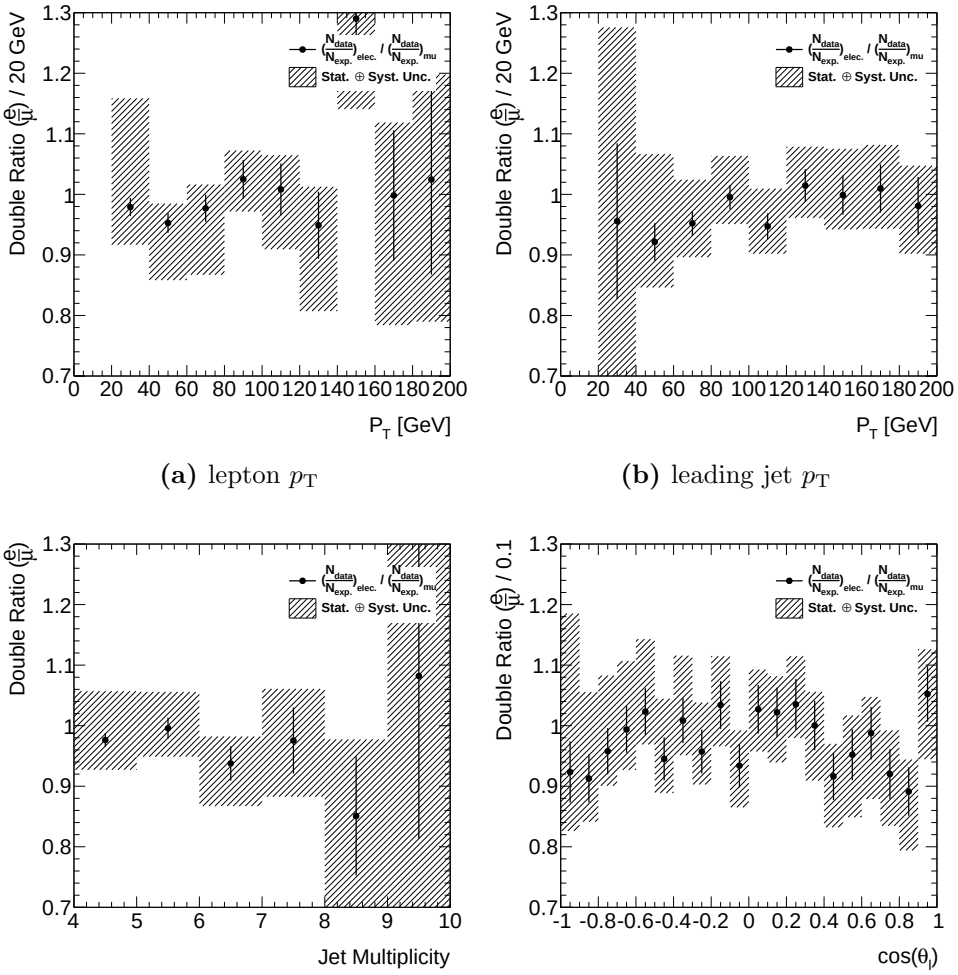

(a) lepton p_{T} **(b)** leading jet p_{T}

(c) Number of jets **(d)** $\cos\theta_\ell$

Figure 4.4.: Double ratio of the electron channel data to expectation and the muon channel data to expectation; the statistical and systematic uncertainties are incorporated into the error band.

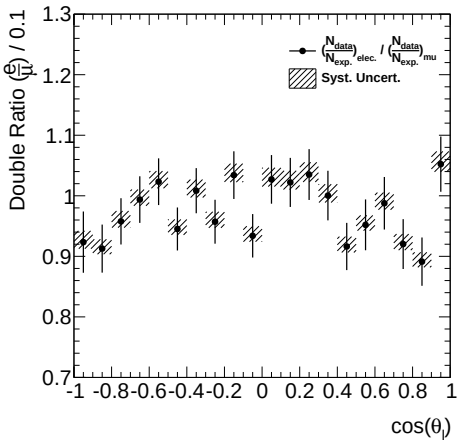

(a) electron fake efficiency systematic

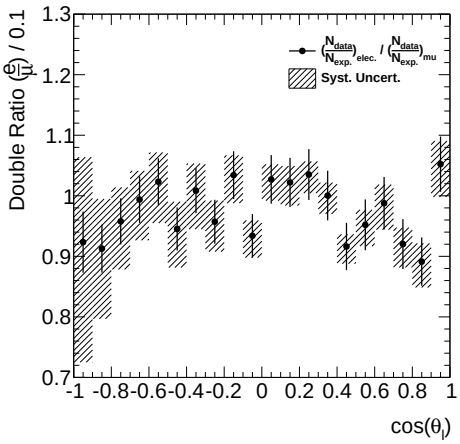

(b) muon fake systematic

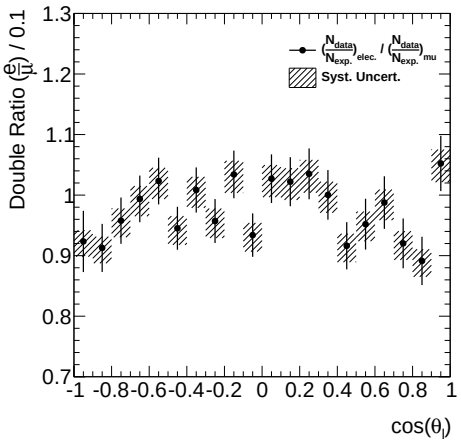

(c) electron lepton scale factor systematic

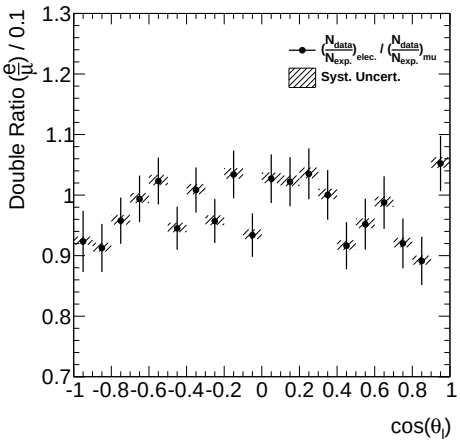

(d) muon lepton scale factor

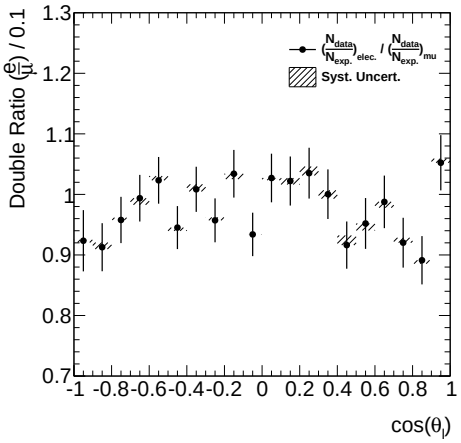

(e) b-jet JES uncertainty

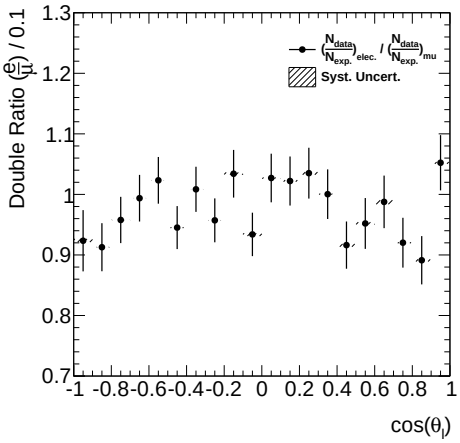

(f) jet efficiency systematic

Figure 4.5.: Contributions from individual systematic uncertainties to the double ratio of the $\cos\theta_\ell$ distribution.

4.3. Kinematic Likelihood Fit

To determine $\cos\theta_\ell$, the top and antitop quark's 4-momentum must be reconstructed. The event topology in the ℓ+jets channel has one top quark decaying into a b-quark and a leptonically decaying W-boson ($W \to \ell\nu_\ell$), with the other top quark decaying into a b-quark and a hadronically decaying W-boson ($W \to q_1 q_2$). Since the neutrino goes unmeasured in the event, its longitudinal momentum must be determined. In addition, the selected jets in the event must be associated to one of the two b-quarks from the top decays and to quarks from the hadronically decaying W-boson. The $t\bar{t}$ reconstruction method employed in this analysis is a kinematic likelihood method, entitled KLFitter, which utilizes the Bayesian Analysis Toolkit (BAT) [74]. A top mass measurement by ATLAS [75] provides detailed information regarding KLFitter and its performance.

For each event, a set of permutations for the five highest p_{T} jets is constructed, and for each permutation, a likelihood function is built. Each permutation places the jets into a unique quark slot: the b-quark associated with the leptonically decaying top quark (b_{Lep}), the b-quark associated with the hadronically decaying top quark (b_{Had}), and the two slots associated with the quarks from the hadronically decaying W-boson. The likelihood function consists of a few free parameters: the energies of the 4 jets placed into the quark slots, the energy of the electron or the p_{T} of the muon, and the p_x, p_y, and p_z of the neutrino. Double gaussian transfer functions (TF), functions that are defined as the conditional probability to obtain a certain response after reconstruction given the true value, are incorporated into the likelihood function for all objects energies or p_{T}; the TF's were obtained through fits to simulation using BAT and depend upon the particles true energy or p_{T}. Light quark and b-quark TF's are treated separately and depend upon the slot associated with the jet. A single gaussian TF, which depends upon the fits to simulation of the true neutrino's p_x and p_y, is implemented within the likelihood to determine the resolution of the $E_{\mathrm{T}}^{\mathrm{miss}}$. In addition, the likelihood function contains

separate Breit-Wigner PDFs for each W-boson and top quark. Taking all of this into consideration, the likelihood function is given by

$$
\begin{aligned}
L \;=\; & BW\left\{m(q_1q_2) \mid m_W, \Gamma_W\right\} \cdot BW\left\{m(l\nu) \mid m_W, \Gamma_W\right\} \cdot \\
& BW\left\{m(q_1q_2b_{\text{had}}) \mid m_{\text{top}}, \Gamma_{\text{top}}\right\} \cdot BW\left\{m(l\nu b_{\text{had}}) \mid m_{\text{top}}, \Gamma_{\text{top}}\right\} \cdot \\
& W\left(\tilde{E}_{\text{jet}_1} \mid E_{b_{\text{had}}}\right) \cdot W\left(\tilde{E}_{\text{jet}_2} \mid E_{b_{\text{lep}}}\right) \cdot W\left(\tilde{E}_{\text{jet}_3} \mid E_{q_1}\right) \cdot W\left(\tilde{E}_{\text{jet}_4} \mid E_{q_2}\right) \cdot \\
& W\left(\tilde{E}_{\text{x}}^{\text{miss}} \mid p_{x,\nu}\right) \cdot W\left(\tilde{E}_{\text{y}}^{\text{miss}} \mid p_{y,\nu}\right) \cdot \begin{cases} W\left(\tilde{E}_{\text{l}} \mid E_l\right) \;, & e\text{+jets} \\ W\left(\tilde{p}_{\text{T,l}} \mid p_{\text{T},l}\right) \;, & \mu\text{+jets} \end{cases} ,
\end{aligned}
\tag{4.3}
$$

where BW corresponds to a Breit-Wigner PDF, TF's are given by W, and variables with tildes ($\tilde{x}$) are the measured values of those parameters. After the construction of the likelihood function, it is maximized with respect to the free parameters for each permutation of jets. Along with the likelihood, additional information regarding b-jet identification efficiencies and light quark rejection factors[5] are implemented to form an event probability for that given permutation. The fit parameters for the permutation with the largest probability is considered as the proper $t\bar{t}$ reconstruction, and is used for the analysis. Figure 4.6 compares the event probabilities for the permutation in an event that has each jet correctly matched to its truth level partons[6] and for the permutation in that event with the highest probability. A comparison of the event probability between data and expectation is depicted in Fig. 4.7. After the $t\bar{t}$ system is reconstructed for an event, $\cos\theta_\ell$ is calculated from the top quarks and charged leptons 4-momenta; Fig. 4.8 shows the comparison between data and expectation for the distribution of $\cos\theta_\ell$ after

[5]Simply stated, the b-jet efficiencies are an indication of how likely a tagged jet originated from a b-quark, which helps determine the probability that a tagged jet belongs in a b-quark slot. The light quark rejection factor reduces the probability of an event if a non-tagged jet is placed in a b-quark slot.

[6]Reconstructed objects are matched to truth objects if they are within a cone of $\Delta R < 0.4$.

reconstruction. The performance of the kinematic likelihood fitter is detailed in the following sections.

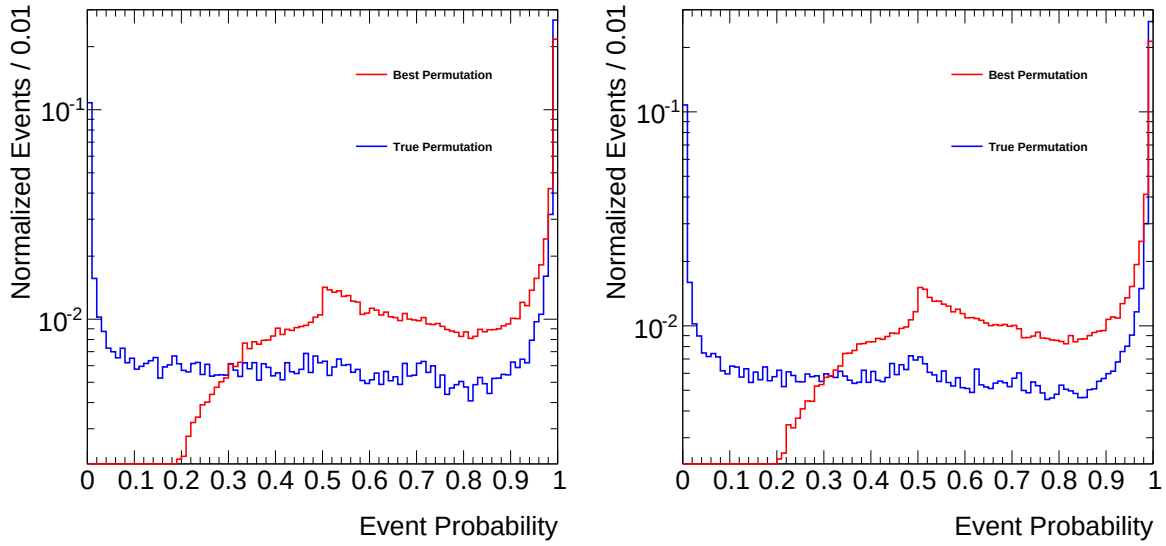

(a) Electron channel **(b)** Muon Channel

Figure 4.6.: Comparison of the event probability for the permutation that has each jet correctly matched to its truth level parton and for the permutation in an event that has the highest event probability.

4.3.1. Kinematic likelihood fit performance

A study on the performance of KLFitter was performed to validate it as an adequate reconstruction method. In an ideal scenario, one could correctly identify b_{Lep}, b_{Had}, q_1, and q_2 from the selected jets in the event. However, this is an impossible task, and what this study found is that correctly identifying b_{Lep} is the most important feature of properly reconstructing the $t\bar{t}$ system.

To reconstruct the leptonically decaying top quark, one needs the 4-moment of the charged lepton, neutrino, and leptonic b-quark. The 4-momentum of the lepton is measured at a high resolution, which can be seen in the residual of the fitted charged lepton's energy and the energy of the truth level charged lepton depicted in Fig. 4.9,

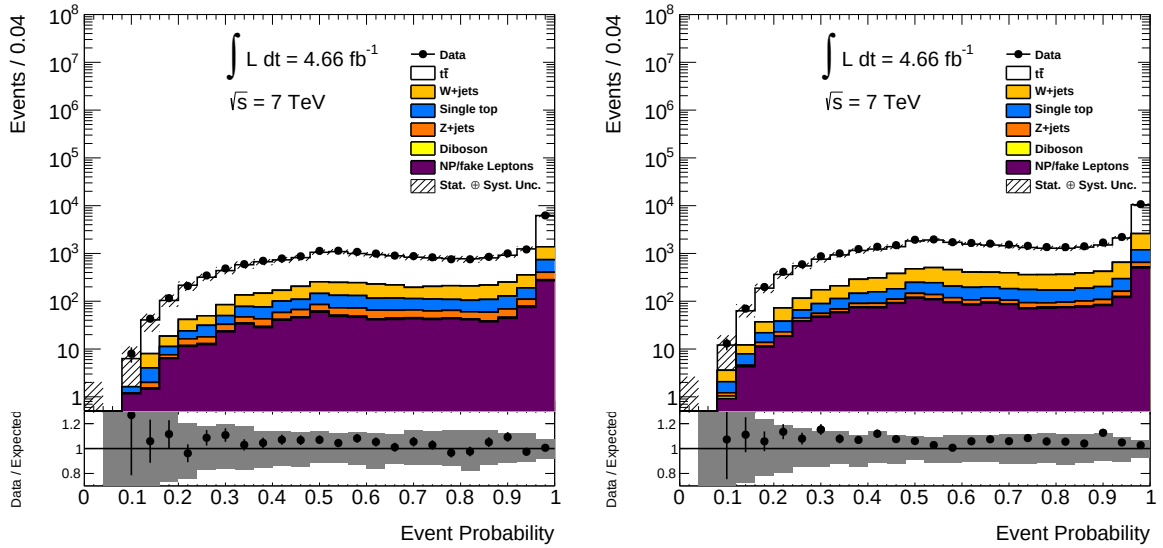

(a) Electron Channel **(b)** Muon Channel

Figure 4.7.: Comparison of the data to expectation for the event probability after performing the kinematic fit. The error bands account for the statistical and systematic uncertainties.

but the neutrino momentum is not measured at all, requiring a proper determination of the b_{Lep} from the selected jets to reconstruct the neutrino's momentum accurately. Figure 4.10 show the residual of the energies for the fitted leptonic b-jet and the truth level b-quark for two separate categories: events with the b-jet correctly identified (matching to the truth level b-quark) and events with the b-jet incorrectly identified (matched to the hadronic b-quark, matched to a light quark from hadronic W-boson decay, or not matched to any of the (anti)top's decay products). The case where the leptonic b-jet is incorrectly identified causes the energy residual to be smeared in comparison to the correctly identified case, in turn, this causes the neutrino's energy to be mis-reconstructed, which can be observed in the residual of the fitted neutrino's momentum components and the truth level neutrino's momentum components depicted in Figs. 4.11 and 4.12. The residuals for p_x and p_y of the neutrino for the incorrectly identified b_{Lep} case are much more narrow than that of p_Z since the transverse components are constrained by the measured $E_{\text{T}}^{\text{miss}}$.

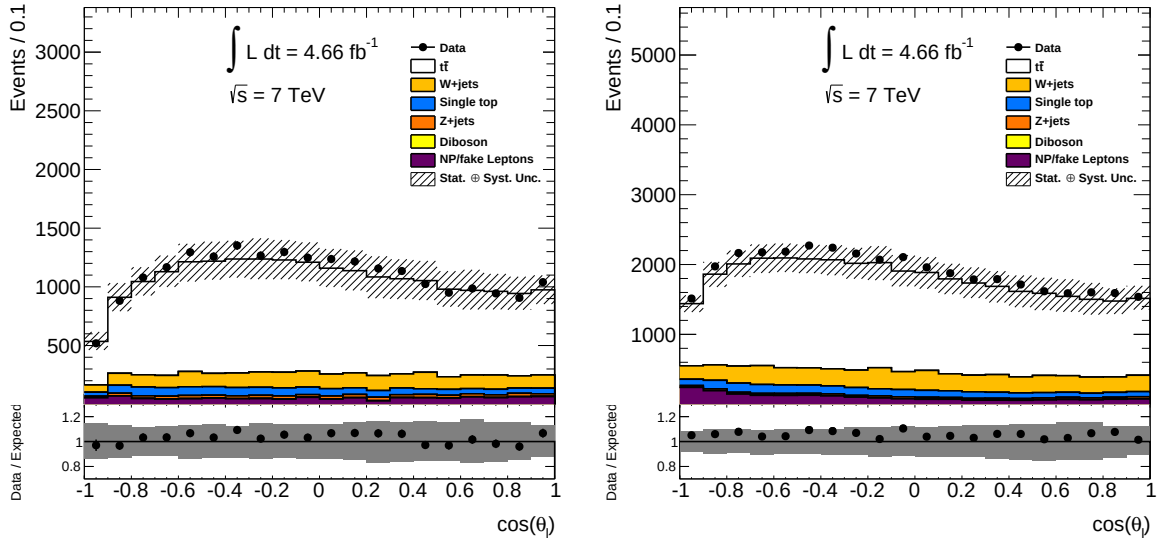

(a) Electron channel **(b)** Muon Channel

Figure 4.8.: Comparison of the data to expectation for $\cos\theta_\ell$ after $t\bar{t}$ reconstruction. The error bands account for the statistical and systematic uncertainties.

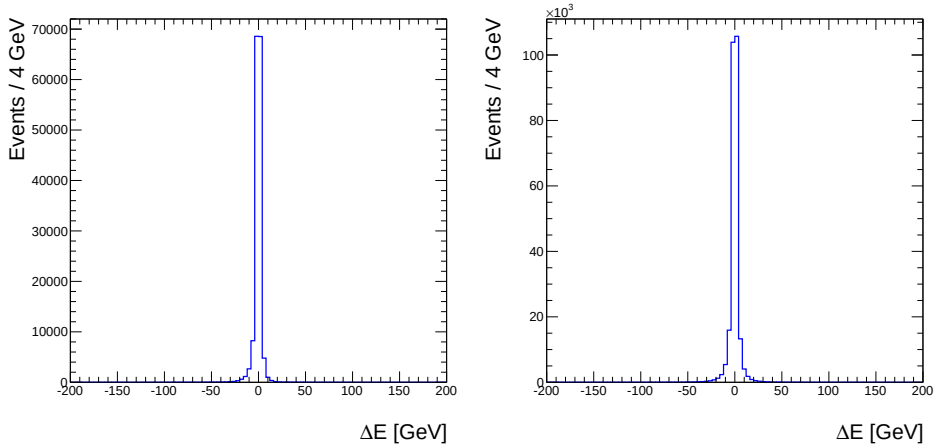

(a) Electron Channel **(b)** Muon Channel

Figure 4.9.: Residual of the fitted charged lepton energy and the energy of the truth level charged lepton.

It has been shown that selecting b_{Lep} is crucial in properly reconstructing the leptonic b-quark and the neutrino, and therefore, reconstructing the leptonically decaying top. This in turn has an impact on the determination of $\cos\theta_\ell$, since its calculation requires

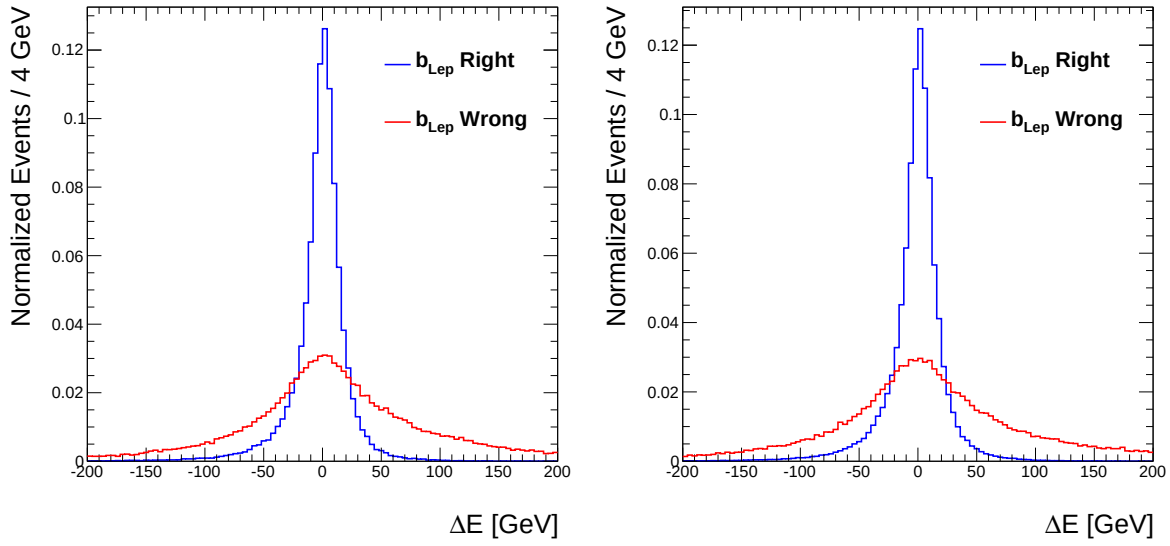

(a) Electron Channel **(b)** Muon Channel

Figure 4.10.: Residual of the fitted leptonic b-jet energy and the truth level b-quark energy for both channels. Each plot contains two categories: events with the b-jet correctly matched to the truth level b-quark and events where the b-jet is incorrectly identified.

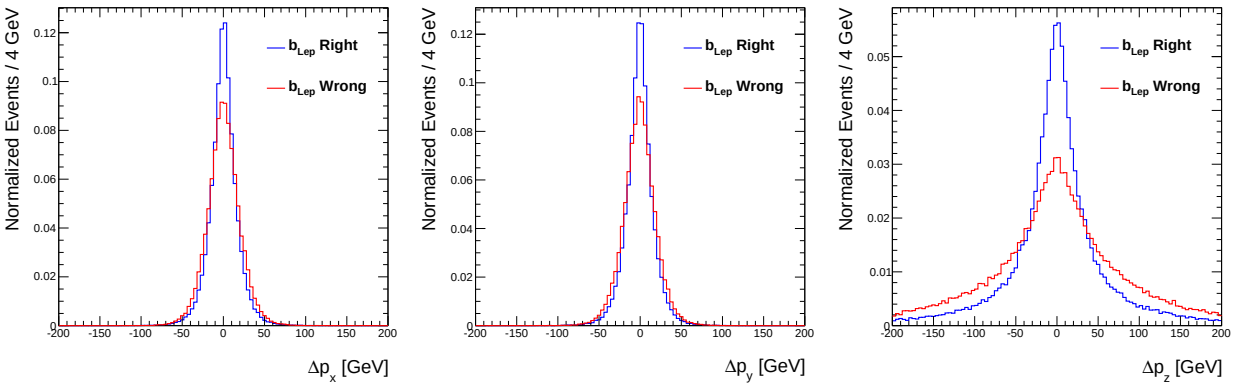

(a) p_x **(b)** p_y **(c)** p_z

Figure 4.11.: Residual of the fitted neutrino energy and the truth level neutrino energy for e+jets channel. Each plot contains two categories: events with the b-jet correctly matched to the truth level b-quark and events where the b-jet is incorrectly identified.

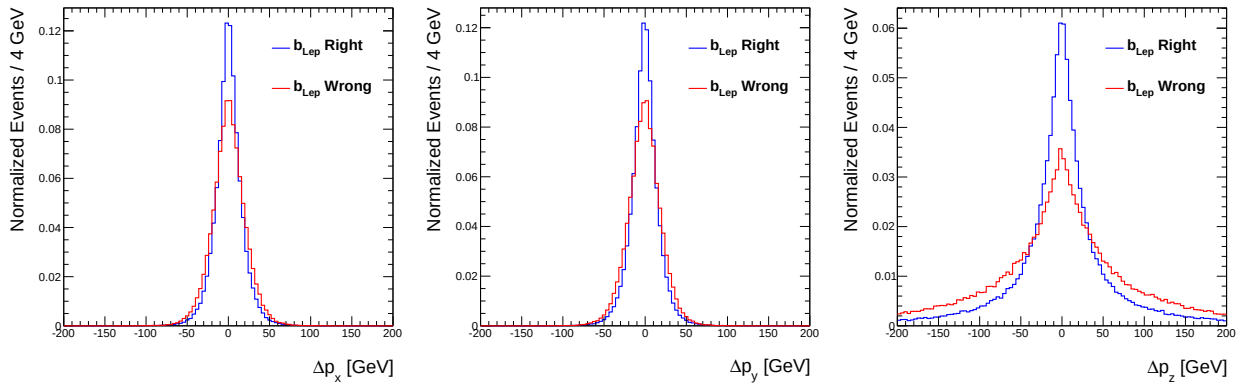

(a) p_x **(b)** p_y **(c)** p_z

Figure 4.12.: Residual of the fitted neutrino energy and the truth level neutrino energy for μ+jets channel. Each plot contains two categories: events with the b-jet correctly matched to the truth level b-quark and events where the b-jet is incorrectly identified.

knowledge of the top and antitop's 4-momentum. Figures 4.13 and 4.14 shows the residual of the reconstructed $\cos\theta_\ell$ and the truth level $\cos\theta_\ell$ ($\cos\theta_\ell^{\text{true}}$) in bins of $\cos\theta_\ell^{\text{true}}$ for both categories of rightly and wrongly selecting b_{Lep}. The residuals are asymmetric in the rightly selected category for values of $\cos\theta_\ell^{\text{true}}$ near -1 and 1 due to the fact that $\cos\theta_\ell$ is constrained to be between those values; the residual becomes symmetric for values of $\cos\theta_\ell^{\text{true}}$ near 0. The wrongly selected category is more flat for most bins of $\cos\theta_\ell^{\text{true}}$. The category of selecting b_{Lep} correctly contains events where the hadronically decaying top is misreconstructed, which affects the reconstruction of the quantization axis, and therefore $\cos\theta_\ell$. Despite the mis-reconstruction of the hadronically decaying top, it causes the residual of $\cos\theta_\ell$ for those events to smear out about the true value, leaving them sensitive to top quark polarization. The impact that selecting the correct b_{Lep} has on the nominal distribution of $\cos\theta_\ell$ is shown in Figs. 4.15a and 4.16a, where the total reconstructed distribution of true single lepton events are shown compared to their truth level distribution. Incorrectly selecting b_{Lep} has the effect of flattening out the $\cos\theta_\ell$ distribution. This analysis uses reweighted events to induce polarization of the top quarks, Section 4.4 explains in detail how this reweighting procedure is conducted, and

Figs. 4.15b, 4.15c, 4.16b and 4.16c shows that reweighting has little effect on the shape of the incorrectly selected b_{Lep} distribution; therefore, the total reconstructed distribution is still sensitive to polarized top quarks.

A study on the efficiency for properly selecting a jet to its true quark was conducted; Fig. 4.17 shows the efficiency as a function of quark flavor and of decay channel. The efficiency for selecting all jets to their matching truth quark is 30%, meanwhile, the b_{Lep} is selected approximately 60% of the time. The figure of 30% for selecting all jets properly is low, but as stated before, events when selecting b_{Lep} correctly and the hadronic top jets incorrectly, which has 60% efficiency, will still be sensitive to top quark polarization. The cause for incorrectly identifying b_{Lep} is shown in Fig. 4.18, where five cases are considered: b_{Lep} is correctly identified, the jets matching b_{Lep} and b_{Had} are switched in the fitter, a jet matching b_{Had} is used for the leptonic b-jet and the jet matching b_{Lep} is not used for the hadronic b-jet in the fitter, a jet matching a light quark is mis-tagged and chosen for the leptonic b-jet in the fitter, and events where none of the five highest p_{T} jets match b_{Lep}. The break down of why b_{Lep} was not properly selected is as follows: none of the five highest p_{T} jets are matched to b_{Lep} (20%), the jet matching b_{Had} is used for the leptonic b-jet (10%), a jet from the hadronic W-boson decay is mis-tagged and used for the leptonic b-jet in the fitter (10%).

A comparison between events with 4 jets and those with ≥ 5 jets was conducted, with the goal of seeing if there would be an enhancement on performance for events with only 4 jets. Figure 4.19 shows the ratio of the jet matching efficiencies between events with ≥ 5 jet and events with 4 jets. The efficiency for matching a jet to a particular quark is similar between the two jet bins, which means that b_{Lep} is selected correctly at about the same rate in both bins; however, the efficiency for selecting all 4 jets correctly is approximately 18% lower in the ≥ 5 jet bin. Events with ≥ 5 jets will lose some sensitivity to the top quark's polarization since the reconstruction will smear their $\cos\theta_\ell$

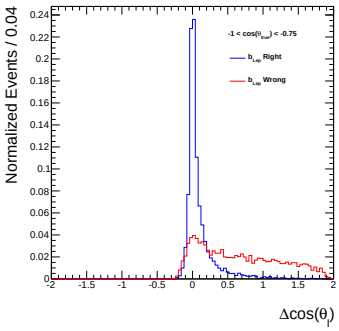

(a) $-1 < \cos\theta_\ell^{\text{true}} < -0.75$

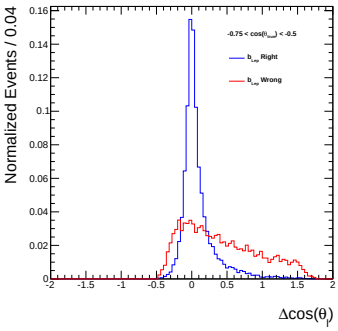

(b) $-0.75 < \cos\theta_\ell^{\text{true}} < -0.5$

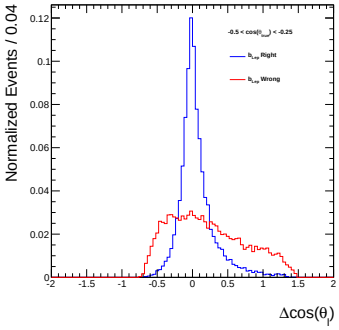

(c) $-0.5 < \cos\theta_\ell^{\text{true}} < -0.25$

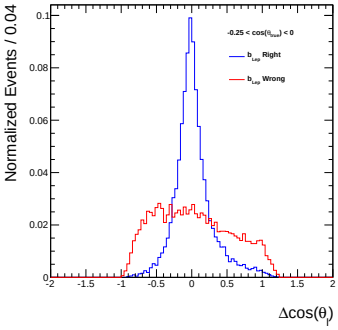

(d) $-0.25 < \cos\theta_\ell^{\text{true}} < 0$

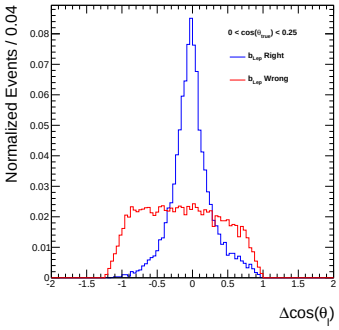

(e) $0 < \cos\theta_\ell^{\text{true}} < 0.25$

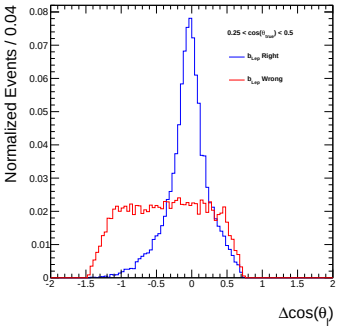

(f) $0.25 < \cos\theta_\ell^{\text{true}} < 0.5$

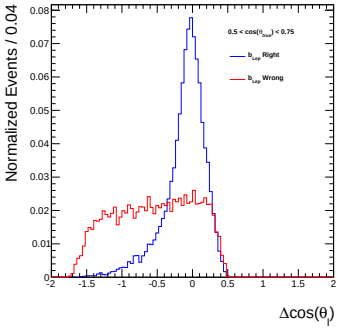

(g) $0.5 < \cos\theta_\ell^{\text{true}} < 0.75$

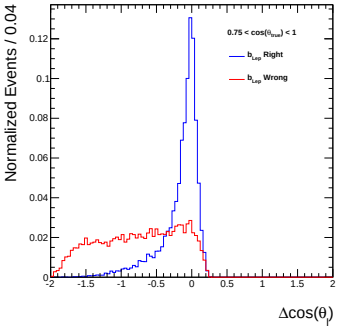

(h) $0.75 < \cos\theta_\ell^{\text{true}} < 1$

Figure 4.13.: Residuals, in bins of $\cos\theta_\ell^{\text{true}}$, of the reconstructed $\cos\theta_\ell$ and $\cos\theta_\ell^{\text{true}}$, for the categories of rightly and wrongly selecting b_{Lep}, in the electron channel.

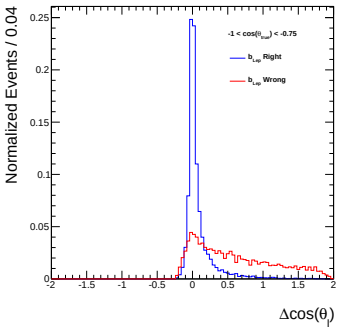

(a) $-1 < \cos\theta_\ell^{\text{true}} < -0.75$

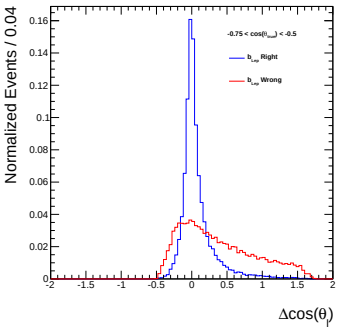

(b) $-0.75 < \cos\theta_\ell^{\text{true}} < -0.5$

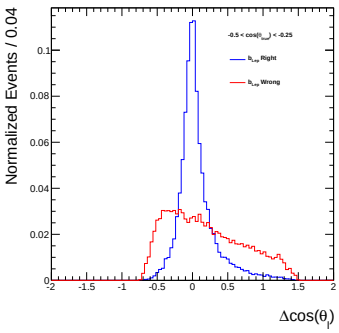

(c) $-0.5 < \cos\theta_\ell^{\text{true}} < -0.25$

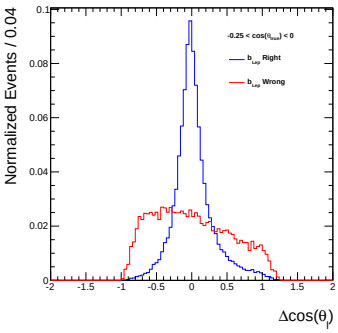

(d) $-0.25 < \cos\theta_\ell^{\text{true}} < 0$

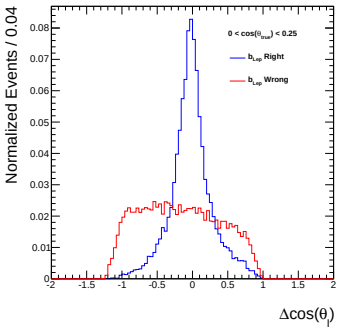

(e) $0 < \cos\theta_\ell^{\text{true}} < 0.25$

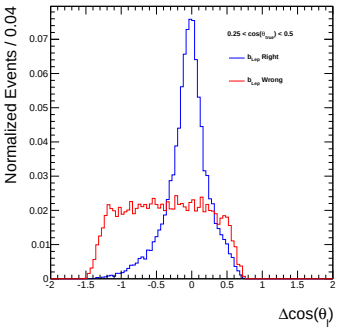

(f) $0.25 < \cos\theta_\ell^{\text{true}} < 0.5$

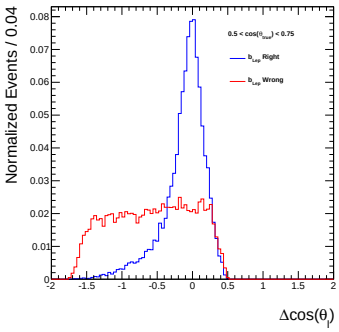

(g) $0.5 < \cos\theta_\ell^{\text{true}} < 0.75$

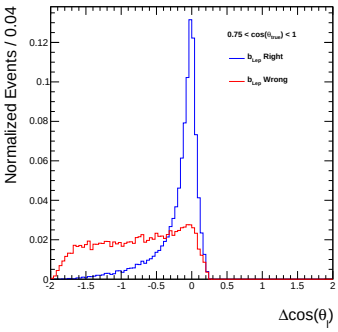

(h) $0.75 < \cos\theta_\ell^{\text{true}} < 1$

Figure 4.14.: Residuals, in bins of $\cos\theta_\ell^{\text{true}}$, of the reconstructed $\cos\theta_\ell$ and $\cos\theta_\ell^{\text{true}}$, for the categories of rightly and wrongly selecting b_{Lep}, in the muon channel.

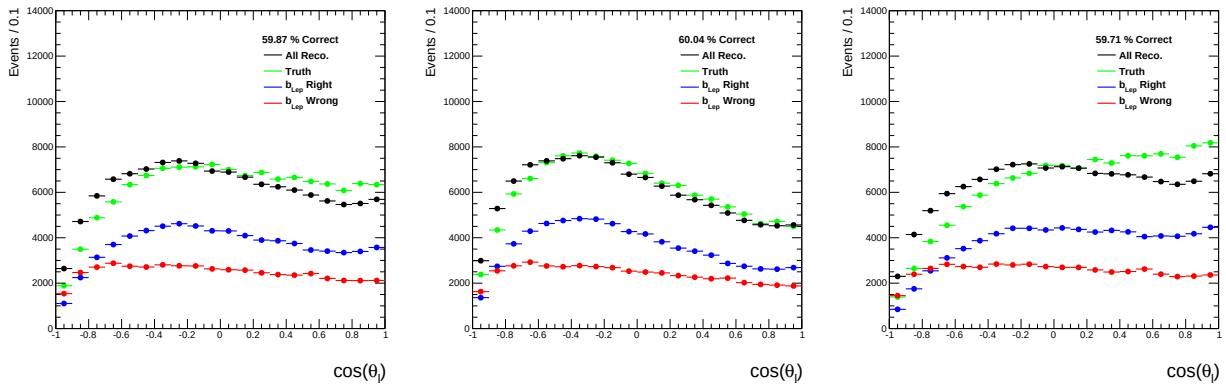

(a) Nominal **(b)** Reweighted, $\alpha_\ell P = -0.3$ **(c)** Reweighted, $\alpha_\ell P = 0.3$

Figure 4.15.: Nominal and reweighted distributions of $\cos\theta_\ell$ for true e+jets events. The truth level distribution is shown, along with the total reconstructed distribution, which is also split into right and wrong categories for selecting b_{Lep}. The percentage of events that have b_{Lep} correct are also shown.

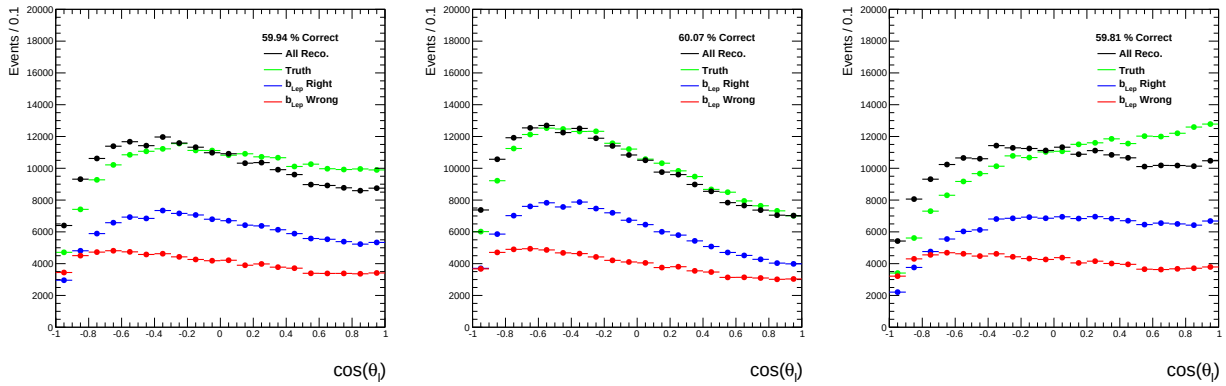

(a) Nominal simulation **(b)** Reweighted, $\alpha_\ell P = -0.3$ **(c)** Reweighted, $\alpha_\ell P = 0.3$

Figure 4.16.: Nominal and reweighted distributions of $\cos\theta_\ell$ for true μ+jets events. The truth level distribution is shown, along with the total reconstructed distribution, which is also split into right and wrong categories for selecting b_{Lep}. The percentage of events that have b_{Lep} correct are also shown.

distribution. Figures 4.20 and 4.21 shows the residuals of $\cos\theta_\ell$ in the ≥ 5 jet bin and can be compared to the residuals of the ≥ 4 jet inclusive bin, shown in Figs. 4.13 and 4.14. The decision to keep events with ≥ 5 jets was motivated by the fact that selecting events with only 4 jets would cut out approximately 40% of the signal; moreover, the efficiencies for matching b_{Lep} are essentially the same for both bins and events where b_{Lep} is matched correctly still shows sensitivity to top quark polarization.

To conclude the study on the kinematic fitter's performance, a comparison of the data to expectation for the kinematic fitter's output was conducted. Figures 4.22 to 4.25 show comparisons between the data and expectation for the leptonically decaying top quark and its decay products; other comparison plots may be found in Appendix B. The comparison for $\cos\theta_\ell$ in the 0 b-tagged control region may be found in Fig. 4.26. All distribution's data and expectations are found to be in agreement.

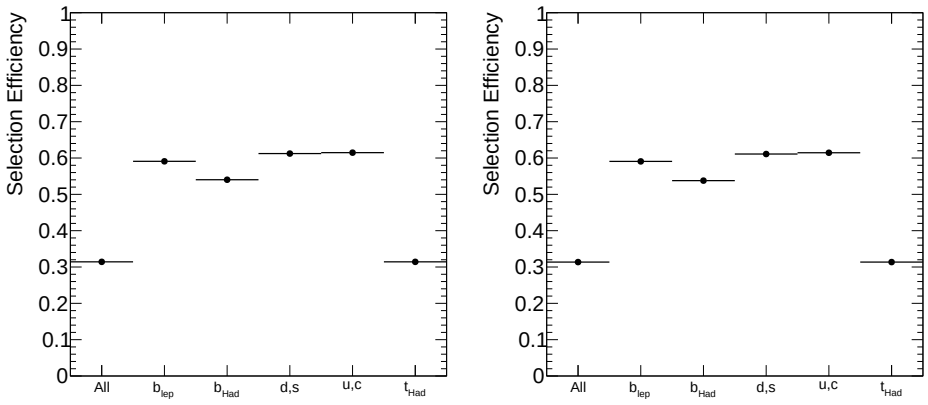

(a) Electron Channel **(b)** Muon Channel

Figure 4.17.: Matching efficiency for jets to their true quarks.

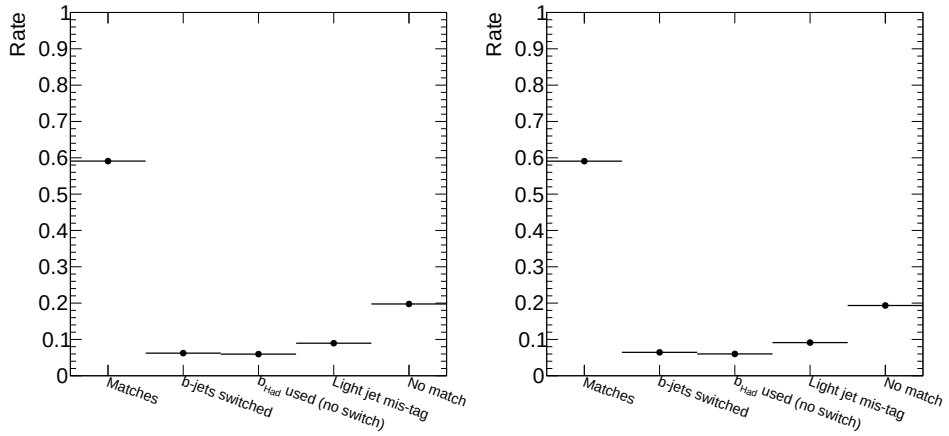

(a) Electron Channel **(b)** Muon Channel

Figure 4.18.: Categorization of matched quarks to b_{Lep}. The cases refer to b_{Lep} being correctly identified (Matches), the jets matching b_{Lep} and b_{Had} are switched (b-jets switched), a jet matching b_{Had} is used for the leptonic b-jet and the jet matching b_{Lep} is not used for the hadronic b-jet (b_{Had} used (no switch)), a jet matched to a light quark is mis-tagged and was chosen for the leptonic b-jet (Light jet mis-tag), and the case where no jet matched b_{Lep} (No match)

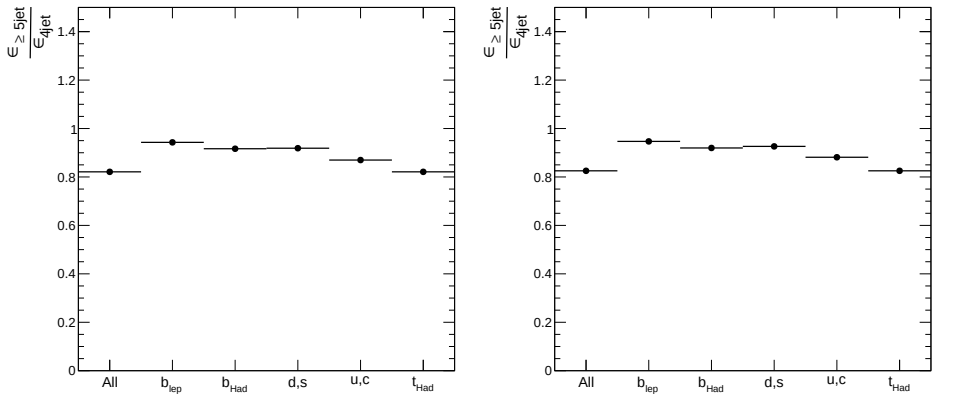

(a) Electron Channel **(b)** Muon Channel

Figure 4.19.: Ratio of the jet matching efficiencies for events with ≥ 5 jets to events with 4 jets in single lepton $t\bar{t}$ decays.

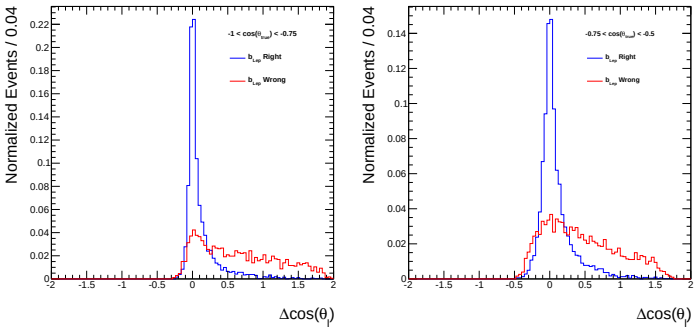

(a) $-1 < \cos\theta_\ell^{\text{true}} < -0.75$ **(b)** $-0.75 < \cos\theta_\ell^{\text{true}} < -0.5$

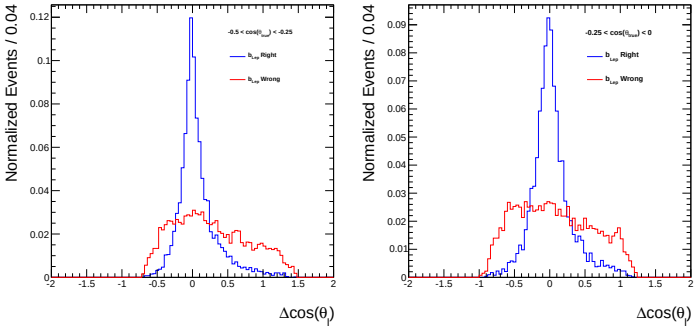

(c) $-0.5 < \cos\theta_\ell^{\text{true}} < -0.25$ **(d)** $-0.25 < \cos\theta_\ell^{\text{true}} < 0$

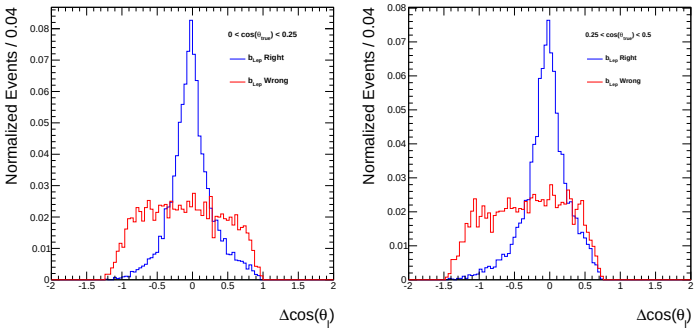

(e) $0 < \cos\theta_\ell^{\text{true}} < 0.25$ **(f)** $0.25 < \cos\theta_\ell^{\text{true}} < 0.5$

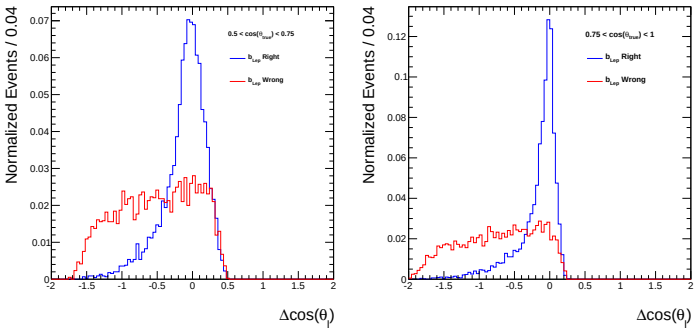

(g) $0.5 < \cos\theta_\ell^{\text{true}} < 0.75$ **(h)** $0.75 < \cos\theta_\ell^{\text{true}} < 1$

Figure 4.20.: Residuals, in bins of $\cos\theta_\ell^{\text{true}}$, of the reconstructed $\cos\theta_\ell$ and $\cos\theta_\ell^{\text{true}}$, for the categories of rightly and wrongly selecting b_{Lep}, for events with ≥ 5 jets in the electron channel.

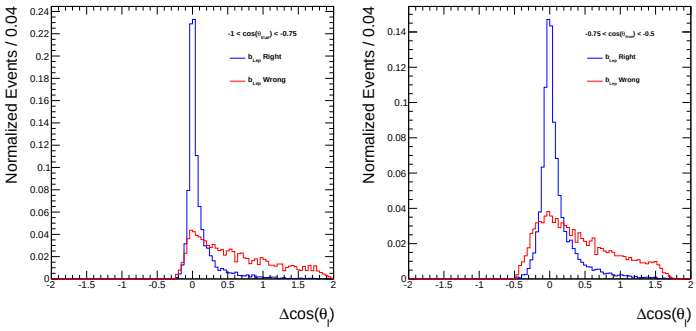

(a) $-1 < \cos\theta_\ell^{\text{true}} < -0.75$ **(b)** $-0.75 < \cos\theta_\ell^{\text{true}} < -0.5$

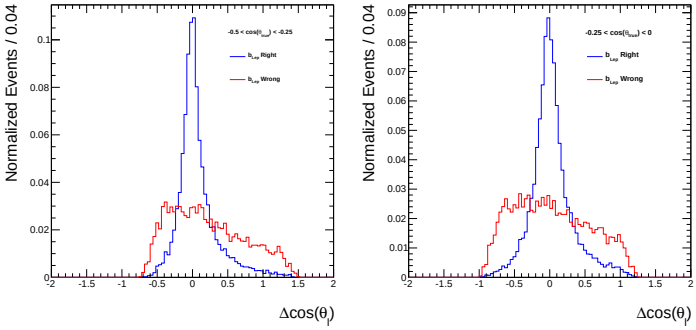

(c) $-0.5 < \cos\theta_\ell^{\text{true}} < -0.25$ **(d)** $-0.25 < \cos\theta_\ell^{\text{true}} < 0$

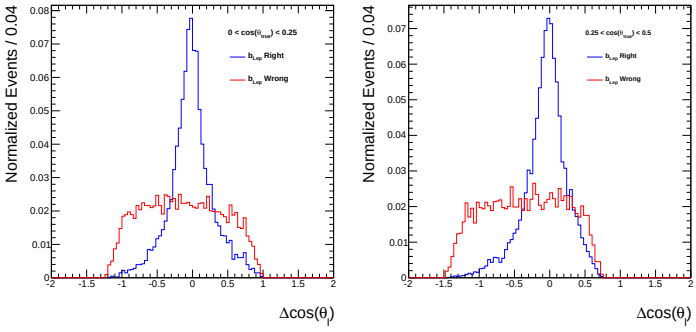

(e) $0 < \cos\theta_\ell^{\text{true}} < 0.25$ **(f)** $0.25 < \cos\theta_\ell^{\text{true}} < 0.5$

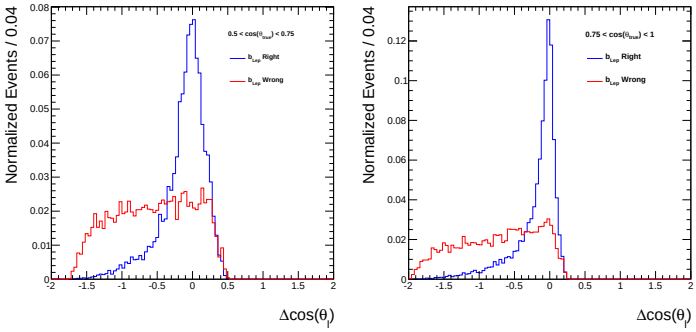

(g) $0.5 < \cos\theta_\ell^{\text{true}} < 0.75$ **(h)** $0.75 < \cos\theta_\ell^{\text{true}} < 1$

Figure 4.21.: Residuals, in bins of $\cos\theta_\ell^{\text{true}}$, of the reconstructed $\cos\theta_\ell$ and $\cos\theta_\ell^{\text{true}}$, for the categories of rightly and wrongly selecting b_{Lep}, for events with ≥ 5 jets in the muon channel.

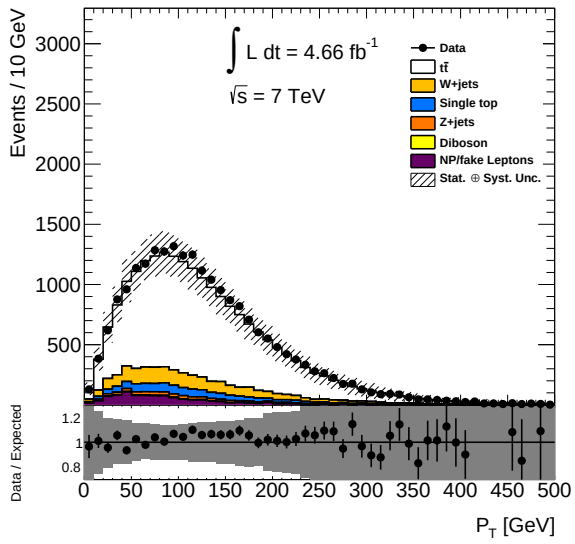

(a) Electron Channel

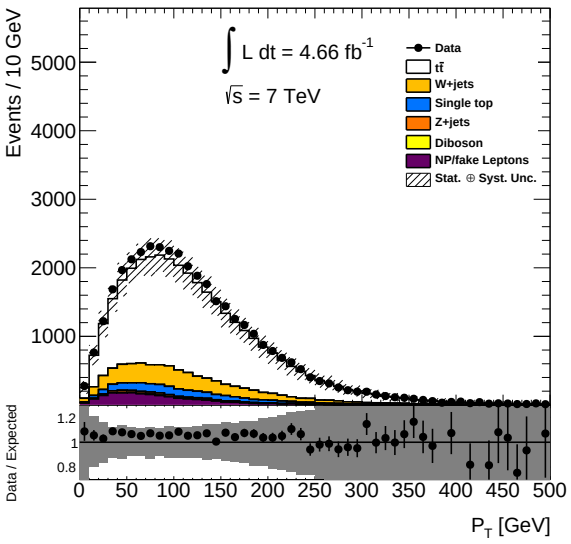

(b) Muon Channel

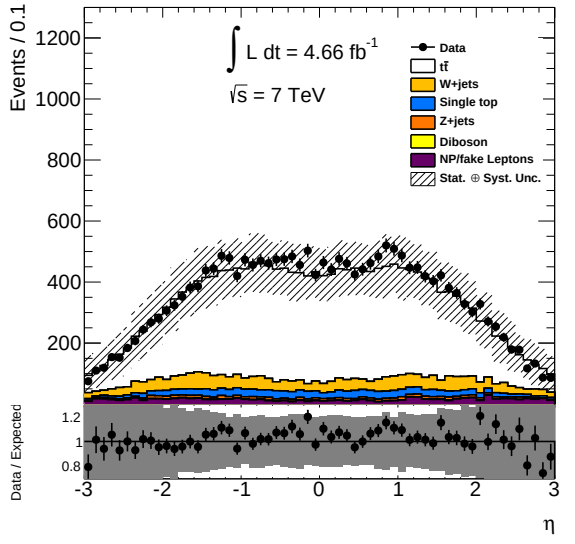

(c) Electron Channel

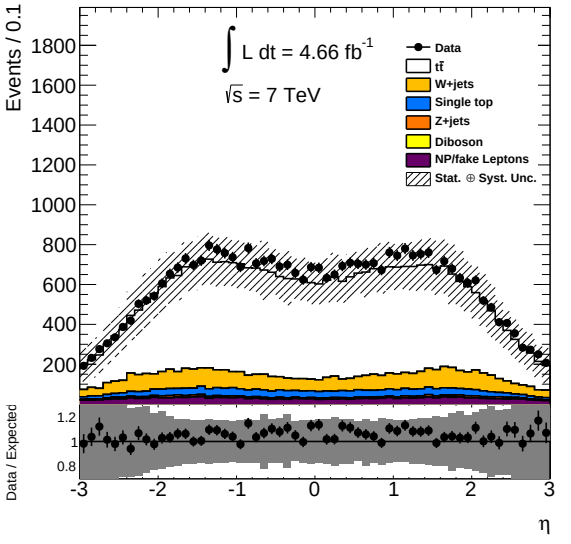

(d) Muon Channel

Figure 4.22.: Comparison of the leptonically decaying top quark's p_{T} and η between data and expectation in the e+jets and μ+jets channels, including the ratio of the data to the expectation.

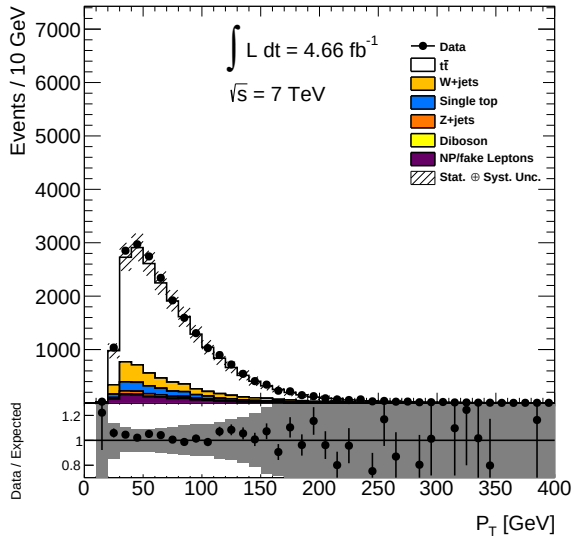

(a) Electron Channel

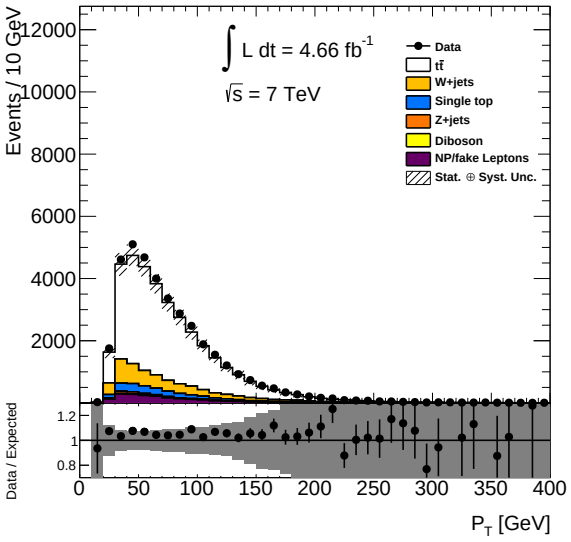

(b) Muon Channel

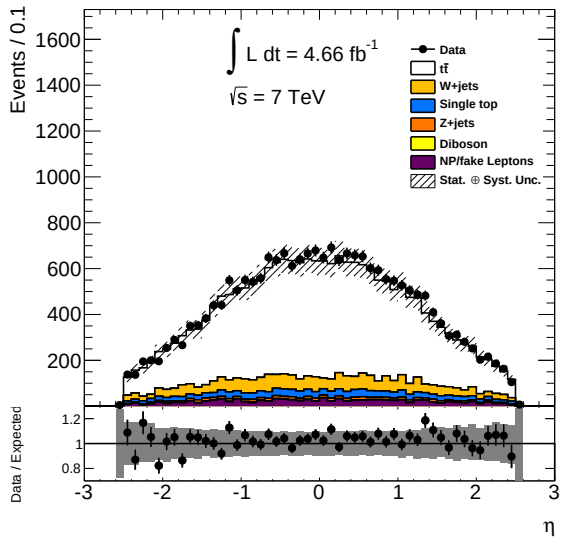

(c) Electron Channel

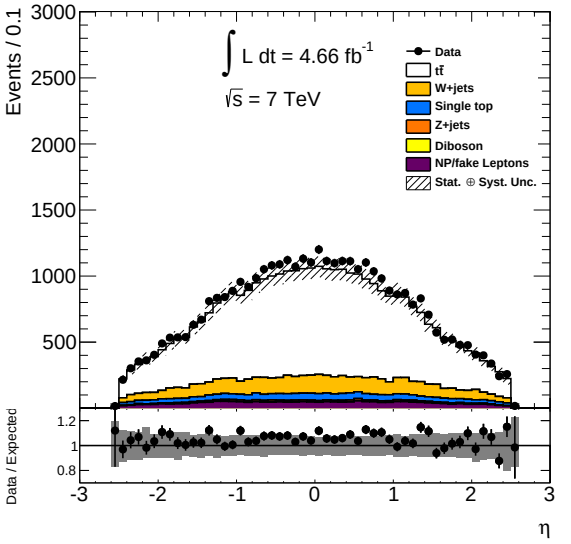

(d) Muon Channel

Figure 4.23.: Comparison of b_{Lep} 's p_{T} and η between data and expectation in the e+jets and μ+jets channels, including the ratio of the data to the expectation.

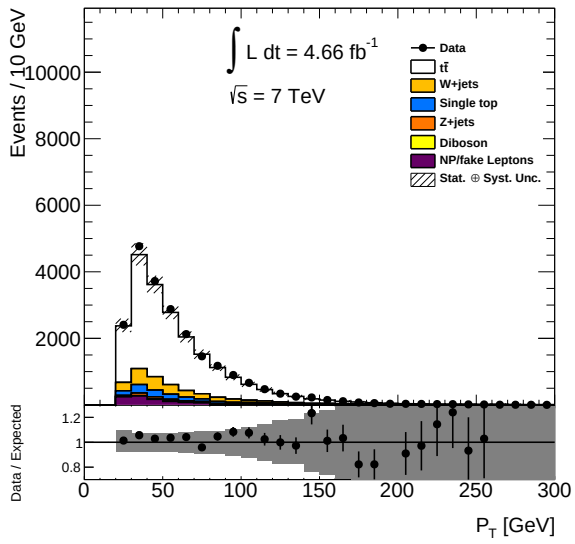

(a) Electron Channel

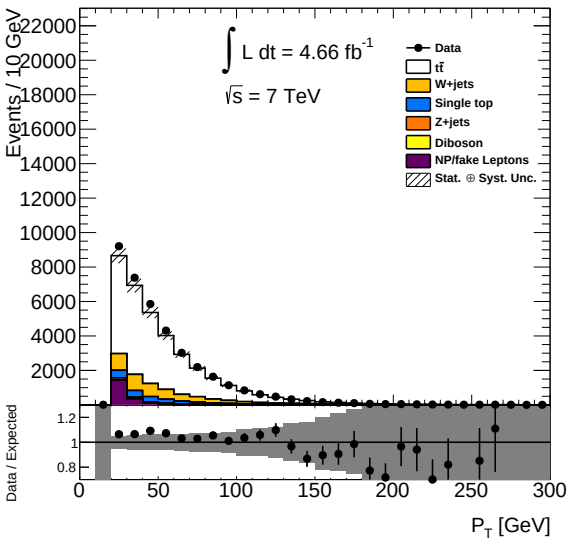

(b) Muon Channel

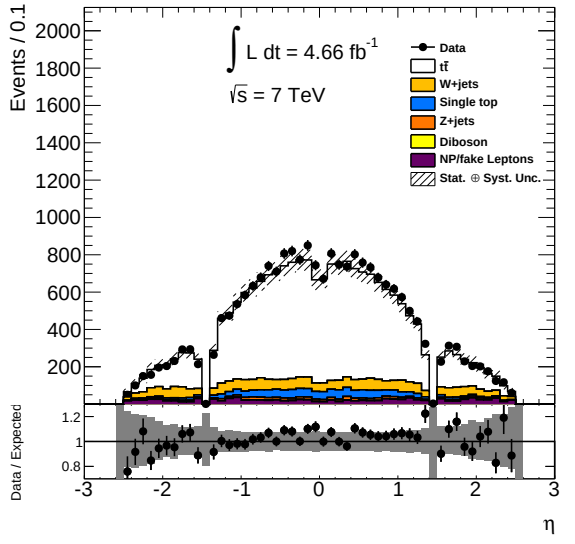

(c) Electron Channel

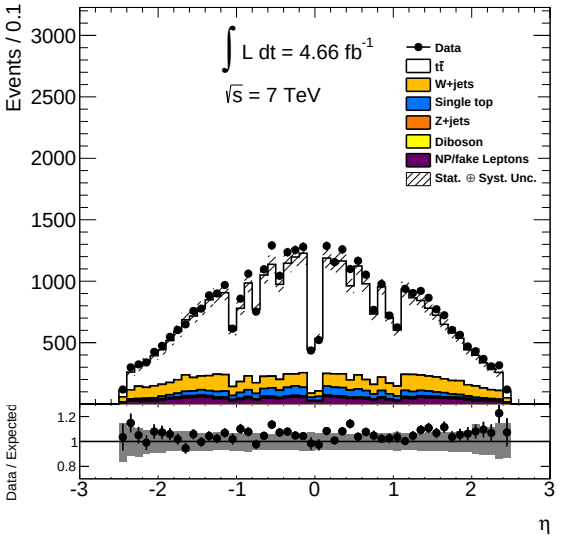

(d) Muon Channel

Figure 4.24.: Comparison of the charged lepton's p_{T} and η between data and expectation in the e+jets and μ+jets channels, including the ratio of the data to the expectation.

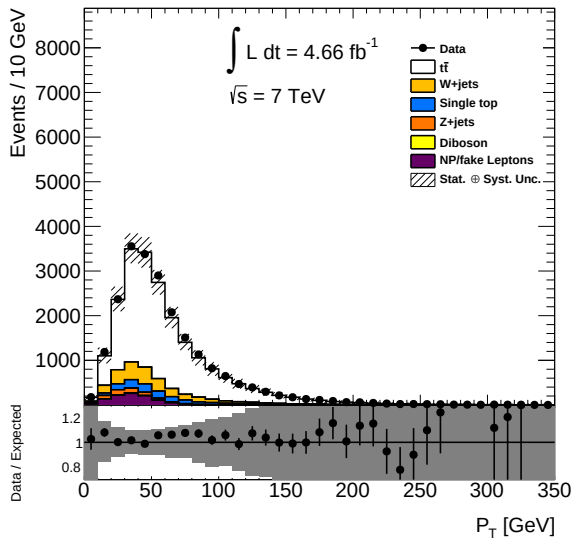

(a) Electron Channel

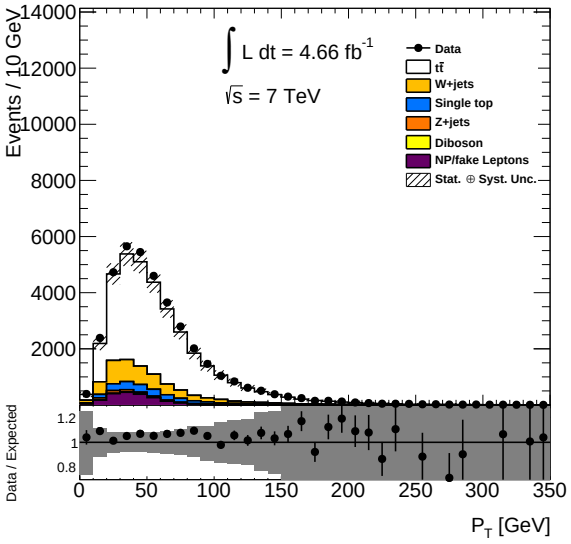

(b) Muon Channel

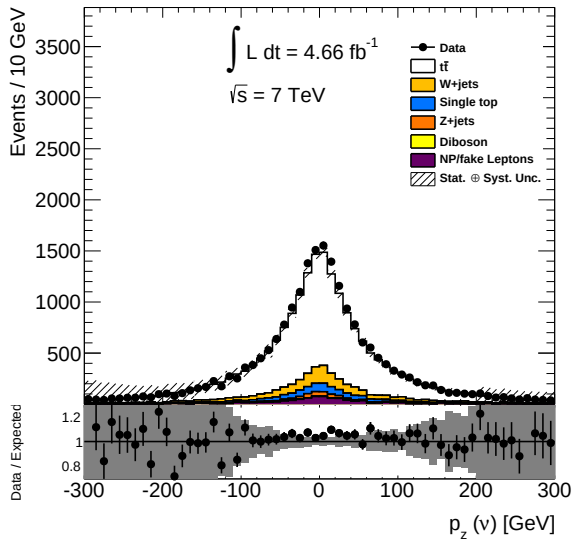

(c) Electron Channel

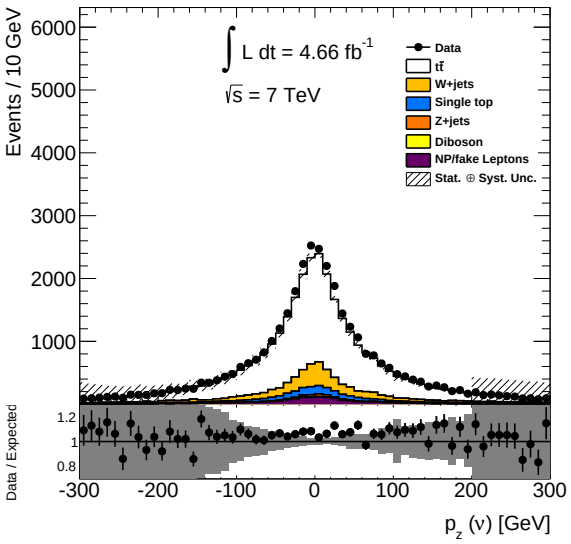

(d) Muon Channel

Figure 4.25.: Comparison of the neutrino's p_{T} and p_z between data and expectation in the e+jets and μ+jets channels, including the ratio of the data to the expectation.

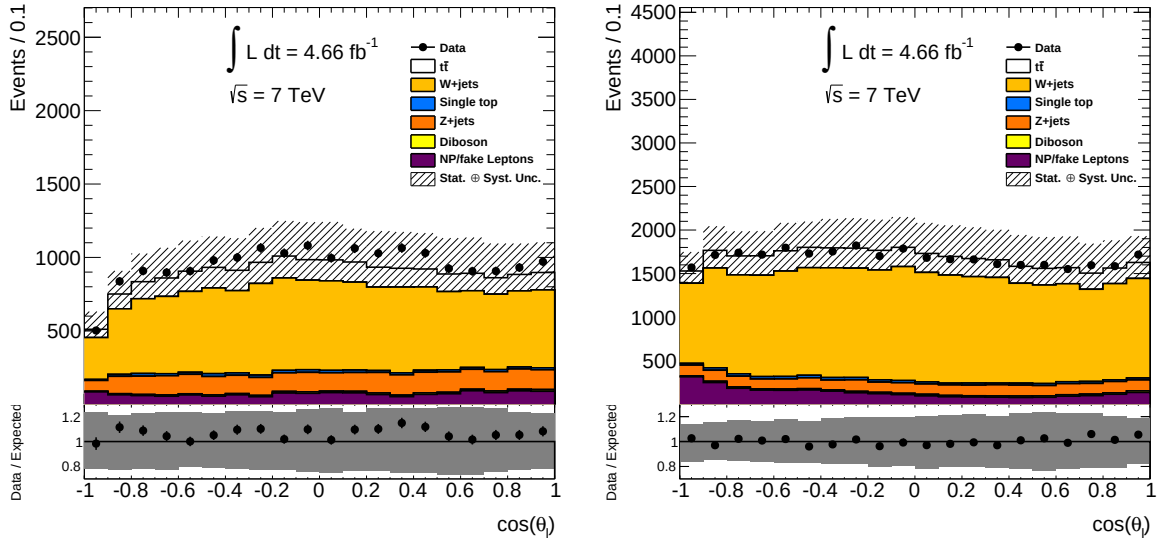

(a) Electron Channel **(b)** Muon Channel

Figure 4.26.: Comparison of $\cos\theta_\ell$ between data and expectation in the control region with 0 b-tagged jets.

4.4. Reweighting

Currently, ATLAS MC samples for $t\bar{t}$ production that contain polarized top quarks do not exist; nor do the samples that do exist have the spin information of the tops in their truth information[7]. This fact necessitates an alternative method for introducing polarization to the signal $t\bar{t}$ MC used in this analysis. To induce polarization in the signal MC, a reweighting technique utilizing the truth information of the (anti)top and their final state decay products is used. An event weight is created based on the double differential cross section for $t\bar{t}$ decays with respect to the polar angles from one of the final state decay products of the top and from one of the final state decay products of the antitop. After reweighting the events in the signal MC, a study was performed that finds that the resulting truth level polar angle distributions of the (anti)top decay final state products are in agreement with theorized expectations, thus validating the

[7]Most generators integrate over spin states.

reweighting procedure. The technique used to reweight events in this analysis [51] was an improvement upon the preliminary measurement's [50] reweighting technique, so as to accommodate the dilepton channel since the preliminary measurement was only in the ℓ+jets channel. A dedicated study, which may be found in Appendix C, was performed to motivate and validate the evolution of the reweighting procedure from the preliminary analysis to this analysis.

4.4.1. Reweighting Procedure

Each signal $t\bar{t}$ MC event is reweighted based on the double differential cross section [23] for $t\bar{t}$ production with respect to the polar angle of one of the top's decay products and one of the antitop's decay products:

$$\frac{1}{\sigma}\frac{d^2\sigma}{d\cos\theta_1 d\cos\theta_2} = \frac{1}{4}(1 + \alpha_1 P_1 \cos\theta_1 + \alpha_2 P_2 \cos\theta_2 - C\cos\theta_1\cos\theta_2), \tag{4.4}$$

where $\alpha_1 P_1$ ($\alpha_2 P_2$) correspond to the spin-analyzing power of one of the final state decay products of the top (antitop) quark times the magnitude of the longitudinal polarization of the top (antitop) quark and C represents the $t\bar{t}$ spin correlation. The angle θ_1 (θ_2) corresponds to the polar angle of the final state decay product used to determine $\alpha_1 P_1$ ($\alpha_2 P_2$) of the top (antitop) quark. The values of α for each of the final state decay products may be found in Table 4.1. For each event, the values of $\alpha_1 P_1$, $\alpha_2 P_2$, $\cos\theta_1$, and $\cos\theta_2$ are taken from the its truth level information and are used to calculate an event weight given by

$$W = \frac{1 + \alpha_1 P_1 \cos\theta_1 + \alpha_2 P_2 \cos\theta_2 - C\cos\theta_1\cos\theta_2}{1 - C\cos\theta_1\cos\theta_2}, \tag{4.5}$$

where the denominator, $1 - C\cos\theta_1\cos\theta_2$, is employed to ensure that the spin correlation already present in the MC is not introduced twice. Constraints are placed on $\alpha_1 P_1$, $\alpha_2 P_2$

and C, to ensure that the differential cross section remains positive. In this analysis, two cases of polarized top quarks are considered, a CP conserving case and a maximally CP violating case, each with their own constraints. In the CP conserving scenario, $\alpha_1 P_1 = \alpha_2 P_2$, which places the constraint:

$$|\alpha_{1,2} P| \leq \frac{1 - C}{2}. \tag{4.6}$$

On the other hand, the maximally CP violating scenario requires $\alpha_1 P_1$ = -$\alpha_2 P_2$, which places the constraint:

$$|\alpha_{1,2} P| \leq \frac{1 + C}{2}. \tag{4.7}$$

The value of C was determined from the signal MC by performing a quadratic fit to the two dimensional histogram of $\cos\theta_1$ and $\cos\theta_2$, finding the value of C to be 0.307. Therefore, $|\alpha_{1,2} P|$ must be less than 0.346, which places a limitation on the value of P since $\alpha_{1,2}$ has definite values. For this analysis, a value of 0.3 was chosen for $|\alpha_{1,2} P|$, which falls within both constraints given in Eqs. (4.6) and (4.7).

4.4.2. Polarized top quark signal templates

As stated previously, the signal MC used in this analysis contains unpolarized top quarks; therefore, their truth level polar angle distribution is flat. This is shown in Fig. 4.27 using the charged lepton's truth level polar angle distribution before reweighting. This analysis performs a template fit to the data and requires a positively polarized top quark template and a negatively polarized top quark template for each fit; in addition, a separate fit is done for a CP conserving case (CPC) and a maximally CP violating case

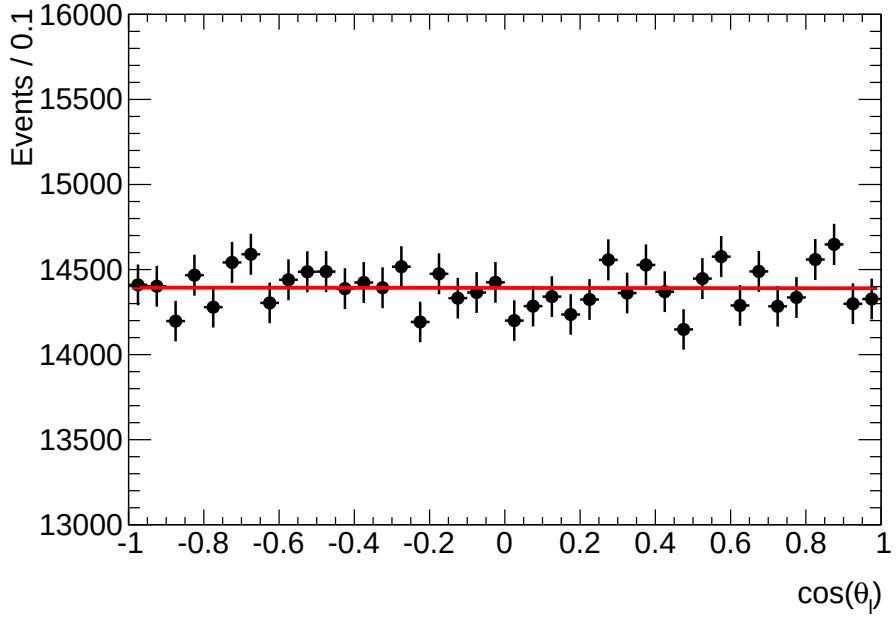

Figure 4.27.: Charged lepton's truth level polar angle distribution before reweighting, fit to a first degree polynomial $y = p0\,(1 + p1 \cdot x)$. The fit results are: $p0 = 28790.0 \pm 38.0$ and $p1 = -0.0002 \pm 0.002$.

(CPV). Therefore, four separate weights are needed to produce the templates:

$$W_{\mathrm{CPC}} = \frac{1 \pm 0.3\cos\theta_1 \pm 0.3\cos\theta_2 - 0.307\cos\theta_1\cos\theta_2}{1 - 0.307\cos\theta_1\cos\theta_2}, \tag{4.8}$$

$$W_{\mathrm{CPV}} = \frac{1 \pm 0.3\cos\theta_1 \mp 0.3\cos\theta_2 - 0.307\cos\theta_1\cos\theta_2}{1 - 0.307\cos\theta_1\cos\theta_2}, \tag{4.9}$$

where $\cos\theta_1$ ($\cos\theta_2$) correspond to the truth level polar angles of the charged lepton or down/strange quark from the top (antitop) decay. The upper sign of $\pm$ ($\mp$) in W_{CPC} (W_{CPV}) will be referred to as the positive template and the bottom sign will be referred to as the negative template.

The weights provided in Eqs. (4.8) and (4.9) induce the proper truth level polar angle distributions for each of the (anti)top final state decay products. After reweighting the events, each of the final state decay products polar angle distributions are fit to a second

degree polynomial of the form $y = p0\,(1 + p1 \cdot x + p2 \cdot x^2)$, where, following Eq. (4.1), $p1$ corresponds to $\alpha_{1,2}P$ and $p2$ is a check to ensure that there is no deviation from the linear expectation that may arise from improperly accounting for spin correlation. The quadratic fits to the truth level polar angle distributions for the charged lepton and down/strange quark after reweighting by W_{CPC} are shown in Fig. 4.28. The fitted and predicted values of $p1$ and $p2$ for each final state decay product after reweighting by W_{CPC} are summarized in Table 4.3, which shows that the proper angular distributions for each final state decay product are achieved after conducting the reweighting procedure.

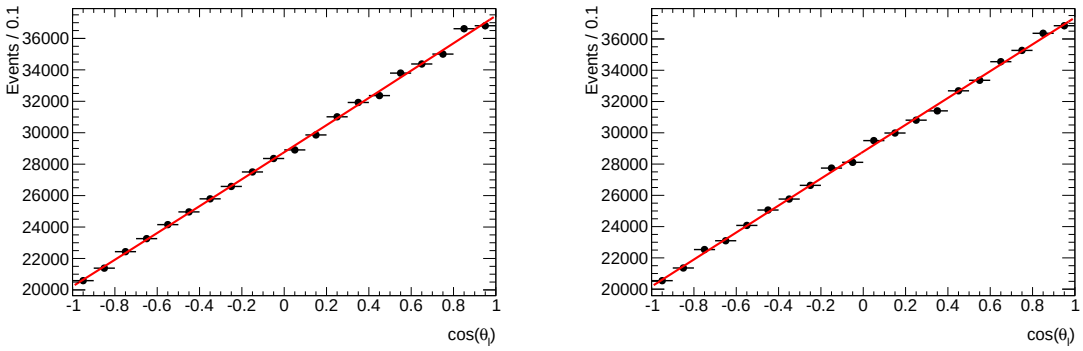

(a) Charged Lepton **(b)** Down and Strange Quark

Figure 4.28.: Truth level polar angle distributions weighted by W_{CPC} and fitted to a second degree polynomial.

Particle Type	Predicted p1	Measured p1	Predicted p2	Measured p2
Charged Lepton	0.30	0.30 ± 0.002	0.0	0.003 ± 0.004
Neutrino	-0.09	-0.10 ± 0.002	0.0	0.001 ± 0.005
Leptonic b Quark	-0.12	-0.12 ± 0.002	0.0	-0.002 ± 0.005
Down and Strange Quarks	0.30	0.30 ± 0.002	0.0	-0.007 ± 0.004
Up Type Quark	-0.09	-0.11 ± 0.002	0.0	-0.001 ± 0.005
Hadronic b Quark	-0.12	-0.11 ± 0.002	0.0	-0.002 ± 0.005

Table 4.3.: Fitted and predicted values of $p1$ and $p2$ for the truth level polar angle distributions of each final state decay product after reweighting by W_{CPC}.

4.5. Binned Maximum Likelihood Fit

A template fit to the data is employed to extract $\alpha_\ell P$ from the data. Templates of $\cos\theta_\ell$ using partially polarized top quarks are produced, as discussed in Section 4.4.2, and added to templates of $\cos\theta_\ell$ from the expected background. For this analysis, a binned maximum likelihood fit is used to fit the fraction of the positive template component, f, which is related to α_ℓ by

$$\frac{1}{2}f\underbrace{(1+0.3\cos\theta_\ell)}_{\text{Positive Template}}+\frac{1}{2}(1-f)\underbrace{(1-0.3\cos\theta_\ell)}_{\text{Negative Template}}=\frac{1}{2}(1+\alpha_\ell P\cos\theta_\ell) \tag{4.10}$$

The $t\bar{t}$ cross section is simultaneously fit[8] with f, so as to reduce normalization uncertainties on the final measurement, meanwhile, the background templates are not varied during the fit.

Another fitting method, equally as valid as the one described by Eq. (4.10) could have been used to extract f. This method will be referred to as the positive/negative template fitting method, while the method used for this analysis will be referred to as the normal fitting method. The positive/negative method consists of two separate fits, a positive (negative) fit is a template fit that uses the positive (negative) templates described in Eq. (4.10) and a flat template corresponding to a distribution that is flat in $\cos\theta_\ell$. The fitting function for the positive fit is defined as

$$\frac{1}{2}f\underbrace{(1+0.3\cos\theta_\ell)}_{\text{Positive Template}}+(1-f)\times\underbrace{(1/2)}_{\text{Flat Template}}=\frac{1}{2}(1+\alpha_\ell P\cos\theta_\ell), \tag{4.11}$$

[8]The number of events in the signal $t\bar{t}$ templates are allowed to float.

while the fitting function for the negative fit is defined as

$$\frac{1}{2}f\underbrace{(1-0.3\cos\theta_\ell)}_{\text{Negative Template}}+(1-f)\times\underbrace{(1/2)}_{\text{Flat Template}}=\frac{1}{2}(1+\alpha_\ell P\cos\theta_\ell). \tag{4.12}$$

After performing the positive and negative fits, a χ^2 fit of the results to the data is performed. The fit with the lowest value of χ^2/NDF, indicating the best fit, is taken as the proper fit result. Appendix D.1 details a study performed using a toy model to compare the results of the normal and positive/negative fit results; both methods were shown to give the same result. However, Appendix D.2 details a comparison of results between the two methods using the data and templates for this analysis; the results of the two methods do not agree in this case. A more robust study should be performed to determine the origin of the disagreement between the two methods.

For each channel (e+jets and μ+jets), charge separated templates are produced for the CPC and CPV scenarios. The binned maximum likelihood fit is performed for each template by calculating the number of events in each bin and comparing the expectation to the number of events observed. The likelihood function is given by

$$\mathcal{L}=\prod_{i=1}^{bins}\mathcal{P}(n_i,m_i), \tag{4.13}$$

where $\mathcal{P}$ is the Poisson probability to observe n events when m are expected. The number of events predicted for each bin is the sum of the predicted background and the expected number of $t\bar{t}$ events, which is a function of f, given by

$$m\left(t\bar{t}\right)=f\times m\left(t\bar{t}_{\text{positive template}}\right)+(1-f)\times m\left(t\bar{t}_{\text{negative template}}\right). \tag{4.14}$$

Minuit [76] is used to maximize Eq. (4.13) as a function of f and the $t\bar{t}$ cross section. To obtain a result for the combined charges in the e+jets or μ+jets channel, the likelihoods

are multiplied and maximized; similarly, to obtain the combined ℓ+jets result, the likelihoods of the e+jets and μ+jets channels are multiplied and maximized. This method was tested for any biases by conducting a linearity test. Templates representing true values of f between -1 and 2, in steps of 0.1, were generated and each truth template was fit to an ensemble of 1,000 pseudo datasets. For each fit, the mean of the measured f's was plotted against the true f, with only statistical fluctuations taken into account during the test. The resulting linear fit can be found in Fig. 4.29, where no bias in the maximum binned likelihood fit was found.

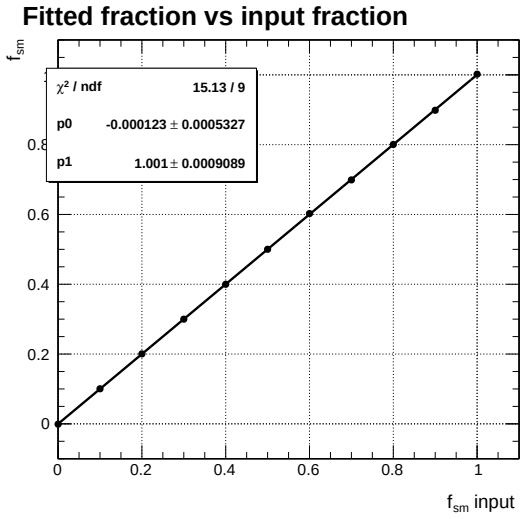

Figure 4.29.: Linear test using the measured f as a function of true f.

Having extracted f from the binned maximum likelihood fit, it is translated into $\alpha_\ell P$ using the equation

$$\alpha_\ell P = 0.6f - 0.3, \tag{4.15}$$

which was derived from Eq. (4.10). The effect of reweighting on the fitting method was also tested using signal templates with varying values of $|\alpha_\ell P|$ ranging from 0.1 to 0.25.

The difference in the results using those values and the central value result, which used $|\alpha_\ell P| = 0.3$, is on the order of 10^{-4}, an order of magnitude below the uncertainties.

Each source of systematic uncertainty is evaluated with two new templates corresponding to the one standard deviation up and down variations. The systematic uncertainty for a given source is quoted as the mean of the distribution of the difference between the central value result and the results from the fit of the up and down templates to 1,000 pseudo-datasets. Systematic uncertainties from the same source are treated as correlated when combined charge or combined channel results are calculated.

Chapter 5.

Results

This chapter discusses the sources of systematic uncertainty and presents the fitted results of $\alpha_\ell P$ in the CPC and CPV scenarios. The results are then compared to the SM and BSM predictions.

5.1. Systematics

For this analysis, systematic uncertainties may be attributed to two causes: assumptions made in the estimation of the $t\bar{t}$ signal and background, whether it be from MC simulation or from data-driven techniques, and intrinsic uncertainties from the detector and reconstruction. This section will illuminate the sources of systematic uncertainty and the determination of their effect on the final result.

As stated in Section 4.5, each source of systematic uncertainty is evaluated with two new templates corresponding to the $\pm 1\sigma$ variations. One thousand pseudo experiments are conducted for each template variation with the difference between the central value fit and the PE fit binned into a histogram. The systematic uncertainty is quoted as the mean of the distribution of those differences for that particular variation. The up and down variation templates that are formed from uncertainties evaluated by the difference

between two points are symmetrized about the nominal value. Systematic uncertainties from the same source are treated as correlated when combined charge or combined channel results are calculated.

Unless noted otherwise, the sources of systematic uncertainty and their prescriptions are standard within the ATLAS Top Working Group and are well documented in [77]

5.1.1. Signal and Background Modeling

The uncertainty inherent in the parameters used to generate MC or to determine background contributions from data driven techniques leads to systematic uncertainty in the final measurement; this section expounds the sources of systematic uncertainty for $t\bar{t}$ and background modeling.

$t\bar{t}$ modeling

The systematic uncertainty in the modeling of the signal $t\bar{t}$ MC is broken down into seven categories:

- **MC Generator:** The systematic uncertainty from the choice of MC generator is determined by comparing the results between the default sample that uses the MC@NLO generator and a sample that uses the POWHEG [78] generator, both of which are interfaced to HERWIG for parton shower and underlying event modeling.
- **Parton Shower/Fragmentation:** The systematic uncertainty from the choice of parton shower/fragmentation model is determined by comparing the results from two different samples generated by POWHEG, one of which is interfaced to HERWIG, the other to PYTHIA.

- **ISR/FSR:** The systematic uncertainty due to the modeling of initial/final state radiation (ISR/FSR) is determined by comparing the results from two dedicated samples generated with AcerMC and interfaced to PYTHIA. The PYTHIA parameters that are responsible for steering the parton shower activity are tuned in each sample to produce more or less ISR/FSR activity, with the ISR constrained by the ATLAS measurement of $t\bar{t}$ production with a veto on central jet activity in pp collisions [79].

- **Color Reconnection:** The systematic uncertainty from the modeling of color reconnection (CR) is evaluated by comparing the results between samples generated with AcerMC and interfaced to PYTHIA; each sample uses a set of dedicated PYTHIA tunes for CR.

- **Underlying Event:** The systematic uncertainty from the modeling of the underlying event (UE) is evaluated by comparing the results between two samples generated with POWHEG and interfaced with PYTHIA; each sample is tuned to have 10% more or less UE activity than the central tune (charged particle multiplicity, average leading jet p_{T}).

- **Top Mass Uncertainty:** The uncertainty in the top mass is evaluated using a non-standard method; signal templates for seven MC@NLO fast simulation $t\bar{t}$ samples, each with varying mass from 165 GeV to 180 GeV, are fit to the data and their values of f plotted against the true mass. The plot is then fit to a line and the uncertainty is quoted as the interpolated change in f along the fitted line, corresponding to a change in mass of $\pm$ 1.4 GeV from the central value of 172.5 GeV. Figure 5.1 shows the fitted values of f as a function of top mass along with the linear fit.

- **Spin Correlation Uncertainty:** The uncertainty in the degree of spin correlation for the reweighting procedure is a non-standard method; the degree of spin correlation

used in the reweighting procedure was varied based on the difference between the spin correlation present in the nominal MC@NLO sample and the POWHEG sample. The difference in spin correlation between the two samples was much larger than the theoretical uncertainty, thus the method is conservative in its approach.

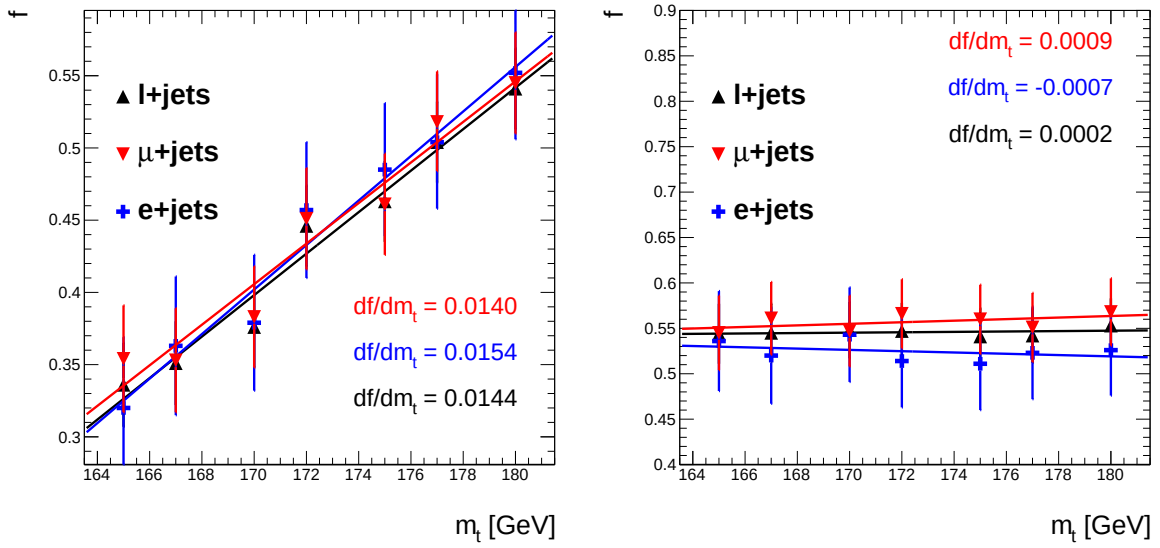

(a) CP Conserving **(b)** CP Violating

Figure 5.1.: The fitted values of f as a function of top quark mass for seven MC@NLO fast simulation $t\bar{t}$ samples, fitted to a linear function. The uncertainty is quoted as the interpolated value of f along the fitted line corresponding to a change in top mass of $\pm$ 1.4 GeV.

W+jets modeling

The largest background in the ℓ+jets channel is the production of a W-boson in association with jets, therefore, it is necessary to evaluate an extensive number of systematic uncertainties for W+jets modeling. As discussed in Section 4.1.2, the W+jets overall normalization is scaled based on ATLAS' charge asymmetry measurement. The systematic uncertainty due to the applied normalization scale factors is evaluated by varying the scale factors by their residual uncertainties. Also, theoretical predictions for the associated

heavy quark flavor (HF) fractions[1] have a large uncertainty, therefore, the shape and normalization of the W+jets template is varied by reweighting events based on those uncertainties. In addition, the normalization and shape of the W+jets template is varied based on the uncertainties of the hard process scale (labeled by iqopt3) and the uncertainty in the threshold for parton production (labeled by ptjmin), both of which are parameters of the simulation of extra jets.

Non-prompt/Fake Leptons modeling

As described in Sections 4.1.3 and 4.2.3, the background from NP/fake leptons is derived from two different matrix methods in the case of the μ+jets channel and a separate matrix method for the e+jets channel. The uncertainty due to the matrix methods in the μ+jets channel is estimated as the difference between the two methods employed. For the e+jets channel, the uncertainty in the matrix method is evaluated by varying the efficiencies of the real and fake electrons (ϵ_{real} and ϵ_{fake}) by their uncertainties and recalculating the event weight.

5.1.2. Detector Modeling Systematic Uncertainty

The systematic uncertainties in detector modeling are related to the determination of the energy/momentum scales, resolution, and efficiencies for electrons, muons, jets, and $E_{\mathrm{T}}^{\mathrm{miss}}$. The reconstructed objects in MC are scaled to agree with the kinematic distributions observed in data; these scale factors are varied, using standard ATLAS Top WG prescriptions, based on their uncertainties to produce systematic templates. This section highlights the important facets of the detector modeling systematic uncertainty for each type of object.

[1] This analysis is particularly sensitive to the relative amount of HF ($Wb\bar{b}$,$Wc\bar{c}$,Wc) since the event selection requires a b-tagged jet.

Charged Leptons

The uncertainty in the charged lepton's (electrons and muons) scale factors relating to their trigger, reconstruction, identification, and momentum scale/resolution are all evaluated individually to produce systematic templates [80–82]. The scale factors and their uncertainties are determined by analyzing charged and neutral current Drell-Yan (DY) processes[2].

Jets

The detector modeling uncertainties for jet reconstruction are divided into four categories: jet energy scale (JES), jet vertex fraction, jet reconstruction efficiency, and jet energy resolution [83, 84]. The 21 components of the JES, each evaluated separately, are determined from p_{T} and η dependent uncertainties derived from LHC data in the lower scale production processes (in situ) and from simulation. This analysis is sensitive to the b-jet JES, which is evaluated separately from the light quark JES. Jet tagging, c-tag, b-tag, and light quark mis-tag, scale factors are varied according to the b-tagging combined performance working group's recommendations.

$\boldsymbol{E}_{\mathbf{T}}^{\mathbf{miss}}$

Each variation in the charged lepton and jet scale factors are propagated to the $E_{\mathrm{T}}^{\mathrm{miss}}$. The uncertainty due to pile-up and to soft jets and calorimeter cells that are not associated with any jets (labeled by cellout) are considered [85].

[2] The neutral current DY process leads to $Z \to \ell\ell$, while the charged current DY process leads to $W \to \ell\nu_{\ell}$.

5.1.3. Other Sources of Systematic Uncertainty

PDF Uncertainty

The systematic uncertainty due to the PDF sets used to model the $t\bar{t}$ signal MC were evaluated using a standard framework [86] that determines the intra- and inter-PDF uncertainties. The intra-PDF uncertainty was calculated using a reweighting procedure that compares the difference in the final result using the nominal CT10 PDF set and results obtained using two different NLO PDF sets, NNPDF 2.0 and MSTW2008, with the largest difference quoted as the inter-PDF uncertainty. The inter-PDF uncertainty is then added in quadrature with the nominal CT10 PDF set intra-PDF uncertainties and quoted as the PDF uncertainty.

Normalization Uncertainty

The $t\bar{t}$ cross section is floated during the fitting procedure, however, the background cross sections are not; therefore, the uncertainty due to the normalization of the background contributions is treated as a systematic. The normalization uncertainty is determined by rescaling the background templates[3] according to a standard prescription and performing a fit using each modified background template separately. The resulting uncertainty for each background is then added in quadrature and quoted as the normalization uncertainty.

Template Statistics Uncertainty

The uncertainty in the template fit due to finite MC statistics is evaluated by performing pseudo experiments on the data. A gaussian function is formed for each bin in the nominal template, with its mean equal to the bin content and its width equal to the

[3]The overall normalization of the template is changed, but their respective shapes remain the same.

statistical uncertainty of the bin content. The bin content of each bin in the nominal template is modified by drawing a new bin content from the gaussian function for that particular bin. The modified template is then fit to the data and the difference between the fit result and the nominal result is then calculated and entered into a histogram. This process is repeated 1,000 times; the resulting histogram forms a gaussian with its width quoted as the template statistics uncertainty.

5.1.4. CPV Combined Charge Systematic Uncertainty

The magnitude of the systematic uncertainties for the combined charge CPV fits are dramatically different from those in the combined charge CPC fits; this section discusses the cause for this discrepancy.

In the CPC scenario, the positive (negative) template retains the same shape for both charges, as depicted in Fig. 5.4; however, in the CPV scenario, the positive template for one charge takes the shape of the negative template for the other charge, which is depicted in Fig. 5.5. In the case of the combined charge CPC fits, if the data agree with the positive template for one charge, it will agree with the positive template for the other charge, resulting in a fitted value of $f > 0$. Conversely, in the case of the combined charge CPV fits, if the data agree with the positive template for one charge, it will agree with the negative template for the other charge, creating tension in the fit and resulting in the fitted value of f to tend towards zero.

The tension in the CPV combined charge fits has a profound effect on its systematic uncertainty, provided that the source of uncertainty is independent of lepton charge. In the event that a source of systematic uncertainty affects ℓ+jets events with positively charged leptons differently than ℓ+jets events with negatively charged leptons, the

positive template for one charge may not have the same shape as the negative template for the other charge, thus reducing the tension in the fit.

To illustrate the effect that charge independent sources of systematic uncertainty have on the charge combined CPV fit, a study was performed on two of the largest uncertainties in the charge combined CPC fit, the JES uncertainty and the b-tag scale factor uncertainty. Figures 5.2 and 5.3 depicts the ratios of the systematically shifted template and the nominal template for both lepton charges; a difference of zero between the ratios of the different charges indicates that the systematic uncertainty is independent of charge, therefore, explaining why the JES and b-tag SF uncertainties were dramatically reduced between the combined charge CPC and CPV fits.

5.1.5. Correlation of Systematics for Combined Channel Fits

All systematics, except for template statistics and Monte Carlo statistics, are treated as being correlated between the e+jets and μ+jets channels in the fitting procedure.

5.1.6. Systematic Uncertainty Results

A summary of the systematic uncertainties for the combined charge ℓ+jets fit are shown in Table 5.1. The major sources of systematic uncertainty come from the jet energy scale, top mass uncertainty, b-tagging scale efficiency, and the NP/fake lepton estimation. Each of the major sources of systematic uncertainty introduce a shape change to the $\cos\theta_\ell$ distribution, to which the fitted result of $\alpha_\ell P$ is sensitive.

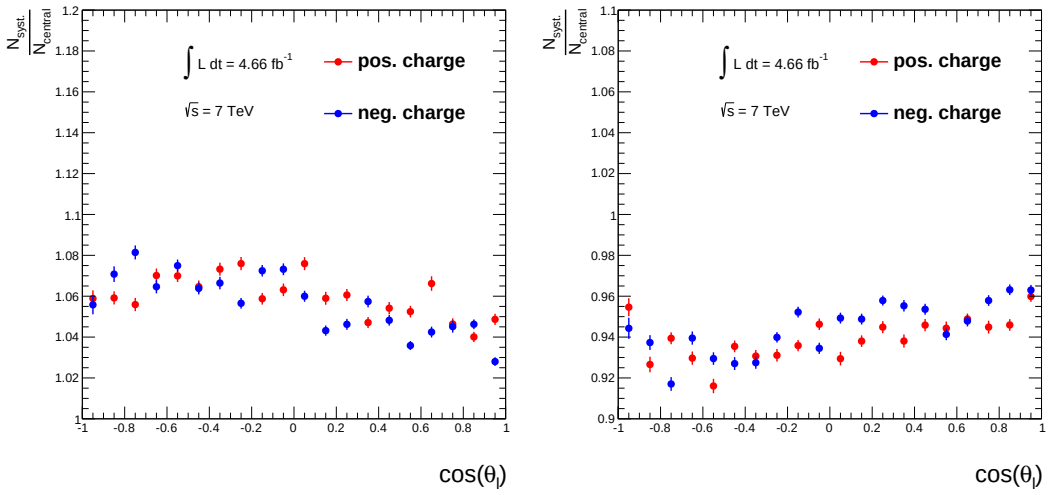

(a) JES Uncertainty Up

(b) JES Uncertainty Down

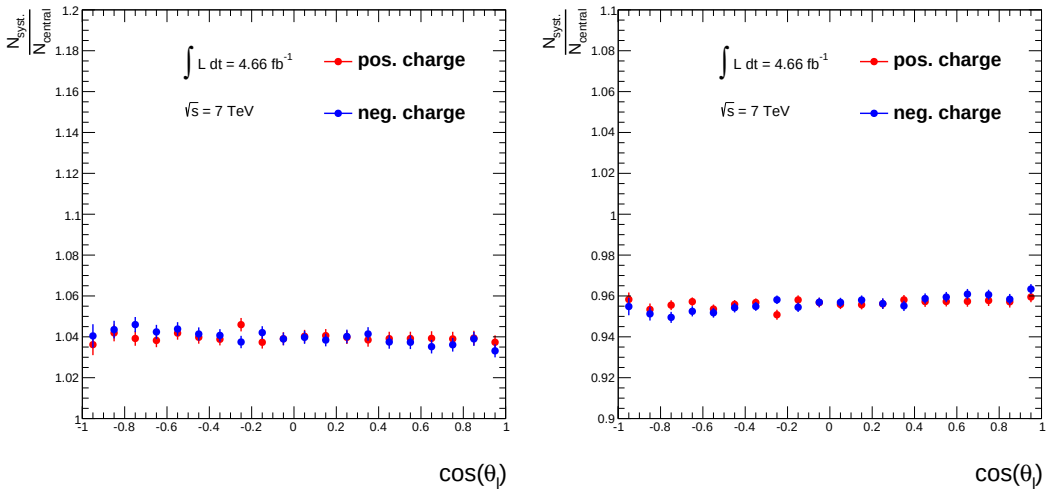

(c) b-Tag SF Uncertainty Up

(d) b-Tag SF Uncertainty Down

Figure 5.2.: e+jets: Ratio of the number of events between the systematically shifted template and the nominal template separated by charge. The small differences between the two charges indicate that the systematic shifts are independent of charge.

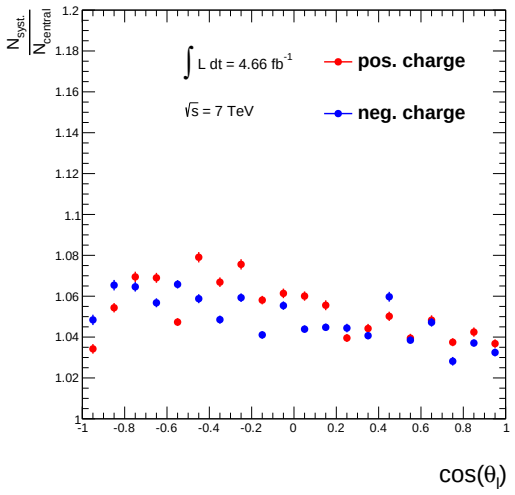

(a) JES Uncertainty Up

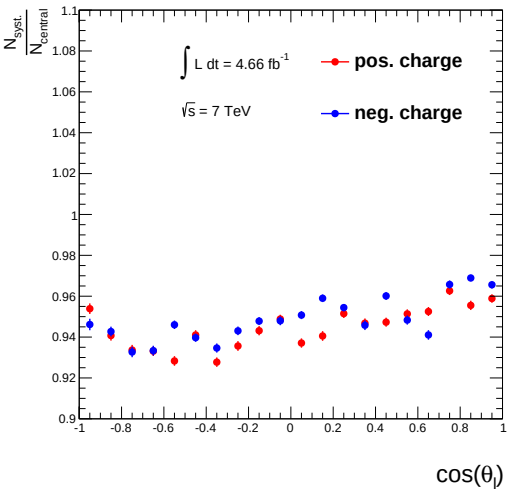

(b) JES Uncertainty Down

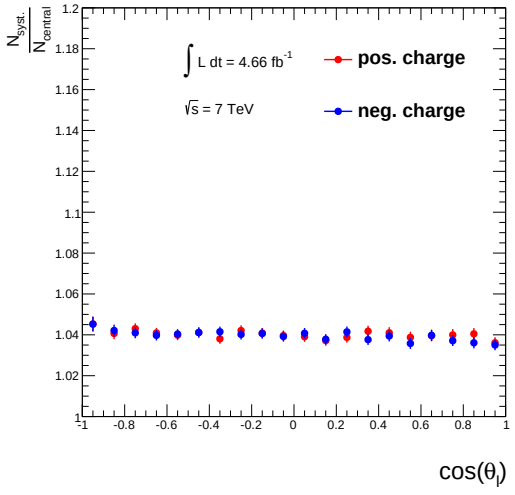

(c) b-Tag SF Uncertainty Up

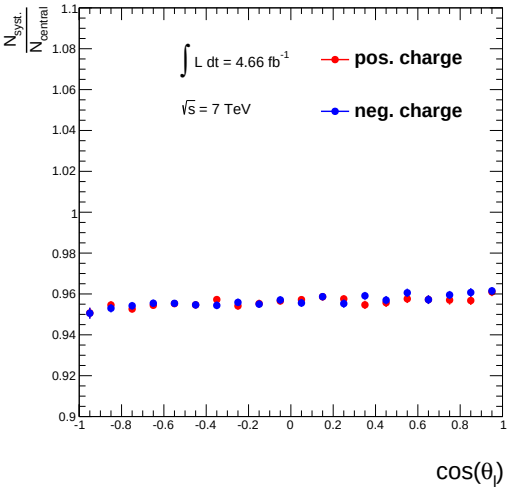

(d) b-Tag SF Uncertainty Down

Figure 5.3.: μ+jets: Ratio of the number of events between the systematically shifted template and the nominal template separated by charge. The small differences between the two charges indicate that the systematic shifts are independent of charge.

Table 5.1.: Summary of the systematic uncertainties on $\alpha_\ell P$. The systematic uncertainties have been added in quadrature to obtain the total systematic uncertainty.

Source	$\Delta\alpha_\ell P_{\text{CPC}}$		$\Delta\alpha_\ell P_{\text{CPV}}$	
Jet Reconstruction	$+0.032$	-0.032	$+0.007$	-0.005
Lepton Reconstruction	$+0.005$	-0.005	$+0.001$	-0.001
$E_{\text{T}}^{\text{miss}}$ Reconstruction	$+0.005$	-0.003	$+0.003$	-0.002
Signal Modeling	$+0.013$	-0.013	$+0.005$	-0.005
Background Modeling	$+0.016$	-0.014	$+0.005$	-0.005
Template Statistical Uncertainty	$+0.006$	-0.006	$+0.007$	-0.007
Total Systematic Uncertainty	$+0.038$	-0.037	$+0.012$	-0.011

5.2. Results

This section contains the results for the fitted values of $\alpha_\ell P$ and $t\bar{t}$ cross section, σ, after conducting the binned maximum likelihood fit described in Section 4.5. Appendix F contains tables presenting a full summary of the systematic uncertainty on the fitted values of $\alpha_\ell P$ and σ for the combined, channel-separated, and charge-separated fits for both the CPC and CPV scenarios. The results for the CPC and CPV scenarios are presented in Sections 5.2.1 and 5.2.2. Section 5.2.4 sets confidence limits for the exclusion of the BSM models described in Section 2.3.4 using the results from the combined charge ℓ+jets CPC fit. The section concludes in Section 5.2.5 with a summary of the results and a discussion of how they relate to the expectation.

5.2.1. CP Conserving Results

The fitted results for $\alpha_\ell P$ and σ for the CPC combined charge fit in the e+jets, μ+jets, and ℓ+jets channels are presented in Table 5.2. The results for the charge separated fits are presented in Tables 5.3 and 5.4. Figure 5.4 depicts the templates, data, and fit result for each channel in the CPC scenario.

Table 5.2.: Summary of the fitted values for $\alpha_\ell P$ and σ for combined charges in the e+jets, μ+jets, and ℓ+jets channels in the CP conserving scenario.

Channel	$\alpha_\ell P$	σ
ℓ+jets CPC	$-0.034^{+0.017}_{-0.017}(\text{stat.})^{+0.038}_{-0.037}(\text{syst.})$	$177.57^{+0.98}_{-0.98}(\text{stat.})^{+26.722}_{-25.342}(\text{syst.})$
e+jets CPC	$-0.031^{+0.028}_{-0.028}(\text{stat.})^{+0.043}_{-0.040}(\text{syst.})$	$174.22^{+1.59}_{-1.59}(\text{stat.})^{+27.626}_{-26.237}(\text{syst.})$
μ+jets CPC	$-0.033^{+0.021}_{-0.021}(\text{stat.})^{+0.040}_{-0.040}(\text{syst.})$	$179.64^{+1.25}_{-1.25}(\text{stat.})^{+26.693}_{-25.380}(\text{syst.})$

Table 5.3.: Summary of the fitted values for $\alpha_\ell P$ and σ for positively charged leptons in the e+jets, μ+jets, and ℓ+jets channels in the CP conserving scenario.

Channel	$\alpha_\ell P$	σ
ℓ+jets pos. CPC	$-0.013^{+0.025}_{-0.025}(\text{stat.})^{+0.050}_{-0.050}(\text{syst.})$	$177.57^{+1.41}_{-1.41}(\text{stat.})^{+34.922}_{-32.800}(\text{syst.})$
e+jets pos. CPC	$-0.030^{+0.041}_{-0.041}(\text{stat.})^{+0.049}_{-0.048}(\text{syst.})$	$174.20^{+2.29}_{-2.27}(\text{stat.})^{+36.876}_{-34.471}(\text{syst.})$
μ+jets pos. CPC	$-0.001^{+0.031}_{-0.030}(\text{stat.})^{+0.059}_{-0.056}(\text{syst.})$	$179.72^{+1.80}_{-1.79}(\text{stat.})^{+34.267}_{-32.368}(\text{syst.})$

5.2.2. CP Violating Results

The fitted results for $\alpha_\ell P$ and σ for the CPV combined charge fit in the e+jets, μ+jets, and ℓ+jets channels are presented in Table 5.5. The sign of $\alpha_\ell P$ in the CPV scenario corresponds to the sign of the coefficient in the angular distribution for the positively charged lepton. The results for the charge separated fits are presented in Tables 5.6 and 5.7. Figure 5.5 depicts the templates, data, and fit result for each channel in the CPV scenario.

Table 5.4.: Summary of the fitted values for $\alpha_\ell P$ and σ for negatively charged leptons in the e+jets, μ+jets, and ℓ+jets channels in the CP conserving scenario.

Channel	$\alpha_\ell P$	σ
ℓ+jets neg. CPC	$-0.053^{+0.023}_{-0.023}(\text{stat.})^{+0.040}_{-0.041}(\text{syst.})$	$177.56^{+1.37}_{-1.36}(\text{stat.})^{+32.188}_{-30.041}(\text{syst.})$
e+jets neg. CPC	$-0.031^{+0.039}_{-0.039}(\text{stat.})^{+0.044}_{-0.040}(\text{syst.})$	$174.23^{+2.22}_{-2.21}(\text{stat.})^{+34.608}_{-32.022}(\text{syst.})$
μ+jets neg. CPC	$-0.064^{+0.029}_{-0.029}(\text{stat.})^{+0.047}_{-0.048}(\text{syst.})$	$179.54^{+1.74}_{-1.73}(\text{stat.})^{+31.113}_{-29.245}(\text{syst.})$

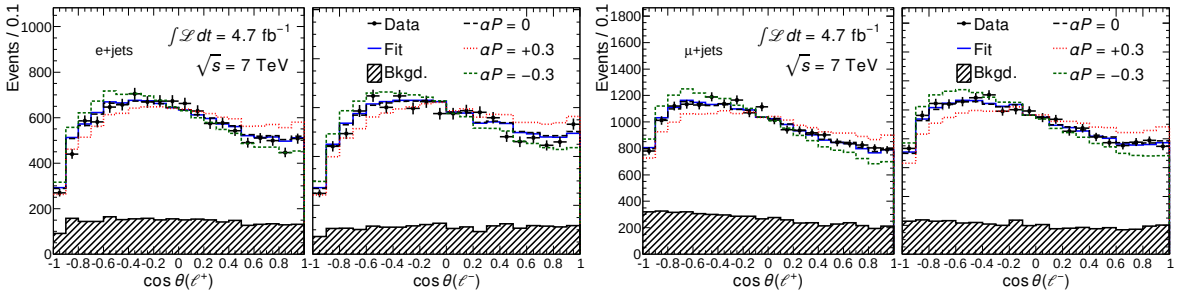

(a) e+jets

(b) μ+jets

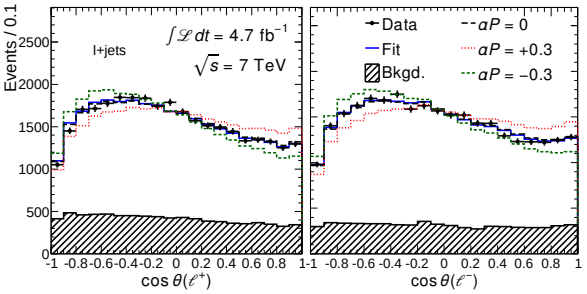

(c) ℓ+jets

Figure 5.4.: Result of the CP conserving fit (blue) for $\cos\theta_\ell$ in comparison to data and the templates for the e+jets, μ+jets, and ℓ+jets channels. Positive (left) and negative (right) leptons are shown in the same histogram, which is indicated by the superscript $+$ and $-$ in the axis label.

Table 5.5.: Summary of the fitted values for $\alpha_\ell P$ and σ for combined charges in the e+jets, μ+jets, and ℓ+jets channels in the CP violating scenario.

Channel	$\alpha_\ell P$	σ
ℓ+jets CPV	$0.023^{+0.019}_{-0.019}(\text{stat.})^{+0.012}_{-0.011}(\text{syst.})$	$177.11^{+0.95}_{-0.95}(\text{stat.})^{+26.636}_{-25.283}(\text{syst.})$
e+jets CPV	$0.001^{+0.031}_{-0.031}(\text{stat.})^{+0.019}_{-0.019}(\text{syst.})$	$173.74^{+1.53}_{-1.52}(\text{stat.})^{+27.496}_{-26.090}(\text{syst.})$
μ+jets CPV	$0.036^{+0.023}_{-0.023}(\text{stat.})^{+0.018}_{-0.017}(\text{syst.})$	$179.24^{+1.22}_{-1.22}(\text{stat.})^{+26.635}_{-25.374}(\text{syst.})$

Table 5.6.: Summary of the fitted values for $\alpha_\ell P$ and σ for positively charged leptons in the e+jets, μ+jets, and ℓ+jets channels in the CP conserving scenario.

Channel	$\alpha_\ell P$	σ
ℓ+jets pos. CPV	$-0.017^{+0.026}_{-0.026}(\text{stat.})^{+0.053}_{-0.053}(\text{syst.})$	$177.52^{+1.39}_{-1.38}(\text{stat.})^{+31.320}_{-30.022}(\text{syst.})$
e+jets pos. CPV	$-0.041^{+0.044}_{-0.044}(\text{stat.})^{+0.057}_{-0.055}(\text{syst.})$	$174.15^{+2.24}_{-2.23}(\text{stat.})^{+32.463}_{-31.183}(\text{syst.})$
μ+jets pos. CPV	$0.000^{+0.033}_{-0.033}(\text{stat.})^{+0.058}_{-0.058}(\text{syst.})$	$179.71^{+1.77}_{-1.76}(\text{stat.})^{+31.190}_{-29.969}(\text{syst.})$

Table 5.7.: Summary of the fitted values for $\alpha_\ell P$ and σ for negatively charged leptons in the e+jets, μ+jets, and ℓ+jets channels in the CP conserving scenario.

Channel	$\alpha_\ell P$	σ
ℓ+jets neg. CPV	$0.060^{+0.026}_{-0.026}(\text{stat.})^{+0.046}_{-0.045}(\text{syst.})$	$177.27^{+1.34}_{-1.34}(\text{stat.})^{+28.599}_{-27.199}(\text{syst.})$
e+jets neg. CPV	$0.041^{+0.043}_{-0.043}(\text{stat.})^{+0.047}_{-0.050}(\text{syst.})$	$174.12^{+2.17}_{-2.16}(\text{stat.})^{+30.025}_{-28.533}(\text{syst.})$
μ+jets neg. CPV	$0.068^{+0.032}_{-0.032}(\text{stat.})^{+0.052}_{-0.050}(\text{syst.})$	$179.17^{+1.72}_{-1.71}(\text{stat.})^{+28.138}_{-26.831}(\text{syst.})$

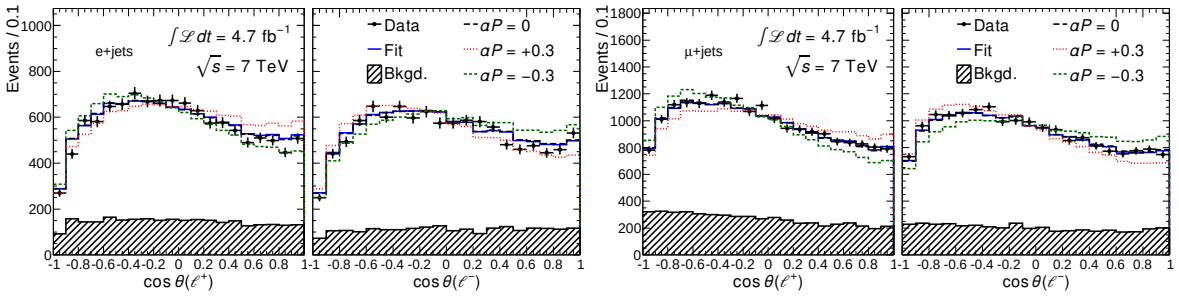

(a) e+jets **(b)** μ+jets

(c) ℓ+jets

Figure 5.5.: Result of the CPV fit (blue) for $\cos\theta_\ell$ in comparison to data and the templates for the e+jets, μ+jets, and ℓ+jets channels. Positive (left) and negative (right) leptons are shown in the same histogram, which is indicated by the superscript + and − in the axis label.

5.2.3. Additional Study of Results

Two short studies were performed to get an idea of how well the binned maximum likelihood fit performed. Figure 5.6 shows the log likelihood values for the combined

charge ℓ+jets CPC fit as a function of the fit parameters, the fraction of positive polarization f and the $t\bar{t}$ cross section σ. In addition, Fig. 5.7 shows the 1, 2, and 3 σ contour plots of the fit parameters f and the $t\bar{t}$ cross section.

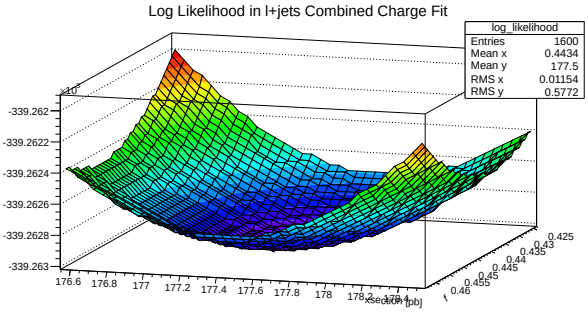

Figure 5.6.: Values of the log likelihood as a function of the fit parameters f and σ for the combined charge ℓ+jets CPC fit.

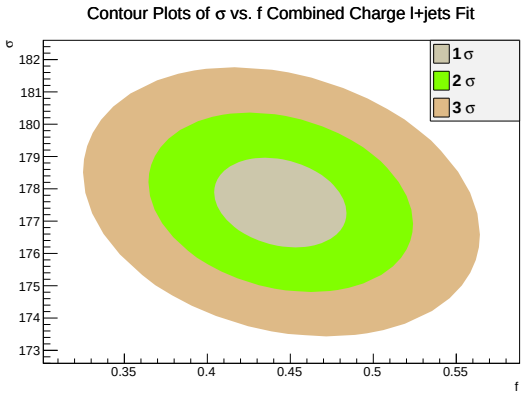

Figure 5.7.: The 1, 2, and 3 σ contours for the fit parameters of the combined charge ℓ+jets CPC fit.

5.2.4. Comparison of results to BSM predictions

The results of $\alpha_\ell P$ from the combined charge CPC ℓ+jets fit were used to set limits on some of the BSM models discussed in Section 2.3.4. The $1-\alpha$ confidence level (CL) was determined for the exclusion of the BSM models given the ℓ+jets result. Table 5.8 lists the $1-\alpha$ CL for the exclusion of the BSM models given the combined charge CPC ℓ+jets result.

Model	Predicted $\alpha_\ell P$	$1-\alpha$	Exclusion Level
NP_C	$0.538 \pm 4\%$	$1.0 - 2.89 \times 10^{-34}$	$\approx 100\%$
G_A	$0.01 \pm 1.2\%$	0.7095	70.95%
G_L	$-0.01 \pm 1.2\%$	0.43574	43.57%
G_R	$0.04 \pm 1.2\%$	0.9245	92.45%
W'	$0.18 \pm 1.2\%$	$1.0 - 2.84 \times 10^{-7}$	$\approx 100\%$

Table 5.8.: Summary of the $1-\alpha$ CL for the exclusion of each of the BSM models discussed in Section 2.3.4 given the combined charged CPC result in the ℓ+jets channel ($\alpha_\ell P = -0.034^{+0.017}_{-0.017}(\text{stat.})^{+0.038}_{-0.037}(\text{syst.})$). Predicted values for $\alpha_\ell P$ in the helicity basis for each model at the LHC operating at $\sqrt{s} = 7$ TeV are also reported.

The NP_C and W' models can be excluded by the combined charge ℓ+jets CPC result at an almost certain level. The right handed axigluon model has been excluded at less than the 2σ level, while the purely axial axigluon model has been excluded at approximately the 1σ level. The left handed axi gluon model is excluded at less than the 1σ level.

5.2.5. Results Summary

The results for the e+jets, μ+jets, and ℓ+jets channels in the CPC and CPV scenarios are summarized and compared to the SM expectation in Table 5.9. The difference in magnitudes of the CPC and CPV uncertainties are explained in Section 5.1.4. The results agree with the SM prediction within the uncertainties. In addition, the fitted $t\bar{t}$ cross sections listed in Sections 5.2.1 and 5.2.2 are in agreement with the NNLO+NNLL SM prediction of $172.0^{+4.4,+4.7}_{5.8,-4.8}$pb for the LHC operating at $\sqrt{s} =$ 7 TeV [4]. The first uncertainty in the prediction of the $t\bar{t}$ production is from scale dependence and the second is from parton distribution functions.

Table 5.9.: Summary of fitted $\alpha_\ell P$ in the e+jets, μ+jets, and ℓ+jets channels for the CP conserving and CP violating fits compared to expectation. The uncertainties quoted are first statistical and then systematic.

Channel	$\alpha_\ell P_{\mathrm{CPC}}$	$\alpha_\ell P_{\mathrm{CPV}}$
e+jets	$-0.031 \pm 0.028^{+0.043}_{-0.040}$	$0.001 \pm 0.031^{+0.019}_{-0.019}$
μ+jets	$-0.033 \pm 0.021^{+0.039}_{-0.039}$	$0.036 \pm 0.023^{+0.018}_{-0.017}$
ℓ+jets	$-0.034 \pm 0.017^{+0.038}_{-0.037}$	$0.023 \pm 0.019^{+0.012}_{-0.011}$
SM Prediction	0.003	0.0

The result from the combined charge ℓ+jets CPC fit was also used to set confidence limits on the exclusion of BSM models that predict longitudinally polarized top quarks in top-antitop quark pair production. The W' and N_{PC} models were excluded at over a 5σ confidence level.

There are three main issues that make this a difficult and challenging analysis: it is systematically limited, it is difficult to reconstruct the $t\bar{t}$ system accurately and efficiently, and the MC available to the analyzers does not include longitudinally polarized top quarks in $t\bar{t}$ production. The issue of systematics will get better with detailed studies. For instance, an analyzer that worked on this analysis was able to reduce a portion of the Jet Energy Scale uncertainty after having performed a study that revealed the method was overestimating the systematic effect. In terms of the kinematic reconstruction of the $t\bar{t}$ system, one option that may improve the method would be to change the selection requirements for signal events, such as requiring the number of b-tags to be equal to two. As for the MC issue, there are many ways to work around it, such as the reweighting technique described in this thesis. One could also employ an unfolding technique to obtain their observable.

The study of top quark properties offers analyzers the opportunity to study new and interesting physics. One of the most promising topics to cover might be the transverse polarization of the top quark. As mentioned before, calculations show that QCD

absorptive parts in the strong production of $t\bar{t}$ give rise to a transverse polarization of the top and antitop quark [40–42].

In conclusion, a measurement of the longitudinal polarization of the top quark in $t\bar{t}$ events in the lepton plus jets final state, considering a CP conserving and maximally CP violating scenario, has been performed with 4.7 fb^{-1} of proton-proton collision data at $\sqrt{s} = 7$ TeV collected by the ATLAS detector at the LHC. The e+jets, μ+jets, and ℓ+jets channels were analyzed and no deviation from the SM prediction of negligible polarization in the CPC and CPV cases was detected.

Appendix A.

Data and MC Comparison Appendix

This appendix continues to show the kinematic distributions for the comparison of data to expectation that was discussed in Appendix A.1, as well as comparisons from the control region with no b-tagged jets.

A.1. Data and MC Comparison

A.1.1. Signal Region

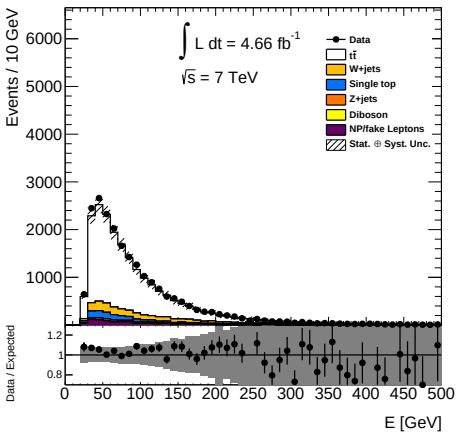

(a) electron energy

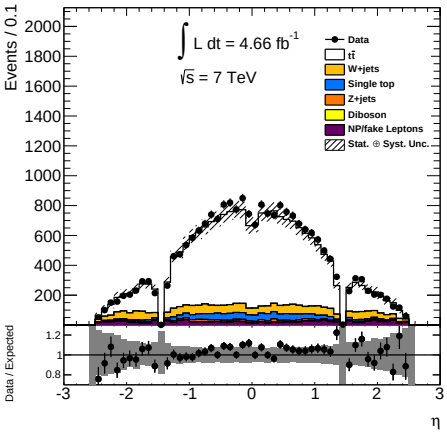

(b) electron η

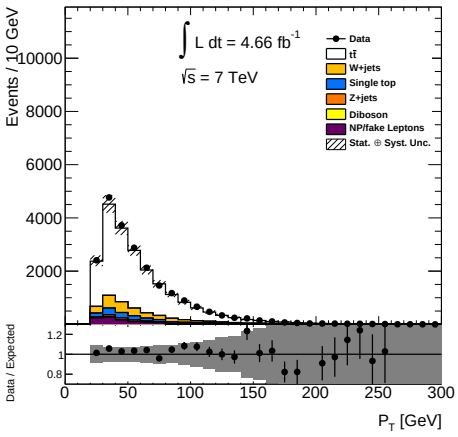

(c) electron p_{T}

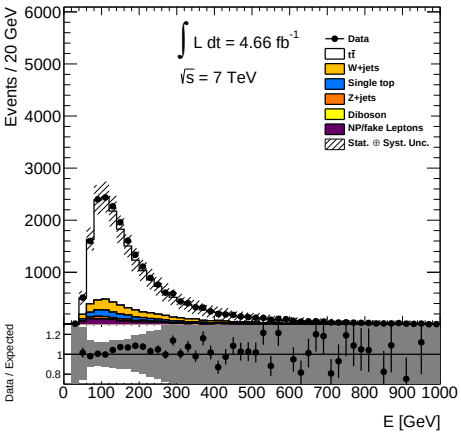

(d) leading jet energy

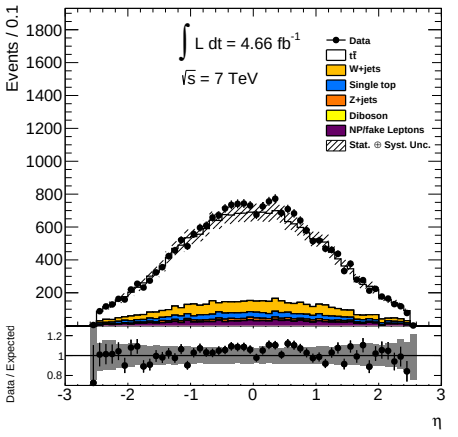

(e) leading jet η

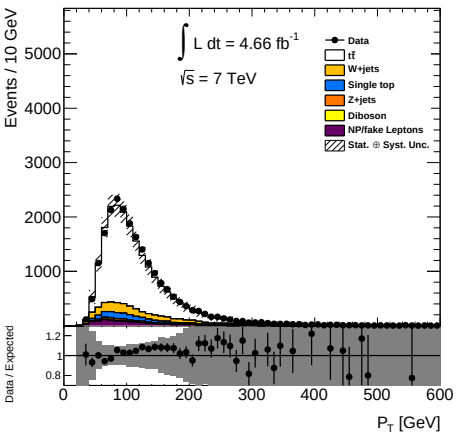

(f) leading jet p_{T}

Figure A.1.: Kinematic distributions for the electron channel, including the ratio of the data to the expectation.

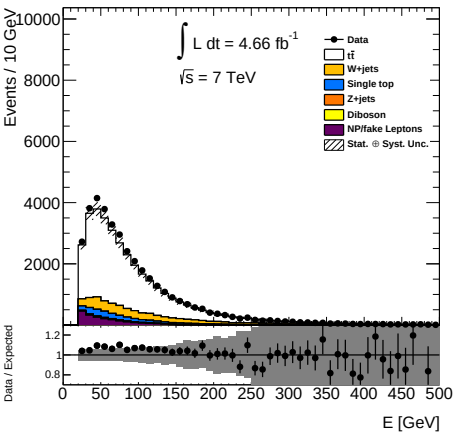

(a) muon energy

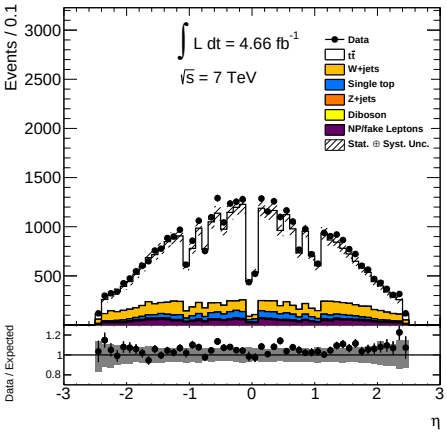

(b) muon η

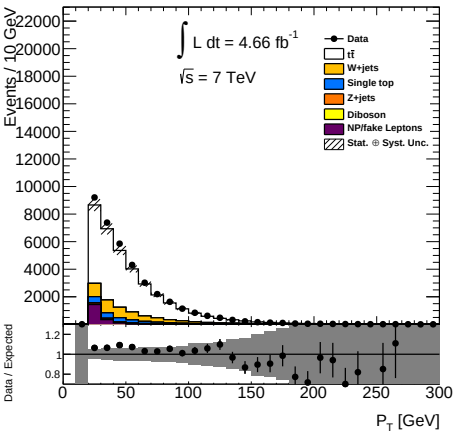

(c) muon p_{T}

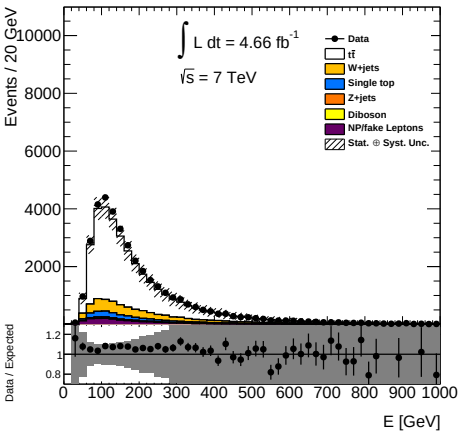

(d) leading jet energy

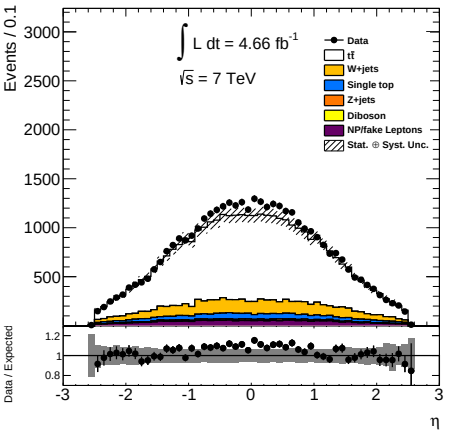

(e) leading jet η

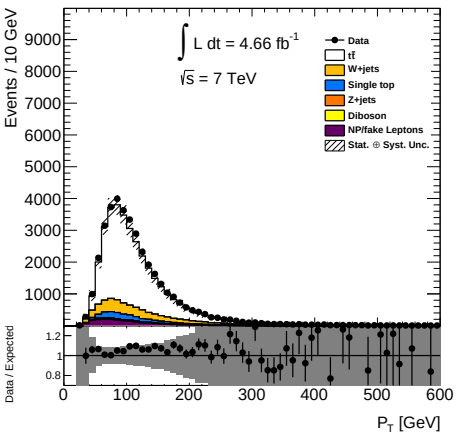

(f) leading jet p_{T}

Figure A.2.: Kinematic distributions for the muon channel, including the ratio of the data to the expectation.

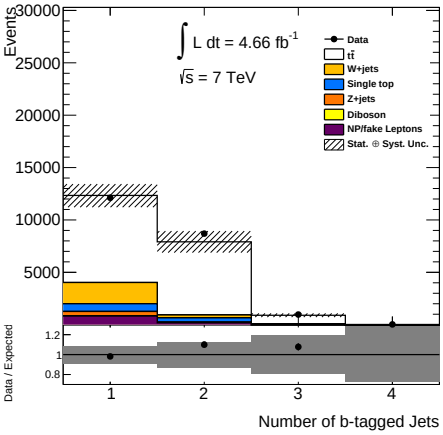

(a) Number of b-tagged jets

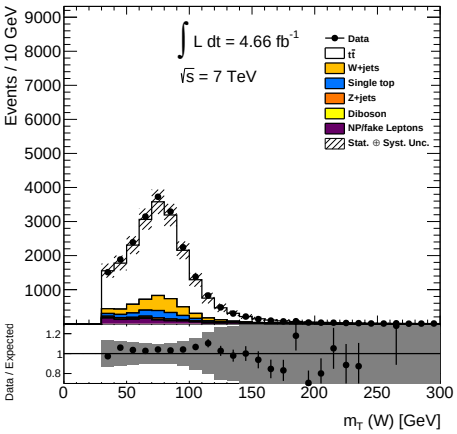

(b) m_{T}

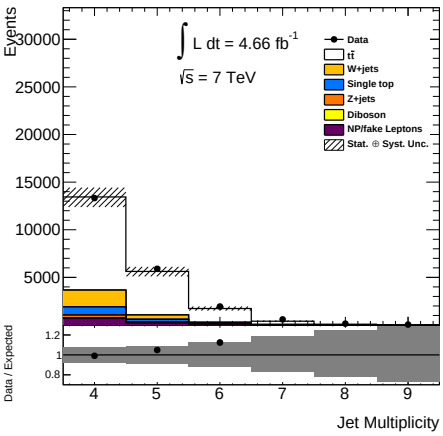

(c) Number of jets

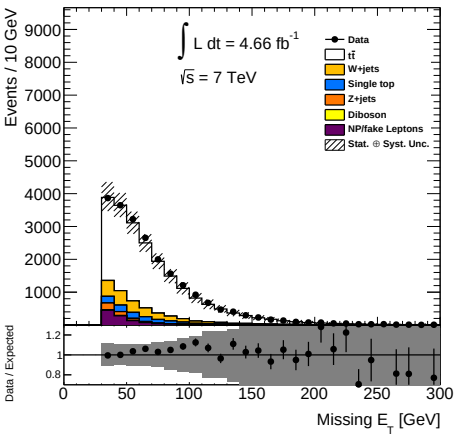

(d) $E_{\mathrm{T}}^{\mathrm{miss}}$

Figure A.3.: Event distributions for the electron channel, including the ratio of the data to the expectation.

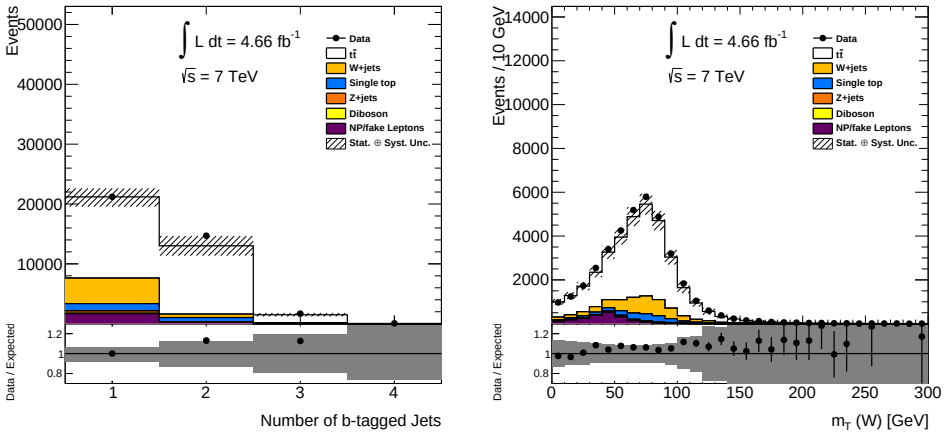

(a) Number of b-tagged jets **(b)** m_{T}

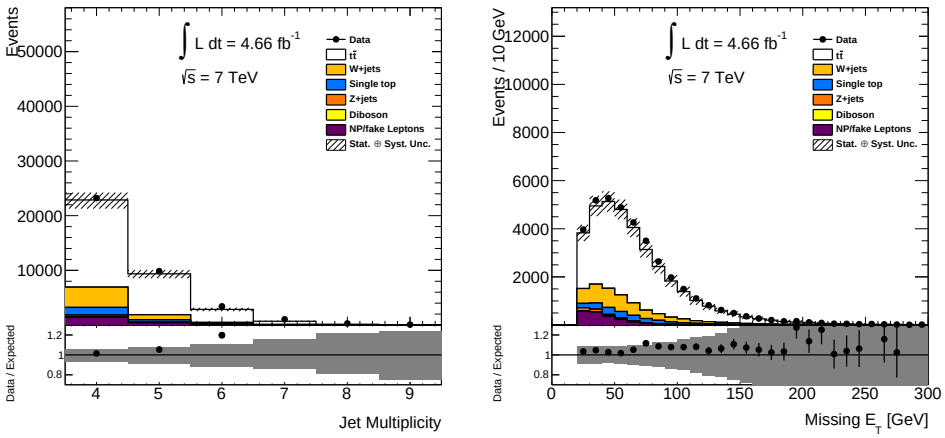

(c) Number of jets **(d)** $E_{\mathrm{T}}^{\mathrm{miss}}$

Figure A.4.: Event distributions for the muon channel, including the ratio of the data to the expectation.

A.1.2. Control Region with no b-tagged jets

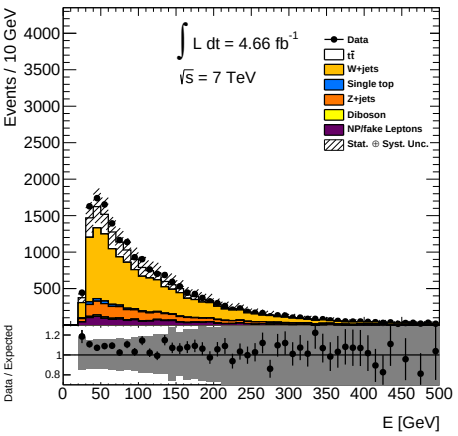

(a) electron energy

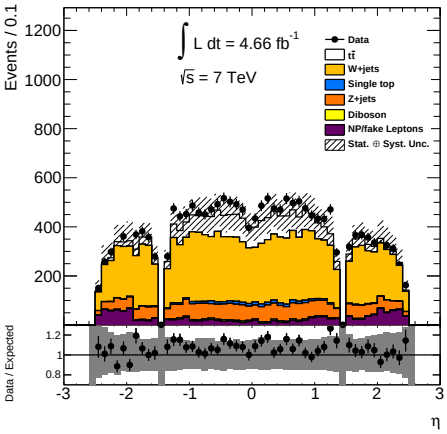

(b) electron η

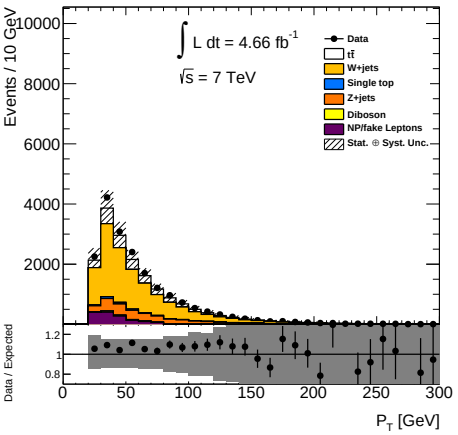

(c) electron p_{T}

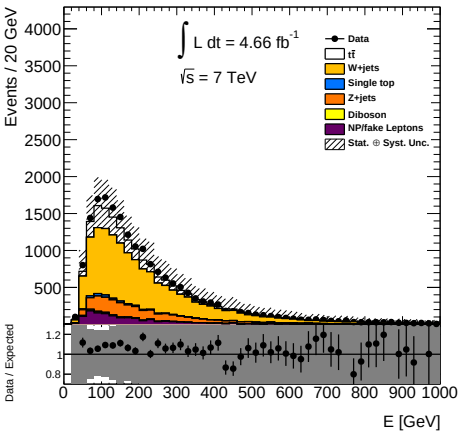

(d) leading jet energy

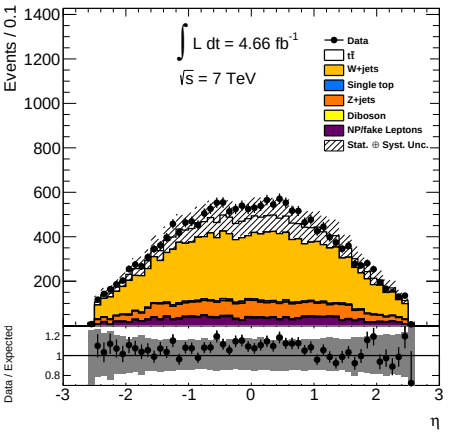

(e) leading jet η

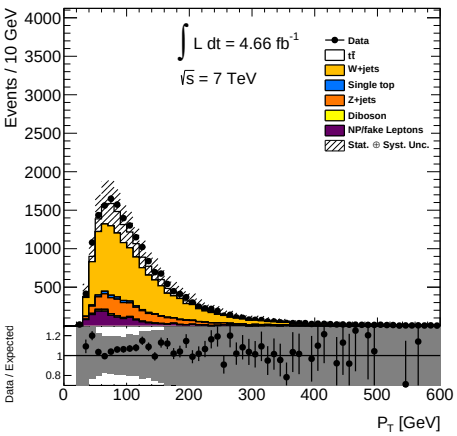

(f) leading jet p_{T}

Figure A.5.: Kinematic distributions for the electron channel, including the ratio of the data to the expectation.

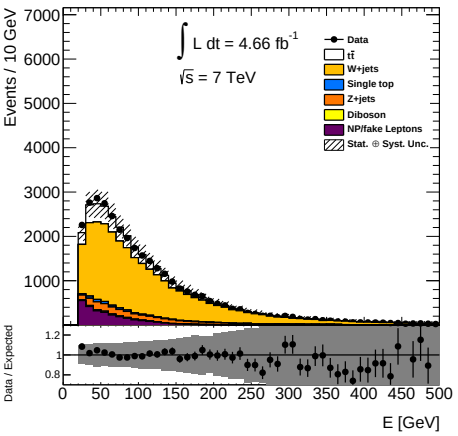

(a) muon energy

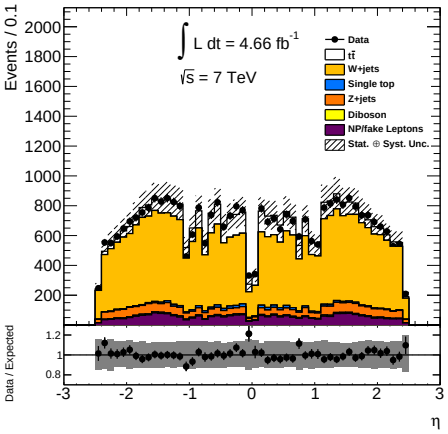

(b) muon η

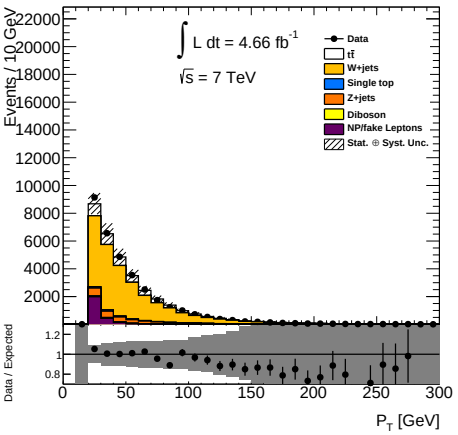

(c) muon p_{T}

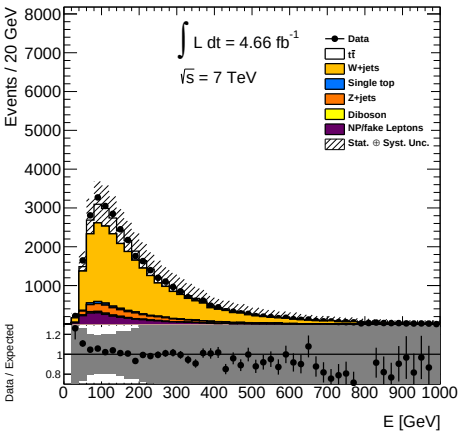

(d) leading jet energy

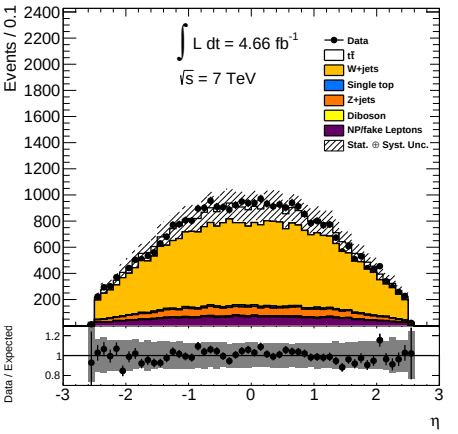

(e) leading jet η

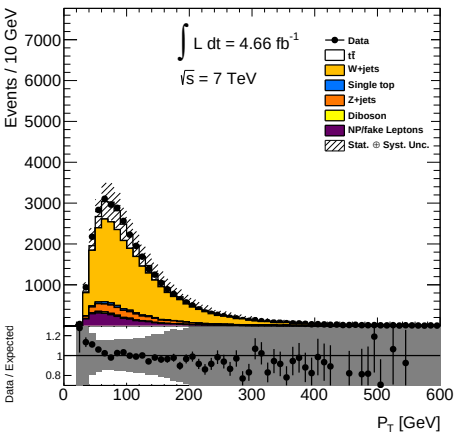

(f) leading jet p_{T}

Figure A.6.: Kinematic distributions for the muon channel, including the ratio of the data to the expectation.

Appendix B.

Kinematic Fitter Data and MC Comparison Appendix

This appendix continues to show comparisons of the data to expectation for the kinematic fitters output that was discussed in Section 4.3.1, as well as comparisons from the control region with no b-tagged jets.

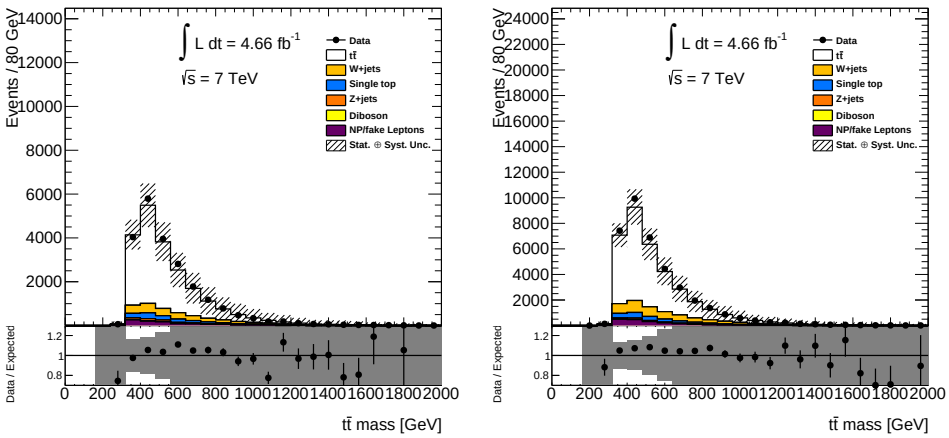

(a) Electron Channel **(b)** Muon Channel

Figure B.1.: Comparison of the fitted mass of the $t\bar{t}$ system between data and expectation in the e+jets and μ+jets channels.

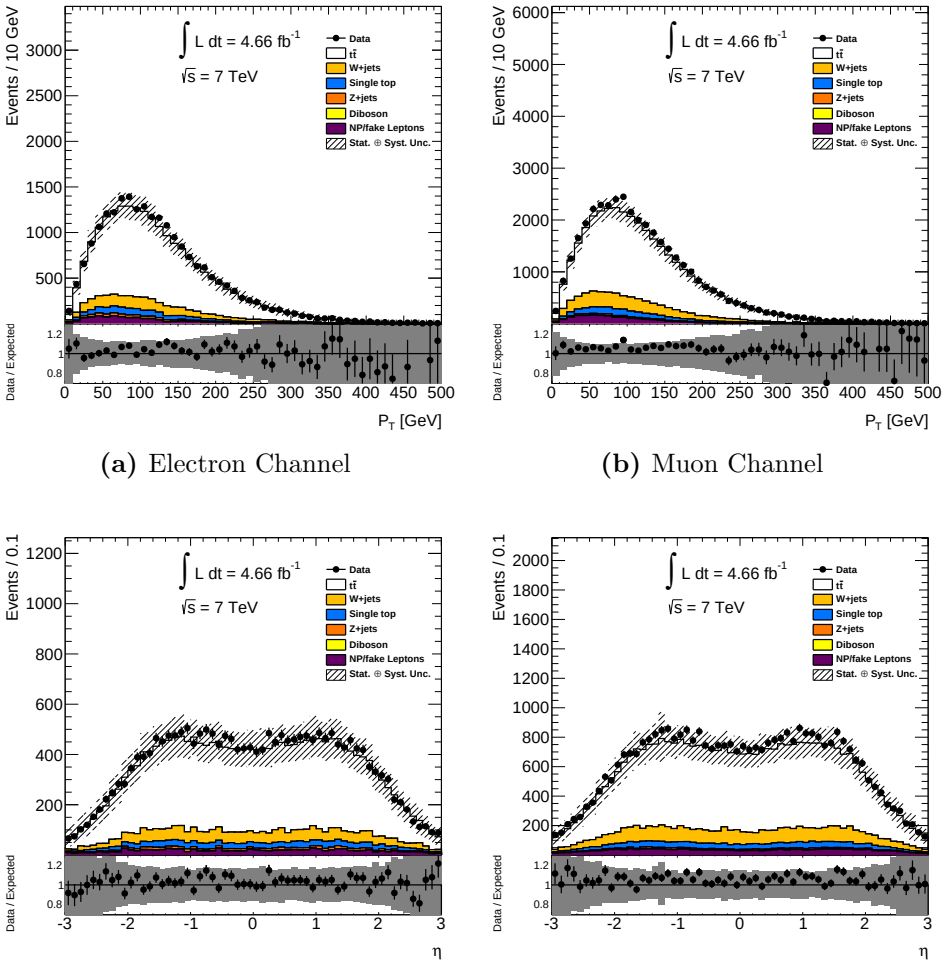

(a) Electron Channel **(b)** Muon Channel

(c) Electron Channel **(d)** Muon Channel

Figure B.2.: Comparison of hadronically decaying top quark's p_{T} and η between data and expectation in the e+jets and μ+jets channels.

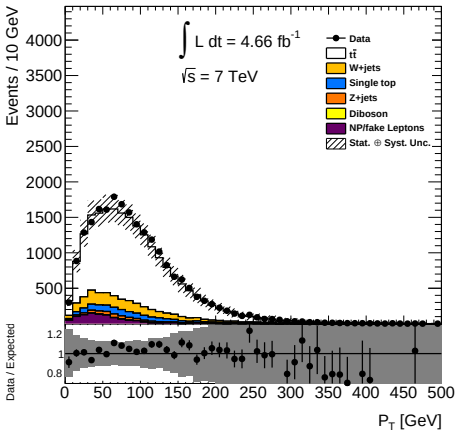

(a) Electron Channel

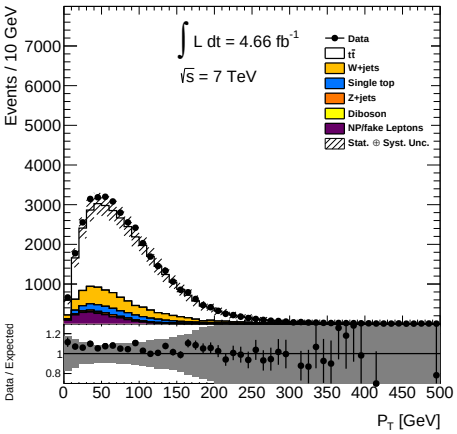

(b) Muon Channel

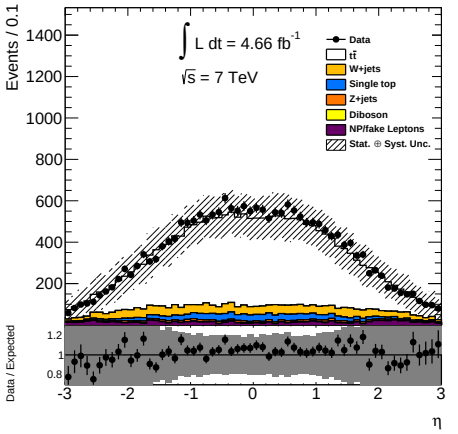

(c) Electron Channel

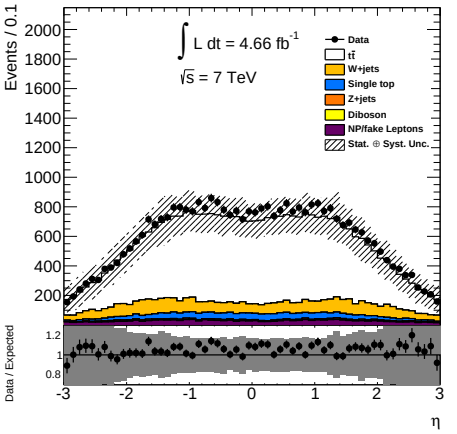

(d) Muon Channel

Figure B.3.: Comparison of leptonically decaying W's p_{T} and η between data and expectation in the e+jets and μ+jets channels.

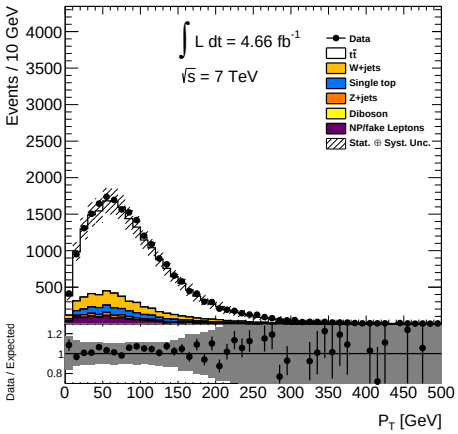

(a) Electron Channel

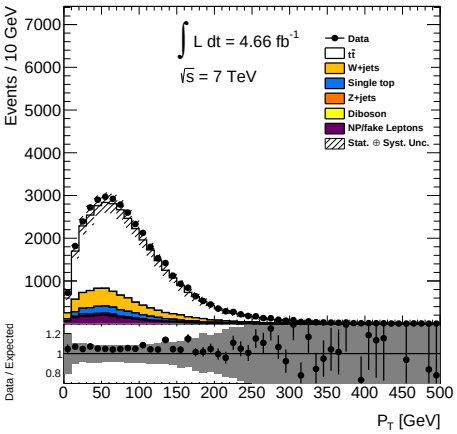

(b) Muon Channel

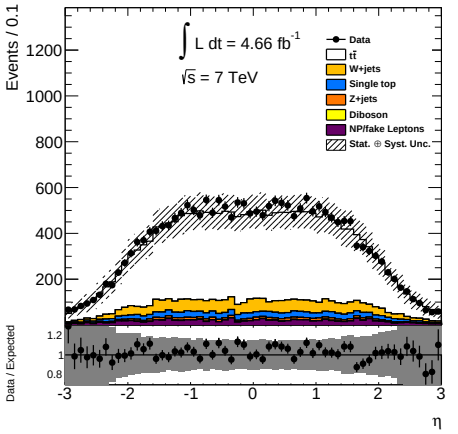

(c) Electron Channel

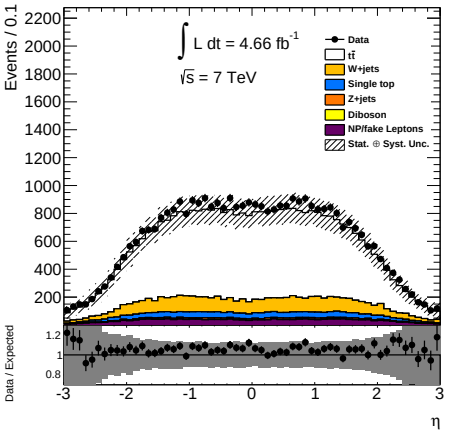

(d) Muon Channel

Figure B.4.: Comparison of hadronically decaying W's p_{T} and η between data and expectation in the e+jets and μ+jets channels.

Appendix C.

Reweighting Appendix

This appendix serves the purpose of motivating and validating the evolution of the reweighting procedure from the preliminary analysis [50] to this analysis [51]. It elucidates the necessity to reformulate the preliminary analysis' reweighting procedure due to spin correlation effects. By accounting for spin correlation effects, the refined reweighting technique is able to produce the correct truth level polar angle distributions for each $t\bar{t}$ decay product. In addition, Appendix C.0.6 demonstrates that the templates used in the preliminary results are consistent with templates generated using the technique described in Section 4.4, validating the method used for the preliminary result.

C.0.3. Reweighting Study

The following sections contain a study on the effects of reweighting $t\bar{t}$ MC to produce longitudinal polarization of top quarks in $t\bar{t}$ production. Standard MC@NLO $t\bar{t}$ MC, which is used as the signal MC for this analysis, is generated with unpolarized top quarks. At the moment, MC containing polarized top quarks is unavailable, therefore, it is necessary to generate polarization in the MC available, to generate polarized templates for a template fit. The preliminary measurement's event weights were based off of the differential decay width, given by[27]:

$$\frac{1}{\Gamma}\frac{d\Gamma}{d\cos\theta_i} \propto 1 + \alpha_i P \cos\theta_i, \tag{C.1}$$

where P represents the degree of polarization along the parent top quark's rest frame, α_i is the spin analyzing power; which is a measure of the sensitivity of the daughter particle to the parent particle's spin state, and $\cos\theta_i$ is the polar angle of one of the top's final state decay products (labeled by i) with respect to the top quark's momentum direction in the $t\bar{t}$ center-of-mass frame. Table C.1 lists the values for the spin analyzing power at tree level for the top's final state decay products.

α_i	Particle Type
1.0	Charged Lepton
1.0	Down and Strange Quarks
-0.4	b Quark
-0.3	Neutrino
-0.3	Up Type Quark

Table C.1.: Values of α_i

This study begins by looking at the ℓ+jets channel to determine the effects of reweighting by looking at how reweighting the MC by the charged lepton's $\cos\theta$ affects the other final state decay products' $\cos\theta$ distributions in the signal MC used for this analysis, the 105200 MC@NLO $t\bar{t}$ sample, which contains spin correlation between the top and antitop. Then, the same study is repeated on the nominal 117200 MC@NLO $t\bar{t}$ sample which does not contain spin correlation. This is followed by studying the effects of reweighting by both the charged lepton's $\cos\theta$ and the down type quark's $\cos\theta$, which will be called weighting by the leptonic and hadronic side of the decay. Having performed these studies, a weight is constructed that accurately produces the predicted polar angle distributions for each of the top quark's final state decay products in the ℓ+jets channel.

These results are confirmed by reproducing this study in the dilepton channel. Finally, a study on the effects of reweighting the MC to produce polarized top quarks in a CP violating scenario is conducted.

C.0.4. Weighting by Leptonic Side

This section describes the reweighting procedure used in the preliminary measurement.

Data Sets Used:

With Spin Correlation

- 115200 MC@NLO $t\bar{t}$ With Spin Correlation (Will be referred to as 105200 MC Sample)

Without Spin Correlation

- 117200 MC@NLO $t\bar{t}$ No Spin Correlation (Will be referred to as 117200 MC Sample)

As stated before, these MC samples do not have polarized top quarks built in, so the truth level distributions of the polar angles of the final state decay products with respect to their parent top quark's momentum direction in the $t\bar{t}$ center-of-mass frame are flat. Figure C.1 shows the charged lepton's polar angle distribution before reweighting.

The first degree polynomial fit to Figure C.1 represents the equation:

$$Constant * (1 + \alpha_i P \cos\theta_i), \tag{C.2}$$

where $p0 = Constant$ and $p1 = \alpha_i P$. The results of the fit show that p1 is consistent with zero, equating to $\alpha_i P = 0$, meaning an unpolarized top quark.

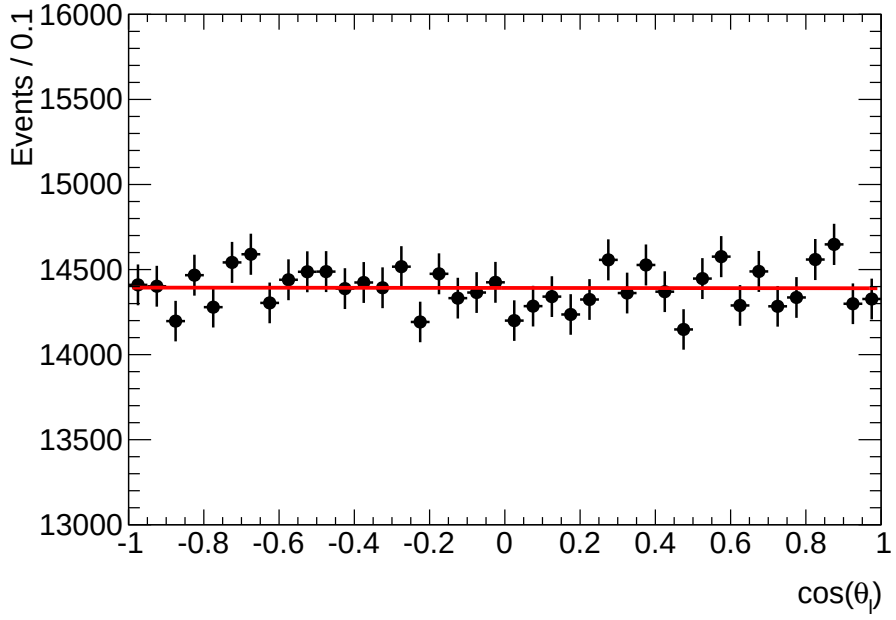

Figure C.1.: Charged lepton's truth level polar angle distribution before reweighting, fit to a first degree polynomial $y = p0\,(1 + p1 \cdot x)$. The fit results are: $p0 = 28790.0 \pm 38.0$ and $p1 = -0.0002 \pm 0.002$.

The method used in the preliminary measurement to produce polarized top quarks in $t\bar{t}$ MC weighted each event by $1 + \cos\theta_\ell$. This will be referred to as weighting by the "leptonic side", producing a maximal positively polarized top quark by setting P equal to +1 and allowing α_ℓ to equal its tree level value of +1. Figure C.2 shows the charged lepton's truth level polar angle distribution after reweighting each event by the leptonic side using the 105200 MC sample. The results of the fit show that p1, corresponding to $\alpha_\ell P$, is consistent with +1, equating to a maximal positively polarized top quark when analyzing the charged lepton's polar angle distribution.

Having verified that the leptonic side reweighting procedure produces the proper value of $\alpha_\ell P$ for the charged lepton's polar angle distribution, we must check that the fits from the other final state decay product's polar angle distributions agree with the predicted $\alpha_i P$. Since only the leptonic side is being reweighted, the hadronically decaying top's final state decay products should show no polarization. However, reweighting by

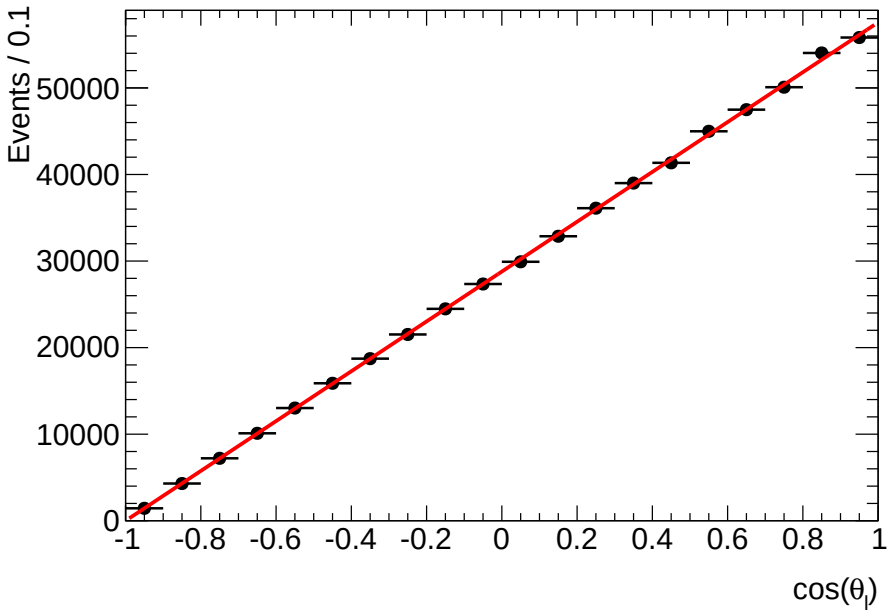

Figure C.2.: Charged lepton's truth level polar angle distribution after reweighting by the leptonic side, fit to a first degree polynomial $y = p0\,(1 + p1 \cdot x)$. The fit results are: $p0 = 28785.0 \pm\ 40.0$ and $p1 = 1.0 \pm\ 0.0003$.

the leptonic side should induce polarization into the neutrino and leptonic b quark's polar angle distributions. Table C.2 shows the predicted and fitted values for the p1, corresponding to $\alpha_i P$, parameter for each truth level final state decay product using the 105200 MC sample.

Particle Type	Predicted p1	Fitted p1
Charged Lepton	1.0	$1.0 \pm\ 0.0003$
Neutrino	-0.3	$-0.35 \pm\ 0.002$
Leptonic b Quark	-0.4	$-0.38 \pm\ 0.002$
Down and Strange Quarks	0.0	$-0.11 \pm\ 0.003$
Up Type Quark	0.0	$0.04 \pm\ 0.003$
Hadronic b Quark	0.0	$0.04 \pm\ 0.003$

Table C.2.: Predicted and fitted values of the fit parameter p1 using the 105200 MC sample.

The leptonic final state decay product's value of p1, corresponding to $\alpha_i P$ are close to the predicted values, however, it is clear that reweighting by the leptonic side produces a slight polarization in the hadronic top quark. This is most evident in the value of p1 for the down and strange quark's, which is -0.11, corresponding to $P = -0.11$. The assumption is that this effect can be attributed to the spin correlation between the top and antitop that is present in the 105200 MC sample. Simply stated, if spin correlation is present between the top and antitop, any effect introduced to one of the top's spin sates will result in a change to the other top's spin state. To test this theory, the same analysis was performed on the 117200 MC sample, which does not contain spin correlation. Table C.4 shows the predicted and fitted values for the p1 parameter for each decay product using the 117200 MC sample.

Table C.3.: Predicted and Fitted values of the fit parameter p1 using the 117200 MC sample.

Particle Type	Predicted p1	Fitted p1
Charged Lepton	1.0	1.0 ± 0.0001
Neutrino	-0.3	-0.35 ± 0.003
Leptonic b Quark	-0.4	-0.38 ± 0.0001
Down Type Quark	0.0	0.003 ± 0.0001
Up Type Quark	0.0	0.002 ± 0.0001
Hadronic b Quark	0.0	-0.002 ± 0.0001

Table C.4.: Predicted and Fitted values of the fit parameter p1 using the 117200 MC sample.

We see the same agreement between the predicted and fitted values of p1 for the leptonic variables as with the 115200 MC sample. However, the hadronic final state decay products values of the fitted p1 are in much better agreement with 0 for the non-spin correlated 1175200 sample compared to the 115200 sample with spin correlation. A discussion on how to deal with spin correlation can be found in Appendix C.0.6. Having discovered that the preliminary measurement's reweighting procedure does not reproduce

the expected values of $\alpha_i P$ for every final state decay product in the 115200 sample, a new method for reweighting must be employed.

C.0.5. Weighting by the Leptonic and Hadronic Sides

To perform a proper treatment of longitudinally polarized top quarks in $t\bar{t}$ production, the reweighting procedure must reweight both the leptonic and hadronic sides of the top decays. In Appendix C.0.4, the effects that reweighting by the charged lepton's $\cos\theta$ had on the hadronic final sate decay products was discussed. In this section, it will be shown how reweighting by the leptonic and hadronic side affects the final sate decay products polar angle distributions.

To reweight events by the leptonic and hadronic side, the charged lepton and down/strange quarks are used since their spin analyzing powers are equal to 1 at tree level. A weight is constructed as such:

$$W_{combined} = (1 + \cos\theta_{\ell}) * (1 + \cos\theta_{dsquark}), \tag{C.3}$$

where θ_{ℓ} is the polar angle between the charged lepton and the leptonically decaying top quark's momentum direction in the $t\bar{t}$ center-of-mass frame and $\theta_{dsquark}$ is the polar angle between the down/strange quark and the hadronically decaying top quark's momentum direction in the $t\bar{t}$ center-of-mass frame. $W_{combined}$ represents a maximally positive polarized top and antitop quark. Figure C.3 shows the charged lepton's truth level polar angle distribution along with the down/strange quark's truth level polar angle distribution when each event is weighted by $W_{combined}$ using the 105200 MC sample. Each distribution in Figure C.3 is fit to the same first degree polynomial as in Appendix C.0.4.

Both the charged lepton and down/ strange quark's values for p1, corresponding to $\alpha_i P$, are consistent with 1, however, the distributions appear to be non linear. To

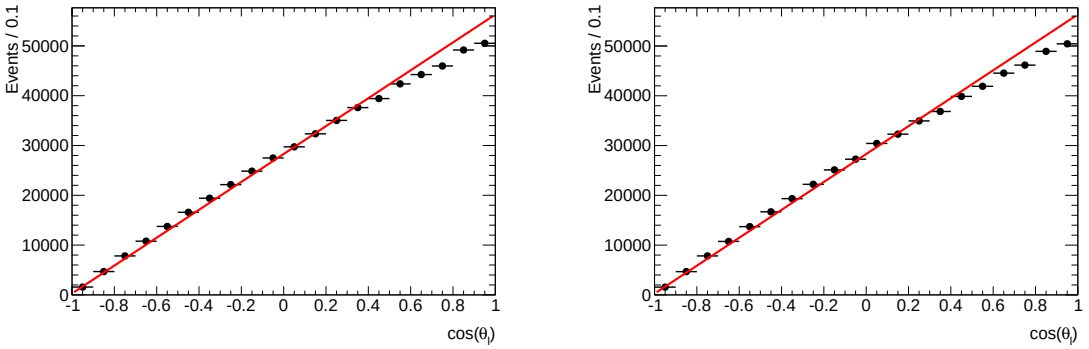

(a) Charged Lepton **(b)** Down and Strange Quarks

Figure C.3.: Truth level $\cos\theta$ distributions weighted by $W_{combined}$ for (a): Charged Lepton; (b): Down and Strange Quarks. Each is fit to a first degree polynomial. The fit results are: $p1_{\ell} = 1.0 \pm 0.004$ and $p1_{dsquark} = 1.0 \pm 0.004$

verify this, the same distributions are fit to a second degree polynomial. Figure C.4 shows the same distributions as Figure C.3, but fit to a second degree polynomial, $y = p0\,(1 + p1 \cdot x + p2 \cdot x^2)$.

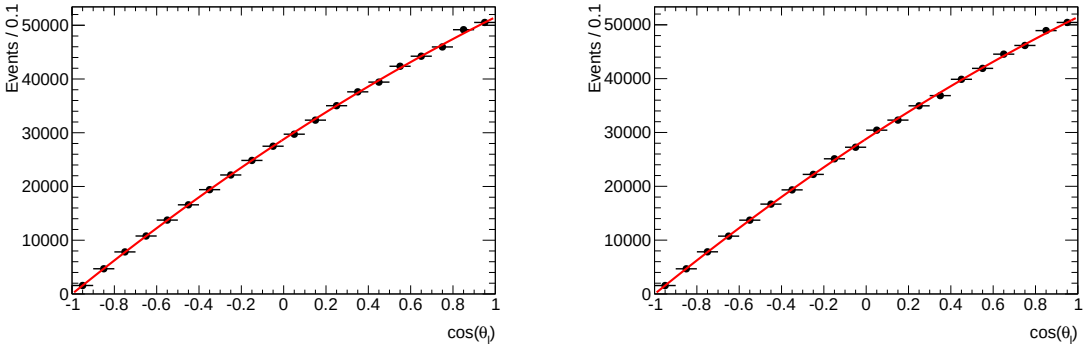

(a) Charged Lepton **(b)** Down and Strange Quarks

Figure C.4.: Truth level $\cos\theta$ distributions weighted by $W_{combined}$ for (a): Charged Lepton; (b): Down and Quarks. Each is fit to a second degree polynomial.

Both the down/strange quark's and charged lepton's truth level polar angle distributions have a quadratic term present in their fit. This can be attributed to the spin correlation present in the 105200 MC sample. To verify this, a quadratic fit to the same distributions using the 117200 MC sample was performed. Table C.5 lists the values

of the fit parameter p2 for both the 105200 and 117200 samples. The fit parameter p2 for the 117200 MC sample is consistent with 0, therefore verifying that the non linear behavior in the polar angle distributions for the combined weight is due to the spin correlation between the top and antitop. Having performed this study, it has been concluded that weighting each event by $W_{combined}$ is not the proper way to treat the spin correlated 105200 MC sample. A more robust technique is described in Appendix C.0.6.

MC Sample	Charged Lepton p2	Down and Strange Quarks p2
105200	-0.106 ± 0.003	-0.108 ± 0.003
117200	0.0002 ± 0.005	-0.0005 ± 0.005

Table C.5.: Values of the fit parameter p2 for the 105200 and 117200 MC samples.

C.0.6. Weighting While Considering Spin Correlation

The previous sections have proven that weighting MC samples with spin correlation must be treated in a more delicate manner; the start of which is by looking at the double differential cross section [23] for $t\bar{t}$ decays with respect to the polar angle of one of the top's decay products and one of the antitop's decay products:

$$\frac{1}{\sigma}\frac{d^2\sigma}{d\cos\theta_1 d\cos\theta_2} = \frac{1}{4}(1 + \alpha_1 P_1 \cos\theta_1 + \alpha_2 P_2 \cos\theta_2 - C\cos\theta_1\cos\theta_2), \tag{C.4}$$

where $\alpha_1 P_1$ ($\alpha_2 P_2$) correspond to the spin-analyzing power of one of the final state decay products of the top (antitop) quark times the magnitude of the longitudinal polarization of the top (antitop) quark and C represents the $t\bar{t}$ spin correlation. The angle θ_1 (θ_2) correspond to the polar angle of the final state decay product used to determine $\alpha_1 P_1$ ($\alpha_2 P_2$) of the top (antitop) quark. Equation (C.4) will be the basis for the new event weight. Constraints are placed on $\alpha_1 P_1$ $\alpha_2 P_2$ and C, to ensure that the differential cross

section remains positive. Assuming that $\alpha_1 P_1 = \alpha_2 P_2$ [1], the case where $\cos\theta_1$ and $\cos\theta_2$ are -1 is examined, which places the constraint on $|\alpha_{1,2}P|$:

$$|\alpha_{1,2}P| \leq \frac{1-C}{2} \tag{C.5}$$

The value of C was determined from the 105200 MC sample by performing a quadratic fit to the two dimensional histogram of $\cos\theta_1$ and $\cos\theta_2$, finding the value of C to be 0.307. Therefore, $|\alpha_{1,2}P|$ must be less than 0.346, which places a limitation on the value of P since $\alpha_{1,2}$ has definite values. To account for this, a value of 0.3 was chosen for $|\alpha_{1,2}P|$ in the following study, since the study will be using the charged lepton and down/strange quarks truth information to reweight the events. The double differential cross section is shown in Figure C.5, which is the two dimensional histogram of $\cos\theta_1$ and $\cos\theta_2$ from the 105200 MC sample.

To produce a sample that has both leptonic and hadronic sides weighted to have positive polarization of $P = 0.3$, a new weight is constructed:

$$W_{Corrected} = \frac{1 + 0.3\cos\theta_\ell + 0.3\cos\theta_{dsquark} - 0.307\cos\theta_\ell\cos\theta_{dsquark}}{1 - 0.307\cos\theta_\ell\cos\theta_{dsquark}}, \tag{C.6}$$

where the denominator, $1 - 0.307\cos\theta_\ell\cos\theta_{dsquark}$, ensures that the spin correlation is not introduced twice to the 105200 MC sample. $W_{Corrected}$ produces truth level polar angle distributions with the correct values of $\alpha_i P$ for both the leptonic and hadronic side final state decay particles. To validate, the truth level polar angles of each final state decay particle is fit to a second degree polynomial. Table C.6 lists the values of the fit parameters p1 and p2 and their expected values of $\alpha_i P$ using the 105200 MC sample, which indicates that $W_{Corrected}$ weights both the leptonic and hadronic sides

[1] $\alpha_1 P_1 = \alpha_2 P_2$ refers to a CP conserving mechanism generating longitudinal polarization of top quarks in $t\bar{t}$ production. The CP violating case where $\alpha_1 P_1 = \alpha_2 P_2$ will be considered in Appendix C.0.8

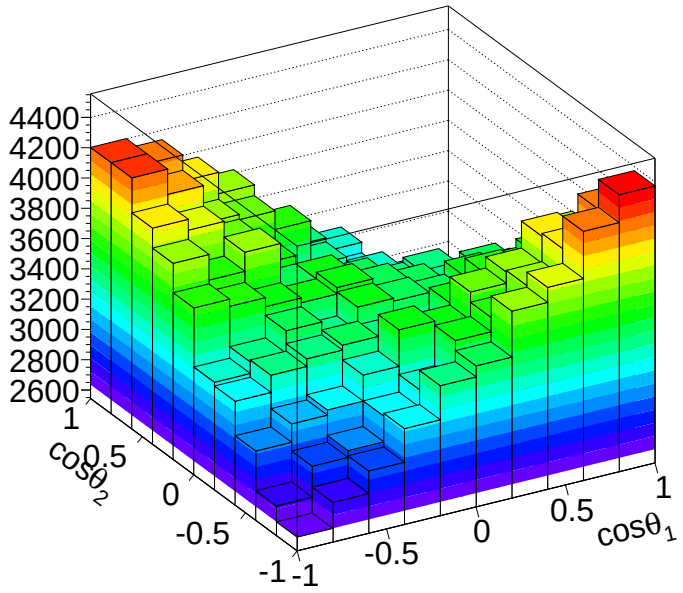

Figure C.5.: Two dimensional histogram representing the double differential cross section using the 105200 MC sample.

correctly. Figure C.6 shows the quadratic fits to the truth level $\cos\theta_\ell$ and $\cos\theta_{dsquark}$ when weighted by $W_{Corrected}$ using the 105200 MC sample.

It is also important to see how applying $W_{Corrected}$ to each event affects the kinematic distributions of the top, antitop, and the $t\bar{t}$ system. Appendix C.0.9 provides plots detailing the unweighted and $W_{Corrected}$ weighted kinematic distributions for the top, antitop, and $t\bar{t}$ system. They show an agreement between the unweighted and weighted distributions consistent with our expectations.

Applying cuts in this analysis could possibly affect the reweighting technique. To address this issue, the full ℓ+jetsselection, described in Section 4.2, was performed on the reconstructed 105200 MC sample and $W_{Corrected}$ was applied using each underlying truth level event. The truth level polar angle distributions were constructed and the ratio was taken between the $WCorrected$ weighted truth level polar angle distributions and the

Particle Type	Predicted p1	Measured p1	Predicted p2	Measured p2
Charged Lepton	0.30	0.30 ± 0.002	0.0	0.003 ± 0.004
Neutrino	-0.09	-0.10 ± 0.002	0.0	0.001 ± 0.005
Leptonic b Quark	-0.12	-0.12 ± 0.002	0.0	-0.002 ± 0.005
Down and Strange Quarks	0.30	0.30 ± 0.002	0.0	-0.007 ± 0.004
Up Type Quark	-0.09	-0.11 ± 0.002	0.0	-0.001 ± 0.005
Hadronic b Quark	-0.12	-0.11 ± 0.002	0.0	-0.002 ± 0.005

Table C.6.: Fitted and predicted values of $p1$ and $p2$ for the truth level polar angle distributions of each final state decay product using the 105200 MC sample.

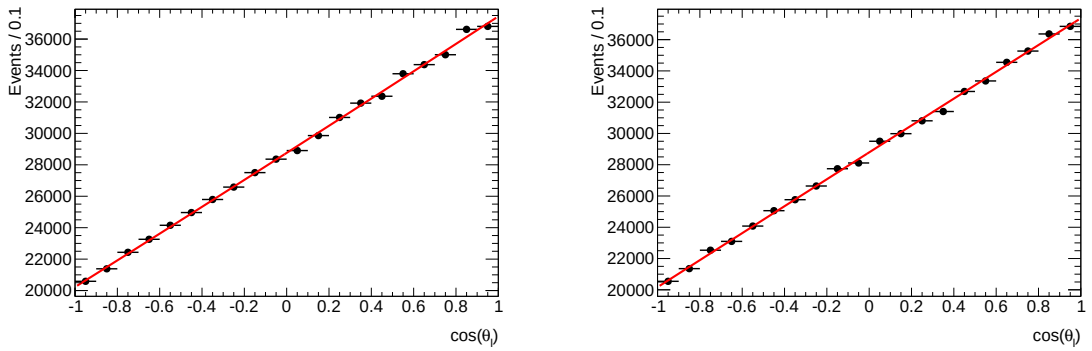

(a) Charged Lepton **(b)** Down and Strange Quark

Figure C.6.: Truth level polar angle distributions weighted by $W_{Corrected}$ and fitted to a second degree polynomial, using the 105200 MC sample.

unweighted truth level polar angle distributions. Figure C.7 shows these distributions for the charged lepton and the down/strange quark. The slope of the ratio should be equal to αP. This is found to be true as the charged lepton and down/strange quark should have $\alpha P = 0.3$, and the slopes of their respective ratios to the unweighted distributions are 0.30 ± 0.003 and 0.29 ± 0.003.

Since a new weight, $W_{Corrected}$, was introduced, a check to see how different the reweighted distributions of the polar angle look compared to when they are reweighted by just the leptonic side; which was the technique used in the preliminary result. To check their level of agreement, the reconstructed polar angle distribution of the charged

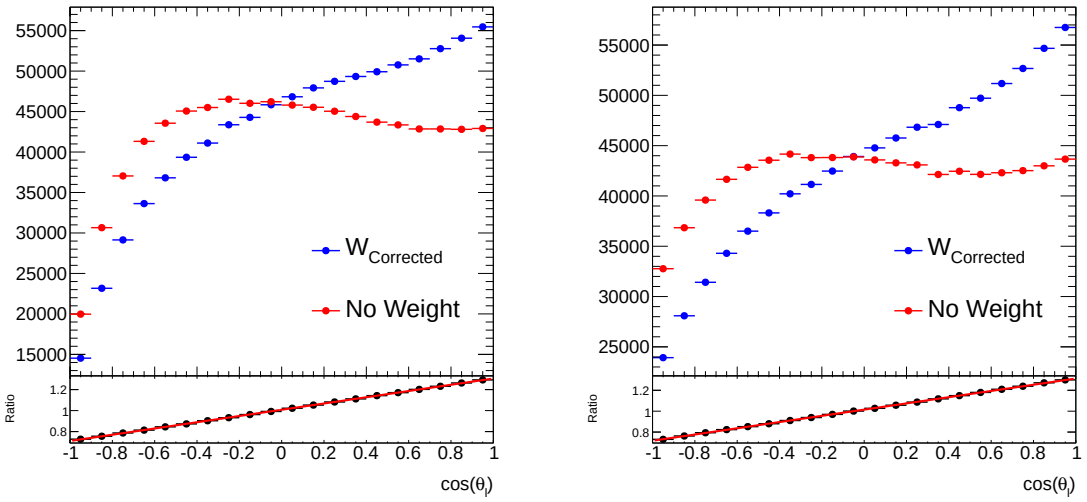

(a) Charged Lepton **(b)** Down and Strange Quark

Figure C.7.: Truth level polar angle distributions after selection has been applied. The blue distribution is weighted by $W_{Corrected}$ and the red distribution is unweighted, using the 105200 MC sample. Their ratio is fitted to a first degree polynomial. The fitted values of p1 are: $p1_{\ell} = 0.30 \pm 0.003$ and $p1_{dsquark} = 0.29 \pm 0.003$.

lepton was used. Figure C.8 shows the reconstructed level polar angle distributions of the charged lepton weighted by $W_{Corrected}$ and by $1 + 0.3 \cdot \cos\theta_{truth\ell}$, using the 105200 MC sample. It also includes the ratio of their distributions fitted to a first degree polynomial.

The fit shows a slope of 0.006 ± 0.003 with an intercept of 1.008 ± 0.002, which indicates that the technique for reweighting in the preliminary result renders a slightly different $\cos\theta_{\ell}$ distribution than reweighting with the $W_{Corrected}$ technique.

C.0.7. Weighting Dilepton Events

The analysis in this thesis represents the measurement of the longitudinal polarization in $t\bar{t}$ using the ℓ+jets channel, meanwhile, there was also a measurement in the dilepton channel, as well as a combined measurement between the two channels [51]. Therefore, it was necessary to check that the $W_{Corrected}$ reweighting technique was also valid for dilepton events. By replacing the contribution from the down/strange quark by the polar

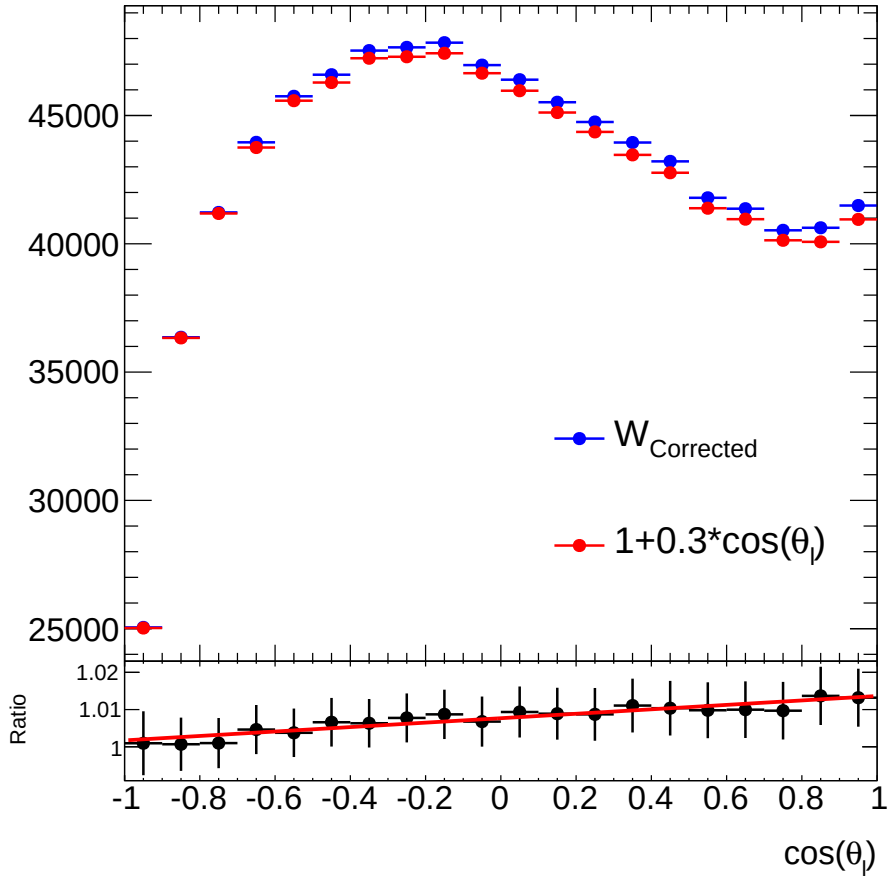

Figure C.8.: Reconstructed level polar angle distributions weighted by $W_{Corrected}$ (in blue) and $1 + 0.3\cos\theta_{truth\ell}$ (in red).

angle of the charged lepton from the other leptonic top decay, a modified weight for dilepton events is given by:

$$W_{Dilep} = \frac{1 + 0.3\cos\theta_{\ell^+} + 0.3\cos\theta_{\ell^-} - 0.307\cos\theta_{\ell^+}\cos\theta_{\ell^-}}{1 - 0.307\cos\theta_{\ell^+}\cos\theta_{\ell^-}}, \tag{C.7}$$

where $\cos\theta_{\ell^+}$ refers to the truth level polar angle of the positively charged lepton with respect to the top quark's momentum direction in the $t\bar{t}$ center-of-mass frame and $\cos\theta_{\ell^-}$ refers to the truth level polar angle of the negatively charged lepton with respect to the antitop quark's momentum direction in the $t\bar{t}$ center-of-mass frame. Figure C.9 shows the positively and negatively charged lepton's truth level polar angle distributions when

each event is weighted by W_{Dilep}. For the sake of being thorough, a check was made to see the affect that W_{Dilep} has on the other final state decay product's polar angle distributions, by fitting them to a second degree polynomial and comparing the fit results to their expected values. Table C.7 lists the values of the fit parameters p1 and p2 and their expected values for each truth level final state decay product in dilepton events using the 105200 MC sample. As expected, the fitted values are consistent with the expectation, thus validating W_{Dilep}.

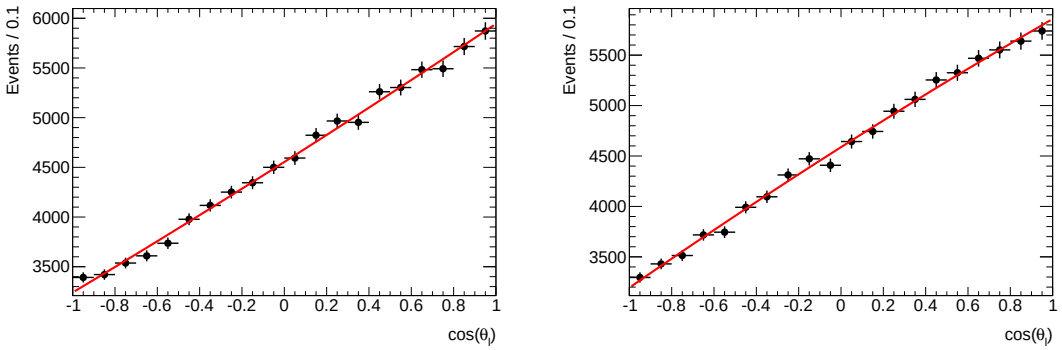

(a) Charged Lepton from Top Decay **(b)** Charged Lepton from Antitop Decay

Figure C.9.: Truth level polar angle distributions weighted by W_{Dilep} and fitted to a second degree polynomial, using the 105200 MC sample.

Particle Type	Predicted p1	Measured p1	Predicted p2	Measured p2
Lepton	0.30	0.31 ± 0.006	0.0	0.009 ± 0.01
Anti-Neutrino	-0.09	-0.10 ± 0.006	0.0	-0.005 ± 0.01
b Quark	-0.12	-0.12 ± 0.006	0.0	-0.02 ± 0.01
Anti-Lepton	0.30	0.30 ± 0.006	0.0	-0.01 ± 0.01
Neutrino	-0.09	-0.10 ± 0.006	0.0	-0.009 ± 0.01
Anti-b Quark	-0.12	-0.11 ± 0.006	0.0	-0.0005 ± 0.01

Table C.7.: Fitted and predicted values of $p1$ and $p2$ for the truth level polar angle distributions of each final state decay product using the 105200 MC sample.

C.0.8. Considering CP Violation

As discussed in Section 4.4, this analysis is interested in probing new physics by looking at a CP violating scenario for longitudinally polarized top quarks in $t\bar{t}$ production. CP violation occurs when $\alpha_1 P = -\alpha_2 P$, referring to Equation (C.4). For the CP violating case, the double differential cross section has a minimum at $\cos\theta_1 = -\cos\theta_2$ which places a new constraint on $|\alpha_{1,2}P|$:

$$|\alpha_{1,2}P| \leq \frac{1+C}{2}. \tag{C.8}$$

Using the previous value of $C = 0.307$, Equation (C.8) limits $|\alpha_{1,2}P|$ to be less than 0.634. To determine the viability of the reweighting technique for CP violating polarization, the 105200 MC sample is reweighted by the CP violating weight:

$$W_{CPviolating} = \frac{1 + 0.3\cos\theta_1 - 0.3\cos\theta_2 - 0.307\cos\theta_1\cos\theta_2}{1 - 0.307\cos\theta_1\cos\theta_2}, \tag{C.9}$$

which corresponds to $\alpha_1 P_1 = 0.3$ and $\alpha_2 P_2$ = -0.3. The value of $|\alpha_{1,2}P|$ was kept at 0.3 since it falls within the constraint of Equation (C.8). To properly treat CP violation, the affects of $W_{CPviolating}$ on charge separated polar angle distributions i.e. top decay products and antitop decay products must be studied. In addition, a study was conducted to look at the difference between the charge separated distributions when $\cos\theta_1 = \cos\theta_\ell$ and $\cos\theta_2 = \cos\theta_{dsquark}$ versus $\cos\theta_2 = \cos\theta_\ell$ and $\cos\theta_1 = \cos\theta_{dsquark}$. The same validation procedure as in previous sections is followed by fitting the truth level polar angle distributions for charged lepton's to a second degree polynomial and comparing the fit parameters to their predicted values. Table C.8 shows the predicted

and measured fit parameters p1 and p2 for each charge and $\cos\theta_i$ combination when weighted by $W_{CPviolating}$, which clearly shows that the reweighting technique is also valid for the CP violating case of polarized $t\bar{t}$ production.

ℓ^+ (top decay) $\cos_1 = \cos_\ell$ $\cos_2 = \cos_{dsquark}$			
Predicted p1	Measured p1	Predicted p2	Measured p2
0.30	0.31 ± 0.003	0.0	0.006 ± 0.006

ℓ^+ (top decay) $\cos_1 = \cos_{dsquark}$ $\cos_2 = \cos_\ell$			
Predicted p1	Measured p1	Predicted p2	Measured p2
-0.30	-0.31 ± 0.003	0.0	0.01 ± 0.006

ℓ^- (antitop decay) $\cos_1 = \cos_\ell$ $\cos_2 = \cos_{dsquark}$			
Predicted p1	Measured p1	Predicted p2	Measured p2
0.30	0.30 ± 0.003	0.0	-0.002 ± 0.006

ℓ^- (antitop decay) $\cos_1 = \cos_{dsquark}$ $\cos_2 = \cos_\ell$			
Predicted p1	Measured p1	Predicted p2	Measured p2
-0.30	-0.31 ± 0.003	0.0	-0.004 ± 0.006

Table C.8.: CP violating fitted and predicted values of $p1$ and $p2$ for the truth level polar angle distributions of each final state decay product. using the 105200 MC sample.

C.0.9. Top, Antitop, and TTbar Kinematics

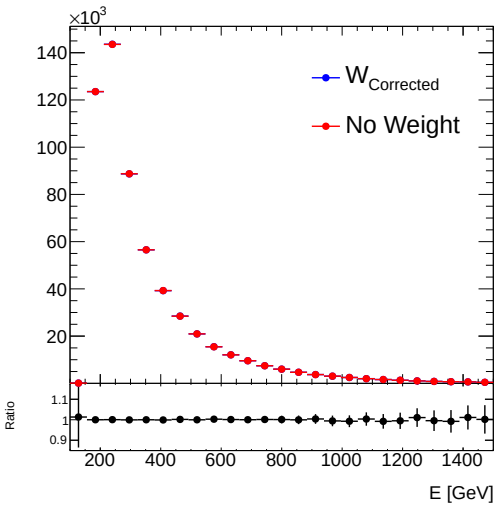

(a) Energy

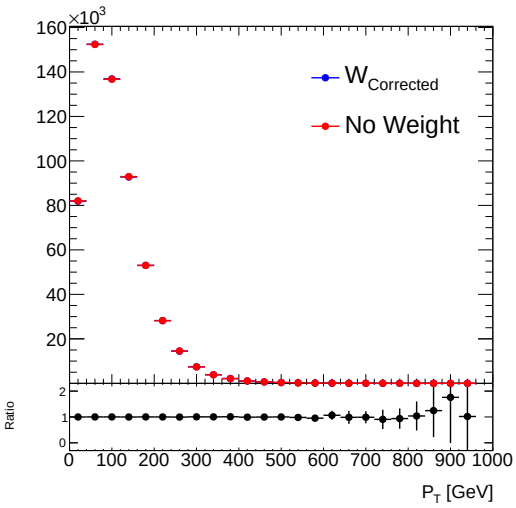

(b) P_T

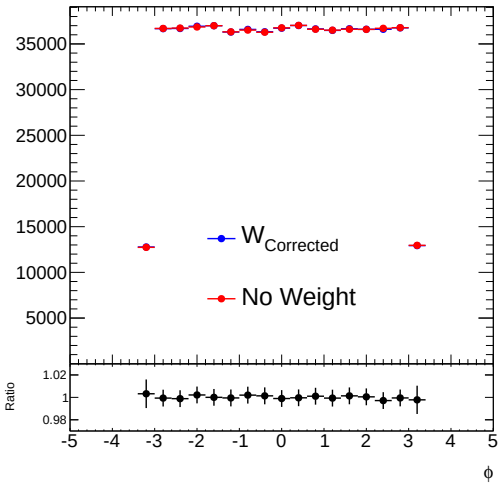

(c) ϕ

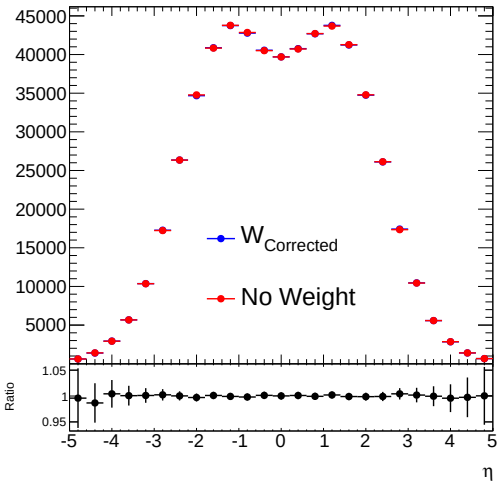

(d) η

Figure C.10.: Truth level kinematic distributions for the top quark, un-weighted (red) and weighted by $W_{Corrected}$ (blue)

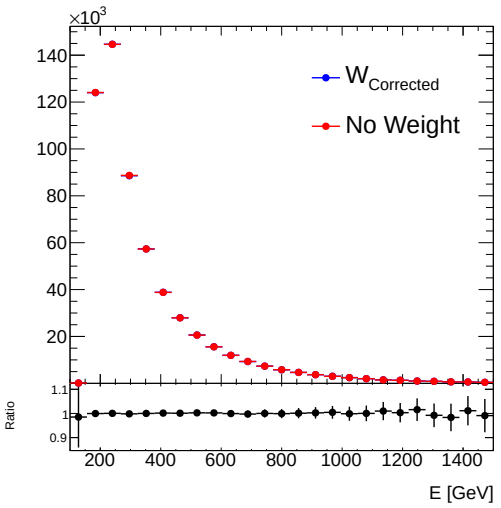

(a) Energy

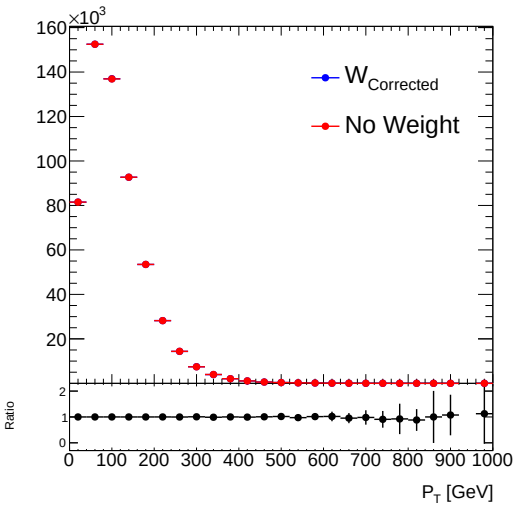

(b) P_T

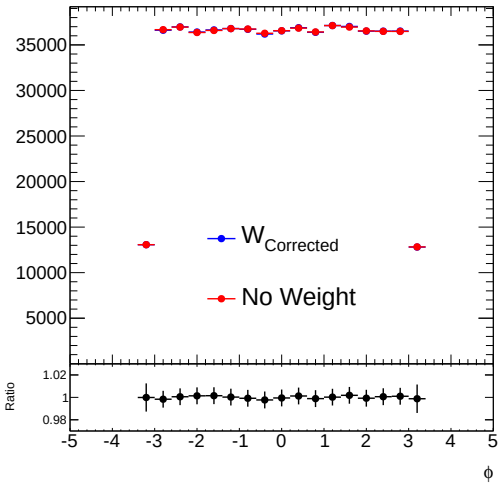

(c) ϕ

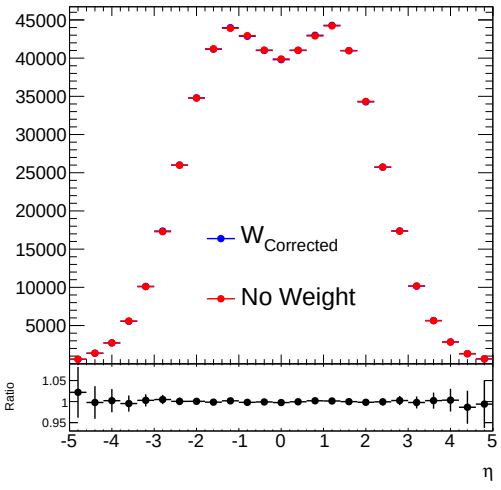

(d) η

Figure C.11.: Truth level kinematic distributions for the antitop quark, un-weighted (red) and weighted by $W_{Corrected}$ (blue)

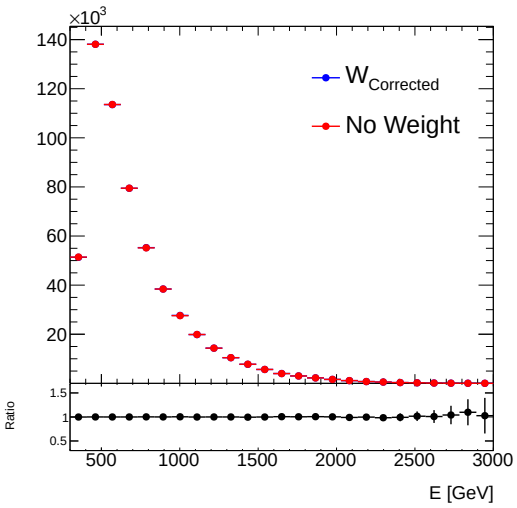

(a) Energy

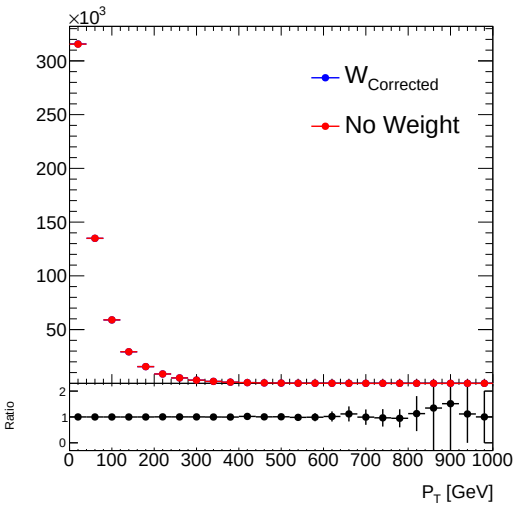

(b) P_T

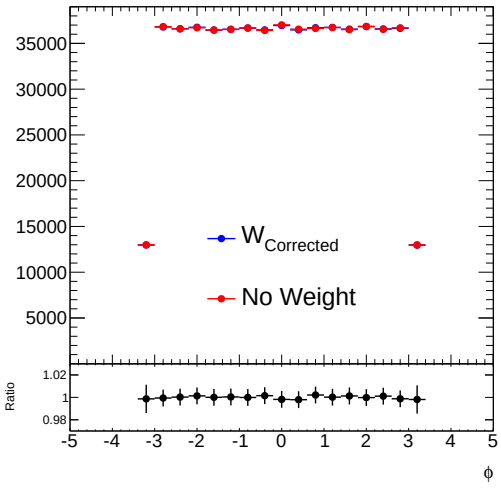

(c) ϕ

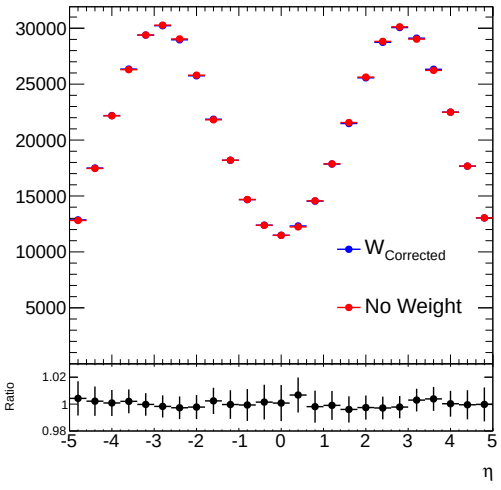

(d) η

Figure C.12.: Truth level kinematic distributions for the $t\bar{t}$ system, un-weighted (red) and weighted by $W_{Corrected}$ (blue)

Appendix D.

Template Fit Study

This appendix details a study on the performance of the two different template fitting techniques described in Section 4.5. For this study, ROOT's [87] TFractionFitter was used to perform the fractional fits of the templates to the data.

Two methods for fitting templates to the data are explored: the normal fitting method, and the positive/negative fitting method. The normal fitting method refers to the technique used for this analysis in which a positively polarized and a negatively polarized template are used to extract the fraction of positive polarization from the data. The positive/negative method may also be used to extract the fraction of positive or negative polarization; this method consists of fitting a positively polarized template and a flat template to the data as well as fitting a negatively polarized template and a flat template to the data. After performing the positive/negative template fits, a χ^2 fit is performed for the positive fit result to the data and for the negative fit result to the data. The fit which produces the best "goodness of fit", the smallest value of χ^2 divided by the number of degrees of freedom (χ^2/NDF), is chosen as the proper result. In principle, both the normal and positive/negative fitting methods will produce the same results.

Appendix D.1 presents a study that shows that both the normal and positive/negative fitting techniques produce equivalent results, using a toy model to demonstrate their consistency. Appendix D.2 presents the same study using the templates and data used

for the measurement presented in this thesis. A discrepancy between the results of the normal and positive/negative fitting techniques is exposed when using the analysis templates. This issue should be investigated further if one plans to use the same fitting procedure for future measurements.

D.1. Toy Model

To test the two fitting techniques, pseudo data sets of $\cos(\theta)$ were created, one with a positive slope and one with a negative slope. The distributions follow the form

$$y = Constant + m \times \cos(\theta_\ell), \tag{D.1}$$

where m can be thought of as $\alpha_\ell P$; however, the values of m used in this appendix are not constrained to have values of 0.3 and -0.3, as was the case in Section 4.5. The positive pseudo data set has $m = 44.78$ and the negative pseudo data set has a value of $m = -9.0$. In addition, three templates were created, one with a positive slope ($m = 50.0$), one with a negative slope ($m = -50.0$), and one with a completely flat distribution ($m = 0.0$).

The fraction of positive polarization, f, is extracted from the pseudo data by the normal fitting technique using the equation

$$f \underbrace{(Constant + 50\cos\theta_\ell)}_{\text{Positive Template}} + (1-f) \underbrace{(Constant - 50\cos\theta_\ell)}_{\text{Negative Template}} = (Constant + m \times \cos\theta_\ell). \tag{D.2}$$

The fitted value of f can be translated into the slope m of the pseudo data set using the equation

$$m = 100f - 50. \tag{D.3}$$

If the pseudo data set has a slope of 44.78, then the normal fitting technique should return a value of $f = 0.95$.

The positive/negative fitting technique works in a similar way. The template fit using a positively polarized template and a flat template, which will be referred to as the positive fit, uses the equation

$$f \underbrace{(Constant + 50\cos\theta_\ell)}_{\text{Positive Template}} + (1-f) \underbrace{Constant}_{\text{Flat Template}} = (Constant + m \times \cos\theta_\ell). \quad \text{(D.4)}$$

The fitted value of f can be translated into the slope m of the pseudo data set using the equation

$$m = 50f. \quad \text{(D.5)}$$

The template fit using a negatively polarized template and a flat template, which will be referred to as the negative fit, uses the equation

$$f \underbrace{(Constant - 50\cos\theta_\ell)}_{\text{Negative Template}} + (1-f) \underbrace{Constant}_{\text{Flat Template}} = (Constant + m \times \cos\theta_\ell). \quad \text{(D.6)}$$

The fitted value of f can be translated into the slope m of the pseudo data set using the equation

$$m = -50f. \quad \text{(D.7)}$$

If the pseudo data set has a positive slope, then the template fit using the positively polarized template and the flat template will produce the best fit, i.e. a χ^2 fit of the result to the pseudo data set will produce a smaller χ^2/NDF value than a χ^2 fit of the negative result to the data. The opposite is true for a pseudo data set with a negative slope; the negative fit will produce the smallest χ^2/NDF value.

Table D.1.: Results of the normal and positive/negative template fits to the positive slope pseudo data set. The fitted results of m should be compared to the slope of the pseudo data set $m_{data} = 44.78$.

Fitting Technique	f	m	χ^2/NDF
Normal Fit	0.95 ± 0.066	44.78 ± 6.66	7.11×10^{-10}
Positive Fit	0.89 ± 0.083	44.78 ± 4.15	2.77×10^{-9}
Negative Fit	$1.32 \times 10^{-10} \pm 0.004$	$6.60 \times 10^{-9} \pm 0.20$	2.50

The results for the normal, positive, and negative fits to the pseudo dataset with positive slope, $m_{data} = 44.78$, are listed in Table D.1. The distributions for the pseudo data, templates, and fit results are shown in Fig. D.1. The positive fit's value of χ^2/NDF is smaller than that for the negative fit; therefore, the positive fit is taken as the proper fit between the positive and negative fits. The normal fit produces a fitted result of $m_{normal} = 44.78 \pm 6.66$ and is consistent with the true slope of the the pseudo data set $m_{data} = 44.78$. The positive fit result, $m_{positive} = 44.78 \pm 4.15$, is also consistent with the value of the slope of the pseudo data set.

The results for the normal, positive, and negative fits to the pseudo dataset with negative slope, $m_{data} = -9.0$, are listed in Table D.2. The distributions for the pseudo data, templates, and fit results are shown in Fig. D.2. The negative fit's value of χ^2/NDF is smaller than that for the positive fit; therefore, the negative fit is taken as the proper fit between the positive and negative fits. The normal fit produces a fitted result of $m_{normal} = -9.01 \pm 5.12$ and is consistent with the true slope of the the pseudo data set $m_{data} = -9.0$. The negative fit result, $m_{negative} = -9.01 \pm 4.95$, is also consistent with the value of the slope of the pseudo data set.

Table D.2.: Results of the normal and positive/negative template fits to the negative slope pseudo data set. The fitted results of m should be compared to the slope of the pseudo data set $m_{data} = -9.0$.

Fitting Technique	f	m	χ^2/NDF
Normal Fit	0.41 ± 0.051	-9.01 ± 5.12	1.36×10^{-9}
Positive Fit	$9.47 \times 10^{-12} \pm 0.030$	$4.74 \times 10^{-10} \pm 1.51$	0.072
Negative Fit	0.18 ± 0.10	-9.01 ± 4.95	1.50×10^{-9}

D.2. Analysis Templates

The study performed in Appendix D.1 is repeated using the data and templates produced for the measurement presented in this thesis. As mentioned in Appendix C.0.4, the distribution of $\cos\theta_\ell$ produced in ATLAS MC is flat because it was generated with unpolarized top quarks; therefore, the flat template in this study corresponds to the unweighted $\cos\theta_\ell$ distribution produced in the MC. The positively and negatively polarized templates used in this study correspond to the partially polarized templates described in Section 4.4.2. The fit results for the normal and positive/negative fits for the analysis templates should show the same level of consistency demonstrated using the toy model in Appendix D.1

In the case of the analysis templates, the normal fit uses fractionally positively and negatively polarized templates of $\cos\theta_\ell$, corresponding to a value of $\alpha_\ell P = \pm\ 0.3$. The positive and negative templates are then fit to the data to extract the the fraction of positive polarization, f, using the equation

$$\frac{1}{2} f \underbrace{(1 + 0.3\cos\theta_\ell)}_{\text{Positive Template}} + \frac{1}{2}(1-f)\underbrace{(1 - 0.3\cos\theta_\ell)}_{\text{Negative Template}} = \frac{1}{2}(1 + \alpha_\ell P \cos\theta_\ell). \tag{D.8}$$

The fitted value of f can then be related to $\alpha_\ell P$ using the equation

$$\alpha_\ell P = 0.6f - 0.3. \tag{D.9}$$

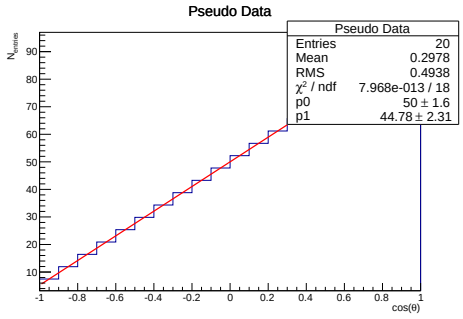

(a) Pseudo Data

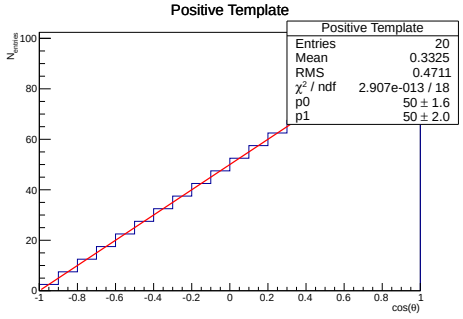

(b) Positive Slope Template

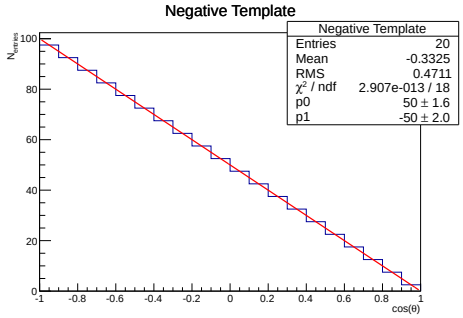

(c) Negative Slope Template

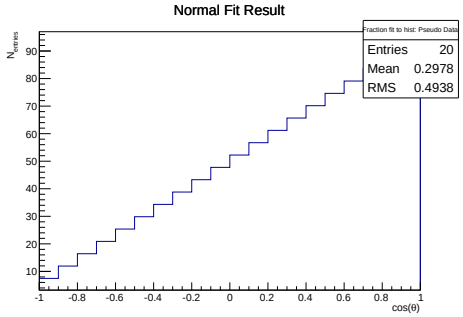

(d) Resulting Fit Normal Method

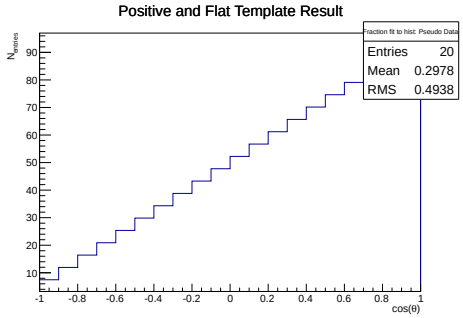

(e) Resulting Fit Positive Method

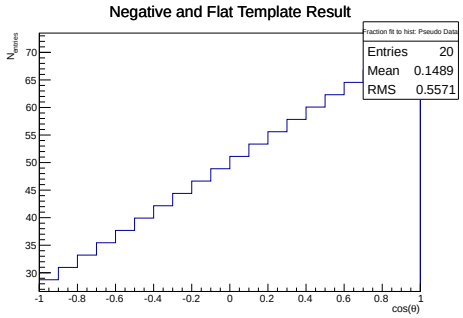

(f) Resulting Fit Negative Method

Figure D.1.: Figures D.1b and D.1c depict the templates used to fit to the pseudo data shown in Fig. D.1a. The fit results for the template fits using the normal and positive/negative methods are shown in Figs. D.1d to D.1f.

The positive fit, in this case, fits the positive and flat template to the data using the equation

$$\frac{1}{2} f \underbrace{(1 + 0.3 \cos\theta_\ell)}_{\text{Positive Template}} + (1 - f) \times \underbrace{(1/2)}_{\text{Flat Template}} = \frac{1}{2}(1 + \alpha_\ell P \cos\theta_\ell). \tag{D.10}$$

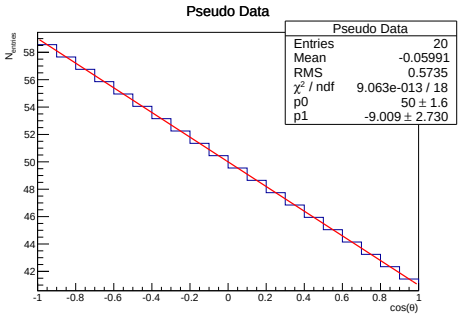

(a) Pseudo Data

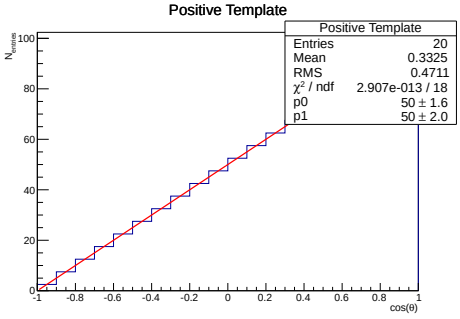

(b) Positive Slope Template

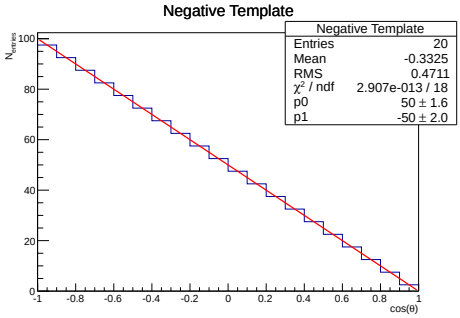

(c) Negative Slope Template

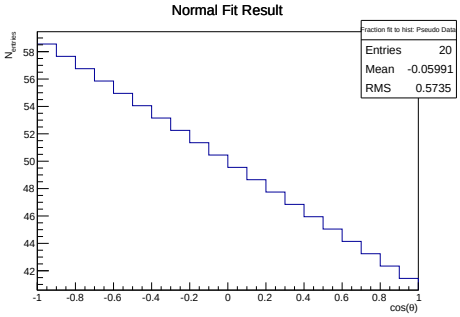

(d) Resulting Fit Normal Method

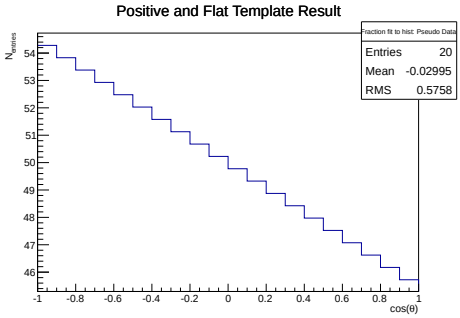

(e) Resulting Fit Positive Method

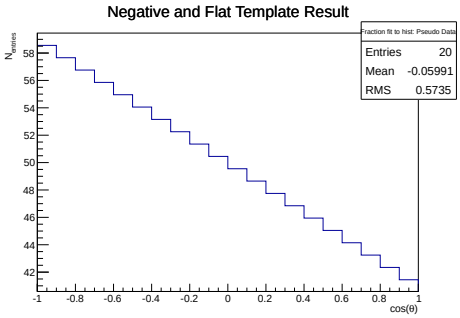

(f) Resulting Fit Negative Method

Figure D.2.: Figures D.2b and D.2c depict the templates used to fit to the negative slope pseudo data shown in Fig. D.2a. The fit results for the template fits using the normal and positive/negative methods are shown in Figs. D.2d to D.2f.

The fitted value of f can then be related to $\alpha_\ell P$ using the equation

$$\alpha_\ell P = 0.3 f. \tag{D.11}$$

Similarly, the negative fitting technique fits the negative and flat template to the data using the equation

$$\frac{1}{2}f\underbrace{(1-0.3\cos\theta_\ell)}_{\text{Negative Template}}+(1-f)\times\underbrace{(1/2)}_{\text{Flat Template}}=\frac{1}{2}(1+\alpha_\ell P\cos\theta_\ell). \tag{D.12}$$

The fitted value of f can then be related to $\alpha_\ell P$ using the equation

$$\alpha_\ell P = -0.3f. \tag{D.13}$$

Three sets of fits are performed: the normal and positive/negative fits to the positively charged lepton data for the e+jets, μ+jets, and ℓ+jets channels. Tables D.3 to D.5 lists the fitted values of f and $\alpha_\ell P$, as well as the χ^2/NDF values from the χ^2 fits of the results to the data for each set of fits. Unlike the toy model's fit results, the normal and positive/negative fit results for the analysis templates do not agree. For instance, the positive fit for the e+jets channel, which has the smallest χ^2/NDF between the positive/negative fits, results in a value of $\alpha_\ell P = 3.92\times10^{-10}\pm\ 0.017$. This fitted value of $\alpha_\ell P$ is approximately eight orders of magnitude smaller than the normal fit result of $\alpha_\ell P = -0.026\pm\ 0.040$. Similar discrepancies are found between the normal and positive/negative fits in the μ+jets and ℓ+jets channels.

Given the consistency between the normal and positive/negative fits using the toy model, the disagreement between results using the analysis templates and data is worth investigating further. This study was performed very late in the thesis writing process and could benefit from a more thorough investigation. The discrepancy in results using the analysis templates and data may be the cause of a systematic effect due to detector level reconstruction. The discrepancy could also arise as a systematic issue in the production of the analysis templates. A more robust study of this issue should yield an understanding of how this discrepancy originates.

Table D.3.: Results of the normal and positive/negative template fits to the e+jets positively charged data.

Fitting Technique	f	$\alpha_\ell P$	χ^2/NDF
Normal Fit	0.46 ± 0.063	-0.026 ± 0.040	0.66
Positive Fit	$1.31 \times 10^{-9} \pm 0.055$	$3.92 \times 10^{-10} \pm 0.017$	0.38
Negative Fit	$6.92 \times 10^{-9} \pm 0.018$	$-3.46 \times 10^{-7} \pm 0.005$	0.37

Table D.4.: Results of the normal and positive/negative template fits to the μ+jets positively charged data.

Fitting Technique	f	$\alpha_\ell P$	χ^2/NDF
Normal Fit	0.51 ± 0.045	0.006 ± 0.027	0.44
Positive Fit	$4.43 \times 10^{-8} \pm 0.11$	$1.33 \times 10^{-8} \pm 0.033$	0.25
Negative Fit	$1.45 \times 10^{-9} \pm 0.079$	$-7.27 \times 10^{-8} \pm 0.024$	0.24

Table D.5.: Results of the normal and positive/negative template fits to the ℓ+jets positively charged data.

Fitting Technique	f	$\alpha_\ell P$	χ^2/NDF
Normal Fit	0.49 ± 0.036	-0.006 ± 0.022	0.57
Positive Fit	$4.04 \times 10^{-8} \pm 0.059$	$1.21 \times 10^{-8} \pm 0.018$	0.32
Negative Fit	$8.10 \times 10^{-11} \pm 0.090$	$-4.05 \times 10^{-9} \pm 0.027$	0.32

Appendix E.

ATLAS Analysis Appendix

This appendix details the ATLAS analysis software packages and datasets used to perform the measurements presented in this thesis; it is intended for ATLAS analyzers who are interested in repeating or improving the measurement. The analysis is documented in the ATLAS internal note: ATL-COM-PHYS-2013-367. Appendix E.1 details the software packages used for object and event selection, kinematic likelihood fitting, and template fitting. The data and MC samples used for this analysis are listed in Appendix E.2.

E.1. Analysis Software

The analysis code used for this thesis is located on svn and may be accessed via WebSVN at:

https://svnweb.cern.ch/cern/wsvn/atlas-samhamil .

Text files entitled Readme.txt are included in each package to explain the contents.

E.1.1. Top Root Core

Object and event selection was performed using the Top Working Group's software package TopRootCore, using the version TopRootCoreRelease-11-00-00-07. In addition to the standard ℓ+jets object and event selection, ≥ 4 jets and ≥ 1 b-tags are required. The object and event selection requirements are documented at:

https://twiki.cern.ch/twiki/bin/viewauth/AtlasProtected/TopCommonObjects2011 ,

while the object and event scale factors are documented at:

https://twiki.cern.ch/twiki/bin/viewauth/AtlasProtected/TopCommonScales2011 .

To reduce the jet energy scale uncertainty, the ApplyJetCalibration and JetUncertainties packages are updated to versions ApplyJetCalibration-00-02-07 and JetUncertainties-00-07-07. In addition, analysis specific n-jet dependent gluon fraction root files were created, which are used by the MultijetJESUncertaintyProvider to calculate the flavor composition and flavor response uncertainties. The procedure for producing the gluon fraction files is documented in Section 5.5 of ATL-COM-PHYS-2013-367.

After performing selection, custom mini ntuples based on the MiniSL class are created to interface with the Kinematic Likelihood Fitter. The custom class creating these ntuples is entitled MiniPolTuple and may be found via the svn link listed above.

E.1.2. Kinematic Likelihood Fitter

The $t\bar{t}$ event reconstruction was performed using the kinematic likelihood fitter (KLFitter), version KLFitter-00-05-12. Only the five highest p_{T} jets were considered when forming the set of permutations.

E.1.3. Binned Maximum Likelihood Fit

The code used to perform the template fit may be found at:

https://svnweb.cern.ch/trac/atlasinst/browser/Institutes/DESY-HH/Analysis/TopDileptonPolarization/Fitting .

The fit function used for the binned maximum likelihood fit is maximized using Minuit [76].

E.2. Datasets

The data and MC samples used for this analysis were in the form of standard Top Working Group Ntuples (NTUP_TOP). The specific samples used are listed in Appendices E.2.1 to E.2.8.

E.2.1. Data

The full 2011 ATLAS data set was used, corresponding to an integrated luminosity of 4.66 ± 0.08 fb^{-1}. Data quality requirements were implemented using the standard Top Working Group good run list:

data11_7TeV.periodAllYear_DetStatus-v36-pro10_CoolRunQuery-00-04-08_Top_allchannels.xml

E.2.2. Single Top Samples

Single top samples created using AcerMC+Pythia or MC@NLO+Herwig/Jimmy:

mc11_7TeV.117360.st_tchan_enu_AcerMC.merge.NTUP_TOP.e835_s1310_s1300_r3043_r2993_p937/

mc11_7TeV.117361.st_tchan_mumu_AcerMC.merge.NTUP_TOP.e835_s1310_s1300_r3043_r2993_p937/

mc11_7TeV.117362.st_tchan_taunu_AcerMC.merge.NTUP_TOP.e825_s1310_s1300_r3043_r2993_p937/

mc11_7TeV.108345.st_schan_taunu_McAtNlo_Jimmy.merge.NTUP_TOP.e835_s1310_s1300_r3043_r2993_p937/

mc11_7TeV.108343.st_schan_enu_McAtNlo_Jimmy.merge.NTUP_TOP.e835_s1310_s1300_r3043_r2993_p937/

mc11_7TeV.108344.st_chan_munu_McAtNlo_Jimmy.merge.NTUP_TOP.e835_s1310_s1300_r3043_r2993_p937/

mc11_7TeV.108346.st_Wt_McAtNlo_Jimmy.merge.NTUP_TOP.e835_s1310_s1300_r3043_r2993_p937/

E.2.3. $t\bar{t}$ Signal Systematics Samples

Samples used for systematics, created using AcerMC+Pythia, Powheg+Herwig, or Powheg+Pythia:

Underlying Event:

mc11_7TeV.117429.TTbar_PowHeg_Pythia_P2011mpiHi.merge.NTUP_TOP.e1683_a131_s1353_a145_r2993_p937/

mc11_7TeV.117428.TTbar_PowHeg_Pythia_P2011.merge.NTUP_TOP.e1683_a131_s1353_a145_r2993_p937/

Color Reconnection:

mc11_7TeV.117430.TTbar_PowHeg_Pythia_P2011noCR.merge.NTUP_TOP.e1683_a131_s1353_a145_r2993_p937/

mc11_7TeV.117428.TTbar_PowHeg_Pythia_P2011.merge.NTUP_TOP.e1683_a131_s1353_a145_r2993_p937/

Shower/Fragmentation:

mc11_7TeV.117050.TTbar_PowHeg_Pythia_P2011C.merge.NTUP_TOP.e1377_a131_s1353_a139_r2900_p937/

mc11_7TeV.105860.TTbar_PowHeg_Jimmy.merge.NTUP_TOP.e1198_a131_s1353_a139_r2900_p937/

ISR/FSR:

mc11_7TeV.117862.AcerMCttbar_Perugia2011C_MorePS.merge.NTUP_TOP.e1449_a131_s1353_a145_r2993_p937/

mc11_7TeV.117863.AcerMCttbar_Perugia2011C_LessPS.merge.NTUP_TOP.e1449_a131_s1353_a145_r2993_p937/

MC Generator:

mc11_7TeV.105200.T1_McAtNlo_Jimmy.merge.NTUP_TOP.e835_a131_s1354_a139_r2900_p937/

mc11_7TeV.105860.TTbar_PowHeg_Jimmy.merge.NTUP_TOP.e1198_a131_s1353_a139_r2900_p937/

E.2.4. W+jets Samples

Samples used to estimate the W+jets background, created using MC@NLO+Herwig/Jimmy:

mc11_7TeV.107680.AlpgenJimmyWenuNp0_pt20.merge.NTUP_TOP.e825_s1299_s1300_r3043_r2993_p937/

mc11_7TeV.107681.AlpgenJimmyWenuNp1_pt20.merge.NTUP_TOP.e825_s1299_s1300_r3043_r2993_p937/

mc11_7TeV.107682.AlpgenJimmyWenuNp2_pt20.merge.NTUP_TOP.e825_s1299_s1300_r3043_r2993_p937/

mc11_7TeV.107683.AlpgenJimmyWenuNp3_pt20.merge.NTUP_TOP.e825_s1299_s1300_r3043_r2993_p937/

mc11_7TeV.107684.AlpgenJimmyWenuNp4_pt20.merge.NTUP_TOP.e825_s1299_s1300_r3043_r2993_p937/

mc11_7TeV.107685.AlpgenJimmyWenuNp5_pt20.merge.NTUP_TOP.e825_s1299_s1300_r3043_r2993_p937/

mc11_7TeV.107690.AlpgenJimmyWmunuNp0_pt20.merge.NTUP_TOP.e825_s1299_s1300_r3043_r2993_p937/

mc11_7TeV.107691.AlpgenJimmyWmunuNp1_pt20.merge.NTUP_TOP.e825_s1299_s1300_r3043_r2993_p937/

mc11_7TeV.107692.AlpgenJimmyWmunuNp2_pt20.merge.NTUP_TOP.e825_s1299_s1300_r3043_r2993_p937/

mc11_7TeV.107693.AlpgenJimmyWmunuNp3_pt20.merge.NTUP_TOP.e825_s1299_s1300_r3043_r2993_p937/

mc11_7TeV.107694.AlpgenJimmyWmunuNp4_pt20.merge.NTUP_TOP.e825_s1299_s1300_r3043_r2993_p937/

mc11_7TeV.107695.AlpgenJimmyWmunuNp5_pt20.merge.NTUP_TOP.e825_s1299_s1300_r3043_r2993_p937/

mc11_7TeV.107280.AlpgenJimmyWbbFullNp0_pt20.merge.NTUP_TOP.e887_s1310_s1300_r3043_r2993_p937/

mc11_7TeV.107281.AlpgenJimmyWbbFullNp1_pt20.merge.NTUP_TOP.e887_s1310_s1300_r3043_r2993_p937/

mc11_7TeV.107282.AlpgenJimmyWbbFullNp2_pt20.merge.NTUP_TOP.e887_s1310_s1300_r3043_r2993_p937/

mc11_7TeV.107283.AlpgenJimmyWbbFullNp3_pt20.merge.NTUP_TOP.e887_s1310_s1300_r3043_r2993_p937/

mc11_7TeV.117284.AlpgenWccFullNp0_pt20.merge.NTUP_TOP.e887_s1310_s1300_r3043_r2993_p937/

mc11_7TeV.117285.AlpgenWccFullNp1_pt20.merge.NTUP_TOP.e887_s1310_s1300_r3043_r2993_p937/

mc11_7TeV.117286.AlpgenWccFullNp2_pt20.merge.NTUP_TOP.e887_s1310_s1300_r3043_r2993_p937/

mc11_7TeV.117287.AlpgenWccFullNp3_pt20.merge.NTUP_TOP.e887_s1310_s1300_r3043_r2993_p937/

mc11_7TeV.117293.AlpgenWcNp0_pt20.merge.NTUP_TOP.e887_s1310_s1300_r3043_r2993_p937/

mc11_7TeV.117294.AlpgenWcNp1_pt20.merge.NTUP_TOP.e887_s1310_s1300_r3043_r2993_p937/

mc11_7TeV.117295.AlpgenWcNp2_pt20.merge.NTUP_TOP.e887_s1310_s1300_r3043_r2993_p937/

mc11_7TeV.117296.AlpgenWcNp3_pt20.merge.NTUP_TOP.e887_s1310_s1300_r3043_r2993_p937/

mc11_7TeV.117297.AlpgenWcNp4_pt20.merge.NTUP_TOP.e887_s1310_s1300_r3043_r2993_p937/

mc11_7TeV.107700.AlpgenJimmyWtaunuNp0_pt20.merge.NTUP_TOP.e835_s1299_s1300_r3043_r2993_p937/

mc11_7TeV.107701.AlpgenJimmyWtaunuNp1_pt20.merge.NTUP_TOP.e835_s1299_s1300_r3043_r2993_p937/

mc11_7TeV.107702.AlpgenJimmyWtaunuNp2_pt20.merge.NTUP_TOP.e835_s1299_s1300_r3043_r2993_p937/

mc11_7TeV.107703.AlpgenJimmyWtaunuNp3_pt20.merge.NTUP_TOP.e835_s1299_s1300_r3043_r2993_p937/

mc11_7TeV.107704.AlpgenJimmyWtaunuNp4_pt20.merge.NTUP_TOP.e835_s1299_s1300_r3043_r2993_p937/

mc11_7TeV.107705.AlpgenJimmyWtaunuNp5_pt20.merge.NTUP_TOP.e835_s1299_s1300_r3043_r2993_p937/

E.2.5. Z+jets Samples

Samples used to estimate the Z+jets background, created using Alpgen+Herwig/Jimmy:

mc11_7TeV.109300.AlpgenJimmyZeebbNp0_nofilter.merge.NTUP_TOP.e835_s1310_s1300_r3043_s2993_p937/

mc11_7TeV.109301.AlpgenJimmyZeebbNp1_nofilter.merge.NTUP_TOP.e835_s1310_s1300_r3043_s2993_p937/

mc11_7TeV.109302.AlpgenJimmyZeebbNp2_nofilter.merge.NTUP_TOP.e835_s1310_s1300_r3043_s2993_p937/

mc11_7TeV.109303.AlpgenJimmyZeebbNp3_nofilter.merge.NTUP_TOP.e835_s1310_s1300_r3043_s2993_p937/

mc11_7TeV.109305.AlpgenJimmyZmumubbNp0_nofilter.merge.NTUP_TOP.e835_s1310_s1300_r3043_s2993_p937/

mc11_7TeV.109306.AlpgenJimmyZmumubbNp1_nofilter.merge.NTUP_TOP.e835_s1310_s1300_r3043_s2993_p937/

mc11_7TeV.109307.AlpgenJimmyZmumubbNp2_nofilter.merge.NTUP_TOP.e835_s1310_s1300_r3043_s2993_p937/

mc11_7TeV.109308.AlpgenJimmyZmumubbNp3_nofilter.merge.NTUP_TOP.e835_s1310_s1300_r3043_s2993_p937/

mc11_7TeV.109310.AlpgenJimmyZtautaubbNp0_nofilter.merge.NTUP_TOP.e835_s1310_s1300_r3043_s2993_p937/

mc11_7TeV.109311.AlpgenJimmyZtautaubbNp1_nofilter.merge.NTUP_TOP.e835_s1310_s1300_r3043_s2993_p937/

mc11_7TeV.109312.AlpgenJimmyZtautaubbNp2_nofilter.merge.NTUP_TOP.e835_s1310_s1300_r3043_s2993_p937/

mc11_7TeV.109313.AlpgenJimmyZtautaubbNp3_nofilter.merge.NTUP_TOP.e835_s1310_s1300_r3043_s2993_p937/

mc11_7TeV.107650.AlpgenJimmyZeeNp0_pt20.merge.NTUP_TOP.e835_s1299_s1300_r3043_r2993_p937/

mc11_7TeV.107651.AlpgenJimmyZeeNp1_pt20.merge.NTUP_TOP.e835_s1299_s1300_r3043_r2993_p937/

mc11_7TeV.107652.AlpgenJimmyZeeNp2_pt20.merge.NTUP_TOP.e835_s1299_s1300_r3043_r2993_p937/

mc11_7TeV.107653.AlpgenJimmyZeeNp3_pt20.merge.NTUP_TOP.e835_s1299_s1300_r3043_r2993_p937/

mc11_7TeV.107654.AlpgenJimmyZeeNp4_pt20.merge.NTUP_TOP.e835_s1299_s1300_r3043_r2993_p937/

mc11_7TeV.107655.AlpgenJimmyZeeNp5_pt20.merge.NTUP_TOP.e835_s1299_s1300_r3043_r2993_p937/

mc11_7TeV.107660.AlpgenJimmyZmumuNp0_pt20.merge.NTUP_TOP.e835_s1299_s1300_r3043_r2993_p937/

mc11_7TeV.107661.AlpgenJimmyZmumuNp1_pt20.merge.NTUP_TOP.e835_s1299_s1300_r3043_r2993_p937/

mc11_7TeV.107662.AlpgenJimmyZmumuNp2_pt20.merge.NTUP_TOP.e835_s1299_s1300_r3043_r2993_p937/

mc11_7TeV.107663.AlpgenJimmyZmumuNp3_pt20.merge.NTUP_TOP.e835_s1299_s1300_r3043_r2993_p937/

mc11_7TeV.107664.AlpgenJimmyZmumuNp4_pt20.merge.NTUP_TOP.e835_s1299_s1300_r3043_r2993_p937/

mc11_7TeV.107665.AlpgenJimmyZmumuNp5_pt20.merge.NTUP_TOP.e835_s1299_s1300_r3043_r2993_p937/

mc11_7TeV.107670.AlpgenJimmyZtautauNp0_pt20.merge.NTUP_TOP.e835_s1299_s1300_r3043_r2993_p937/

mc11_7TeV.107671.AlpgenJimmyZtautauNp1_pt20.merge.NTUP_TOP.e835_s1299_s1300_r3043_r2993_p937/

mc11_7TeV.107672.AlpgenJimmyZtautauNp2_pt20.merge.NTUP_TOP.e835_s1299_s1300_r3043_r2993_p937/

mc11_7TeV.107673.AlpgenJimmyZtautauNp3_pt20.merge.NTUP_TOP.e835_s1299_s1300_r3043_r2993_p937/

mc11_7TeV.107674.AlpgenJimmyZtautauNp4_pt20.merge.NTUP_TOP.e835_s1299_s1300_r3043_r2993_p937/

mc11_7TeV.107675.AlpgenJimmyZtautauNp5_pt20.merge.NTUP_TOP.e835_s1299_s1300_r3043_r2993_p937/

mc11_7TeV.116250.AlpgenJimmyZeeNp0_Mll10to40_pt20.merge.NTUP_TOP.e959_s1310_s1300_r3043_r2993_p937/

mc11_7TeV.116251.AlpgenJimmyZeeNp1_Mll10to40_pt20.merge.NTUP_TOP.e959_s1310_s1300_r3043_r2993_p937/

mc11_7TeV.116252.AlpgenJimmyZeeNp2_Mll10to40_pt20.merge.NTUP_TOP.e944_s1310_s1300_r3043_r2993_p937/

mc11_7TeV.116253.AlpgenJimmyZeeNp3_Mll10to40_pt20.merge.NTUP_TOP.e944_s1310_s1300_r3043_r2993_p937/

mc11_7TeV.116254.AlpgenJimmyZeeNp4_Mll10to40_pt20.merge.NTUP_TOP.e944_s1310_s1300_r3043_r2993_p937/

mc11_7TeV.116255.AlpgenJimmyZeeNp5_Mll10to40_pt20.merge.NTUP_TOP.e944_s1310_s1300_r3043_r2993_p937/

mc11_7TeV.116260.AlpgenJimmyZmumuNp0_Mll10to40_pt20.merge.NTUP_TOP.e959_s1310_s1300_r3043_r2993_p937/

mc11_7TeV.116261.AlpgenJimmyZmumuNp1_Mll10to40_pt20.merge.NTUP_TOP.e959_s1310_s1300_r3043_r2993_p937/

mc11_7TeV.116262.AlpgenJimmyZmumuNp2_Mll10to40_pt20.merge.NTUP_TOP.e944_s1310_s1300_r3043_r2993_p937/

mc11_7TeV.116263.AlpgenJimmyZmumuNp3_Mll10to40_pt20.merge.NTUP_TOP.e944_s1310_s1300_r3043_r2993_p937/

mc11_7TeV.116264.AlpgenJimmyZmumuNp4_Mll10to40_pt20.merge.NTUP_TOP.e944_s1310_s1300_r3043_r2993_p937/

mc11_7TeV.116265.AlpgenJimmyZmumuNp5_Mll10to40_pt20.merge.NTUP_TOP.e944_s1310_s1300_r3043_r2993_p937/

mc11_7TeV.116270.AlpgenJimmyZtautauNp0_Mll10to40_pt20.merge.NTUP_TOP.e959_s1310_s1300_r3043_r2993_p937/

mc11_7TeV.116271.AlpgenJimmyZtautauNp1_Mll10to40_pt20.merge.NTUP_TOP.e959_s1310_s1300_r3043_r2993_p937/

mc11_7TeV.116272.AlpgenJimmyZtautauNp2_Mll10to40_pt20.merge.NTUP_TOP.e959_s1310_s1300_r3043_r2993_p937/

mc11_7TeV.116273.AlpgenJimmyZtautauNp3_Mll10to40_pt20.merge.NTUP_TOP.e959_s1310_s1300_r3043_r2993_p937/

mc11_7TeV.116274.AlpgenJimmyZtautauNp4_Mll10to40_pt20.merge.NTUP_TOP.e959_s1310_s1300_r3043_r2993_p937/

mc11_7TeV.116275.AlpgenJimmyZtautauNp5_Mll10to40_pt20.merge.NTUP_TOP.e959_s1310_s1300_r3043_r2993_p937/

E.2.6. Diboson Samples

Diboson samples created with Herwig or Alpgen+Jimmy:

mc11_7TeV.105985.WW_Herwig.merge.NTUP_TOP.e825_s1310_s1300_r3043_r2993_p937/

mc11_7TeV.105986.ZZ_Herwig.merge.NTUP_TOP.e825_s1310_s1300_r3043_r2993_p937/

mc11_7TeV.105987.WZ_Herwig.merge.NTUP_TOP.e825_s1310_s1300_r3043_r2993_p937/

mc11_7TeV.107100.AlpgenJimmyWWlnulnuNp0.merge.NTUP_TOP.e835_s1372_s1370_r3043_r2993_p937/

mc11_7TeV.107101.AlpgenJimmyWWlnulnuNp1.merge.NTUP_TOP.e835_s1372_s1370_r3043_r2993_p937/

mc11_7TeV.107102.AlpgenJimmyWWlnulnuNp2.merge.NTUP_TOP.e835_s1372_s1370_r3043_r2993_p937/

mc11_7TeV.107103.AlpgenJimmyWWlnulnuNp3.merge.NTUP_TOP.e835_s1372_s1370_r3043_r2993_p937/

mc11_7TeV.107104.AlpgenJimmyWZincllNp0.merge.NTUP_TOP.e995_s1372_s1370_r3043_r2993_p937/

mc11_7TeV.107105.AlpgenJimmyWZincllNp1.merge.NTUP_TOP.e995_s1372_s1370_r3043_r2993_p937/

mc11_7TeV.107106.AlpgenJimmyWZincllNp2.merge.NTUP_TOP.e995_s1372_s1370_r3043_r2993_p937/

mc11_7TeV.107107.AlpgenJimmyWZincllNp3.merge.NTUP_TOP.e995_s1372_s1370_r3043_r2993_p937/

mc11_7TeV.107108.AlpgenJimmyZZincllNp0.merge.NTUP_TOP.e995_s1372_s1370_r3043_r2993_p937/

mc11_7TeV.107109.AlpgenJimmyZZincllNp1.merge.NTUP_TOP.e995_s1372_s1370_r3043_r2993_p937/

mc11_7TeV.107110.AlpgenJimmyZZincllNp2.merge.NTUP_TOP.e995_s1372_s1370_r3043_r2993_p937/

mc11_7TeV.107111.AlpgenJimmyZZincllNp3.merge.NTUP_TOP.e995_s1372_s1370_r3043_r2993_p937/

E.2.7. $t\bar{t}$ Signal Samples

Samples used for $t\bar{t}$ baseline created using MC@NLO+Herwig:

mc11_7TeV.105200.T1_McAtNlo_Jimmy.merge.NTUP_TOP.e835_s1272_s1274_r3043_r2993_p937/

E.2.8. $t\bar{t}$ Mass Variation Samples

Samples used for the top mass systematic, created using MC@NLO+Herwig:

mc11_7TeV.106208.TTbar_McAtNlo_Jimmy_165GeV.merge.NTUP_TOP.e1021_a131_s1353_a145_r2993_p937/

mc11_7TeV.106205.TTbar_McAtNlo_Jimmy_167GeV.merge.NTUP_TOP.e1019_a131_s1353_a145_r2993_p937/

mc11_7TeV.106201.TTbar_McAtNlo_Jimmy_170GeV.merge.NTUP_TOP.e1021_a131_s1353_a145_r2993_p937/

mc11_7TeV.106206.TTbar_McAtNlo_Jimmy_175GeV.merge.NTUP_TOP.e1021_a131_s1353_a145_r2993_p937/

mc11_7TeV.106207.TTbar_McAtNlo_Jimmy_177GeV.merge.NTUP_TOP.e1019_a131_s1353_a145_r2993_p937/

mc11_7TeV.106202.TTbar_McAtNlo_Jimmy_180GeV.merge.NTUP_TOP.e967_a131_s1353_a145_r2993_p937/

Appendix F.

Systematic Tables

This appendix shows the tables of systematic uncertainties on the fitted values for $\alpha_\ell P$ and the cross section, σ, for the combined, channel separated, and charged separated fits for both the CPC and CPV scenarios.

F.1. CPC Systematic Tables

Table F.1.: Uncertainties on $\alpha_\ell P$ and σ for the ℓ+jets fit using both lepton charges for the CP conserving scenario.

Central values:	$\alpha_\ell P = -0.0336$		$\sigma = +177.57$	
Source of Uncertainty	$\Delta\alpha_\ell P$		$\Delta\sigma$	
Statistical Uncertainty	+0.0168	-0.0168	+0.98	-0.98
Electron identification and smearing	+0.0024	-0.0024	+1.861	-1.831
Electron reconstruction	+0.0006	-0.0006	+0.729	-0.724
Electron trigger	+0.0006	-0.0006	+0.467	-0.465
Electron scale	+0.0024	-0.0036	+0.235	-0.273

Continued on next page

Continued from previous page

Central values:	$\alpha_\ell P = -0.0336$		$\sigma = +177.57$	
Source of Uncertainty	$\Delta\alpha_\ell P$		$\Delta\sigma$	
Electron resolution	+0.0000	-0.0006	+0.044	-0.007
Muon identification	+0.0000	0.0000	+0.000	-0.000
Muon reconstruction	+0.0000	0.0000	+0.004	-0.003
Muon trigger	+0.0006	-0.0006	+0.005	-0.004
Muon rescaling	+0.0030	-0.0030	+0.038	-0.038
Muon spectrometer	+0.0006	0.0000	+0.000	-0.006
Muon tracker	+0.0006	0.0000	+0.000	-0.009
b-JES	+0.0066	-0.0078	+1.719	-1.558
JES Closeby	+0.0018	0.0000	+4.208	-3.991
JES Detector 1	+0.0126	-0.0138	+2.455	-2.335
JES Detector 2	+0.0012	0.0000	+0.182	-0.205
JES Eta Intercalib.Tot. Stat.	+0.0018	0.0000	+1.271	-1.202
JES Eta Intercalib. Theo.	+0.0156	-0.0168	+4.126	-3.852
JES flavor component	+0.0048	-0.0042	+2.054	-1.992
JES flavor response	+0.0036	-0.0030	+4.653	-4.543
JES mixed 1	+0.0018	0.0000	+0.209	-0.222
JES mixed 2	+0.0012	-0.0006	+0.848	-0.772
JES modelling 1	+0.0018	-0.0042	+5.207	-5.243

Continued on next page

Continued from previous page

Central values:	$\alpha_\ell P = -0.0336$		$\sigma = +177.57$	
Source of Uncertainty	$\Delta\alpha_\ell P$		$\Delta\sigma$	
JES modelling 2	+0.0072	-0.0042	+0.045	-0.103
JES modelling 3	+0.0090	-0.0060	+0.008	-0.048
JES modelling 4	+0.0012	0.0000	+0.158	-0.165
JES Pileup offset NPV	+0.0036	-0.0012	+0.837	-0.790
JES Pileup offset mu	+0.0006	0.0000	+6.974	-6.735
JES relative nonclosure	+0.0030	0.0000	+0.882	-0.873
JES single particle	+0.0000	0.0000	+0.002	-0.000
JES statistical 1	+0.0066	-0.0078	+2.917	-2.896
JES statistical 2	+0.0018	0.0000	+0.021	-0.035
JES statistical 3	+0.0042	-0.0030	+0.373	-0.393
Jet vertex fraction	+0.0006	-0.0012	+3.445	-2.868
Jet efficiency	+0.0012	-0.0012	+0.451	-0.448
Jet energy resolution	+0.0150	-0.0150	+5.318	-5.188
b-tag eff.	+0.0054	-0.0078	+9.657	-8.084
c-tag eff.	+0.0042	-0.0042	+2.786	-2.734
mistag rate	+0.0024	-0.0024	+2.500	-2.485
Pile up	+0.0042	-0.0012	+7.024	-6.782
Cellout	+0.0030	-0.0024	+0.042	-0.097

Continued on next page

Continued from previous page

Central values:	$\alpha_\ell P = -0.0336$		$\sigma = +177.57$	
Source of Uncertainty	$\Delta\alpha_\ell P$		$\Delta\sigma$	
W heavy flavor factors	+0.0090	-0.0096	+4.711	-4.835
W iqopt3	+0.0012	-0.0012	+0.755	-0.752
W ptjmin	+0.0012	-0.0012	+0.163	-0.162
QCD/Fakes	+0.0114	-0.0078	+0.089	-0.114
MC Generator	+0.0006	-0.0006	+9.780	-8.812
Color reconnection	+0.0006	-0.0006	+0.202	-0.205
ISR/FSR variation	+0.0018	-0.0018	+1.184	-1.174
Fragmentation/Parton shower	+0.0018	-0.0018	+0.070	-0.074
Underlying event	+0.0006	-0.0006	+0.063	-0.065
CT10 PDF	+0.0018	-0.0018	+7.864	-7.620
Spin correlation value	+0.0024	-0.0024	+0.042	-0.042
Monte Carlo background x-section	+0.0060	-0.0060	+3.671	-3.909
Monte Carlo signal & bkg branching ratio	+0.001	-0.001	+1.623	-1.594
Monte Carlo statistics	+0.0006	-0.0006	+0.348	-0.347
Luminosity	+0.0000	0.0000	+3.559	-3.431
Template statistics for template fits	+0.0060	-0.0060	+0.000	-0.000
Top Mass	+0.0120	-0.0120	+2.474	-2.474

Continued on next page

Continued from previous page

Central values:	$\alpha_\ell P = -0.0336$	$\sigma = +177.57$
Source of Uncertainty	$\Delta\alpha_\ell P$	$\Delta\sigma$
InterPDF	+0.0012 -0.0012	+6.500 -6.500
Total Systematic Uncertainty	+0.0378 -0.0372	+26.722 -25.342

Table F.2.: Uncertainties on $\alpha_\ell P$ and σ for the ℓ+jets fit using negatively charged leptons for the CP conserving scenario.

Central values:	$\alpha_\ell P = -0.0534$	$\sigma = +177.56$
Source of Uncertainty	$\Delta\alpha_\ell P$	$\Delta\sigma$
Statistical Uncertainty	+0.0234 -0.0234	+1.37 -1.36
Electron identification and smearing	+0.0024 -0.0024	+1.791 -1.763
Electron reconstruction	+0.0006 -0.0006	+0.705 -0.699
Electron trigger	+0.0006 -0.0006	+0.450 -0.447
Electron scale	+0.0018 -0.0036	+0.240 -0.249
Electron resolution	+0.0000 0.0000	+0.082 -0.000
Muon identification	+0.0000 0.0000	+0.000 -0.000
Muon reconstruction	+0.0000 0.0000	+0.004 -0.004
Muon trigger	+0.0006 -0.0006	+0.005 -0.005
Muon rescaling	+0.0108 -0.0090	+0.101 -0.113

Continued on next page

Continued from previous page

Central values:	$\alpha_\ell P = -0.0534$		$\sigma = +177.56$	
Source of Uncertainty	$\Delta\alpha_\ell P$		$\Delta\sigma$	
Muon spectrometer	+0.0006	0.0000	+0.000	-0.005
Muon tracker	+0.0006	0.0000	+0.003	-0.004
b-JES	+0.0060	-0.0090	+1.692	-1.492
JES Closeby	+0.0030	-0.0024	+3.989	-3.829
JES Detector 1	+0.0126	-0.0126	+2.301	-2.173
JES Detector 2	+0.0000	-0.0006	+0.210	-0.184
JES Eta Intercalib.Tot. Stat.	+0.0012	0.0000	+1.179	-1.110
JES Eta Intercalib. Theo.	+0.0150	-0.0150	+4.009	-3.678
JES flavor component	+0.0042	-0.0030	+1.914	-1.846
JES flavor response	+0.0024	-0.0006	+4.363	-4.246
JES mixed 1	+0.0012	-0.0018	+0.237	-0.207
JES mixed 2	+0.0018	-0.0024	+0.780	-0.701
JES modelling 1	+0.0042	-0.0054	+4.852	-4.928
JES modelling 2	+0.0048	-0.0066	+0.091	-0.077
JES modelling 3	+0.0072	-0.0066	+0.017	-0.002
JES modelling 4	+0.0006	-0.0006	+0.165	-0.146
JES Pileup offset NPV	+0.0036	-0.0006	+0.730	-0.737
JES Pileup offset mu	+0.0024	0.0000	+6.568	-6.256

Continued on next page

Continued from previous page

Central values:	$\alpha_\ell P = -0.0534$		$\sigma = +177.56$	
Source of Uncertainty	$\Delta\alpha_\ell P$		$\Delta\sigma$	
JES relative nonclosure	+0.0012	-0.0012	+0.834	-0.774
JES single particle	+0.0000	0.0000	+0.002	-0.000
JES statistical 1	+0.0090	-0.0078	+2.768	-2.681
JES statistical 2	+0.0006	-0.0018	+0.046	-0.019
JES statistical 3	+0.0036	-0.0036	+0.388	-0.375
Jet vertex fraction	+0.0012	-0.0018	+3.316	-2.742
Jet efficiency	+0.0018	-0.0018	+1.099	-1.090
Jet energy resolution	+0.0162	-0.0186	+19.929	-18.271
b-tag eff.	+0.0042	-0.0060	+9.383	-7.840
c-tag eff.	+0.0054	-0.0054	+2.569	-2.526
mistag rate	+0.0036	-0.0036	+2.070	-2.053
Pile up	+0.0042	-0.0018	+6.608	-6.299
Cellout	+0.0024	-0.0024	+0.054	-0.083
W heavy flavor factors	+0.0108	-0.0114	+3.650	-3.823
W iqopt3	+0.0006	-0.0006	+0.558	-0.558
W ptjmin	+0.0012	-0.0012	+0.215	-0.215
QCD/Fakes	+0.0108	-0.0072	+0.086	-0.111
MC Generator	+0.0030	-0.0030	+9.642	-8.695

Continued on next page

Continued from previous page

Central values:	$\alpha_\ell P = -0.0534$		$\sigma = +177.56$	
Source of Uncertainty	$\Delta\alpha_\ell P$		$\Delta\sigma$	
Color reconnection	+0.0012	-0.0012	+0.222	-0.225
ISR/FSR variation	+0.0006	-0.0006	+1.180	-1.167
Fragmentation/Parton shower	+0.0048	-0.0048	+0.076	-0.079
Underlying event	+0.0030	-0.0030	+0.031	-0.035
CT10 PDF	+0.0018	-0.0018	+7.878	-7.633
Spin correlation value	+0.0024	-0.0024	+0.046	-0.046
Monte Carlo background x-section	+0.0084	-0.0090	+3.121	-3.309
Monte Carlo signal & bkg branching ratio	+0.001	-0.001	+1.623	-1.594
Monte Carlo statistics	+0.0012	-0.0012	+0.458	-0.458
Luminosity	+0.0000	0.0000	+3.524	-3.396
Template statistics for template fits	+0.0084	-0.0084	+0.000	-0.000
Top Mass	+0.0114	-0.0114	+2.445	-2.445
InterPDF	+0.0012	-0.0012	+6.470	-6.470
Total Systematic Uncertainty	+0.0402	-0.0408	+32.188	-30.041

Table F.3.: Uncertainties on $\alpha_\ell P$ and σ for the ℓ+jets fit using positively charged leptons for the CP conserving scenario.

Central values:	$\alpha_\ell P = -0.0126$		$\sigma = +177.57$	
Source of Uncertainty	$\Delta\alpha_\ell P$		$\Delta\sigma$	
Statistical Uncertainty	+0.0246	-0.0246	+1.41	-1.41
Electron identification and smearing	+0.0018	-0.0018	+1.936	-1.906
Electron reconstruction	+0.0000	0.0000	+0.755	-0.750
Electron trigger	+0.0000	0.0000	+0.485	-0.484
Electron scale	+0.0030	-0.0042	+0.230	-0.297
Electron resolution	+0.0006	-0.0012	+0.004	-0.033
Muon identification	+0.0000	0.0000	+0.000	-0.000
Muon reconstruction	+0.0000	-0.0006	+0.004	-0.003
Muon trigger	+0.0000	-0.0006	+0.004	-0.004
Muon rescaling	+0.0180	-0.0150	+0.177	-0.194
Muon spectrometer	+0.0006	0.0000	+0.000	-0.010
Muon tracker	+0.0012	0.0000	+0.000	-0.013
b-JES	+0.0066	-0.0066	+1.747	-1.627
JES Closeby	+0.0030	0.0000	+4.441	-4.163
JES Detector 1	+0.0126	-0.0156	+2.618	-2.506
JES Detector 2	+0.0036	0.0000	+0.150	-0.228
JES Eta Intercalib.Tot. Stat.	+0.0030	-0.0006	+1.368	-1.299

Continued on next page

Continued from previous page

Central values:	$\alpha_\ell P = -0.0126$		$\sigma = +177.57$	
Source of Uncertainty	$\Delta\alpha_\ell P$		$\Delta\sigma$	
JES Eta Intercalib. Theo.	+0.0162	-0.0186	+4.251	-4.041
JES flavor component	+0.0054	-0.0060	+2.201	-2.148
JES flavor response	+0.0048	-0.0054	+4.963	-4.856
JES mixed 1	+0.0024	0.0000	+0.179	-0.239
JES mixed 2	+0.0012	0.0000	+0.922	-0.851
JES modelling 1	+0.0000	-0.0030	+5.587	-5.577
JES modelling 2	+0.0096	-0.0024	+0.000	-0.133
JES modelling 3	+0.0102	-0.0048	+0.000	-0.097
JES modelling 4	+0.0018	0.0000	+0.151	-0.187
JES Pileup offset NPV	+0.0036	-0.0012	+0.952	-0.846
JES Pileup offset mu	+0.0012	-0.0030	+7.402	-7.247
JES relative nonclosure	+0.0048	0.0000	+0.930	-0.980
JES single particle	+0.0000	0.0000	+0.002	-0.000
JES statistical 1	+0.0048	-0.0072	+3.076	-3.125
JES statistical 2	+0.0024	0.0000	+0.000	-0.053
JES statistical 3	+0.0048	-0.0018	+0.355	-0.412
Jet vertex fraction	+0.0000	-0.0006	+3.581	-3.003
Jet efficiency	+0.0018	-0.0018	+1.289	-1.276

Continued on next page

Continued from previous page

Central values:	$\alpha_\ell P = -0.0126$		$\sigma = +177.57$	
Source of Uncertainty	$\Delta\alpha_\ell P$		$\Delta\sigma$	
Jet energy resolution	+0.0270	-0.0300	+21.701	-19.949
b-tag eff.	+0.0072	-0.0096	+9.945	-8.340
c-tag eff.	+0.0024	-0.0024	+3.018	-2.956
mistag rate	+0.0006	-0.0012	+2.957	-2.948
Pile up	+0.0048	-0.0030	+7.463	-7.297
Cellout	+0.0036	-0.0024	+0.038	-0.112
W heavy flavor factors	+0.0132	-0.0138	+6.175	-6.234
W iqopt3	+0.0018	-0.0018	+1.081	-1.078
W ptjmin	+0.0006	-0.0006	+0.405	-0.401
QCD/Fakes	+0.0120	-0.0078	+0.093	-0.115
MC Generator	+0.0024	-0.0024	+9.925	-8.926
Color reconnection	+0.0000	0.0000	+0.183	-0.185
ISR/FSR variation	+0.0030	-0.0030	+1.187	-1.179
Fragmentation/Parton shower	+0.0006	-0.0006	+0.064	-0.066
Underlying event	+0.0012	-0.0012	+0.098	-0.100
CT10 PDF	+0.0018	-0.0018	+7.848	-7.604
Spin correlation value	+0.0024	-0.0024	+0.038	-0.038
Monte Carlo background x-section	+0.0036	-0.0036	+4.296	-4.592

Continued on next page

Continued from previous page

Central values:	$\alpha_\ell P = -0.0126$		$\sigma = +177.57$	
Source of Uncertainty	$\Delta\alpha_\ell P$		$\Delta\sigma$	
Monte Carlo signal & bkg branching ratio	+0.001	-0.001	+1.623	-1.594
Monte Carlo statistics	+0.0006	-0.0006	+0.527	-0.527
Luminosity	+0.0006	-0.0006	+3.597	-3.467
Template statistics for template fits	+0.0096	-0.0096	+0.000	-0.000
Top Mass	+0.0126	-0.0126	+2.504	-2.504
InterPDF	+0.0012	-0.0012	+6.540	-6.540
Total Systematic Uncertainty	+0.0504	-0.0498	+34.922	-32.800

Table F.4.: Uncertainties on $\alpha_\ell P$ and σ for the e+jets fit using both lepton charges for the CP conserving scenario.

Central values:	$\alpha_\ell P = -0.0306$		$\sigma = +174.22$	
Source of Uncertainty	$\Delta\alpha_\ell P$		$\Delta\sigma$	
Statistical Uncertainty	+0.0282	-0.0282	+1.59	-1.59
Electron identification and smearing	+0.0018	-0.0018	+4.866	-4.655
Electron reconstruction	+0.0006	-0.0006	+1.893	-1.858
Electron trigger	+0.0000	0.0000	+1.209	-1.195
Electron scale	+0.0060	-0.0096	+0.590	-0.674

Continued on next page

Continued from previous page

Central values:	$\alpha_\ell P = -0.0306$		$\sigma = +174.22$	
Source of Uncertainty	$\Delta\alpha_\ell P$		$\Delta\sigma$	
Electron resolution	+0.0006	-0.0018	+0.119	-0.018
Muon identification	+0.0000	0.0000	+0.000	-0.000
Muon reconstruction	+0.0000	0.0000	+0.000	-0.000
Muon trigger	+0.0000	0.0000	+0.000	-0.000
Muon rescaling	+0.0000	0.0000	+0.000	-0.000
Muon spectrometer	+0.0000	0.0000	+0.000	-0.000
Muon tracker	+0.0000	0.0000	+0.000	-0.000
b-JES	+0.0084	-0.0084	+1.800	-1.709
JES Closeby	+0.0012	-0.0018	+4.516	-4.147
JES Detector 1	+0.0138	-0.0138	+2.565	-2.494
JES Detector 2	+0.0018	0.0000	+0.170	-0.184
JES Eta Intercalib.Tot. Stat.	+0.0018	0.0000	+1.232	-1.241
JES Eta Intercalib. Theo.	+0.0192	-0.0192	+4.287	-4.068
JES flavor component	+0.0060	-0.0054	+2.090	-2.005
JES flavor response	+0.0060	-0.0030	+4.619	-4.565
JES mixed 1	+0.0012	0.0000	+0.182	-0.181
JES mixed 2	+0.0030	-0.0012	+0.815	-0.789
JES modelling 1	+0.0000	-0.0006	+5.223	-5.283

Continued on next page

Continued from previous page

Central values:	$\alpha_\ell P = -0.0306$		$\sigma = +174.22$	
Source of Uncertainty	$\Delta\alpha_\ell P$		$\Delta\sigma$	
JES modelling 2	+0.0072	-0.0030	+0.009	-0.083
JES modelling 3	+0.0096	-0.0036	+0.059	-0.118
JES modelling 4	+0.0006	0.0000	+0.149	-0.134
JES Pileup offset NPV	+0.0084	-0.0006	+0.814	-0.819
JES Pileup offset mu	+0.0054	-0.0024	+6.946	-6.892
JES relative nonclosure	+0.0048	-0.0006	+0.938	-0.950
JES single particle	+0.0000	0.0000	+0.003	-0.000
JES statistical 1	+0.0072	-0.0042	+2.866	-2.859
JES statistical 2	+0.0012	0.0000	+0.025	-0.033
JES statistical 3	+0.0060	-0.0024	+0.405	-0.429
Jet vertex fraction	+0.0000	-0.0006	+3.330	-2.750
Jet efficiency	+0.0006	-0.0006	+0.581	-0.579
Jet energy resolution	+0.0150	-0.0150	+6.173	-6.007
b-tag eff.	+0.0054	-0.0078	+9.523	-7.951
c-tag eff.	+0.0036	-0.0036	+2.442	-2.393
mistag rate	+0.0024	-0.0024	+2.249	-2.224
Pile up	+0.0096	-0.0030	+6.994	-6.940
Cellout	+0.0024	-0.0024	+0.067	-0.084

Continued on next page

Continued from previous page

Central values:	$\alpha_\ell P = -0.0306$		$\sigma = +174.22$	
Source of Uncertainty	$\Delta\alpha_\ell P$		$\Delta\sigma$	
W heavy flavor factors	+0.0084	-0.0084	+4.739	-4.562
W iqopt3	+0.0006	-0.0006	+0.705	-0.704
W ptjmin	+0.0012	-0.0012	+0.132	-0.132
QCD/Fakes	+0.0024	-0.0078	+0.135	-0.045
MC Generator	+0.0012	-0.0012	+10.167	-9.118
Color reconnection	+0.0000	-0.0006	+0.664	-0.661
ISR/FSR variation	+0.0012	-0.0012	+2.463	-2.400
Fragmentation/Parton shower	+0.0024	-0.0024	+0.492	-0.496
Underlying event	+0.0036	-0.0036	+0.140	-0.143
CT10 PDF	+0.0018	-0.0018	+7.650	-7.419
Spin correlation value	+0.0024	-0.0024	+0.048	-0.049
Monte Carlo background x-section	+0.0066	-0.0072	+4.588	-4.581
Monte Carlo signal & bkg branching ratio	+0.001	-0.001	+1.605	-1.575
Monte Carlo statistics	+0.0006	-0.0006	+0.503	-0.503
Luminosity	+0.0000	0.0000	+3.518	-3.391
Template statistics for template fits	+0.0102	-0.0102	+0.000	-0.000
Top Mass	+0.0132	-0.0132	+2.629	-2.629

Continued on next page

Continued from previous page

Central values:	$\alpha_\ell P = -0.0306$	$\sigma = +174.22$
Source of Uncertainty	$\Delta\alpha_\ell P$	$\Delta\sigma$
InterPDF	+0.0036 -0.0036	+6.870 -6.870
Total Systematic Uncertainty	+0.0432 -0.0396	+27.626 -26.237

Table F.5.: Uncertainties on $\alpha_\ell P$ and σ for the e+jets fit using negatively charged leptons for the CP conserving scenario.

Central values:	$\alpha_\ell P = -0.0312$	$\sigma = +174.23$
Source of Uncertainty	$\Delta\alpha_\ell P$	$\Delta\sigma$
Statistical Uncertainty	+0.0390 -0.0390	+2.22 -2.21
Electron identification and smearing	+0.0024 -0.0024	+4.702 -4.498
Electron reconstruction	+0.0006 0.0000	+1.839 -1.803
Electron trigger	+0.0000 0.0000	+1.169 -1.153
Electron scale	+0.0048 -0.0090	+0.606 -0.616
Electron resolution	+0.0006 -0.0006	+0.214 -0.000
Muon identification	+0.0000 0.0000	+0.000 -0.000
Muon reconstruction	+0.0000 0.0000	+0.000 -0.000
Muon trigger	+0.0000 0.0000	+0.000 -0.000
Muon rescaling	+0.0000 0.0000	+0.000 -0.000

Continued on next page

Continued from previous page

Central values:	$\alpha_\ell P = -0.0312$		$\sigma = +174.23$	
Source of Uncertainty	$\Delta\alpha_\ell P$		$\Delta\sigma$	
Muon spectrometer	+0.0000	0.0000	+0.000	-0.000
Muon tracker	+0.0000	0.0000	+0.000	-0.000
b-JES	+0.0114	-0.0102	+1.848	-1.688
JES Closeby	+0.0012	-0.0030	+4.361	-4.032
JES Detector 1	+0.0144	-0.0108	+2.378	-2.308
JES Detector 2	+0.0000	0.0000	+0.186	-0.186
JES Eta Intercalib.Tot. Stat.	+0.0024	0.0000	+1.088	-1.188
JES Eta Intercalib. Theo.	+0.0204	-0.0186	+4.215	-3.906
JES flavor component	+0.0048	-0.0054	+2.010	-1.835
JES flavor response	+0.0042	-0.0024	+4.354	-4.218
JES mixed 1	+0.0018	0.0000	+0.182	-0.186
JES mixed 2	+0.0042	-0.0012	+0.733	-0.726
JES modelling 1	+0.0018	-0.0012	+4.892	-4.938
JES modelling 2	+0.0054	-0.0054	+0.046	-0.061
JES modelling 3	+0.0078	-0.0048	+0.074	-0.078
JES modelling 4	+0.0006	0.0000	+0.134	-0.129
JES Pileup offset NPV	+0.0066	0.0000	+0.728	-0.710
JES Pileup offset mu	+0.0066	-0.0012	+6.527	-6.375

Continued on next page

Continued from previous page

Central values:	$\alpha_\ell P = -0.0312$		$\sigma = +174.23$	
Source of Uncertainty	$\Delta\alpha_\ell P$		$\Delta\sigma$	
JES relative nonclosure	+0.0036	-0.0024	+0.889	-0.797
JES single particle	+0.0000	0.0000	+0.006	-0.000
JES statistical 1	+0.0090	-0.0072	+2.755	-2.586
JES statistical 2	+0.0012	-0.0012	+0.046	-0.023
JES statistical 3	+0.0054	-0.0030	+0.402	-0.445
Jet vertex fraction	+0.0006	-0.0012	+3.215	-2.636
Jet efficiency	+0.0012	-0.0012	+1.562	-1.544
Jet energy resolution	+0.0048	-0.0066	+22.841	-20.600
b-tag eff.	+0.0060	-0.0078	+9.272	-7.727
c-tag eff.	+0.0042	-0.0042	+2.220	-2.182
mistag rate	+0.0042	-0.0042	+1.875	-1.855
Pile up	+0.0096	-0.0024	+6.571	-6.415
Cellout	+0.0024	-0.0036	+0.232	-0.046
W heavy flavor factors	+0.0108	-0.0108	+3.566	-3.446
W iqopt3	+0.0012	-0.0012	+0.562	-0.562
W ptjmin	+0.0012	-0.0012	+0.217	-0.217
QCD/Fakes	+0.0018	-0.0072	+0.128	-0.042
MC Generator	+0.0012	-0.0012	+10.004	-8.970

Continued on next page

Continued from previous page

Central values:	$\alpha_\ell P = -0.0312$		$\sigma = +174.23$	
Source of Uncertainty	$\Delta\alpha_\ell P$		$\Delta\sigma$	
Color reconnection	+0.0036	-0.0036	+0.763	-0.758
ISR/FSR variation	+0.0018	-0.0018	+2.347	-2.287
Fragmentation/Parton shower	+0.0042	-0.0042	+0.472	-0.479
Underlying event	+0.0072	-0.0072	+0.065	-0.067
CT10 PDF	+0.0024	-0.0024	+7.653	-7.420
Spin correlation value	+0.0024	-0.0024	+0.046	-0.046
Monte Carlo background x-section	+0.0096	-0.0096	+3.854	-3.851
Monte Carlo signal & bkg branching ratio	+0.001	-0.001	+1.607	-1.577
Monte Carlo statistics	+0.0012	-0.0012	+0.666	-0.664
Luminosity	+0.0000	0.0000	+3.483	-3.357
Template statistics for template fits	+0.0138	-0.0138	+0.000	-0.000
Top Mass	+0.0132	-0.0132	+2.614	-2.614
InterPDF	+0.0042	-0.0042	+6.870	-6.870
Total Systematic Uncertainty	+0.0444	-0.0402	+34.608	-32.022

Table F.6.: Uncertainties on $\alpha_\ell P$ and σ for the e+jets fit using positively charged leptons for the CP conserving scenario.

Central values:	$\alpha_\ell P = -0.03$		$\sigma = +174.20$	
Source of Uncertainty	$\Delta\alpha_\ell P$		$\Delta\sigma$	
Statistical Uncertainty	+0.0414	-0.0408	+2.29	-2.27
Electron identification and smearing	+0.0012	-0.0012	+5.036	-4.823
Electron reconstruction	+0.0006	-0.0006	+1.950	-1.918
Electron trigger	+0.0000	0.0000	+1.251	-1.238
Electron scale	+0.0072	-0.0108	+0.572	-0.732
Electron resolution	+0.0018	-0.0042	+0.024	-0.090
Muon identification	+0.0000	0.0000	+0.000	-0.000
Muon reconstruction	+0.0000	0.0000	+0.000	-0.000
Muon trigger	+0.0000	0.0000	+0.000	-0.000
Muon rescaling	+0.0000	0.0000	+0.000	-0.000
Muon spectrometer	+0.0000	0.0000	+0.000	-0.000
Muon tracker	+0.0000	0.0000	+0.000	-0.000
b-JES	+0.0048	-0.0060	+1.749	-1.727
JES Closeby	+0.0054	-0.0054	+4.681	-4.272
JES Detector 1	+0.0138	-0.0168	+2.762	-2.689
JES Detector 2	+0.0036	0.0000	+0.154	-0.182
JES Eta Intercalib.Tot. Stat.	+0.0012	0.0000	+1.382	-1.293

Continued on next page

Continued from previous page

Central values:	$\alpha_\ell P = -0.03$		$\sigma = +174.20$	
Source of Uncertainty	$\Delta\alpha_\ell P$		$\Delta\sigma$	
JES Eta Intercalib. Theo.	+0.0174	-0.0198	+4.362	-4.240
JES flavor component	+0.0078	-0.0060	+2.172	-2.187
JES flavor response	+0.0084	-0.0036	+4.902	-4.929
JES mixed 1	+0.0018	0.0000	+0.184	-0.174
JES mixed 2	+0.0024	-0.0012	+0.902	-0.855
JES modelling 1	+0.0012	-0.0030	+5.576	-5.648
JES modelling 2	+0.0090	-0.0006	+0.000	-0.108
JES modelling 3	+0.0114	-0.0024	+0.043	-0.161
JES modelling 4	+0.0012	-0.0006	+0.165	-0.138
JES Pileup offset NPV	+0.0102	-0.0018	+0.908	-0.935
JES Pileup offset mu	+0.0042	-0.0042	+7.389	-7.434
JES relative nonclosure	+0.0066	0.0000	+0.988	-1.114
JES single particle	+0.0000	0.0000	+0.001	-0.000
JES statistical 1	+0.0054	-0.0006	+2.985	-3.148
JES statistical 2	+0.0018	0.0000	+0.003	-0.043
JES statistical 3	+0.0060	-0.0012	+0.408	-0.411
Jet vertex fraction	+0.0000	-0.0006	+3.451	-2.871
Jet efficiency	+0.0000	0.0000	+1.756	-1.737

Continued on next page

Continued from previous page

Central values:	$\alpha_\ell P = -0.03$		$\sigma = +174.20$	
Source of Uncertainty	$\Delta\alpha_\ell P$		$\Delta\sigma$	
Jet energy resolution	+0.0216	-0.0258	+23.823	-21.600
b-tag eff.	+0.0048	-0.0072	+9.780	-8.190
c-tag eff.	+0.0030	-0.0030	+2.676	-2.616
mistag rate	+0.0006	-0.0006	+2.645	-2.615
Pile up	+0.0108	-0.0048	+7.444	-7.493
Cellout	+0.0042	-0.0030	+0.052	-0.153
W heavy flavor factors	+0.0084	-0.0084	+6.155	-5.935
W iqopt3	+0.0006	-0.0006	+1.001	-1.000
W ptjmin	+0.0006	-0.0006	+0.336	-0.336
QCD/Fakes	+0.0030	-0.0084	+0.152	-0.054
MC Generator	+0.0042	-0.0042	+10.355	-9.262
Color reconnection	+0.0048	-0.0048	+0.558	-0.555
ISR/FSR variation	+0.0000	0.0000	+2.584	-2.515
Fragmentation/Parton shower	+0.0006	-0.0012	+0.513	-0.510
Underlying event	+0.0000	0.0000	+0.363	-0.363
CT10 PDF	+0.0018	-0.0018	+7.648	-7.415
Spin correlation value	+0.0024	-0.0024	+0.052	-0.052
Monte Carlo background x-section	+0.0036	-0.0036	+5.414	-5.414

Continued on next page

Continued from previous page

Central values:	$\alpha_\ell P = -0.03$		$\sigma = +174.20$	
Source of Uncertainty	$\Delta\alpha_\ell P$		$\Delta\sigma$	
Monte Carlo signal & bkg branching ratio	+0.001	-0.001	+1.603	-1.574
Monte Carlo statistics	+0.0006	-0.0006	+0.760	-0.760
Luminosity	+0.0006	-0.0006	+3.553	-3.427
Template statistics for template fits	+0.0156	-0.0156	+0.000	-0.000
Top Mass	+0.0132	-0.0132	+2.650	-2.650
InterPDF	+0.0024	-0.0024	+6.870	-6.870
Total Systematic Uncertainty	+0.0486	-0.0480	+36.876	-34.471

Table F.7.: Uncertainties on $\alpha_\ell P$ and σ for the μ+jets fit using both lepton charges for the CP conserving scenario.

Central values:	$\alpha_\ell P = -0.033$		$\sigma = +179.64$	
Source of Uncertainty	$\Delta\alpha_\ell P$		$\Delta\sigma$	
Statistical Uncertainty	+0.0210	-0.0210	+1.25	-1.25
Electron identification and smearing	+0.0000	0.0000	+0.000	-0.000
Electron reconstruction	+0.0000	0.0000	+0.000	-0.000
Electron trigger	+0.0000	0.0000	+0.000	-0.000
Electron scale	+0.0000	0.0000	+0.000	-0.000

Continued on next page

Continued from previous page

Central values:	$\alpha_\ell P = -0.033$		$\sigma = +179.64$	
Source of Uncertainty	$\Delta\alpha_\ell P$		$\Delta\sigma$	
Electron resolution	+0.0000	0.0000	+0.000	-0.000
Muon identification	+0.0000	0.0000	+0.000	-0.000
Muon reconstruction	+0.0006	-0.0006	+0.005	-0.005
Muon trigger	+0.0006	-0.0006	+0.007	-0.006
Muon rescaling	+0.0054	-0.0054	+0.053	-0.052
Muon spectrometer	+0.0012	0.0000	+0.000	-0.008
Muon tracker	+0.0012	0.0000	+0.000	-0.012
b-JES	+0.0054	-0.0078	+1.668	-1.466
JES Closeby	+0.0036	0.0000	+4.024	-3.890
JES Detector 1	+0.0120	-0.0144	+2.384	-2.236
JES Detector 2	+0.0012	0.0000	+0.186	-0.215
JES Eta Intercalib.Tot. Stat.	+0.0024	-0.0006	+1.289	-1.177
JES Eta Intercalib. Theo.	+0.0138	-0.0150	+4.032	-3.724
JES flavor component	+0.0036	-0.0036	+2.032	-1.986
JES flavor response	+0.0024	-0.0030	+4.673	-4.531
JES mixed 1	+0.0024	-0.0006	+0.223	-0.246
JES mixed 2	+0.0006	0.0000	+0.863	-0.759
JES modelling 1	+0.0030	-0.0066	+5.202	-5.228

Continued on next page

Continued from previous page

Central values:	$\alpha_\ell P = -0.033$		$\sigma = +179.64$	
Source of Uncertainty	$\Delta\alpha_\ell P$		$\Delta\sigma$	
JES modelling 2	+0.0072	-0.0054	+0.067	-0.119
JES modelling 3	+0.0084	-0.0072	+0.000	-0.029
JES modelling 4	+0.0018	0.0000	+0.162	-0.181
JES Pileup offset NPV	+0.0012	-0.0012	+0.850	-0.784
JES Pileup offset mu	+0.0012	-0.0018	+6.992	-6.647
JES relative nonclosure	+0.0018	0.0000	+0.846	-0.830
JES single particle	+0.0000	0.0000	+0.001	-0.000
JES statistical 1	+0.0066	-0.0096	+2.947	-2.928
JES statistical 2	+0.0018	0.0000	+0.019	-0.034
JES statistical 3	+0.0036	-0.0030	+0.351	-0.374
Jet vertex fraction	+0.0006	-0.0018	+3.517	-2.943
Jet efficiency	+0.0012	-0.0012	+0.371	-0.368
Jet energy resolution	+0.0138	-0.0144	+4.781	-4.675
b-tag eff.	+0.0054	-0.0078	+9.739	-8.165
c-tag eff.	+0.0042	-0.0042	+3.001	-2.946
mistag rate	+0.0024	-0.0024	+2.654	-2.647
Pile up	+0.0018	-0.0018	+7.044	-6.693
Cellout	+0.0036	-0.0024	+0.055	-0.175

Continued on next page

Continued from previous page

Central values:	$\alpha_\ell P = -0.033$		$\sigma = +179.64$	
Source of Uncertainty	$\Delta\alpha_\ell P$		$\Delta\sigma$	
W heavy flavor factors	+0.0090	-0.0102	+4.709	-5.018
W iqopt3	+0.0018	-0.0018	+0.783	-0.779
W ptjmin	+0.0012	-0.0012	+0.183	-0.181
QCD/Fakes	+0.0180	-0.0114	+0.104	-0.152
MC Generator	+0.0012	-0.0012	+9.534	-8.620
Color reconnection	+0.0018	-0.0012	+0.091	-0.094
ISR/FSR variation	+0.0012	-0.0012	+0.382	-0.382
Fragmentation/Parton shower	+0.0024	-0.0024	+0.195	-0.196
Underlying event	+0.0036	-0.0036	+0.208	-0.209
CT10 PDF	+0.0018	-0.0018	+8.001	-7.748
Spin correlation value	+0.0024	-0.0024	+0.038	-0.038
Monte Carlo background x-section	+0.0072	-0.0090	+4.743	-5.306
Monte Carlo signal & bkg branching ratio	+0.001	-0.001	+1.634	-1.605
Monte Carlo statistics	+0.0006	-0.0006	+0.450	-0.450
Luminosity	+0.0000	0.0000	+3.584	-3.457
Template statistics for template fits	+0.0078	-0.0078	+0.000	-0.000
Top Mass	+0.0120	-0.0120	+2.360	-2.360

Continued on next page

Continued from previous page

Central values:	$\alpha_\ell P = -0.033$		$\sigma = +179.64$	
Source of Uncertainty	$\Delta\alpha_\ell P$		$\Delta\sigma$	
InterPDF	+0.0012	-0.0012	+6.270	-6.270
Total Systematic Uncertainty	+0.0396	-0.0396	+26.693	-25.380

Table F.8.: Uncertainties on $\alpha_\ell P$ and σ for the μ+jets fit using negatively charged leptons for the CP conserving scenario.

Central values:	$\alpha_\ell P = -0.0636$		$\sigma = +179.54$	
Source of Uncertainty	$\Delta\alpha_\ell P$		$\Delta\sigma$	
Statistical Uncertainty	+0.0294	-0.0294	+1.74	-1.73
Electron identification and smearing	+0.0000	0.0000	+0.000	-0.000
Electron reconstruction	+0.0000	0.0000	+0.000	-0.000
Electron trigger	+0.0000	0.0000	+0.000	-0.000
Electron scale	+0.0000	0.0000	+0.000	-0.000
Electron resolution	+0.0000	0.0000	+0.000	-0.000
Muon identification	+0.0000	0.0000	+0.000	-0.000
Muon reconstruction	+0.0006	-0.0006	+0.005	-0.005
Muon trigger	+0.0006	-0.0006	+0.007	-0.007
Muon rescaling	+0.0174	-0.0144	+0.135	-0.150

Continued on next page

Continued from previous page

Central values:	$\alpha_\ell P = -0.0636$		$\sigma = +179.54$	
Source of Uncertainty	$\Delta\alpha_\ell P$		$\Delta\sigma$	
Muon spectrometer	+0.0006	0.0000	+0.000	-0.007
Muon tracker	+0.0006	-0.0006	+0.004	-0.005
b-JES	+0.0030	-0.0090	+1.598	-1.386
JES Closeby	+0.0036	-0.0018	+3.758	-3.695
JES Detector 1	+0.0120	-0.0132	+2.246	-2.091
JES Detector 2	+0.0000	-0.0018	+0.222	-0.183
JES Eta Intercalib.Tot. Stat.	+0.0006	0.0000	+1.228	-1.062
JES Eta Intercalib. Theo.	+0.0120	-0.0132	+3.891	-3.550
JES flavor component	+0.0036	-0.0018	+1.859	-1.853
JES flavor response	+0.0012	0.0000	+4.372	-4.266
JES mixed 1	+0.0006	-0.0030	+0.266	-0.222
JES mixed 2	+0.0000	-0.0024	+0.800	-0.686
JES modelling 1	+0.0054	-0.0084	+4.831	-4.932
JES modelling 2	+0.0048	-0.0066	+0.118	-0.090
JES modelling 3	+0.0072	-0.0078	+0.043	-0.024
JES modelling 4	+0.0012	-0.0006	+0.183	-0.156
JES Pileup offset NPV	+0.0018	-0.0018	+0.728	-0.760
JES Pileup offset mu	+0.0042	-0.0030	+6.593	-6.193

Continued on next page

Continued from previous page

Central values:	$\alpha_\ell P = -0.0636$		$\sigma = +179.54$	
Source of Uncertainty	$\Delta\alpha_\ell P$		$\Delta\sigma$	
JES relative nonclosure	+0.0000	-0.0006	+0.804	-0.766
JES single particle	+0.0000	0.0000	+0.000	-0.000
JES statistical 1	+0.0090	-0.0084	+2.774	-2.738
JES statistical 2	+0.0006	-0.0024	+0.044	-0.016
JES statistical 3	+0.0030	-0.0042	+0.378	-0.337
Jet vertex fraction	+0.0012	-0.0018	+3.378	-2.807
Jet efficiency	+0.0018	-0.0018	+0.813	-0.808
Jet energy resolution	+0.0204	-0.0228	+18.156	-16.832
b-tag eff.	+0.0030	-0.0054	+9.445	-7.911
c-tag eff.	+0.0060	-0.0060	+2.787	-2.741
mistag rate	+0.0030	-0.0036	+2.187	-2.173
Pile up	+0.0048	-0.0036	+6.634	-6.240
Cellout	+0.0024	-0.0024	+0.068	-0.250
W heavy flavor factors	+0.0108	-0.0126	+3.730	-4.081
W iqopt3	+0.0000	0.0000	+0.554	-0.554
W ptjmin	+0.0012	-0.0018	+0.214	-0.214
QCD/Fakes	+0.0168	-0.0108	+0.100	-0.148
MC Generator	+0.0042	-0.0036	+9.417	-8.520

Continued on next page

Continued from previous page				
Central values:	$\alpha_\ell P = -0.0636$		$\sigma = +179.54$	
Source of Uncertainty	$\Delta\alpha_\ell P$		$\Delta\sigma$	
Color reconnection	+0.0000	0.0000	+0.109	-0.113
ISR/FSR variation	+0.0018	-0.0018	+0.450	-0.449
Fragmentation/Parton shower	+0.0054	-0.0054	+0.171	-0.170
Underlying event	+0.0090	-0.0090	+0.041	-0.042
CT10 PDF	+0.0018	-0.0018	+8.019	-7.766
Spin correlation value	+0.0024	-0.0024	+0.046	-0.047
Monte Carlo background x-section	+0.0114	-0.0132	+3.900	-4.343
Monte Carlo signal & bkg branching ratio	+0.000	-0.000	+1.633	-1.605
Monte Carlo statistics	+0.0012	-0.0012	+0.591	-0.590
Luminosity	+0.0000	0.0000	+3.548	-3.418
Template statistics for template fits	+0.0102	-0.0102	+0.000	-0.000
Top Mass	+0.0108	-0.0108	+2.325	-2.325
InterPDF	+0.0018	-0.0018	+6.220	-6.220
Total Systematic Uncertainty	+0.0468	-0.0480	+31.113	-29.245

Table F.9.: Uncertainties on $\alpha_\ell P$ and σ for the μ+jets fit using positively charged leptons for the CP conserving scenario.

Central values:	$\alpha_\ell P = -0.0006$		$\sigma = +179.72$	
Source of Uncertainty	$\Delta\alpha_\ell P$		$\Delta\sigma$	
Statistical Uncertainty	+0.0306	-0.0300	+1.80	-1.79
Electron identification and smearing	+0.0000	0.0000	+0.000	-0.000
Electron reconstruction	+0.0000	0.0000	+0.000	-0.000
Electron trigger	+0.0000	0.0000	+0.000	-0.000
Electron scale	+0.0000	0.0000	+0.000	-0.000
Electron resolution	+0.0000	0.0000	+0.000	-0.000
Muon identification	+0.0000	0.0000	+0.000	-0.000
Muon reconstruction	+0.0006	-0.0006	+0.006	-0.005
Muon trigger	+0.0006	-0.0006	+0.006	-0.005
Muon rescaling	+0.0282	-0.0234	+0.243	-0.269
Muon spectrometer	+0.0012	0.0000	+0.000	-0.014
Muon tracker	+0.0018	0.0000	+0.000	-0.019
b-JES	+0.0078	-0.0072	+1.741	-1.555
JES Closeby	+0.0036	0.0000	+4.306	-4.099
JES Detector 1	+0.0126	-0.0150	+2.528	-2.390
JES Detector 2	+0.0030	0.0000	+0.145	-0.251
JES Eta Intercalib.Tot. Stat.	+0.0036	-0.0018	+1.353	-1.297

Continued on next page

Continued from previous page

Central values:	$\alpha_\ell P = -0.0006$		$\sigma = +179.72$	
Source of Uncertainty	$\Delta\alpha_\ell P$		$\Delta\sigma$	
JES Eta Intercalib. Theo.	+0.0162	-0.0174	+4.185	-3.919
JES flavor component	+0.0036	-0.0060	+2.219	-2.128
JES flavor response	+0.0030	-0.0060	+4.997	-4.822
JES mixed 1	+0.0036	0.0000	+0.175	-0.274
JES mixed 2	+0.0030	0.0000	+0.930	-0.839
JES modelling 1	+0.0012	-0.0048	+5.598	-5.542
JES modelling 2	+0.0096	-0.0036	+0.010	-0.153
JES modelling 3	+0.0096	-0.0066	+0.000	-0.062
JES modelling 4	+0.0030	0.0000	+0.140	-0.210
JES Pileup offset NPV	+0.0006	-0.0006	+0.981	-0.807
JES Pileup offset mu	+0.0000	-0.0024	+7.414	-7.133
JES relative nonclosure	+0.0036	0.0000	+0.891	-0.901
JES single particle	+0.0000	0.0000	+0.002	-0.000
JES statistical 1	+0.0042	-0.0114	+3.130	-3.128
JES statistical 2	+0.0030	0.0000	+0.000	-0.055
JES statistical 3	+0.0042	-0.0018	+0.321	-0.415
Jet vertex fraction	+0.0000	-0.0012	+3.665	-3.088
Jet efficiency	+0.0024	-0.0024	+0.999	-0.989

Continued on next page

Continued from previous page

Central values:	$\alpha_\ell P = -0.0006$		$\sigma = +179.72$	
Source of Uncertainty	$\Delta\alpha_\ell P$		$\Delta\sigma$	
Jet energy resolution	+0.0288	-0.0306	+20.392	-18.902
b-tag eff.	+0.0084	-0.0108	+10.043	-8.432
c-tag eff.	+0.0024	-0.0024	+3.230	-3.168
mistag rate	+0.0012	-0.0012	+3.152	-3.157
Pile up	+0.0024	-0.0024	+7.479	-7.179
Cellout	+0.0060	-0.0024	+0.040	-0.093
W heavy flavor factors	+0.0162	-0.0168	+6.204	-6.424
W iqopt3	+0.0024	-0.0024	+1.128	-1.123
W ptjmin	+0.0006	-0.0006	+0.447	-0.442
QCD/Fakes	+0.0186	-0.0120	+0.106	-0.154
MC Generator	+0.0012	-0.0018	+9.659	-8.710
Color reconnection	+0.0030	-0.0030	+0.068	-0.071
ISR/FSR variation	+0.0042	-0.0036	+0.313	-0.313
Fragmentation/Parton shower	+0.0012	-0.0012	+0.218	-0.219
Underlying event	+0.0018	-0.0018	+0.390	-0.391
CT10 PDF	+0.0018	-0.0018	+7.982	-7.729
Spin correlation value	+0.0024	-0.0024	+0.030	-0.030
Monte Carlo background x-section	+0.0036	-0.0036	+5.668	-6.374

Continued on next page

Continued from previous page

Central values:	$\alpha_\ell P = -0.0006$		$\sigma = +179.72$	
Source of Uncertainty	$\Delta\alpha_\ell P$		$\Delta\sigma$	
Monte Carlo signal & bkg branching ratio	+0.001	-0.001	+1.635	-1.605
Monte Carlo statistics	+0.0006	-0.0006	+0.686	-0.685
Luminosity	+0.0006	-0.0006	+3.624	-3.494
Template statistics for template fits	+0.0114	-0.0114	+0.000	-0.000
Top Mass	+0.0132	-0.0132	+2.396	-2.396
InterPDF	+0.0018	-0.0018	+6.320	-6.320
Total Systematic Uncertainty	+0.0588	-0.0564	+34.267	-32.368

F.2. CPV Systematic Tables

Table F.10.: Uncertainties on $\alpha_\ell P$ and σ for the ℓ+jets fit using both lepton charges for the CP violating scenario.

Central values:	$\alpha_\ell P = 0.0234$		$\sigma = +177.11$	
Source of Uncertainty	$\Delta\alpha_\ell P$		$\Delta\sigma$	
Statistical Uncertainty	+0.0186	-0.0186	+0.95	-0.95
Electron identification and smearing	+0.0000	0.0000	+1.888	-1.857
Electron reconstruction	+0.0000	0.0000	+0.733	-0.728

Continued on next page

Continued from previous page

Central values:	$\alpha_\ell P = 0.0234$		$\sigma = +177.11$	
Source of Uncertainty	$\Delta\alpha_\ell P$		$\Delta\sigma$	
Electron trigger	+0.0000	0.0000	+0.471	-0.469
Electron scale	+0.0006	0.0000	+0.267	-0.323
Electron resolution	+0.0006	-0.0006	+0.036	-0.005
Muon identification	+0.0000	0.0000	+0.000	-0.000
Muon reconstruction	+0.0000	0.0000	+0.000	-0.000
Muon trigger	+0.0000	0.0000	+0.000	-0.000
Muon rescaling	+0.0006	-0.0006	+0.007	-0.005
Muon spectrometer	+0.0000	0.0000	+0.003	-0.000
Muon tracker	+0.0006	0.0000	+0.002	-0.000
b-JES	+0.0018	0.0000	+1.618	-1.475
JES Closeby	+0.0024	0.0000	+4.225	-3.980
JES Detector 1	+0.0000	-0.0012	+2.257	-2.160
JES Detector 2	+0.0024	0.0000	+0.197	-0.192
JES Eta Intercalib.Tot. Stat.	+0.0006	-0.0006	+1.271	-1.171
JES Eta Intercalib. Theo.	+0.0000	-0.0012	+3.890	-3.637
JES flavor component	+0.0000	-0.0012	+1.983	-1.923
JES flavor response	+0.0006	-0.0012	+4.592	-4.476
JES mixed 1	+0.0018	0.0000	+0.207	-0.196

Continued on next page

Continued from previous page

Central values:	$\alpha_\ell P = 0.0234$		$\sigma = +177.11$	
Source of Uncertainty	$\Delta\alpha_\ell P$		$\Delta\sigma$	
JES mixed 2	+0.0018	0.0000	+0.864	-0.776
JES modelling 1	+0.0012	-0.0018	+5.220	-5.284
JES modelling 2	+0.0024	0.0000	+0.140	-0.163
JES modelling 3	+0.0012	0.0000	+0.070	-0.070
JES modelling 4	+0.0006	0.0000	+0.159	-0.147
JES Pileup offset NPV	+0.0000	0.0000	+0.821	-0.736
JES Pileup offset mu	+0.0000	-0.0018	+6.954	-6.710
JES relative nonclosure	+0.0018	0.0000	+0.876	-0.833
JES single particle	+0.0000	0.0000	+0.001	-0.000
JES statistical 1	+0.0000	-0.0024	+3.003	-2.989
JES statistical 2	+0.0024	0.0000	+0.022	-0.013
JES statistical 3	+0.0012	0.0000	+0.334	-0.333
Jet vertex fraction	+0.0006	-0.0006	+3.442	-2.877
Jet efficiency	+0.0000	0.0000	+0.461	-0.458
Jet energy resolution	+0.0000	0.0000	+5.532	-5.395
b-tag eff.	+0.0006	-0.0006	+9.507	-7.989
c-tag eff.	+0.0012	-0.0012	+2.834	-2.781
mistag rate	+0.0006	-0.0006	+2.527	-2.513

Continued on next page

Continued from previous page

Central values:	$\alpha_\ell P = 0.0234$		$\sigma = +177.11$	
Source of Uncertainty	$\Delta\alpha_\ell P$		$\Delta\sigma$	
Pile up	+0.0024	-0.0018	+7.002	-6.750
Cellout	+0.0012	0.0000	+0.019	-0.075
W heavy flavor factors	+0.0048	-0.0048	+4.761	-4.893
W iqopt3	+0.0006	-0.0006	+0.736	-0.733
W ptjmin	+0.0006	-0.0006	+0.178	-0.177
QCD/Fakes	+0.0000	0.0000	+0.044	-0.020
MC Generator	+0.0024	-0.0030	+9.764	-8.796
Color reconnection	+0.0006	-0.0006	+0.193	-0.197
ISR/FSR variation	+0.0018	-0.0018	+1.217	-1.207
Fragmentation/Parton shower	+0.0030	-0.0030	+0.044	-0.047
Underlying event	+0.0024	-0.0024	+0.074	-0.076
CT10 PDF	+0.0000	0.0000	+7.851	-7.609
Spin correlation value	+0.0000	0.0000	+0.010	-0.010
Monte Carlo background x-section	+0.0024	-0.0024	+3.733	-3.971
Monte Carlo signal & bkg branching ratio	+0.000	-0.000	+1.614	-1.585
Monte Carlo statistics	+0.0000	0.0000	+0.350	-0.350
Luminosity	+0.0000	0.0000	+3.546	-3.419
Template statistics for template fits	+0.0066	-0.0066	+0.000	-0.000

Continued on next page

Continued from previous page

Central values:	$\alpha_\ell P = 0.0234$	$\sigma = +177.11$
Source of Uncertainty	$\Delta\alpha_\ell P$	$\Delta\sigma$
Top Mass	+0.0000 0.0000	+2.306 -2.306
InterPDF	+0.0006 -0.0006	+6.470 -6.470
Total Systematic Uncertainty	+0.0120 -0.0108	+26.636 -25.283

Table F.11.: Uncertainties on $\alpha_\ell P$ and σ for the ℓ+jets fit using negatively charged leptons for the CP violating scenario.

Central values:	$\alpha_\ell P = 0.06$	$\sigma = +177.27$
Source of Uncertainty	$\Delta\alpha_\ell P$	$\Delta\sigma$
Statistical Uncertainty	+0.0258 -0.0258	+1.34 -1.34
Electron identification and smearing	+0.0030 -0.0030	+1.803 -1.774
Electron reconstruction	+0.0006 -0.0006	+0.707 -0.701
Electron trigger	+0.0006 -0.0006	+0.452 -0.449
Electron scale	+0.0036 -0.0024	+0.252 -0.268
Electron resolution	+0.0000 0.0000	+0.084 -0.000
Muon identification	+0.0000 0.0000	+0.000 -0.000
Muon reconstruction	+0.0000 -0.0006	+0.002 -0.002
Muon trigger	+0.0006 -0.0006	+0.003 -0.003

Continued on next page

Continued from previous page

Central values:	$\alpha_\ell P = 0.06$		$\sigma = +177.27$	
Source of Uncertainty	$\Delta\alpha_\ell P$		$\Delta\sigma$	
Muon rescaling	+0.0090	-0.0114	+0.054	-0.053
Muon spectrometer	+0.0000	-0.0006	+0.000	-0.002
Muon tracker	+0.0006	-0.0006	+0.002	-0.002
b-JES	+0.0102	-0.0066	+1.647	-1.457
JES Closeby	+0.0024	-0.0030	+3.992	-3.824
JES Detector 1	+0.0138	-0.0138	+2.219	-2.092
JES Detector 2	+0.0012	0.0000	+0.204	-0.182
JES Eta Intercalib.Tot. Stat.	+0.0000	-0.0012	+1.176	-1.095
JES Eta Intercalib. Theo.	+0.0162	-0.0162	+3.911	-3.582
JES flavor component	+0.0036	-0.0042	+1.882	-1.810
JES flavor response	+0.0012	-0.0024	+4.325	-4.201
JES mixed 1	+0.0018	-0.0012	+0.225	-0.198
JES mixed 2	+0.0024	-0.0018	+0.784	-0.708
JES modelling 1	+0.0066	-0.0042	+4.850	-4.924
JES modelling 2	+0.0072	-0.0054	+0.117	-0.110
JES modelling 3	+0.0072	-0.0078	+0.039	-0.017
JES modelling 4	+0.0006	-0.0012	+0.161	-0.140
JES Pileup offset NPV	+0.0012	-0.0036	+0.718	-0.710

Continued on next page

Continued from previous page

Central values:	$\alpha_\ell P = 0.06$		$\sigma = +177.27$	
Source of Uncertainty	$\Delta\alpha_\ell P$		$\Delta\sigma$	
JES Pileup offset mu	+0.0000	-0.0018	+6.546	-6.219
JES relative nonclosure	+0.0012	-0.0012	+0.823	-0.762
JES single particle	+0.0000	0.0000	+0.001	-0.000
JES statistical 1	+0.0084	-0.0096	+2.807	-2.706
JES statistical 2	+0.0024	-0.0006	+0.035	-0.013
JES statistical 3	+0.0042	-0.0042	+0.364	-0.350
Jet vertex fraction	+0.0018	-0.0012	+3.316	-2.745
Jet efficiency	+0.0012	-0.0012	+0.668	-0.665
Jet energy resolution	+0.0222	-0.0198	+13.511	-13.209
b-tag eff.	+0.0066	-0.0042	+9.315	-7.800
c-tag eff.	+0.0060	-0.0060	+2.593	-2.549
mistag rate	+0.0042	-0.0042	+2.091	-2.075
Pile up	+0.0024	-0.0042	+6.585	-6.259
Cellout	+0.0024	-0.0024	+0.044	-0.075
W heavy flavor factors	+0.0126	-0.0114	+3.703	-3.878
W iqopt3	+0.0006	-0.0006	+0.561	-0.560
W ptjmin	+0.0018	-0.0018	+0.223	-0.222
QCD/Fakes	+0.0078	-0.0114	+0.046	-0.049

Continued on next page

Continued from previous page

Central values:	$\alpha_\ell P = 0.06$		$\sigma = +177.27$	
Source of Uncertainty	$\Delta\alpha_\ell P$		$\Delta\sigma$	
MC Generator	+0.0030	-0.0036	+9.668	-8.719
Color reconnection	+0.0012	-0.0012	+0.216	-0.220
ISR/FSR variation	+0.0000	0.0000	+1.211	-1.199
Fragmentation/Parton shower	+0.0048	-0.0048	+0.055	-0.057
Underlying event	+0.0030	-0.0030	+0.045	-0.049
CT10 PDF	+0.0018	-0.0018	+7.866	-7.622
Spin correlation value	+0.0024	-0.0024	+0.033	-0.033
Monte Carlo background x-section	+0.0096	-0.0090	+3.160	-3.349
Monte Carlo signal & bkg branching ratio	+0.001	-0.001	+1.618	-1.588
Monte Carlo statistics	+0.0012	-0.0012	+0.460	-0.460
Luminosity	+0.0000	0.0000	+3.518	-3.391
Template statistics for template fits	+0.0090	-0.0090	+0.000	-0.000
Top Mass	+0.0132	-0.0132	+2.423	-2.423
InterPDF	+0.0012	-0.0012	+6.450	-6.450
Total Systematic Uncertainty	+0.0456	-0.0450	+28.599	-27.199

Table F.12.: Uncertainties on $\alpha_\ell P$ and σ for the ℓ+jets fit using positively charged leptons for the CP violating scenario.

Central values:	$\alpha_\ell P = -0.0174$		$\sigma = +177.52$	
Source of Uncertainty	$\Delta\alpha_\ell P$		$\Delta\sigma$	
Statistical Uncertainty	+0.0264	-0.0264	+1.39	-1.38
Electron identification and smearing	+0.0024	-0.0024	+1.939	-1.909
Electron reconstruction	+0.0006	-0.0006	+0.753	-0.749
Electron trigger	+0.0006	-0.0006	+0.485	-0.484
Electron scale	+0.0030	-0.0048	+0.245	-0.321
Electron resolution	+0.0006	-0.0012	+0.000	-0.031
Muon identification	+0.0000	0.0000	+0.000	-0.000
Muon reconstruction	+0.0000	-0.0006	+0.002	-0.002
Muon trigger	+0.0000	-0.0006	+0.003	-0.002
Muon rescaling	+0.0162	-0.0138	+0.078	-0.076
Muon spectrometer	+0.0006	0.0000	+0.000	-0.004
Muon tracker	+0.0012	0.0000	+0.000	-0.006
b-JES	+0.0072	-0.0072	+1.710	-1.588
JES Closeby	+0.0030	0.0000	+4.435	-4.140
JES Detector 1	+0.0138	-0.0168	+2.523	-2.434
JES Detector 2	+0.0036	0.0000	+0.167	-0.217
JES Eta Intercalib.Tot. Stat.	+0.0030	-0.0006	+1.365	-1.281

Continued on next page

Continued from previous page

Central values:	$\alpha_\ell P = -0.0174$		$\sigma = +177.52$	
Source of Uncertainty	$\Delta\alpha_\ell P$		$\Delta\sigma$	
JES Eta Intercalib. Theo.	+0.0174	-0.0204	+4.141	-3.946
JES flavor component	+0.0054	-0.0066	+2.162	-2.117
JES flavor response	+0.0054	-0.0054	+4.922	-4.821
JES mixed 1	+0.0030	0.0000	+0.188	-0.225
JES mixed 2	+0.0012	0.0000	+0.926	-0.841
JES modelling 1	+0.0000	-0.0030	+5.578	-5.581
JES modelling 2	+0.0102	-0.0024	+0.046	-0.147
JES modelling 3	+0.0114	-0.0054	+0.000	-0.041
JES modelling 4	+0.0018	0.0000	+0.154	-0.175
JES Pileup offset NPV	+0.0042	-0.0012	+0.944	-0.823
JES Pileup offset mu	+0.0012	-0.0030	+7.376	-7.234
JES relative nonclosure	+0.0054	0.0000	+0.934	-0.954
JES single particle	+0.0000	0.0000	+0.001	-0.000
JES statistical 1	+0.0048	-0.0078	+3.099	-3.159
JES statistical 2	+0.0030	0.0000	+0.007	-0.039
JES statistical 3	+0.0054	-0.0018	+0.345	-0.384
Jet vertex fraction	+0.0000	-0.0006	+3.578	-3.005
Jet efficiency	+0.0024	-0.0024	+0.870	-0.864

Continued on next page

Continued from previous page

Central values:	$\alpha_\ell P = -0.0174$		$\sigma = +177.52$	
Source of Uncertainty	$\Delta\alpha_\ell P$		$\Delta\sigma$	
Jet energy resolution	+0.0264	-0.0300	+15.427	-15.092
b-tag eff.	+0.0072	-0.0102	+9.879	-8.299
c-tag eff.	+0.0030	-0.0030	+3.030	-2.969
mistag rate	+0.0012	-0.0012	+2.960	-2.952
Pile up	+0.0048	-0.0036	+7.436	-7.280
Cellout	+0.0042	-0.0024	+0.024	-0.098
W heavy flavor factors	+0.0144	-0.0150	+6.144	-6.210
W iqopt3	+0.0018	-0.0018	+1.070	-1.067
W ptjmin	+0.0006	-0.0006	+0.408	-0.405
QCD/Fakes	+0.0126	-0.0084	+0.048	-0.044
MC Generator	+0.0024	-0.0030	+9.913	-8.911
Color reconnection	+0.0000	0.0000	+0.180	-0.185
ISR/FSR variation	+0.0030	-0.0030	+1.211	-1.203
Fragmentation/Parton shower	+0.0006	-0.0012	+0.066	-0.068
Underlying event	+0.0012	-0.0018	+0.093	-0.095
CT10 PDF	+0.0018	-0.0018	+7.850	-7.607
Spin correlation value	+0.0024	-0.0024	+0.024	-0.024
Monte Carlo background x-section	+0.0048	-0.0048	+4.305	-4.601

Continued on next page

Continued from previous page

Central values:	$\alpha_\ell P = -0.0174$		$\sigma = +177.52$	
Source of Uncertainty	$\Delta\alpha_\ell P$		$\Delta\sigma$	
Monte Carlo signal & bkg branching ratio	+0.001	-0.001	+1.620	-1.591
Monte Carlo statistics	+0.0006	-0.0006	+0.527	-0.526
Luminosity	+0.0006	-0.0006	+3.593	-3.464
Template statistics for template fits	+0.0108	-0.0108	+0.000	-0.000
Top Mass	+0.0144	-0.0144	+2.441	-2.441
InterPDF	+0.0018	-0.0018	+6.530	-6.530
Total Systematic Uncertainty	+0.0528	-0.0528	+31.320	-30.022

Table F.13.: Uncertainties on $\alpha_\ell P$ and σ for the e+jets fit using both lepton charges for the CP violating scenario.

Central values:	$\alpha_\ell P = 0.0012$		$\sigma = +173.74$	
Source of Uncertainty	$\Delta\alpha_\ell P$		$\Delta\sigma$	
Statistical Uncertainty	+0.0306	-0.0306	+1.53	-1.52
Electron identification and smearing	+0.0000	0.0000	+4.884	-4.670
Electron reconstruction	+0.0000	0.0000	+1.879	-1.844
Electron trigger	+0.0000	0.0000	+1.207	-1.191
Electron scale	+0.0012	-0.0006	+0.682	-0.822

Continued on next page

Continued from previous page

Central values:	$\alpha_\ell P = 0.0012$		$\sigma = +173.74$	
Source of Uncertainty	$\Delta\alpha_\ell P$		$\Delta\sigma$	
Electron resolution	+0.0012	-0.0024	+0.093	-0.012
Muon identification	+0.0000	0.0000	+0.000	-0.000
Muon reconstruction	+0.0000	0.0000	+0.000	-0.000
Muon trigger	+0.0000	0.0000	+0.000	-0.000
Muon rescaling	+0.0000	0.0000	+0.000	-0.000
Muon spectrometer	+0.0000	0.0000	+0.000	-0.000
Muon tracker	+0.0000	0.0000	+0.000	-0.000
b-JES	+0.0024	-0.0042	+1.677	-1.583
JES Closeby	+0.0042	-0.0024	+4.474	-4.118
JES Detector 1	+0.0000	-0.0024	+2.342	-2.270
JES Detector 2	+0.0018	0.0000	+0.200	-0.183
JES Eta Intercalib.Tot. Stat.	+0.0000	-0.0006	+1.260	-1.208
JES Eta Intercalib. Theo.	+0.0000	-0.0030	+3.972	-3.762
JES flavor component	+0.0012	0.0000	+1.989	-1.903
JES flavor response	+0.0012	0.0000	+4.545	-4.453
JES mixed 1	+0.0012	-0.0006	+0.193	-0.160
JES mixed 2	+0.0000	-0.0006	+0.863	-0.804
JES modelling 1	+0.0000	-0.0018	+5.203	-5.270

Continued on next page

Continued from previous page

Central values:	$\alpha_\ell P = 0.0012$		$\sigma = +173.74$	
Source of Uncertainty	$\Delta\alpha_\ell P$		$\Delta\sigma$	
JES modelling 2	+0.0030	0.0000	+0.120	-0.134
JES modelling 3	+0.0018	0.0000	+0.034	-0.001
JES modelling 4	+0.0006	-0.0006	+0.157	-0.131
JES Pileup offset NPV	+0.0012	-0.0012	+0.802	-0.685
JES Pileup offset mu	+0.0006	-0.0030	+6.884	-6.794
JES relative nonclosure	+0.0024	0.0000	+0.929	-0.871
JES single particle	+0.0000	0.0000	+0.001	-0.000
JES statistical 1	+0.0030	-0.0018	+2.976	-2.914
JES statistical 2	+0.0018	0.0000	+0.026	-0.016
JES statistical 3	+0.0012	0.0000	+0.366	-0.337
Jet vertex fraction	+0.0006	-0.0006	+3.324	-2.754
Jet efficiency	+0.0000	0.0000	+0.582	-0.580
Jet energy resolution	+0.0078	-0.0084	+6.453	-6.272
b-tag eff.	+0.0018	-0.0018	+9.357	-7.844
c-tag eff.	+0.0000	0.0000	+2.493	-2.443
mistag rate	+0.0006	-0.0006	+2.284	-2.259
Pile up	+0.0024	-0.0036	+6.931	-6.828
Cellout	+0.0030	-0.0018	+0.053	-0.076

Continued on next page

Continued from previous page

Central values:	$\alpha_\ell P = 0.0012$		$\sigma = +173.74$	
Source of Uncertainty	$\Delta\alpha_\ell P$		$\Delta\sigma$	
W heavy flavor factors	+0.0030	-0.0030	+4.799	-4.621
W iqopt3	+0.0000	0.0000	+0.696	-0.695
W ptjmin	+0.0006	-0.0006	+0.148	-0.148
QCD/Fakes	+0.0006	-0.0006	+0.029	-0.011
MC Generator	+0.0024	-0.0030	+10.125	-9.075
Color reconnection	+0.0048	-0.0048	+0.664	-0.663
ISR/FSR variation	+0.0006	-0.0006	+2.488	-2.423
Fragmentation/Parton shower	+0.0018	-0.0024	+0.456	-0.459
Underlying event	+0.0036	-0.0036	+0.197	-0.202
CT10 PDF	+0.0006	-0.0006	+7.637	-7.408
Spin correlation value	+0.0000	0.0000	+0.010	-0.010
Monte Carlo background x-section	+0.0018	-0.0018	+4.679	-4.670
Monte Carlo signal & bkg branching ratio	+0.000	-0.000	+1.595	-1.566
Monte Carlo statistics	+0.0000	0.0000	+0.507	-0.506
Luminosity	+0.0000	0.0000	+3.503	-3.377
Template statistics for template fits	+0.0120	-0.0120	+0.000	-0.000
Top Mass	+0.0006	-0.0006	+2.428	-2.428

Continued on next page

Continued from previous page

Central values:	$\alpha_\ell P = 0.0012$	$\sigma = +173.74$
Source of Uncertainty	$\Delta\alpha_\ell P$	$\Delta\sigma$
InterPDF	+0.0012 -0.0012	+6.800 -6.800
Total Systematic Uncertainty	+0.0186 -0.0186	+27.496 -26.090

Table F.14.: Uncertainties on $\alpha_\ell P$ and σ for the e+jets fit using negatively charged leptons for the CP violating scenario.

Central values:	$\alpha_\ell P = 0.0408$	$\sigma = +174.12$
Source of Uncertainty	$\Delta\alpha_\ell P$	$\Delta\sigma$
Statistical Uncertainty	+0.0426 -0.0432	+2.17 -2.16
Electron identification and smearing	+0.0030 -0.0030	+4.716 -4.509
Electron reconstruction	+0.0000 -0.0006	+1.836 -1.799
Electron trigger	+0.0000 0.0000	+1.169 -1.153
Electron scale	+0.0102 -0.0054	+0.634 -0.660
Electron resolution	+0.0006 -0.0006	+0.217 -0.000
Muon identification	+0.0000 0.0000	+0.000 -0.000
Muon reconstruction	+0.0000 0.0000	+0.000 -0.000
Muon trigger	+0.0000 0.0000	+0.000 -0.000
Muon rescaling	+0.0000 0.0000	+0.000 -0.000

Continued on next page

Continued from previous page

Central values:	$\alpha_\ell P = 0.0408$		$\sigma = +174.12$	
Source of Uncertainty	$\Delta\alpha_\ell P$		$\Delta\sigma$	
Muon spectrometer	+0.0000	0.0000	+0.000	-0.000
Muon tracker	+0.0000	0.0000	+0.000	-0.000
b-JES	+0.0114	-0.0126	+1.801	-1.625
JES Closeby	+0.0030	-0.0012	+4.357	-4.032
JES Detector 1	+0.0120	-0.0156	+2.314	-2.224
JES Detector 2	+0.0000	-0.0006	+0.185	-0.184
JES Eta Intercalib.Tot. Stat.	+0.0000	-0.0030	+1.095	-1.172
JES Eta Intercalib. Theo.	+0.0204	-0.0228	+4.111	-3.798
JES flavor component	+0.0060	-0.0048	+1.972	-1.801
JES flavor response	+0.0036	-0.0042	+4.324	-4.180
JES mixed 1	+0.0000	-0.0024	+0.178	-0.176
JES mixed 2	+0.0012	-0.0042	+0.751	-0.729
JES modelling 1	+0.0018	-0.0018	+4.887	-4.920
JES modelling 2	+0.0060	-0.0060	+0.071	-0.086
JES modelling 3	+0.0054	-0.0084	+0.050	-0.035
JES modelling 4	+0.0000	-0.0012	+0.132	-0.126
JES Pileup offset NPV	+0.0000	-0.0072	+0.725	-0.671
JES Pileup offset mu	+0.0018	-0.0066	+6.502	-6.321

Continued on next page

Continued from previous page

Central values:	$\alpha_\ell P = 0.0408$		$\sigma = +174.12$	
Source of Uncertainty	$\Delta\alpha_\ell P$		$\Delta\sigma$	
JES relative nonclosure	+0.0024	-0.0036	+0.873	-0.774
JES single particle	+0.0000	0.0000	+0.004	-0.000
JES statistical 1	+0.0078	-0.0096	+2.797	-2.614
JES statistical 2	+0.0012	-0.0012	+0.038	-0.018
JES statistical 3	+0.0036	-0.0060	+0.383	-0.413
Jet vertex fraction	+0.0018	-0.0012	+3.215	-2.640
Jet efficiency	+0.0000	0.0000	+0.929	-0.924
Jet energy resolution	+0.0138	-0.0126	+15.147	-14.755
b-tag eff.	+0.0084	-0.0060	+9.215	-7.688
c-tag eff.	+0.0048	-0.0054	+2.238	-2.198
mistag rate	+0.0048	-0.0048	+1.899	-1.880
Pile up	+0.0030	-0.0102	+6.545	-6.357
Cellout	+0.0042	-0.0030	+0.219	-0.033
W heavy flavor factors	+0.0120	-0.0120	+3.615	-3.493
W iqopt3	+0.0012	-0.0012	+0.568	-0.568
W ptjmin	+0.0018	-0.0018	+0.224	-0.224
QCD/Fakes	+0.0078	-0.0024	+0.097	-0.037
MC Generator	+0.0018	-0.0018	+10.020	-8.991

Continued on next page

Continued from previous page				
Central values:	$\alpha_\ell P = 0.0408$		$\sigma = +174.12$	
Source of Uncertainty	$\Delta\alpha_\ell P$		$\Delta\sigma$	
Color reconnection	+0.0042	-0.0042	+0.744	-0.743
ISR/FSR variation	+0.0018	-0.0018	+2.387	-2.324
Fragmentation/Parton shower	+0.0042	-0.0042	+0.466	-0.465
Underlying event	+0.0078	-0.0084	+0.019	-0.030
CT10 PDF	+0.0024	-0.0024	+7.652	-7.419
Spin correlation value	+0.0024	-0.0024	+0.033	-0.033
Monte Carlo background x-section	+0.0114	-0.0108	+3.899	-3.898
Monte Carlo signal & bkg branching ratio	+0.001	-0.001	+1.602	-1.573
Monte Carlo statistics	+0.0018	-0.0018	+0.668	-0.667
Luminosity	+0.0000	0.0000	+3.482	-3.355
Template statistics for template fits	+0.0156	-0.0156	+0.000	-0.000
Top Mass	+0.0150	-0.0150	+2.562	-2.562
InterPDF	+0.0048	-0.0048	+6.840	-6.840
Total Systematic Uncertainty	+0.0468	-0.0504	+30.025	-28.533

Table F.15.: Uncertainties on $\alpha_\ell P$ and σ for the e+jets fit using positively charged leptons for the CP violating scenario.

Central values:	$\alpha_\ell P = -0.0408$		$\sigma = +174.15$	
Source of Uncertainty	$\Delta\alpha_\ell P$		$\Delta\sigma$	
Statistical Uncertainty	+0.0444	-0.0444	+2.24	-2.23
Electron identification and smearing	+0.0012	-0.0012	+5.041	-4.822
Electron reconstruction	+0.0006	-0.0006	+1.945	-1.913
Electron trigger	+0.0000	0.0000	+1.250	-1.237
Electron scale	+0.0078	-0.0114	+0.605	-0.792
Electron resolution	+0.0024	-0.0036	+0.000	-0.086
Muon identification	+0.0000	0.0000	+0.000	-0.000
Muon reconstruction	+0.0000	0.0000	+0.000	-0.000
Muon trigger	+0.0000	0.0000	+0.000	-0.000
Muon rescaling	+0.0000	0.0000	+0.000	-0.000
Muon spectrometer	+0.0000	0.0000	+0.000	-0.000
Muon tracker	+0.0000	0.0000	+0.000	-0.000
b-JES	+0.0054	-0.0060	+1.717	-1.707
JES Closeby	+0.0060	-0.0042	+4.620	-4.243
JES Detector 1	+0.0150	-0.0180	+2.673	-2.626
JES Detector 2	+0.0042	0.0000	+0.168	-0.182
JES Eta Intercalib.Tot. Stat.	+0.0018	0.0000	+1.387	-1.285

Continued on next page

Continued from previous page

Central values:	$\alpha_\ell P = -0.0408$		$\sigma = +174.15$	
Source of Uncertainty	$\Delta\alpha_\ell P$		$\Delta\sigma$	
JES Eta Intercalib. Theo.	+0.0192	-0.0222	+4.254	-4.161
JES flavor component	+0.0090	-0.0060	+2.131	-2.156
JES flavor response	+0.0096	-0.0036	+4.857	-4.881
JES mixed 1	+0.0018	0.0000	+0.193	-0.174
JES mixed 2	+0.0030	-0.0012	+0.908	-0.858
JES modelling 1	+0.0012	-0.0030	+5.543	-5.631
JES modelling 2	+0.0096	-0.0006	+0.011	-0.114
JES modelling 3	+0.0126	-0.0030	+0.030	-0.109
JES modelling 4	+0.0012	-0.0006	+0.170	-0.139
JES Pileup offset NPV	+0.0108	-0.0018	+0.897	-0.889
JES Pileup offset mu	+0.0048	-0.0042	+7.343	-7.403
JES relative nonclosure	+0.0078	0.0000	+0.990	-1.088
JES single particle	+0.0000	0.0000	+0.000	-0.000
JES statistical 1	+0.0060	0.0000	+3.007	-3.148
JES statistical 2	+0.0018	0.0000	+0.008	-0.039
JES statistical 3	+0.0066	-0.0012	+0.399	-0.383
Jet vertex fraction	+0.0000	-0.0006	+3.445	-2.870
Jet efficiency	+0.0000	0.0000	+1.150	-1.145

Continued on next page

Continued from previous page

Central values:	$\alpha_\ell P = -0.0408$		$\sigma = +174.15$	
Source of Uncertainty	$\Delta\alpha_\ell P$		$\Delta\sigma$	
Jet energy resolution	+0.0300	-0.0336	+16.393	-16.022
b-tag eff.	+0.0048	-0.0078	+9.734	-8.163
c-tag eff.	+0.0030	-0.0036	+2.686	-2.627
mistag rate	+0.0006	-0.0012	+2.644	-2.616
Pile up	+0.0120	-0.0048	+7.397	-7.457
Cellout	+0.0048	-0.0036	+0.040	-0.154
W heavy flavor factors	+0.0090	-0.0090	+6.139	-5.921
W iqopt3	+0.0006	-0.0006	+0.995	-0.994
W ptjmin	+0.0012	-0.0012	+0.339	-0.338
QCD/Fakes	+0.0030	-0.0090	+0.118	-0.044
MC Generator	+0.0048	-0.0054	+10.354	-9.237
Color reconnection	+0.0054	-0.0054	+0.578	-0.581
ISR/FSR variation	+0.0006	-0.0006	+2.609	-2.532
Fragmentation/Parton shower	+0.0006	-0.0006	+0.516	-0.512
Underlying event	+0.0000	0.0000	+0.346	-0.345
CT10 PDF	+0.0018	-0.0018	+7.647	-7.416
Spin correlation value	+0.0024	-0.0024	+0.040	-0.040
Monte Carlo background x-section	+0.0048	-0.0048	+5.420	-5.420

Continued on next page

Continued from previous page

Central values:	$\alpha_\ell P = -0.0408$		$\sigma = +174.15$	
Source of Uncertainty	$\Delta\alpha_\ell P$		$\Delta\sigma$	
Monte Carlo signal & bkg branching ratio	+0.001	-0.001	+1.600	-1.571
Monte Carlo statistics	+0.0006	-0.0006	+0.759	-0.758
Luminosity	+0.0006	-0.0006	+3.554	-3.424
Template statistics for template fits	+0.0174	-0.0174	+0.000	-0.000
Top Mass	+0.0150	-0.0150	+2.604	-2.604
InterPDF	+0.0030	-0.0030	+6.860	-6.860
Total Systematic Uncertainty	+0.0570	-0.0552	+32.463	-31.183

Table F.16.: Uncertainties on $\alpha_\ell P$ and σ for the μ+jets fit using both lepton charges for the CP violating scenario.

Central values:	$\alpha_\ell P = 0.036$		$\sigma = +179.24$	
Source of Uncertainty	$\Delta\alpha_\ell P$		$\Delta\sigma$	
Statistical Uncertainty	+0.0228	-0.0228	+1.22	-1.22
Electron identification and smearing	+0.0000	0.0000	+0.000	-0.000
Electron reconstruction	+0.0000	0.0000	+0.000	-0.000
Electron trigger	+0.0000	0.0000	+0.000	-0.000
Electron scale	+0.0000	0.0000	+0.000	-0.000

Continued on next page

Continued from previous page

Central values:	$\alpha_\ell P = 0.036$		$\sigma = +179.24$	
Source of Uncertainty	$\Delta\alpha_\ell P$		$\Delta\sigma$	
Electron resolution	+0.0000	0.0000	+0.000	-0.000
Muon identification	+0.0000	0.0000	+0.000	-0.000
Muon reconstruction	+0.0000	0.0000	+0.000	-0.000
Muon trigger	+0.0000	0.0000	+0.000	-0.000
Muon rescaling	+0.0006	-0.0006	+0.010	-0.009
Muon spectrometer	+0.0000	-0.0006	+0.005	-0.000
Muon tracker	+0.0006	0.0000	+0.004	-0.000
b-JES	+0.0024	0.0000	+1.579	-1.403
JES Closeby	+0.0012	0.0000	+4.063	-3.887
JES Detector 1	+0.0000	-0.0006	+2.203	-2.087
JES Detector 2	+0.0024	0.0000	+0.195	-0.199
JES Eta Intercalib.Tot. Stat.	+0.0012	-0.0006	+1.277	-1.147
JES Eta Intercalib. Theo.	+0.0012	-0.0024	+3.837	-3.553
JES flavor component	+0.0000	-0.0018	+1.977	-1.935
JES flavor response	+0.0000	-0.0030	+4.619	-4.490
JES mixed 1	+0.0024	0.0000	+0.216	-0.219
JES mixed 2	+0.0030	0.0000	+0.864	-0.757
JES modelling 1	+0.0012	-0.0018	+5.231	-5.290

Continued on next page

Continued from previous page

Central values:	$\alpha_\ell P = 0.036$		$\sigma = +179.24$	
Source of Uncertainty	$\Delta\alpha_\ell P$		$\Delta\sigma$	
JES modelling 2	+0.0024	0.0000	+0.153	-0.181
JES modelling 3	+0.0012	0.0000	+0.093	-0.113
JES modelling 4	+0.0012	0.0000	+0.160	-0.156
JES Pileup offset NPV	+0.0006	-0.0006	+0.833	-0.768
JES Pileup offset mu	+0.0006	-0.0030	+6.992	-6.650
JES relative nonclosure	+0.0024	0.0000	+0.841	-0.809
JES single particle	+0.0000	0.0000	+0.001	-0.000
JES statistical 1	+0.0000	-0.0024	+3.020	-3.035
JES statistical 2	+0.0024	0.0000	+0.019	-0.011
JES statistical 3	+0.0012	0.0000	+0.313	-0.331
Jet vertex fraction	+0.0000	-0.0006	+3.516	-2.955
Jet efficiency	+0.0000	0.0000	+0.384	-0.382
Jet energy resolution	+0.0048	-0.0048	+4.945	-4.835
b-tag eff.	+0.0024	-0.0024	+9.600	-8.078
c-tag eff.	+0.0018	-0.0018	+3.049	-2.994
mistag rate	+0.0000	-0.0006	+2.679	-2.674
Pile up	+0.0024	-0.0030	+7.041	-6.694
Cellout	+0.0024	0.0000	+0.077	-0.156

Continued on next page

Continued from previous page

Central values:	$\alpha_\ell P = 0.036$		$\sigma = +179.24$	
Source of Uncertainty	$\Delta\alpha_\ell P$		$\Delta\sigma$	
W heavy flavor factors	+0.0078	-0.0084	+4.752	-5.077
W iqopt3	+0.0012	-0.0012	+0.760	-0.757
W ptjmin	+0.0006	-0.0006	+0.198	-0.196
QCD/Fakes	+0.0000	0.0000	+0.068	-0.031
MC Generator	+0.0024	-0.0030	+9.525	-8.611
Color reconnection	+0.0018	-0.0018	+0.108	-0.111
ISR/FSR variation	+0.0030	-0.0030	+0.404	-0.406
Fragmentation/Parton shower	+0.0036	-0.0036	+0.220	-0.220
Underlying event	+0.0054	-0.0060	+0.254	-0.255
CT10 PDF	+0.0000	0.0000	+7.990	-7.741
Spin correlation value	+0.0000	0.0000	+0.010	-0.010
Monte Carlo background x-section	+0.0048	-0.0036	+4.821	-5.393
Monte Carlo signal & bkg branching ratio	+0.000	-0.000	+1.626	-1.597
Monte Carlo statistics	+0.0006	-0.0006	+0.454	-0.453
Luminosity	+0.0000	0.0000	+3.574	-3.446
Template statistics for template fits	+0.0084	-0.0084	+0.000	-0.000
Top Mass	+0.0006	-0.0006	+2.213	-2.213

Continued on next page

Continued from previous page

Central values:	$\alpha_\ell P = 0.036$	$\sigma = +179.24$
Source of Uncertainty	$\Delta\alpha_\ell P$	$\Delta\sigma$
InterPDF	+0.0006 -0.0006	+6.260 -6.260
Total Systematic Uncertainty	+0.0180 -0.0174	+26.635 -25.374

Table F.17.: Uncertainties on $\alpha_\ell P$ and σ for the μ+jets fit using negatively charged leptons for the CP violating scenario.

Central values:	$\alpha_\ell P = 0.0684$	$\sigma = +179.17$
Source of Uncertainty	$\Delta\alpha_\ell P$	$\Delta\sigma$
Statistical Uncertainty	+0.0318 -0.0318	+1.72 -1.71
Electron identification and smearing	+0.0000 0.0000	+0.000 -0.000
Electron reconstruction	+0.0000 0.0000	+0.000 -0.000
Electron trigger	+0.0000 0.0000	+0.000 -0.000
Electron scale	+0.0000 0.0000	+0.000 -0.000
Electron resolution	+0.0000 0.0000	+0.000 -0.000
Muon identification	+0.0000 0.0000	+0.000 -0.000
Muon reconstruction	+0.0006 -0.0006	+0.002 -0.002
Muon trigger	+0.0006 -0.0006	+0.004 -0.004
Muon rescaling	+0.0144 -0.0174	+0.061 -0.058

Continued on next page

Continued from previous page

Central values:	$\alpha_\ell P = 0.0684$		$\sigma = +179.17$	
Source of Uncertainty	$\Delta\alpha_\ell P$		$\Delta\sigma$	
Muon spectrometer	+0.0000	-0.0006	+0.002	-0.002
Muon tracker	+0.0006	-0.0006	+0.002	-0.001
b-JES	+0.0096	-0.0030	+1.556	-1.368
JES Closeby	+0.0018	-0.0036	+3.766	-3.685
JES Detector 1	+0.0144	-0.0132	+2.154	-2.011
JES Detector 2	+0.0018	0.0000	+0.211	-0.181
JES Eta Intercalib.Tot. Stat.	+0.0000	-0.0006	+1.221	-1.048
JES Eta Intercalib. Theo.	+0.0138	-0.0126	+3.797	-3.460
JES flavor component	+0.0018	-0.0042	+1.833	-1.814
JES flavor response	+0.0000	-0.0012	+4.330	-4.214
JES mixed 1	+0.0030	-0.0006	+0.248	-0.214
JES mixed 2	+0.0030	0.0000	+0.796	-0.695
JES modelling 1	+0.0090	-0.0054	+4.832	-4.934
JES modelling 2	+0.0072	-0.0048	+0.144	-0.127
JES modelling 3	+0.0084	-0.0078	+0.084	-0.065
JES modelling 4	+0.0006	-0.0012	+0.178	-0.148
JES Pileup offset NPV	+0.0018	-0.0018	+0.711	-0.742
JES Pileup offset mu	+0.0030	-0.0042	+6.578	-6.161

Continued on next page

Continued from previous page

Central values:	$\alpha_\ell P = 0.0684$		$\sigma = +179.17$	
Source of Uncertainty	$\Delta\alpha_\ell P$		$\Delta\sigma$	
JES relative nonclosure	+0.0006	0.0000	+0.794	-0.761
JES single particle	+0.0000	0.0000	+0.000	-0.000
JES statistical 1	+0.0090	-0.0096	+2.812	-2.763
JES statistical 2	+0.0024	-0.0006	+0.030	-0.011
JES statistical 3	+0.0048	-0.0030	+0.350	-0.316
Jet vertex fraction	+0.0024	-0.0012	+3.379	-2.811
Jet efficiency	+0.0012	-0.0012	+0.509	-0.508
Jet energy resolution	+0.0252	-0.0222	+12.505	-12.265
b-tag eff.	+0.0054	-0.0030	+9.379	-7.878
c-tag eff.	+0.0066	-0.0066	+2.816	-2.769
mistag rate	+0.0036	-0.0036	+2.206	-2.193
Pile up	+0.0042	-0.0048	+6.617	-6.206
Cellout	+0.0024	-0.0030	+0.061	-0.240
W heavy flavor factors	+0.0132	-0.0120	+3.783	-4.140
W iqopt3	+0.0000	0.0000	+0.554	-0.554
W ptjmin	+0.0018	-0.0018	+0.222	-0.222
QCD/Fakes	+0.0114	-0.0180	+0.037	-0.047
MC Generator	+0.0036	-0.0042	+9.442	-8.546

Continued on next page

Continued from previous page

Central values:	$\alpha_\ell P = 0.0684$		$\sigma = +179.17$	
Source of Uncertainty	$\Delta\alpha_\ell P$		$\Delta\sigma$	
Color reconnection	+0.0000	0.0000	+0.108	-0.111
ISR/FSR variation	+0.0024	-0.0018	+0.465	-0.463
Fragmentation/Parton shower	+0.0060	-0.0054	+0.208	-0.209
Underlying event	+0.0096	-0.0096	+0.094	-0.094
CT10 PDF	+0.0018	-0.0018	+8.003	-7.752
Spin correlation value	+0.0024	-0.0024	+0.033	-0.033
Monte Carlo background x-section	+0.0144	-0.0126	+3.957	-4.407
Monte Carlo signal & bkg branching ratio	+0.001	-0.000	+1.627	-1.598
Monte Carlo statistics	+0.0018	-0.0018	+0.595	-0.593
Luminosity	+0.0000	0.0000	+3.538	-3.412
Template statistics for template fits	+0.0114	-0.0114	+0.000	-0.000
Top Mass	+0.0120	-0.0120	+2.259	-2.259
InterPDF	+0.0012	-0.0012	+6.210	-6.210
Total Systematic Uncertainty	+0.0522	-0.0498	+28.138	-26.831

Table F.18.: Uncertainties on $\alpha_\ell P$ and σ for the μ+jets fit using positively charged leptons for the CP violating scenario.

Central values:	$\alpha_\ell P = 0$		$\sigma = +179.71$	
Source of Uncertainty	$\Delta\alpha_\ell P$		$\Delta\sigma$	
Statistical Uncertainty	+0.0330	-0.0330	+1.77	-1.76
Electron identification and smearing	+0.0000	0.0000	+0.000	-0.000
Electron reconstruction	+0.0000	0.0000	+0.000	-0.000
Electron trigger	+0.0000	0.0000	+0.000	-0.000
Electron scale	+0.0000	0.0000	+0.000	-0.000
Electron resolution	+0.0000	0.0000	+0.000	-0.000
Muon identification	+0.0000	0.0000	+0.000	-0.000
Muon reconstruction	+0.0006	-0.0006	+0.003	-0.002
Muon trigger	+0.0006	-0.0006	+0.003	-0.003
Muon rescaling	+0.0264	-0.0216	+0.081	-0.074
Muon spectrometer	+0.0012	0.0000	+0.000	-0.004
Muon tracker	+0.0018	0.0000	+0.001	-0.006
b-JES	+0.0084	-0.0078	+1.699	-1.504
JES Closeby	+0.0042	0.0000	+4.331	-4.085
JES Detector 1	+0.0132	-0.0168	+2.431	-2.315
JES Detector 2	+0.0036	0.0000	+0.166	-0.234
JES Eta Intercalib.Tot. Stat.	+0.0036	-0.0018	+1.345	-1.274

Continued on next page

Continued from previous page

Central values:	$\alpha_\ell P = 0$		$\sigma = +179.71$	
Source of Uncertainty	$\Delta\alpha_\ell P$		$\Delta\sigma$	
JES Eta Intercalib. Theo.	+0.0168	-0.0198	+4.072	-3.820
JES flavor component	+0.0036	-0.0066	+2.181	-2.105
JES flavor response	+0.0030	-0.0066	+4.958	-4.801
JES mixed 1	+0.0042	0.0000	+0.186	-0.250
JES mixed 2	+0.0030	0.0000	+0.932	-0.822
JES modelling 1	+0.0012	-0.0054	+5.606	-5.566
JES modelling 2	+0.0108	-0.0036	+0.071	-0.174
JES modelling 3	+0.0102	-0.0072	+0.000	-0.075
JES modelling 4	+0.0030	0.0000	+0.142	-0.190
JES Pileup offset NPV	+0.0006	-0.0006	+0.976	-0.804
JES Pileup offset mu	+0.0000	-0.0030	+7.403	-7.137
JES relative nonclosure	+0.0042	0.0000	+0.894	-0.878
JES single particle	+0.0000	0.0000	+0.002	-0.000
JES statistical 1	+0.0042	-0.0126	+3.155	-3.195
JES statistical 2	+0.0036	0.0000	+0.007	-0.034
JES statistical 3	+0.0042	-0.0018	+0.310	-0.388
Jet vertex fraction	+0.0000	-0.0012	+3.663	-3.095
Jet efficiency	+0.0030	-0.0030	+0.700	-0.693

Continued on next page

Continued from previous page

Central values:	$\alpha_\ell P = 0$		$\sigma = +179.71$	
Source of Uncertainty	$\Delta\alpha_\ell P$		$\Delta\sigma$	
Jet energy resolution	+0.0228	-0.0264	+14.808	-14.504
b-tag eff.	+0.0090	-0.0114	+9.965	-8.383
c-tag eff.	+0.0030	-0.0030	+3.246	-3.184
mistag rate	+0.0012	-0.0018	+3.159	-3.165
Pile up	+0.0030	-0.0030	+7.467	-7.182
Cellout	+0.0066	-0.0024	+0.066	-0.081
W heavy flavor factors	+0.0180	-0.0186	+6.160	-6.392
W iqopt3	+0.0024	-0.0024	+1.114	-1.109
W ptjmin	+0.0006	-0.0006	+0.450	-0.446
QCD/Fakes	+0.0198	-0.0126	+0.029	-0.031
MC Generator	+0.0012	-0.0018	+9.634	-8.702
Color reconnection	+0.0036	-0.0036	+0.089	-0.092
ISR/FSR variation	+0.0042	-0.0036	+0.338	-0.340
Fragmentation/Parton shower	+0.0012	-0.0012	+0.210	-0.210
Underlying event	+0.0018	-0.0018	+0.376	-0.378
CT10 PDF	+0.0018	-0.0018	+7.988	-7.735
Spin correlation value	+0.0024	-0.0024	+0.014	-0.015
Monte Carlo background x-section	+0.0042	-0.0042	+5.680	-6.388

Continued on next page

Continued from previous page				
Central values:	$\alpha_\ell P = 0$		$\sigma = +179.71$	
Source of Uncertainty	$\Delta\alpha_\ell P$		$\Delta\sigma$	
Monte Carlo signal & bkg branching ratio	+0.001	-0.001	+1.632	-1.603
Monte Carlo statistics	+0.0006	-0.0006	+0.686	-0.685
Luminosity	+0.0006	-0.0006	+3.620	-3.491
Template statistics for template fits	+0.0126	-0.0126	+0.000	-0.000
Top Mass	+0.0144	-0.0144	+2.320	-2.320
InterPDF	+0.0012	-0.0012	+6.320	-6.320
Total Systematic Uncertainty	+0.0582	-0.0576	+31.190	-29.969

Bibliography

[1] M. Kobayashi and T. Maskawa, Prog.Theor.Phys. **49** (1973) 652–657.

[2] CDF Collaboration, F. Abe et al., Phys. Rev. Lett. **74** (1995) 2626–2631, arXiv:hep-ex/9503002 [hep-ex].

[3] D0 Collaboration, S. Abachi et al., Phys. Rev. Lett. **74** (1995) 2632–2637, arXiv:hep-ex/9503003 [hep-ex].

[4] Particle Data Group Collaboration, J. Beringer et al., Phys.Rev. **D86** (2012) 010001.

[5] WMAP Collaboration, C. Bennett et al., Astrophys.J.Suppl. **208** (2013) 20, arXiv:1212.5225 [astro-ph.CO].

[6] S. Glashow, Nucl.Phys. **22** (1961) 579–588.

[7] A. Salam and J. C. Ward, Phys.Lett. **13** (1964) 168–171.

[8] S. Weinberg, Phys.Rev.Lett. **19** (1967) 1264–1266.

[9] P. W. Higgs, Phys.Lett. **12** (1964) 132–133.

[10] P. W. Higgs, Phys.Rev.Lett. **13** (1964) 508–509.

[11] F. Englert and R. Brout, Phys.Rev.Lett. **13** (1964) 321–323.

[12] G. Guralnik, C. Hagen, and T. Kibble, Phys.Rev.Lett. **13** (1964) 585–587.

[13] ATLAS Collaboration, G. Aad et al., Phys.Lett. **B716** (2012) 1–29, arXiv:1207.7214 [hep-ex].

[14] CMS Collaboration, S. Chatrchyan et al., Phys.Lett. **B716** (2012) 30–61, arXiv:1207.7235 [hep-ex].

[15] N. Cabibbo, Phys.Rev.Lett. **10** (1963) 531–533.

[16] J. Christenson, J. Cronin, V. Fitch, and R. Turlay, Phys.Rev.Lett. **13** (1964) 138–140.

[17] C. Wu, E. Ambler, R. Hayward, D. Hoppes, and R. Hudson, Phys.Rev. **105** (1957) 1413–1414.

[18] D. J. Gross and F. Wilczek, Phys.Rev.Lett. **30** (1973) 1343–1346.

[19] H. D. Politzer, Phys.Rev.Lett. **30** (1973) 1346–1349.

[20] S. W. Herb, D. C. Hom, L. M. Lederman, J. C. Sens, H. D. Snyder, J. K. Yoh, J. A. Appel, B. C. Brown, C. N. Brown, W. R. Innes, K. Ueno, T. Yamanouchi, A. S. Ito, H. Jöstlein, D. M. Kaplan, and R. D. Kephart, Phys. Rev. Lett. **39** (1977) 252–255. http://link.aps.org/doi/10.1103/PhysRevLett.39.252.

[21] R. Dalitz and G. R. Goldstein, Phys.Rev. **D45** (1992) 1531–1543.

[22] S. L. Glashow, J. Iliopoulos, and L. Maiani, Phys. Rev. D **2** (1970) 1285–1292. http://link.aps.org/doi/10.1103/PhysRevD.2.1285.

[23] W. Bernreuther and Z.-G. Si, Physics Letters **B725** no. 1-3, (August 2013) 115–122, arXiv:1305.2066 [hep-ph].

[24] D0 Collaboration, V. M. Abazov et al., Phys.Rev. **D84** (2011) 112005, arXiv:1107.4995 [hep-ex].

[25] D0 Collaboration, V. M. Abazov et al., Phys.Rev. **D87** (2013) 011103, arXiv:1207.0364 [hep-ex].

[26] CDF Collaboration, T. Aaltonen et al., Phys.Rev. **D87** (2013) 092002, arXiv:1211.1003 [hep-ex].

[27] D. Krohn, T. Liu, J. Shelton, and L.-T. Wang, Phys.Rev. **D84** (2011) 074034, arXiv:1105.3743 [hep-ph].

[28] S. Fajfer, J. F. Kamenik, and B. Melic, JHEP **1208** (2012) 114, arXiv:1205.0264 [hep-ph].

[29] J. Aguilar-Saavedra and M. Perez-Victoria, J.Phys.Conf.Ser. **447** (2013) 012015, arXiv:1302.6618 [hep-ph].

[30] E. L. Berger, Q.-H. Cao, J.-H. Yu, and H. Zhang, Phys.Rev.Lett. **109** (2012) 152004, arXiv:1207.1101 [hep-ph].

[31] G. Mahlon and S. J. Parke, Phys.Rev. **D81** (2010) 074024, arXiv:1001.3422 [hep-ph].

[32] G. Mahlon and S. J. Parke, Phys. Rev. D **53** (1996) 4886, arXiv:hep-ph/9512264.

[33] A. Brandenburg, Z. Si, and P. Uwer, Phys. Lett. B **539** (2002) 235–241, arXiv:hep-ph/0205023.

[34] Tech. Rep. ATLAS-CONF-2013-101, CERN, Geneva, Sep, 2013.

[35] CDF Collaboration, T. Aaltonen et al., Phys.Rev. **D83** (2011) 031104, arXiv:1012.3093 [hep-ex].

[36] D0 Collaboration, V. M. Abazov et al., Phys.Lett. **B702** (2011) 16–23, arXiv:1103.1871 [hep-ex].

[37] D0 Collaboration, V. M. Abazov et al., Phys.Rev.Lett. **107** (2011) 032001, arXiv:1104.5194 [hep-ex].

[38] D0 Collaboration, V. M. Abazov et al., Phys.Rev.Lett. **108** (2012) 032004, arXiv:1110.4194 [hep-ex].

[39] ATLAS Collaboration Collaboration, G. Aad et al., Phys.Rev.Lett. **108** (2012) 212001, arXiv:1203.4081 [hep-ex].

[40] W. G. D. Dharmaratna and G. R. Goldstein, Phys. Rev. D **41** (1990) 1731–1735. http://link.aps.org/doi/10.1103/PhysRevD.41.1731.

[41] W. Bernreuther, A. Brandenburg, and P. Uwer, Phys.Lett. **B368** (1996) 153–162, arXiv:hep-ph/9510300 [hep-ph].

[42] G. L. Kane, G. A. Ladinsky, and C. P. Yuan, Phys. Rev. D **45** (1992) 124–141. http://link.aps.org/doi/10.1103/PhysRevD.45.124.

[43] F. del Aguila and J. Aguilar-Saavedra, Phys.Rev. **D67** (2003) 014009, arXiv:hep-ph/0208171 [hep-ph].

[44] UA1 Collaboration Collaboration, G. Arnison et al., Phys.Lett. **B122** (1983) 103–116.

[45] UA1 Collaboration Collaboration, G. Arnison et al., Phys.Lett. **B126** (1983) 398–410.

[46] L. Evans and P. Bryant, JINST **3** (2008) S08001.

[47] D0 Collaboration, V. M. Abazov et al., Phys. Rev. **D85** (2012) 091104, arXiv:1201.4156 [hep-ex].

[48] D0 Collaboration, V. M. Abazov et al., Phys.Rev. **D87** (2013) 011103, arXiv:1207.0364 [hep-ex].

[49] CMS Collaboration, Tech. Rep. CMS-PAS-TOP-13-001, CERN, Geneva, 2013.

[50] ATLAS Collaboration, Tech. Rep. ATLAS-CONF-2012-133, CERN, Geneva, Sep, 2012.

[51] ATLAS Collaboration, G. Aad et al., Phys.Rev.Lett. **111** (2013) 232002, arXiv:1307.6511 [hep-ex].

[52] GEANT4 Collaboration, S. Agostinelli et al., Nucl. Instrum. Methods Phys. Res., Sect. A **506** (2003) 250.

[53] ATLAS Collaboration, Eur. Phys. J. C **70** (2010) 823, arXiv:1005.4568 [physics.ins-det].

[54] ATLAS Collaboration, G. Aad et al., Phys.Rev. **D83** (2011) 052003, arXiv:1101.0070 [hep-ex].

[55] S. Frixione and B. R. Webber, JHEP **0206** (2002) 029, arXiv:hep-ph/0204244 [hep-ph].

[56] H.-L. Lai, M. Guzzi, J. Huston, Z. Li, P. M. Nadolsky, et al., Phys.Rev. **D82** (2010) 074024, arXiv:1007.2241 [hep-ph].

[57] G. Corcella, I. Knowles, G. Marchesini, S. Moretti, K. Odagiri, et al., JHEP **0101** (2001) 010, arXiv:hep-ph/0011363 [hep-ph].

[58] J. Butterworth, J. R. Forshaw, and M. Seymour, Z.Phys. **C72** (1996) 637–646, arXiv:hep-ph/9601371 [hep-ph].

[59] M. Aliev, H. Lacker, U. Langenfeld, S. Moch, P. Uwer, et al., Comput.Phys.Commun. **182** (2011) 1034–1046, arXiv:1007.1327 [hep-ph].

[60] B. P. Kersevan and E. Richter-Was, arXiv:hep-ph/0405247 [hep-ph].

[61] M. L. Mangano, M. Moretti, F. Piccinini, R. Pittau, and A. D. Polosa, JHEP **0307** (2003) 001, arXiv:hep-ph/0206293 [hep-ph].

[62] ATLAS Collaboration, G. Aad et al., Eur.Phys.J. **C72** (2012) 2039,

arXiv:1203.4211 [hep-ex].

[63] ATLAS Collaboration, G. Aad et al., Eur.Phys.J. **C71** (2011) 1577, arXiv:1012.1792 [hep-ex].

[64] ATLAS Collaboration, G. Aad et al., Eur.Phys.J. **C73** (2013) 2261, arXiv:1207.5644 [hep-ex].

[65] M. Cacciari, G. P. Salam, and G. Soyez, JHEP **0804** (2008) 063, arXiv:0802.1189 [hep-ph].

[66] ATLAS Collaboration, G. Aad et al., Eur.Phys.J. **C71** (2011) 1512, arXiv:1009.5908 [hep-ex].

[67] ATLAS Collaboration, Tech. Rep. ATLAS-CONF-2013-004, CERN, Geneva, Jan, 2013.

[68] N. Bousson, Tech. Rep. ATL-COM-PHYS-2011-1472, CERN, Geneva, Oct, 2011.

[69] ATLAS Collaboration, Tech. Rep. ATLAS-CONF-2012-043, CERN, Geneva, Mar, 2012.

[70] ATLAS Collaboration, Tech. Rep. ATLAS-CONF-2012-040, CERN, Geneva, Mar, 2012.

[71] ATLAS Collaboration, G. Aad et al., Phys.Lett. **B721** (2013) 171–189, arXiv:1301.1583 [hep-ex].

[72] A. Dos Anjos, S. Armstrong, J. Baines, C. Bee, M. Biglietti, et al.,.

[73] ATLAS Collaboration, G. Aad et al., Eur.Phys.J. **C72** (2012) 1844, arXiv:1108.5602 [hep-ex].

[74] A. Caldwell, D. Kollár, and K. Kröninger, Computer Physics Communications **180** (2009) 2197–2209, arXiv:0808.2552 [physics.data-an].

[75] ATLAS Collaboration, G. Aad et al., Eur.Phys.J. **C72** (2012) 2046, arXiv:1203.5755 [hep-ex].

[76] F. James and M. Roos, Comput. Phys. Commun. **10** no. 6, (1975) 343–67.

[77] ATLAS Collaboration, G. Aad et al., JHEP **1301** (2013) 116, arXiv:1211.2202 [hep-ex].

[78] S. Frixione, P. Nason, and C. Oleari, JHEP **0711** (2007) 070, arXiv:0709.2092 [hep-ph].

[79] ATLAS Collaboration, G. Aad et al., Eur.Phys.J. **C72** (2012) 2043, arXiv:1203.5015 [hep-ex].

[80] ATLAS Collaboration, G. Aad et al., Eur.Phys.J. **C72** (2012) 1909, arXiv:1110.3174 [hep-ex].

[81] ATLAS Collaboration, Tech. Rep. ATLAS-CONF-2011-063, CERN, Geneva, Apr, 2011.

[82] ATLAS Collaboration, Tech. Rep. ATLAS-CONF-2011-046, CERN, Geneva, Mar, 2011.

[83] ATLAS Collaboration, Tech. Rep. ATLAS-CONF-2013-004, CERN, Geneva, Jan, 2013.

[84] ATLAS Collaboration, G. Aad et al., Eur.Phys.J. **C73** (2013) 2306, arXiv:1210.6210 [hep-ex].

[85] ATLAS Collaboration, G. Aad et al., Eur.Phys.J. **C72** (2012) 1844, arXiv:1108.5602 [hep-ex].

[86] ATLAS Collaboration, G. Aad et al., JHEP **1301** (2013) 116, arXiv:1211.2202 [hep-ex].

[87] R. Brun and F. Rademakers, Nucl.Inst.& Meth. in Phys. Res. A **389** (1996) 81–86.